FUNCTIONAL LIGNIN FOR COATING AND 3D PRINTING

A Thesis Submitted to the faculty of Graduate Studies of
Lakehead University

by

Banchamlak Bemerw Kassaun

Submitted in partial fulfillment of requirements for the
degree of Doctor of Philosophy in Biotechnology

November 2024

Dedication

To my mom, who taught me the value of hard work, dedication, and sacrifice.

Abstract

The abundance of lignin, aromatic structure, and multifunctional groups uniquely appeal for use in advanced sustainable functional materials. Currently, the available lignin is not derived from a lignin-first strategy; instead, it is a byproduct of the paper and pulp industry, where the primary focus is on cellulose, resulting in structural alterations. Consequently, lignin exhibits variable structural characteristics and includes impurities that restrict its valorization for diverse applications. This thesis employed functionalization and fractionation combined with functionalization to leverage lignin in advanced applications, including functional coatings, composite films, and 3D printing.

The initial portion of this thesis focuses on the eco-friendly grafting of a silsesquioxane chain onto kraft lignin to produce a homogeneous superhydrophobic and flame-retardant lignin. A detailed study was conducted on the chemical interaction between softwood kraft lignin and aminopropyl/methyl silsesquioxane. Nuclear magnetic resonance (NMR) and X-ray photoelectron spectroscopy (XPS) measurements validated the transformation of hydroxyl groups in kraft lignin to Si-O-C by polycondensation. The resulting lignin was employed with an aluminum phosphate binder to dip-coat a stain-grade pine wood species. The second study concentrated on integrating lignin-silsesquioxane copolymer at an elevated concentration with water-based polyurethane (PU) polymer. Sulfoethylated lignin was employed as a dispersant in the lignin-PU composite formulation to enhance the dispersion of the lignin-silsesquioxane polymer in PU. In both studies, the functionalized lignin surpassed unfunctional lignin in hydrophobic and thermal properties, endowing coated wood with superhydrophobic characteristics and flame-retardant features. The functionalized lignin incorporation in PU at a higher concentration (>50) was possible while improving the hydrophobic, thermal, and flame-retardant characteristics of PU. A reduced concentration of functionalized lignin (10%) enhanced the surface, mechanical, and thermal characteristics of pure PU compared to unfunctionalized lignin at an equivalent concentration. This is related to the improved properties of lignin due to functionalization. The optimization conditions derived from the initial investigation were employed in the third study, whereby lignin was functionalized using a fluoro silsesquioxane agent, effectively incorporating lignin into natural rubber latex. The functionalized lignin-natural rubber composite film demonstrated superior surface, mechanical, and thermal characteristics compared to pure natural rubber films and unfunctionalized lignin incorporated into natural rubber latex. The mechanical strength of the functionalized lignin natural rubber sheets demonstrated resistance to moisture and temperature exposure, as well as superhydrophobic properties. The films showed a preference for oil over water, thereby making them suitable for oil-water separation.

This thesis also involves lignin fractionation using ethanol and ring-opening functionalization for fused deposition modeling (FDM)-three-dimensional (3D) printing and wood coating applications. Polymerization takes place in ethanol-soluble fractionated lignin and caprolactone. Ethanol fractionation reduced average molecular weight and decreased polydispersity as hydroxyl group content increased. Lignin-caprolactone polymerization optimizes for its melt temperature, viscosity, and degree of polymerization via the Box-Behnken-Response Surface Methodology. The optimized sample lignin-caprolactone polymer was utilized for FDM-3D printing. The ethanol fractionation enabled 3D printing of lignin-caprolactone polymer, enhancing interfacial adhesion and mechanical properties. In addition, the optimized polymerization conditions were applied to birch alkali, wheat straw alkali, and kraft lignin-caprolactone copolymer following the optimal process. The methods enhanced the lignin-caprolactone polymer's surface, thermal, and flame-retardant characteristics. This thesis generally presents sustainable techniques to improve lignin for advanced applications.

Acknowledgments

I extend my profound thanks to Professor Pedram Fatehi for the invaluable opportunity and for his hands-on supervision, assistance, and patience. His unwavering focus and mentorship have been instrumental in my development as a proficient and independent researcher. I sincerely appreciate the opportunities he provided during this study, which facilitated my growth both in research and as an individual.

Professor Fatehi, you have uniquely influenced my path. Thank you!

I want to thank my thesis committee members, Dr. Ebrahim Rezaei, Dr. Leila Pakzad, and Dr. Baoqiang Liao, for their time and contributions.

I want to express my gratitude to Professor Chunlin Xu, Dr. Luyao Wang, Oskar Backman, and the members of Natural Materials Technology (NMT) in the Faculty of Science and Engineering, Abo Akademi University. Thank you, Professor Chunlin, for offering suitable laboratory facilities and guidance throughout my exchange term in your lab. Dr. Luyao, Oskar Backman, and the LigninReSurf project team thank you for the open and cooperative atmosphere.

I want to extend my appreciation to Dr. Weijue Gao and the members of the Green Research laboratory, both past and present, for the warm work environment, support, and kindness. I want to extend my appreciation to my colleagues Dr. Jonathan Diaz, Saba Khodavandegar, and Fatemeh Hassan Pour for the collaboration outside of this thesis work.

Gratitude is extended to Dr. Guoseheng Wu and Mr. Michael Sorokopud from the LUIL department of Lakehead University for their highly valued technical support. I would like to extend my sincere gratitude to Dr. Brenda Magajna for her unwavering support as the Ph.D. Program Facilitator and International Student Liaison.

I extend my highest admiration and gratitude to Dr. Magdi Gibril and Dr. Tamirat Tesfaye, who enlightened my research perspective and facilitated possibilities at the start of my academic career. I am grateful for the chance and assistance.

Friends and extended relatives, I extend my gratitude to Zewdie Kiflu, Tigist Solomon, Tesfaye Bayeh, Selam Tamirat, Tesfaldet Esubalew, and Ameena Bacchus for their support throughout my times of greatest need. This would not be feasible without your assistance.

My mother, Yeshiwork Anemaw; my brother, Tsehaye Bemerw; my sister, Meteka Bemerw; my cousin, Meles Yigezaw; and my husband, Bewuket Teshome. Thank you for your affection and for motivating me to push my boundaries. I am grateful for all the work you have invested in me over the years. Thank you, my spouse, for your understanding, encouragement, and support. *I extend my gratitude to my nieces and nephews for your prayers, inquiries about my well-being, and presence; you are the reason for my resilience and current endeavors*. I cherish you!

ሁሉ በእርሱ ሆነ!

Table of contents

List of Tables

List of Figures

Chapter 1: Introduction

1.1. Lignin valorization: Importance and challenges

Lignin is the most abundant aromatic biopolymer in nature; the current exploitation of lignin is focused on energy production, use in asphalt for roads, biofuels, bioplastics, thermoplastics, thermosets, and advanced three-dimensional (3D) printing materials to replace petroleum-based materials. The West Fraser Timber kraft pulp mill in Hinton, Alberta, and Resolute Forest Products, in collaboration with FPInnovations, have led the Canadian research space by producing lignin via LignoForce system^{TM} and TMP-Bio^{TM} (Thermomechanical Pulp Biorefinery) in Canada. Globally, the valorization of lignin is expected to expand with in situ lignin functionalization biorefinery processes, such as Ecohelix technology.

Lignin is essential for material manufacturing as a substitute for petroleum-based goods, benefiting biorefining companies and fostering a circular economy. Furthermore, the distinctive properties of lignin, such as its resistance to UV radiation and thermal and moisture stability, will provide significant advantages over other chemicals that offer just a singular performance, hence decreasing production costs and facilitating manufacturing processes. Nonetheless, lignin derived from the biorefining method encounters a limitation for direct use in value-added uses. The variability in structural attributes, including purity, functionality, and molecular weight differences, restricts lignin's utilization in industries like coatings and advanced manufacturing. Therefore, the variability, complexity, and heterogeneity must be addressed to advance its applications.

1.2. Hypothesis and research objectives

The hypotheses of this thesis were as follows:

I. Lignin can be covalently crosslinked with silsesquioxane under a solvent-free system. The reaction conditions, such as the reaction temperature, reaction time, and concentration of silsesquioxane can control the performance of the lignin-silsesquioxane polymer.

II. The water-based lignin-silsesquioxane coating formulation is feasible and will improve the hydrophobicity and thermal stability of coated subjects.

III. The hydrophobic modification of lignin can increase the incorporation of lignin concentration in composite preparation with a hydrophobic polymeric matrix. The resultant composite material could perform better than unfunctionalized lignin due to the improved interfacial interaction of hydrophobized lignin and polymer matrix.

IV. An efficient fractionation approach can refine lignin into altered molar mass, polydispersity, and structural properties, which will facilitate the subsequent functionalization of lignin and improve its thermoplastic properties. The resultant polymer can be utilized for advanced applications, such as 3D printing and coating.

The overall objective of this thesis is the development of methodologies (lignin functionalization and fractionation) for upgrading technical lignin with desired properties for efficient coating formulations, integration with other polymers and 3D printing for functional materials. This approach will introduce a bio-based alternative for coating formulations, composite materials, and 3D printing polymers. More specifically, this thesis utilized advanced experimental design methods, such as Taguchi and Box-Behnken designs, to optimize the characteristics of lignin for targeted applications. This thesis also explored the difference in the characteristics of lignin from different sources with regard to ethanol fractionation and subsequent functionalization for a targeted application.

1.3. Research overview

The objectives and novelty of this thesis are summarized in each chapter as follows :

Chapter one provides the introduction of this thesis.

Chapter two provides a comprehensive literature review on the correlation between lignin types, sources, and extraction methods with structural performances and characteristics. The chapter touched on approaches followed for modifying lignin's characteristics, such as depolymerization, fractionation, and functionalization. Recent studies and advances in tailoring lignin characteristics for improving its hydrophobic, hydrophilic and flame-retardant characteristics are reviewed. The application of lignin in coatings, films, composites, and 3D printing materials is discussed.

Chapter three demonstrates, for the first time, a solvent-free polymerization of kraft lignin (KL) and aminopropyl/methyl silsesquioxane (WAPMSS) to generate a sustainable coating formula with elevated flame retardancy and superhydrophobicity for wood products. A water-soluble inorganic aluminum phosphate (AP) binder was utilized in the formulation to increase the dispersion and adherence of the copolymer. Advanced techniques, such as NMR, XPS, TGA, contact angle, limited oxygen index, and smoke detector analyzers, comprehensively investigated coating formulas' physicochemical, surface, and thermal characteristics. The results revealed that silsesquioxane-copolymerized lignin in fluorine-free aqueous coating formulations could provide impressive superhydrophobic and flame-retardant performance.

Chapter Four focuses on fabricating a novel superhydrophobic, thermally stable, and moisture-resistant sustainable NR film by incorporating lignin-derived polymers into NR. The study was composed of a simple water-based modification of kraft lignin to generate superhydrophobic lignin with improved thermal and oil adsorption characteristics. A water-based Aminopropyl/flurosilsesquioxane oligomer was selected as a silsesquioxane agent for polymerizing with KL. The changes in lignin's chemical, structural, and thermal properties were assessed comprehensively by NMR, XPS, FTIR, and TGA. The modified lignin (W) was used in natural rubber latex as a functional filler following the latex mixing method. The mechanical, thermal, and surface properties of the prepared NR-lignin films were investigated before and after exposure to heat and water. The impact of the dosage of W on NR's physicochemical properties was investigated, and the resulting superhydrophobic films' oil and water adsorption were comprehensively assessed. The results of this work provide a method to generate a sustainable superhydrophobic lignin and NR-based oil and water separator.

Chapter five presents a concise and environmentally conscious approach for synthesizing water-based PU coating materials incorporating softwood kraft lignin. This approach exploits two separate lignin modifications of a water-based silsesquioxane lignin copolymer (WL) obtained through the copolymerization of lignin with aminopropyl/methyl silsesquioxane (WAPMSS) and a sulfoethylated lignin (SL) achieved via the sulfoethylation of lignin with 2-bromoethanesulfonate. The WL was utilized as a superhydrophobic and flame retardant, while the SL was a dispersant in the PU formulation. In opposition to traditional PU/lignin composites, the composite manufacturing process was solvent- and catalyst-free. The resultant materials with a high lignin incorporation (up to 50%) showed superior water repellency, high thermal stability, excellent processability, flame-retardancy, and recyclability. Further investigations revealed that the resultant material can be utilized in a high abrasive environment while maintaining its superhydrophobicity. The contribution of Banchamlak Bemerw Kassaun to this work was the conception of the original draft, visualization, validation, formal analysis, data curation, and conceptualization.

Chapter six presents a ring-opening polymerization of birch alkali lignin (L) and CL to produce a 3D printable polymer with exceptional flow characteristics. The properties of L were enhanced using ethanol fractionation, and the ethanol soluble fractionation (L_E) polymer resulted in a lower average molecular weight than L, which was then used to fabricate lignin-caprolactone polymer with the best properties (L_EPO) following the Box-Behnken (BBD) response surface method (RSM). The printability of the selected sample was assessed by running melt rheology. Then, the 3D printing methods of FDM were employed to study the 3D printing performance of the generated sustainable material. The mechanical strength, surface properties, and appearance of 3D-printed structures were evaluated. This work demonstrates a promising approach to utilizing polymerized lignin for a microstructurally well-organized 3D printed material fabrication. The contribution of Banchamlak Bemerw Kassaun to this work was the conception of the original draft, visualization, validation, formal analysis, data curation, and conceptualization.

Chapter seven examines the impact of three distinct forms of lignin (birch alkali lignin (BL), wheat straw alkali (WL), and softwood kraft lignin (SL)) on the polymerization and performance of lignin-caprolactone polymer, both before and after ethanol fractionation. An investigation was conducted on the resulting polymer's chemical structure and thermal and viscoelastic characteristics. Furthermore, an examination was conducted via water contact angle values, smoke density, and limiting oxygen index values on coated wood to assess the efficacy of these polymers when applied as a protective layer on a wooden surface. This work paves the way for developing more eco-friendly coating materials and opens new possibilities for lignin-caprolactone polymer applications.

Chapter eight states the overall conclusions from this thesis and provides a perspective for future studies in this field.

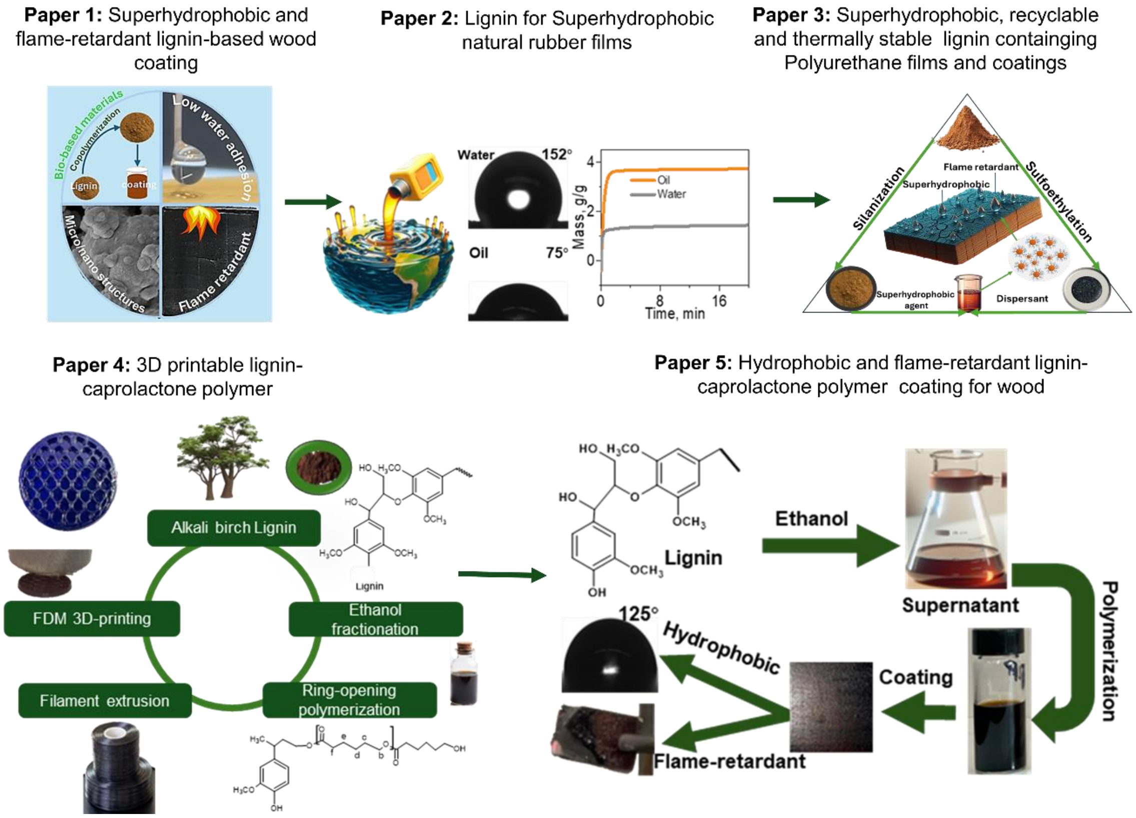

Figure 1.1. Thesis overview.

Chapter 2: Lignin Functionalization for Coating, Composite, and 3D Printing Materials: A review

2.1. Abstract

Lignin is a primary component of lignocellulosic biomass and underutilized feedstock in the growing pulping and biofuel industries. As an abundant natural polymer, lignin is frequently considered a green alternative to petroleum-based polymers, especially when applying biobased coating and 3D printing. However, lignin heterogeneity, complexity, and purity limited its widespread application. Herein, lignin's modifications via depolymerization and functionalization are discussed in many reports to increase the utilization of lignin in various applications. Lignin modifications impart hydrophilic, hydrophobic, superhydrophobic, dispersion, and flame-retardant characteristics are discussed. The applications of lignin as a polymer and composite coating are reviewed using the approach taken to improve the coating performance of lignin for different surfaces. The application of lignin as a thermoplastic polymer via grafting a flexible polymer chain and subsequent polymerization is examined. The application of lignin in the advanced manufacturing of 3D printing to improve the continued utilization of lignin as a biopolymer has been reviewed. Finally, the challenges, opportunities, and future perspectives of lignin utilization are discussed, and a conclusion is drawn.

2.2. Introduction

Urgent global issues like environmental deterioration, resource shortages, and the pursuit of sustainable development emphasize biomass exploration as a feasible alternative to petroleum-based resources [1]. Transitioning to biomass helps achieve carbon neutrality goals and supports rural economies by creating jobs in agriculture and renewable resource sectors [2]. The utilization of biomass also addresses additional challenges, such as waste management by utilizing organic waste and byproducts [3]. Lignin, part of biomass and a significant by-product of the pulp and paper industry, is the ideal polymer to achieve those goals [4]. Lignin, a complex organic polymer found in the cell walls of plants, is increasingly recognized for its potential as a renewable feedstock for various applications, including biofuels, bioplastics, and specialty chemicals [5]. Innovative extraction methods and processes are being developed to isolate lignin more efficiently from sources such as wood, agricultural residues, and industrial byproducts [6]. The global landscape of biomaterial production, mainly focusing on lignin, is rapidly evolving [7].

Lignin has excellent thermal stability and mechanical strength, making it stand out from other biopolymers [8]. Its complex aromatic structure allows for the creation of advanced materials [9]. Additionally, lignin's ability to be chemically modified enhances its compatibility with other materials, filling the gap left by more traditional biomaterials that may lack such adaptability [10]. This makes lignin a promising candidate for sustainable and innovative solutions in various industries. Globally, lignin is produced in vast quantities, with estimates suggesting that plants generate around 20 billion tons annually making the most abundant organic polymers [8, 11]. Lignin composition and structure are highly dependent on the type of lignin and method of extraction. The three primary types of lignin-based on the source are hardwood lignin, softwood lignin, and grass lignin [12]. Hardwood lignin, predominantly composed of guaiacyl (G) and syringyl (S) units, is typically found in deciduous trees [13]. Softwood lignin, mainly consisting of guaiacyl units, is present in coniferous trees and is known for its higher resistance to degradation [14]. Grass lignin in herbaceous plants contains a mix of guaiacyl, syringyl, and p-hydroxyphenyl (H) units, giving it unique properties suitable for various applications [15]. Lignin is extracted from biomass, such as sulfite pulping involving the treatment of biomass with a mixture of sulfur dioxide and metal sulfite such as calcium sulfite or magnesiiym sufite at high tempearues which generate lignosulfonates [16]. Kraft pulping (i.e. one of the most common pulping method), and uses sodium hydroxide and sodium sulfide to break down lignin bonds [17]. Organosolv pulping uses organic solvents like ethanol or methanol to solubilize lignin, producing high-purity lignin suitable for chemical applications [18]. Alkaline extraction employs strong bases, such as sodium hydroxide, to dissolve lignin, often used for agricultural residues [19]. Hydrolysis extraction utilize acid, enzymatic or alkaline hydrolysis to break down lignocellulosic materials and generate hydrolysis lignin [20]. Steam explosion involves treating biomass with high-pressure steam, which is then rapidly depressurized, causing the lignin to separate from the cellulose [21]. Each method varies in efficiency, cost, and the quality of lignin produced; choosing the extraction method is crucial depending on the intended application.

Lignin, despite its abundance and potential, faces several limitations that affect its utilization [22]. One major challenge is its complex and heterogeneous structure, which makes it difficult to process and convert into high-value products [23]. Additionally, lignin's dark color and poor solubility in water and many organic solvents limit its applications in specific industries [24]. Various organic and inorganic impurities (i.e. ash and sulfur content) further complicate its use [25]. The source of lignin also influences its properties and potential uses. For example, lignin from the pulp and paper industry (e.g. kraft lignin) have impurities and higher sulfur content limiting its use in high-value applications while lignin extracted from agricultural residues (e.g. alkaline) are reported to have a lower yield and lower-purity [26, 27]. Organosolv pulping produces high-purity lignin; however, its high cost limits its widespread utilization [28]. While lignin holds great promise, its complex nature and the variability introduced by different sources and extraction methods present significant challenges that need to be addressed to realize its full potential.

Addressing the challenges of lignin's impurities, complex structure, and limited reactivity involves combining advanced techniques, such as depolymerization, fractionation, and functionalization [29]. Depolymerization breaks down lignin into smaller, more manageable molecules, enhancing its reactivity and facilitating further processing [30]. Fractionation separates lignin via molar mass, isolating high-purity fractions that can be tailored for specific applications [31]. While, functionalization introduces new functional groups to the lignin molecules, improving their solubility and compatibility with other materials [32]. This integrated approach mitigates the inherent limitations of lignin and expands its potential for use in high-value products such as coatings, films, composites, biofuels, bioplastics, and specialty chemicals [33]. Lignin can be transformed into a versatile and valuable resource using depolymerization, fractionation, and functionalization.

Lignin’s potential as a dispersant, coating, composite, and 3D printing is significantly enhanced through depolymerization, fractionation, and functionalization [34, 35]. Depolymerization and fractionation are primarily documented when lignin is employed as a substitute for one or more components in polymer synthesis, owing to its reduced molecular weight and heightened reactivity, which facilitates its participation in polymerization with other constituents (e.g., lignin as a phenol in phenol-formaldehyde resin synthesis and as a polyol in polyurethane synthesis) [36]. The incorporation of lignin in polymerization replaces highly harmful components, such as phenol or polyol and imparts additional attributes, including UV-blocking and antibacterial capabilities, to the products [35-38]. Functionalization introduces new functional groups to lignin molecules, reported to improve the compatibility of lignin with polymer matrices in composite synthesis [39]. The functionalization of lignin for composite formulation is essential for 3D printing applications, enabling the production of ecologically sustainable and economical bioplastics from lignin-based materials [40]. Through the integration of these advanced techniques, lignin can be transformed into a versatile and valuable resource for a wide range of high-value applications.

As presented in this review, the source of lignin, extraction methods, and modifications have received significant attention in the past years and are correlated with potential applications. Most studies have focused on modifying the characteristics of lignin via depolymerization, fractionation, functionalization, and a combination of depolymerization-functionalization and fractionation-functionalization for composite and resin formulations. This review followed a new approach to categorizing and discussing the characteristics of lignin nature and modification for improving the hydrophobic, hydrophilic, dispersant, and flame retardant. The existing literature was also explored from an application point of view, such as coatings, composites, thermoplastics, and 3D printing applications. Moreover, the challenges, current trends, and future opportunities associated with lignin-based coating, thermoplastics, composites, and 3D printing.

2.3. Lignin

Lignin is a complex organic polymer synthesized by the deamination of the aromatic amino acid phenylalanine units (p-coumaric alcohol, conifery alcohol, and sinapyl alcohol), generating three phenylpropanoids (p-hydroxyphenyl (H), syringyl (S) and guaiacyl (G) subunits **Figure 2. 1.** a-c) in plants cell walls [12, 41, 42]. The monomeric units of lignin are linked via two significant linkages: the ether (β-O-4, α-O-4, and 4-O-5) and the C-C (β-1, β-β, and β-5) linkages (**Figure 2. 1.** a**)** [43, 44]. Lignin's major functional groups are phenolic hydroxyls, aliphatic hydroxyls, and carboxylic groups [45]. The presence and concentration of each monomeric unit and linkage characterize the properties of lignin from different plant sources [46, 47]. The relative distribution of the lignin building blocks enormously varies between plant species as hardwood lignin is composed of G (50-75%) and S (25-50%) units in equal amounts as well as lower levels of H units (trace), softwood lignin mainly contains G units (90-95%) and H units (0.5-3.4%) while grass lignin contains H (10-25%), G (25-50%) and S (25-50%) units in **Figure 2.1**c [47]. The ether linkages are dominant in all the lignin, while it is higher in the grass (77-85%), followed by hardwood (67-74%) and softwood (49-57%) [48]. Lignin synthesis is complex and affected by plant tissues, cell types, growth duration, and lignification levels, which considerably influence proto-lignin's molecular weight and polydispersity [43, 48]. Lignin heterogeneity is further advanced by the extraction methods that separate lignin, cellulose, and hemicellulose from the lignocellulose biomass [49].

2.3.1. Lignin Types

There are two main categories of industrial methods used for the isolation of lignin: sulfur-bearing (kraft and lignosulfonate lignin) and sulfur-free (organosolv and soda lignin) methods [50]. The sulfur-bearing lignin results from kraft pulping (sodium hydroxide and sodium sulfate treatments) and sulfite pulping (sulfur dioxide, calcium, sodium, magnesium, and ammonium base). In contrast, sulfur-free lignin results from organic solvents (alcohol, ketones, polyols, formic acid, and acetic acid) and alkali (sodium hydroxide) extraction. The purity, structural compositions, and molecular weight are different in **Table 2.1**.

The kraft pulping process dominates paper production, increasing kraft lignin availability (55-90 million tons of lignin per year). The extraction of lignin in the kraft pulping involves the cleavage of phenolic and non-phenolic ether linkages followed by the removal of phenolate species via anchimeric assistance and the formation of thioperoxide [51]. The possible substitution of the C-O link in proto-lignin by a C-C cross-bonded structure is likely due to the change of deoxygenation during kraft pulping [52].

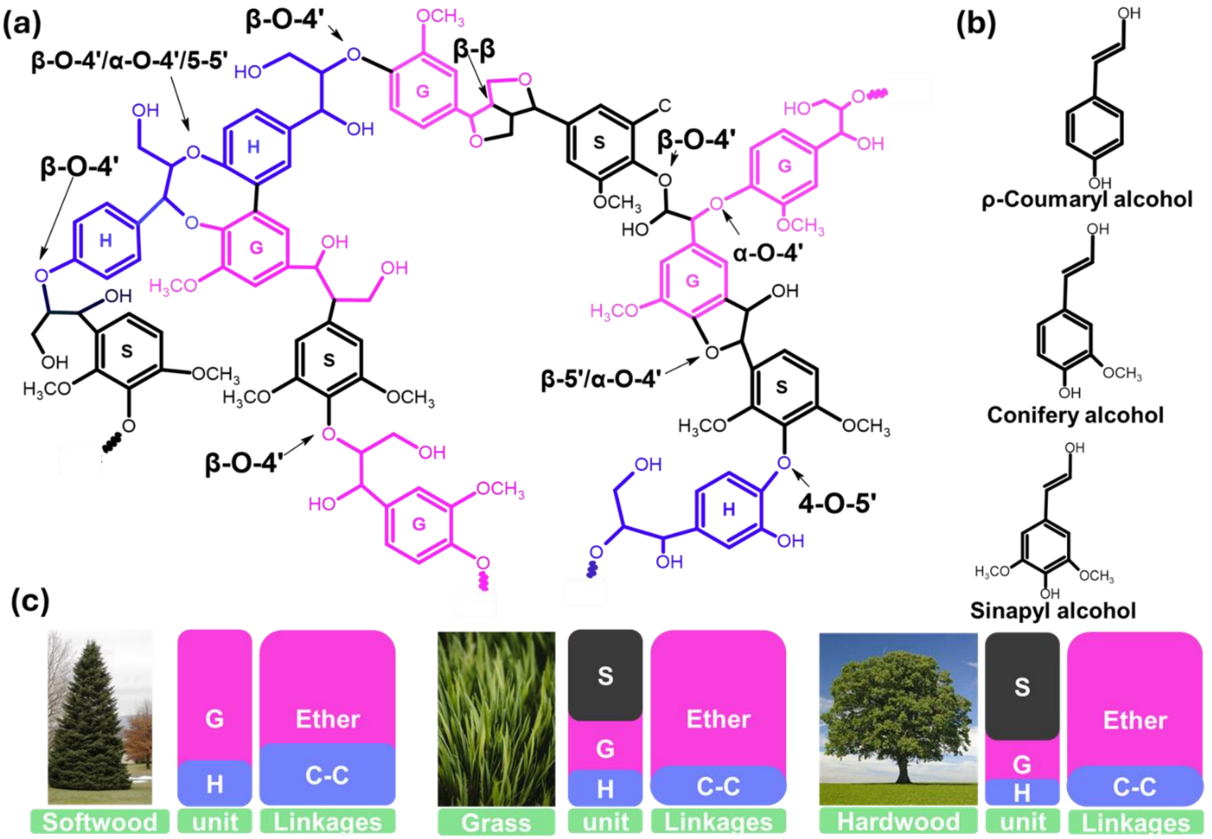

Figure 2.1. Schematic structure of lignin (grass) (a), structure of three lignin monomeric units (b), and lignin monomeric units and linkage contents (c).

Table 2.1. Physicochemical properties of lignin based on extraction methods [50].

Type	Mw, g/mol	Moisture content, wt. %	Sulfur content Wt.%	Ash content wt.%	Polydispersity
Organosolv	< 5000	7.5	0	1.7	1.5-2.4
Soda	< 15000	2.5-5.0	0	0.7-2.3	2.5-3.5

Kraft	< 25000	3.0-6.0	1.0-3.0	0.5-3.0	2.5-4
Hydrolyzed	5000-10000	4.0-9.0	0-1.0	1.0-3.0	1.5-3.0

Two main methods to isolate kraft lignin from black liquor are LignoBoost and LignoForce technologies [53]. The LignoBoost process acidifies the black liquor to precipitate the lignin, followed by filtration and washing [54]. At the same time, LignoForce introduces oxidation before acidification to precipitate lignin, which helps reduce the odor and volatile organic compounds (VOCs) emission [55]. LignoBoost and LignoForce lignin are more appealing to potential commercial applications due to their reduced heterogeneity and lower concentration of impurities than conventional kraft lignin [56]. However, kraft lignin's complex structure, low reactivity, and low solubility limit its large-scale use in various applications [57]. The soda/alkali process is another conventional pulping method that utilizes sodium hydroxide under high pressure at 140-170°C [58].

In contrast to kraft pulping, the alkaline method employs anthraquinone instead of sodium sulfide, promoting the reductive breakage of ether bonds and minimizing carbohydrate loss [59]. The sulfur-free soda lignin is highly appealing and demonstrates significant potential for various applications [60]. However, like kraft lignin, soda lignin needs further modification to produce functional materials.

2.4. Lignin Modification Methods

Today's primary sources of lignin are kraft lignin and soda lignin [61]. In the market, they both fall into the categories of technical lignin and need modification to improve the purity and molecular weight polydispersity [50]. The methods used to reduce the variability in lignin and improve the utilization of lignin are depolymerization, fractionation, and functionalization [62]. The depolymerization of lignin combines the lignin polymer into a mixture of monomeric units via chemical, physical, or thermal methods by breaking the various intermolecular bonds [36]. Like depolymerization, lignin fractionation also reduces lignin molecular weight and polydispersity via the selective succession of the lignin linkages with organic solvents or gradient acid precipitation [31]. Functionalization uses a different approach by engaging lignin functional groups (phenolic, aliphatic, or carboxyl hydroxyl) in grafting and copolymerization [63]. Recent reports also show the combination of depolymerization followed by functionalization or fractionation followed by functionalization [64]. The depolymerization of lignin is not the focus of this thesis; therefore, the literature review is focused on the fractionation, functionalization of lignin, and the combination of the two.

2.4.1. Fractionation

Lignin fractionation is a simple subdivision of heterogeneous lignin into various fractions with decreased polydispersity and molecular weight [65]. Three principal categories of lignin fractionation include gradient acid precipitation, membrane separation with varying cut-offs, and solvent fractionation [66]. The acid gradient fractionation separates lignin of higher and lower molecular weights by precipitating lignin from a stable colloidal form in the alkali solution while gradually reducing the pH [67]. Elevated pH levels yield precipitated lignin with increased molecular weight, whereas lower pH levels produce lignin with reduced molecular weight [68]. On the other hand, membrane separation uses semi-permeable membranes with distinct molecular weight cutoffs to segregate the lignin molecules of diverse molecular weights in a solution [69]. Both acid precipitation and membrane separation have limitations in successfully separating the lignin of varying molecular weights. The acid precipitation method is limited due to the possibility of precipitating lower molecular weight lignin with higher molecular weight at a higher precipitation pH value [48]. The reduced processing throughput from membrane fractionation, caused by the limited solubility of most commercial lignin's, constrains the adoption of membrane filtration-based fractionation [31]. On the other hand, organic solvent precipitation of lignin is very effective due to the selective solvation capacity of organic solvents regarding molecular weight. The Hildebrand solubility analysis method best explains this phenomenon by dividing the solubility parameters (δ), which is regarded as the square root of the cohesive energy density, solvent vaporization energy (E), and the molar volume (V_m) as shown in **Equation 2. 1.** [70].

$$\delta = \left(\frac{E}{V_m}\right)^{1/2} \tag{2.1}$$

Solvents that have a similar δ, like lignin, dissolve lignin the best; however, due to the complexity of lignin, the possibility of partial solubility, which is found by the solubility of lignin increases with the hydrogen bonding capacity of the solvents. The Hansen solubility parameters are further classified the cohesive energy into dispersion forces (δ_D), polar forces (δ_P), and hydrogen bonding (δ_H) (**Equation 2. 2.)** [71].

$$\delta^2 = \left(\delta_H{}^2 + \delta_P{}^2 + \delta_D{}^2\right)^{1/2} \tag{2.2}$$

Solvents with solubility characteristics (δ) in the 11–12 $\mathrm{cal}^{1/2}\cdot\mathrm{cm}^{-3/2}$ range possess enhanced lignin dissolution capabilities [72]. Several studies claim improved the characteristics of lignin by solvent fractionation, including single solvents, solvent combinations with water, and sequential fractionation methods [48, 73]. In a single solvent fractionation process, lignin is treated with only one solvent to obtain the soluble and insoluble fractions, which can be regarded as a straightforward and efficient fractionation approach. Solvents such as ethanol, acetone, THF, and methanol are among the solvents that can partially solubilize lignin and are utilized in the case of single solvent fractionations [65]. Softwood kraft, hardwood alkali, wheat straw, and corn stover kraft lignin are among the lignin types reported in single solvent fractionation reports, as indicated in **Table 2.2**.

Table 2.2. Single solvent fractionation of lignin effect on molecular weight (Mw), polydispersity index (PDI), and yield.

Solvent	Raw material	Parent Mw (g/mol);PDI	Soluble Fraction Mw (g/mol);PDI;Yield (%)	Ref.
Acetone	Softwood kraft	6000;2.22	4250;1.7;57.4	[74]
THF Methanol 2-butanone	Softwood kraft	4680;2.4	2300;1.7 2910 1680	[75]
Acetone	Softwood kraft	4130;2.0	2260;1.6	[76]
	Wheat straw soda	4170;2.1	2580;1.7	
	Wheat straw organosolv	2520;1.7	1590;1.5	

Ethanol	Wheat straw Organosolv	1814;1.8	1195;1.4	[77]

The solubility of lignin in the solvents is reported to be affected by the functionality of the lignin, structural characteristics, molecular weight, and monomeric composition [78]. Increasing syringyl concentration in lignin polymers diminishes the polymer's expansion in organic solvent environments. It reduces the free energy differential relative to aqueous solvent environments, lowering the solubility of high syringyl lignin polymers [79]. In addition to the reduced molecular weight and polydispersity (**Table 2.2),** the major change in the structure of lignin after solvent fractionation is the increase in hydroxyl group content, which is reported to be dependent on the hydrogen bonding interaction between the solvent and lignin [80]. Lignin's fractionated by a solvent possessing a higher δ_H component tends to increase the hydroxyl group of lignin in the soluble fractions [75]. In addition to controlled molecular weight distribution, the increase in the hydroxyl groups of lignin via solvent fractionation is vital since it will improve the solubility, antioxidant properties, and reactivity of lignin for further functionalization [81].

2.4.2. Chemical functionalization of Lignin

The chemical functionalization of lignin is a process that introduces various chemical groups to alter lignin properties and enhances its possible utilization in different applications [63]. There are reactive sites in lignin structure, such as the phenolic, aliphatic, and carboxylic hydroxyl groups and the methoxy groups for reactions, such as esterification, etherification, oxidation, and reduction, as well as grafting other functional groups [82]. The grafting of lignin with different chemical groups or polymers into lignin backbone to create hybrid materials with desirable properties has peaked in recent years [83]. Methods such as esterification [84], epoxidation [85], grafting long alkyl chains [86], acylation [87] and silylation [88] were reported to improve the hydrophobic characteristics of lignin, while sulfonation [89], carboxylation [90], phenolation [91], amination [92], and grafting hydrophilic groups such as polyethylene glycol [93] to improve the hydrophilic characteristics of lignin. The improved hydrophobicity of lignin is reported to enhance the application of lignin in coating formulation and hydrophobic films [94]. Modification to improve lignin's hydrophilic properties makes it an excellent dispersant for pigment and dye, adsorbent in wastewater treatment, and concrete additives [95]. Another primary functionality considered when utilizing lignin is flame retardancy, which can be improved by grafting inorganic molecules such as phosphorus, nitrogen, and silicon incorporation onto the lignin structure via modifications such as phosphorylation and nitrogenization [96]. Additionally, the grafting of lactic acid and caprolactone on the hydroxyl groups and subsequent polymerization of polylactic acid (PLA) [97], and polycaprolactone (PCL) [98], as well as urthanization for the synthesis of polyurethane (PU) on the lignin backbone is reported to impart lignin thermoplastic properties with a melt characteristics and reduce the charring nature of lignin.

2.4.2.1. Hydrophilic, hydrophobic and superhydrophobic lignin

Hydrophilicity, hydrophobicity, and superhydrophobicity represent a spectrum of surface interactions with water that are crucial in various scientific and industrial applications [99]. Hydrophilic surfaces exhibit a pronounced affinity for water, indicated by low water contact angles (WCA < 90°), which facilitates effective spreading and wetting of water on the wet surface [100]. Conversely, hydrophobic surfaces repel water, characterized by elevated WCA higher than 90°, while superhydrophobic surfaces further enhance this property, displaying WCA higher than 150° and minimal adhesion to water droplets **Figure 2. 2**a, resulting in exceptional water repellency [101, 102]. This phenomenon is typically realized through integrating micro- or nanostructured surfaces with hydrophobic traits [103]. In addition to WCA values, the attractive and adhesion forces between a water droplet and a surface can further define the hydrophilic, hydrophobic, and superhydrophobic properties of materials (**Figure 2. 2**b) [104].

Lignin comprises a hydrophobic and hydrophilic part [105]. Lignin’s hydrophobic characteristics are primarily due to its complex and heterogeneous structure, which is rich in aromatic subunits [106]. This hydrophobicity results from non-polar aromatic rings and ether linkages, which repel water molecules [107]. The degree of hydrophobicity can be influenced by the specific types of monolignols (p-coumaryl, coniferyl, and sinapyl alcohols) and their distribution within the lignin polymer and the presence and concentration of hydroxyl groups [108]. The modification of lignin’s hydroxyl f groups by large non-polar molecules increases hydrophobic behavior, not only due to the nature of these grafted polymers but also due to spherical reasons, where non-modified hydrophobic groups can become inaccessible [109]. Functionalization methods for hydrophobic lignin, such as esterification, oxylalkylation, acylation, silanzation and epoxidation are shown in **Figure 2. 3**a-g. Silanzation is one of the most efficient methods to increase the hydrophobicity of lignin by replacing the hydrophilic hydroxyl groups of lignin with an organosilyl group.

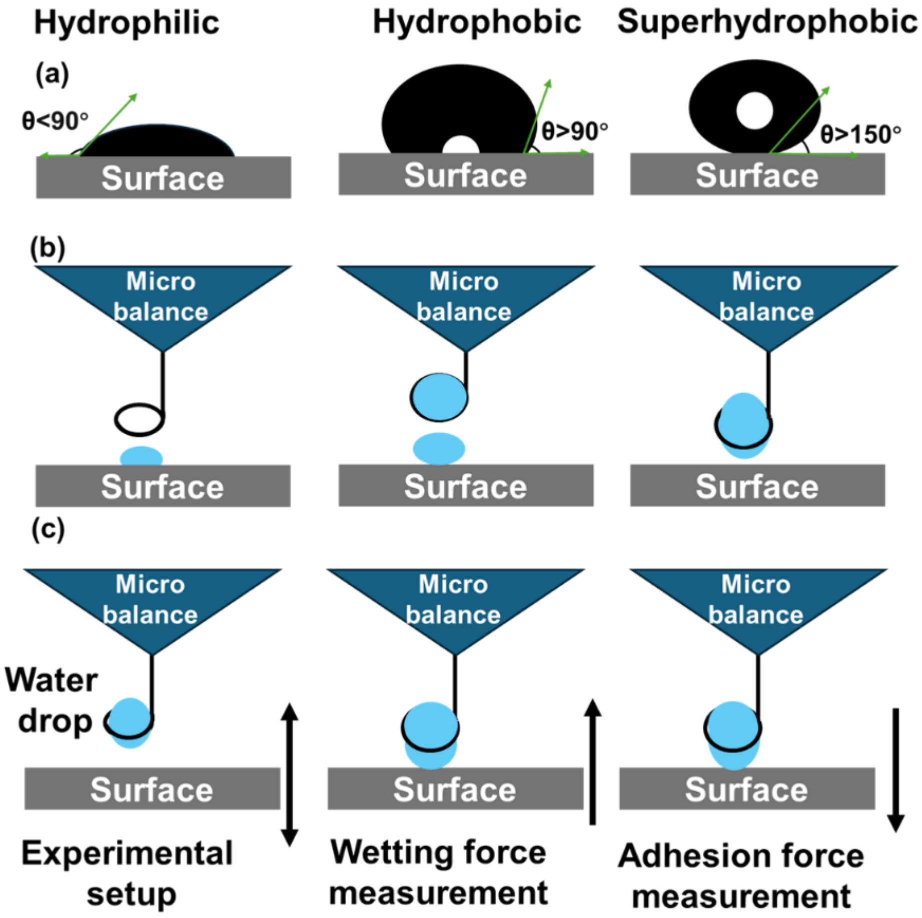

Figure 2.2. Water contact angle values (a), the appearance of water droplets after tensiometer measurement of water droplets (b) on the surfaces of hydrophilic, hydrophobic and superhydrophobic and Schematic of the apparatus and procedures for measuring the wetting and adhesion interactions between water and surfaces (c) [99, 110].

The process forms covalent bonds between the silane groups and the hydroxyl functionalities on lignin, resulting in the grafting of hydrophobic silane chains. Silanization agents, such as 3-(Triethoxysilyl) propyl isocyanate (TEPI) [88] and (3-Aminopropyl) triethoxysilane (APTES) [111] converted the lignin's hydroxyl group into urethane bond and with silicon oxygen bond with carbon of lignin, respectively. The incorporation of these hydrophobic moieties (Si-O-C) significantly reduces the surface energy of lignin, effectively rendering it water-repellent and enhancing its suitability for applications in coatings, adhesives, and composite materials [112-115].

The degree of hydrophobicity achieved through silanization can be tailored by varying the type and concentration of silane agents, as well as the reaction conditions such as temperature and time. Functionalization of lignin to achieve superhydrophobic properties is an emerging area of interest, particularly for applications in coatings, self-cleaning surfaces, and water-repellent materials [116-118]. The hydrophobic features of lignin, attributed to its aromatic structure, need the addition of certain functional groups and surface changes to enhance its water-repellent properties. The surface wettability of lignin is altered by grafting low-surface-energy molecules or by creating micro/nano-structured surfaces on it [119].

One method of achieving superhydrophobic lignin involves the functionalization of its surface with long-chain alkyl groups or fluorinated compounds [118]. Alkylation methods using fluorinated alkyl silanes reduce lignin's surface energy and enhance its hydrophobicity. Another method is the formation of hierarchical surface structures by processes such micro-nanospheres structure generation from lignin, which impart micro- and nano-scale roughness to a surface [120]. This multi-scale roughness, combined with low-surface-energy functional groups, forms air pockets on the surface, contributing to superhydrophobic behavior. These functionalization techniques have enabled the development of lignin-based coatings with water contact angles exceeding 150°, suitable for use in textiles [121], packaging [122], and wood coating [120], offering a sustainable alternative to synthetic, non-biodegradable superhydrophobic materials.

Functionalization of lignin to enhance its hydrophilic properties is a significant area of research aimed at improving its compatibility with aqueous environments and expanding its applications in fields such as water treatment, biomedical materials, and hydrogels [123]. Due to its highly aromatic and cross-linked structure, lignin's natural hydrophobicity limits its solubility and water dispersibility, necessitating chemical modifications to introduce hydrophilic functional groups [124]. By attaching polar moieties such as carboxyl, sulfonate, hydroxyl groups, and amination, the hydrophilicity of lignin can be significantly improved **Figure 2. 3**b [125-127]. These modifications increase lignin's interaction with water molecules, facilitating its use in applications where moisture absorption, solubility, or water binding is critical.

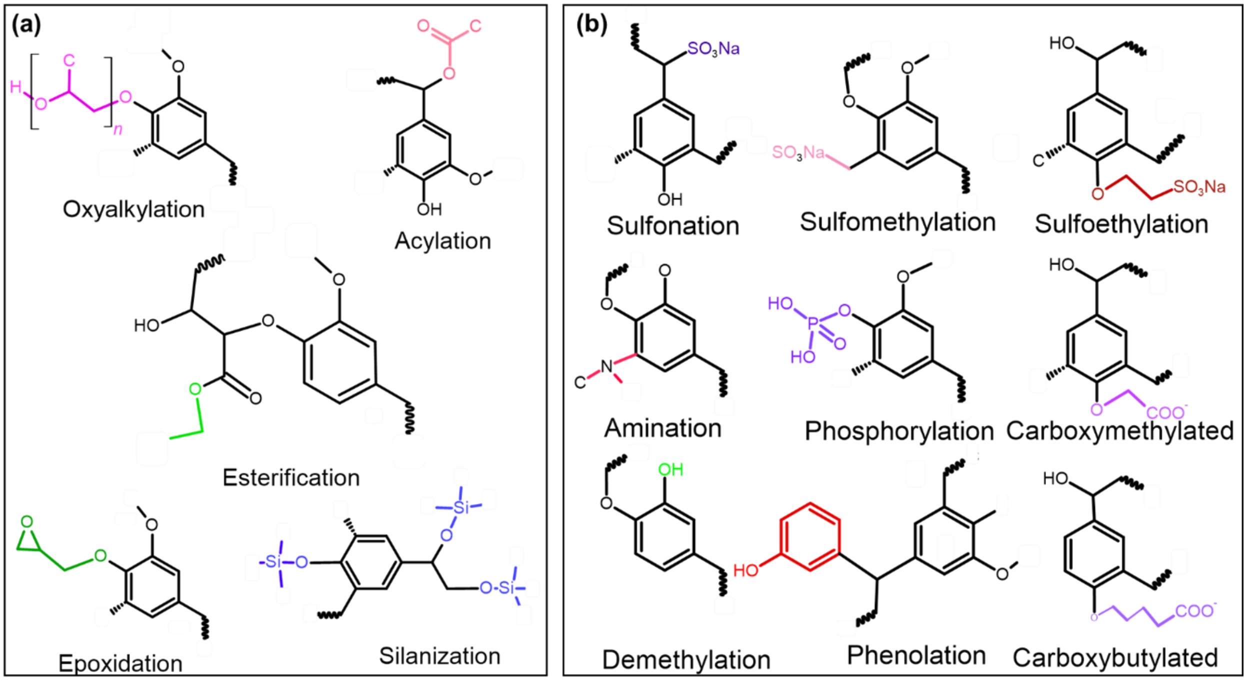

Figure 2.3. Lignin functionalization for hydrophobic (a), and hydrophilic performances (b).

Carboxylation and sulfoalkylation are two efficient functionalization techniques for enhancing the hydrophilicity of lignin [83]. Carboxylation entails the incorporation of carboxyl groups (-COOH) into the structure of lignin, generally by processes like oxidation or esterification [128]. This improves lignin's water solubility and its capacity as a dispersion agent or emulsifier in aqueous systems [129]. Carboxylated lignin has been investigated for its application in the development of biodegradable superabsorbent polymers and as a flocculant in wastewater treatment [130]. Sulfoalkylation, on the other hand, introduces sulfonic acid groups ($-SO_3H$) into lignin via reactions with reagents like sodium vinylsulfonate [131]. Sulfoalkylated lignin exhibits high water solubility and a strong affinity for hydrophilic substrates, making it particularly useful in applications such as dye dispersants and water-soluble polymers [63]. Carboxylation and sulfoalkylation successfully convert lignin from a predominantly hydrophobic polymer into a flexible, hydrophilic substance, improving its use in eco-friendly, water-based applications.

2.4.2.2. Functionalization for thermoplastic lignin

The functionalization of lignin to create thermoplastic polymers is a viable method for converting this abundant, renewable biopolymer into a valuable resource for sustainable products [132]. The intrinsic charring and extensively cross-linked architecture of lignin render its processing into a thermoplastic state, necessitating chemical changes [133]. The goal of making lignin thermoplastic is to provide a sustainable, biobased alternative to traditional petroleum-based plastics. By reducing the complexity of lignin's rigid aromatic structure through fractionation or grafting flexible polymer chains onto its functional groups, its flowability and moldability are enhanced, transforming it into a thermoplastic polymer [134].

The grafting of caprolactone onto lignin exemplifies a practical functionalization approach for thermoplastic lignin. During this procedure, ε-caprolactone monomers undergo polymerization and are grafted onto the hydroxyl groups of lignin by ring-opening polymerization **Figure 2.4** [135]. The resultant lignin-poly(caprolactone) copolymers exhibit enhanced flexibility and processability owing to the soft and elastomeric characteristics of the polycaprolactone (PCL) chains [136]. These grafted copolymers have improved heat stability and flexibility, rendering them appropriate for applications such as biodegradable films and composites [137].

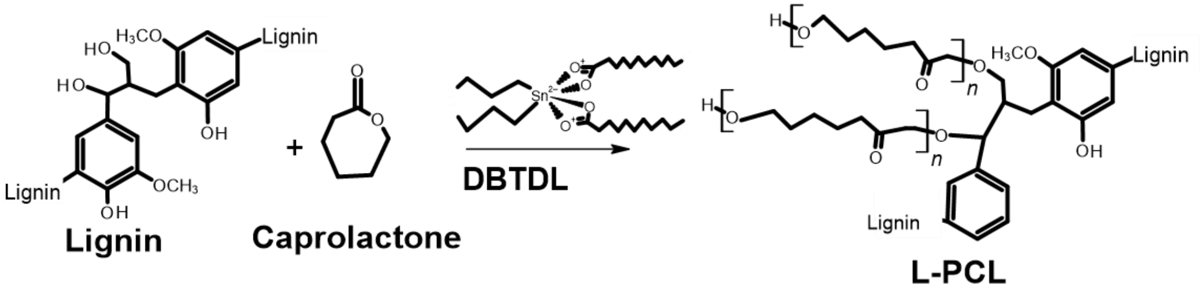

Figure 2.4. The ring opening polymerization of caprolactone monomer with lignin in the presence of dibutyltin dilaurate (DBTDL) for the chain of polycaprolactone (PCL) growth in the lignin backbone.

The degree of grafting and molecular weight of lignin-PCL polymers can be tailored to meet specific performance requirements. The grafting process enhances lignin's flexibility and thermal processability, turning it into a thermoplastic material suitable for injection molding and extrusion [138]. The lignin-caprolactone polymerization improves traditional polycaprolactone polymers' mechanical properties. It opens new possibilities for creating fully bio-based, thermoplastic materials that compete with traditional plastics in various applications. However, the current lignin-caprolactone polymer synthesis faces challenges due to the complex structure of lignin limiting the polymerization and overall performances of the polymer for advanced applications such as 3D printing.

2.4.2.3. Flame-retardant lignin

The functionalization of lignin to produce flame-retardant materials has attracted considerable attention because of lignin's intrinsic thermal stability and aromatic composition, which provide a degree of resistance to flame [139]. Incorporating phosphorus, sulfur, or silicon functional groups into the lignin structure can considerably boost lignin's flame-retardant characteristics, making it a choice for applications such as fire-resistant coatings, textiles, and composites [140]. The flame-retardant mechanism of lignin-based materials involves enhancing char formation, decreasing flammability, and suppressing the emission of volatile flammable gases [141].

Phosphorylation is a highly successful method for functionalizing lignin to enhance its flame-retardant properties [142, 143]. Compounds containing phosphorus, such as phosphoric acid or phosphate esters, can be chemically attached to the hydroxyl groups of lignin [143, 144]. Phosphorus content facilitates char formation during burning, decreasing the emission of combustible gases and improving the material's thermal insulation [145]. Phosphorylated lignin has demonstrated a substantial reduction in heat release rate and an enhancement in the limiting oxygen index (LOI) of polymer composites, making it an effective flame retardant in thermoplastics and thermosetting resins [146]. The phosphate groups in lignin provide phosphoric acid during fire, which catalyzes the polymer's dehydration, resulting in a persistent carbonaceous char that safeguards the underlying substance from additional deterioration [147]. Similarly, sulfonation and silanization effectively impart flame-retardant properties to lignin. Sulfonation involves introducing sulfonic acid groups (-SO_3H) into the lignin structure through reactions with sulfur-containing reagents, such as sulfuric acid or sodium sulfite. The presence of sulfur in lignin enhances its ability to promote char formation, reduce smoke production, and inhibit flame propagation, making sulfonated lignin a valuable additive in flame-retardant materials [148]. On the other hand, silanization introduces silicon-containing groups onto lignin via reactions with silane coupling agents, such as tetraethoxysilane (TEOS) or silane esters. The silicon groups improve flame retardancy by forming a protective silica-based barrier upon combustion, which acts as a thermal insulator and limits the access of oxygen to the burning material [149]. Phosphorylation, sulfonation and silanization not only enhance lignin's flame-retardant properties but also contribute to improved thermal stability and mechanical integrity of lignin-based materials [150].

2.4.2.4. Dispersant

Functionalizing lignin to create effective dispersants is valuable in leveraging its natural abundance and unique chemical structure [151]. However, structural complexity and limited solubility limits application in this sector. Therefore, chemical modifications (carboxyl (-COOH) or sulfonate (-SO_3H) grafting onto lignin), which introduce functional groups that increase its affinity for water and improve its ability to stabilize colloidal systems, was widely reported to enhance lignin's dispersant properties [95]. Lignin dispersants are reported to perform best in various sectors, such as concrete admixtures, dye formulations, and particulate suspensions. For example, carboxylated lignin is widely used in cement and concrete formulations to disperse cement particles evenly, enhancing workability and preventing clumping [152]. The negative charge provided by the carboxyl groups enhances electrostatic repulsion between particles, ensuring a stable and homogeneous dispersion, which is critical in industrial applications requiring consistent particle distribution. Sulfonation is another highly effective functionalization technique for improving lignin's dispersant properties. Sulfonated lignin has excellent water solubility and can provide steric and electrostatic stabilization to dispersed particles in aqueous systems [153]. It has been extensively used in dye formulations, where its ability to prevent particle agglomeration enhances color uniformity and improves dye fastness [154]. Additionally, sulfonated lignin has been found to have applications in the production of drilling fluids, where it acts as a dispersant to maintain the stability of suspended particles, improving the performance and efficiency of drilling operations [155]. The enhanced hydrophilicity and dispersing capacity of sulfonated lignin make it a versatile and sustainable alternative to synthetic dispersants in various industries.

2.4.2.5. Combination of Fractionation and Functionalization of Lignin

Functionalizing lignin through fractionation and grafting offers a versatile approach to tailor its properties for various industrial applications [63]. Solvent fractionation of lignin before functionalization enhances its reactivity with the functionalizing agent and provides more controlled polymerization during grafting polymerization [156]. That is because the reduced molecular weight, reduced molecular weight dispersity, and increased hydroxyl groups of fractionated lignin provide a more defined starting material for further chemical modifications, allowing for the precise tuning of properties. The subsequent grafting of polymer chains onto fractionated lignin significantly enhances its functional attributes, expanding its utility in applications such as thermoplastics, adhesives, and biomedical materials. For example, the bonding strength of a lignin-based phenolic resin was improved with the utilization of ethanol and isopropanol solvent fractionated birch alkali lignin as a phenol in the resin synthesis [156]. The high bonding strength was a result of high purity and more reactive sites for adhesive synthesis, resulting in better accessibility of phenolic hydroxyl groups for the phenol-formaldehyde polymerization because of solvent-fractionated lignin lower molar mass. This combined approach capitalizes on lignin’s inherent properties, such as its aromatic structure, thermal stability, and availability of reactive hydroxyl groups, while overcoming limitations related to its heterogeneity and poor processability.

Perhaps, isolating more homogeneous fractions of lignin via solvent-fractionation and subsequently grafting flexible polymer chains like polycaprolactone can significantly enhance lignin’s mechanical, thermal, and processing properties. This method broadens the range of applications for lignin-based materials. It contributes to developing sustainable, bio-based alternatives to traditional synthetic polymers, aligning with the growing demand for environmentally friendly materials in various industries.

In summary, chemical functionalization and fractionation combined with functionalization are powerful strategies of lignin modification to improve the hydrophobic, superhydrophobic, hydrophilic, flame retardant and thermal characteristics of lignin.

2.5. Lignin Based Coating and Composite Films

Coating entails the application of a material layer to a surface for protection, enhancement, or decoration. Prevalent categories of coating substances include paints, varnishes, and polymers. When choosing a coating, essential considerations include the substrate material, ambient conditions, and required attributes such as durability and attractiveness. The present coating business encounters constraints, including environmental issues related to volatile organic compounds (VOCs) in coating formulations, the necessity for more sustainable and eco-friendly alternatives, and the difficulty of creating coatings that last harsh circumstances without deterioration.

Lignin-based coatings on wood, metal, and paper surfaces represent an innovative and sustainable alternative to conventional petroleum-derived coatings. Lignin-based coatings are receiving spotlight due to lignin's inherent biodegradability, availability as a byproduct of the pulping industry, and unique aromatic structure, which imparts thermal stability and ultraviolet (UV) resistance to the coating materials [157]. However, the natural characteristics of lignin, such as its brittleness, limited solubility, and poor film-forming properties, necessitate its chemical modification to enhance its performance in coating applications. Three approaches are employed when lignin is utilized in coating applications: 1. Only lignin as a coating after lignin modification or grafting (i.e., esterification of lignin, caprolactone grafting, and epoxidation), 2. Lignin replaces one component of the coating formulation (i.e., as a polyol in polyurethane (PU)), and 3. Lignin as an additional functional material in coating composite formulations. Each method is discussed in the subsequent sections.

2.5.1. Lignin modifications for polymer coating

Lignin modifications such as esterification, epoxidation, and caprolactone grafting are among the methods employed for the synthesis of lignin-based polymer coatings [84, 136, 158]. The functionalization of lignin would transform lignin into a functional material suitable for high-performance coatings with tailored properties, including enhanced adhesion, flexibility, and barrier properties [159]. Modifying lignin for coating applications often involves introducing functional groups that improve its solubility, film-forming ability, and hydrophobic characteristics. Esterification, for instance, introduces ester linkages through reactions with fatty acids or anhydrides, which enhance lignin's hydrophobicity [160]. This process improves lignin's ability to form uniform films and contributes to increased water resistance for wood surfaces. Similarly, reacting lignin with alkyl halides or epoxides introduces ether bonds, increasing flexibility and reducing lignin-based epoxy coatings' brittleness [158]. This lignin-based coating also showed improved corrosion resistance of coated steel than commercial epoxy polymer coatings. Graft copolymerization, particularly with caprolactone, further enhances the mechanical properties of lignin-based coatings, making them more suitable for industrial applications where durability and flexibility are critical [161].

2.5.2. Lignin replacing the components of synthetic polymers for coating

Lignin as a biopolymer is getting attention in partially substituting polyol and phenol components of commercial polymers, such as polyurethane (PU) and phenol formaldehyde (PF) resins, respectively [159, 162]. The PU-based coating is widely used in the metal, wood, plastic, leather, paper, and textile industries [163]. PU synthesis is highly dependent on petroleum-based polyols, sparking criticism from the sustainability perspective [164]. The presence of phenolic and hydroxyl groups in lignin makes it a great candidate for replacing polyol in PU synthesis [161]. Using lignin as a polyol in PU synthesis reduces the environmental impact of PU-based materials by increasing their biodegradability and improving their UV resistance and mechanical strength [157]. The replacement of polyol via lignin is accomplished by cross-linking it with an isocyanate, which faces a problem in successfully replacing polyol due to the partial solubility of lignin in the polymerization medium. Lignin modification, such as fractionation [165], demethylation [166], and oxidation [167] are reported to increase the reactivity of lignin with isocyanate. However, reduced hydrophobic characteristics of lignin bases PU coatings is a bottleneck for their application and need further research.

2.5.3. Lignin in coating and composite formulations

Lignin can be incorporated into polymer matrices alongside other bio-based or synthetic resins to enhance the performance of coatings [159]. For example, lignin has been successfully blended with epoxy resins, acrylics, and polyurethanes to improve UV resistance, mechanical strength, and thermal stability [168]. In such composite formulations, lignin acts as a functional additive and a reinforcing filler. Its aromatic structure provides UV-absorbing properties, which protect the underlying substrate from photodegradation, while its ability to promote char formation enhances the flame-retardant properties of the coating [169]. Moreover, lignin’s natural antioxidant properties contribute to the oxidative stability of coatings, which is particularly beneficial in protective applications where long-term durability is essential [170]. The performance of lignin-containing composite formulations is highly dependent on the interfacial bonding of lignin and the matrix polymers, which is highly limited in the case of unmodified lignin due to the complex and heterogenous structure with strong intermolecular forces and it can lead to poor compatibility with many polymeric matrices [171]. In addition, the presence of more oxygen-containing polar groups in the lignin structure makes it relatively hydrophilic to hydrophobic polymer, leading to poor dispersion and agglomeration in the polymer matrices [172]. Furthermore, lignin's rigid and aromatic nature can make achieving good interfacial adhesion with flexible polymer matrices challenging [172]. These challenges are not only limited to the formulation stage but will extend to the application stage when the composite formulations are tried to be coated on a substrate. Therefore, the functionalization of lignin to improve the interaction between the composite formulation and the coating substrate is explored in many literature in **Table 2.3**. The performance of lignin-based coatings depends on the extent of lignin modification and the composition of the coating formulation. Modified lignin-based coatings have been shown to exhibit improved adhesion to various substrates, such as wood, metals, and glass, owing to the introduction of functional groups that promote interfacial bonding **Table 2.3** [34].

Table 2. 3. Lignin-based coatings, modifications, surfaces and characteristics.

Lignin Type	Modification	Max con., %	The goal of lignin	Surfaces	Char.	Ref.
Grass	Hydromethylation, Phenolation, phenol replacement in phenol formaldehyde resin	40	Replacing phenol in PF resin synthesis	NA	T_g=130 °C	[159]
kraft	Grafting of 1*H*, 1*H*, 2*H*, 2*H*-perfluorodecyltriethoxysilane, Epoxy resin composite	21	Superhydrophobic agent	Glass, wood, metal	WCA=164.7°	[118]
Softwood kraft	Salinization, urthanization via 1-isocyanate-3-trimethoxysilylpropane, and nanosizing	20	Coating polymer	Aluminum	T_g=105 °C, WCA=80°	[173]
Kraft	Nanoparticle via Ethanol-THF solubilization and water antisolvent, Glycerol diglycidyl ether as an epoxy compound	4.7	Durability enhancer in Coating composite formulation	Stainless steel metal, wood	WCA=120°	[174]

NA- not reported

Lignin-containing composite coating formulations offer a promising route to sustainable, high-performance materials through the chemical modification of lignin and the formulation of composite coatings. These coatings capitalize on lignin's intrinsic properties, such as UV resistance and thermal stability, and address its limitations through functionalization and blending with other resins. The resulting lignin-based coatings exhibit enhanced mechanical properties, improved barrier performance, and resistance to environmental factors, making them suitable for various industrial applications, including packaging, protective coatings, and outdoor structures. The ongoing development of lignin-based coatings represents a crucial step toward reducing reliance on non-renewable, petroleum-based materials in the coatings industry while contributing to a circular economy. Lignin-based composite represent an innovative and sustainable approach to material science, capitalizing on lignin's natural abundance and intrinsic properties.

2.6. Lignin for 3D Printing

Three-dimensional (3D) printing is a manufacturing process that creates a variety of customized product geometries through the layer-by-layer deposition of materials [175]. The minimal consumables, tailored item shape, and economical, quick, on-demand production relative to conventional manufacturing techniques such as milling, casting, forging, or welding render it an appealing option for contemporary and future industrial sectors [176]. The straightforwardness and precision of 3D printing technologies enable it to prevail across several sectors, including energy, biotechnology, and medical equipment [177]. 3D printing utilizes various feedstocks, including sand, gypsum, ceramics, metals, composites, wax, and acrylonitrile butadiene styrene (ABS) polymers [178]. With the pressing need to transition to sustainable materials, bio-based and biodegradable polymers are becoming preferred for 3D printing polymers [40]. Polylactic acid (PLA) and polycaprolactone (PCL) are among the most popular biodegradable polymers utilized for 3D printing materials [179]. On the other hand, biopolymers such as collagen, alginate, and chitosan are also used to manufacture biobased 3D printable materials [180]. Biopolymers such as cellulose and lignin are at the research and development stage for their assessment of 3D printability [181].

Lignin-based 3D printing signifies a prospective advancement in creating sustainable materials, using the distinctive features of lignin to produce valuable and eco-friendly substances [40]. As a sustainable biopolymer, lignin has several advantageous properties, including biodegradability, UV resistance, and mechanical strength [181]. Theoretically, lignin is appropriate for all types of 3D printing. Still, progress in recent years demonstrates that lignin is only successful for direct ink writing (DIW), selective laser sintering (SLS), and filament deposition method (FDM) [182]. SLS uses a laser to sinter powdered materials and bind them together to form a solid structure without needing a support structure [183]. DIW utilizes a viscous ink, and FDM involves the extrusion of a thermoplastic filament, which is heated and deposited layer-by-layer to create a 3D object [184]. The selection of 3D printing techniques profoundly influences the performance attributes of lignin-based produced items [185]. FDM is a prevalent technology in which a lignin-based filament is extruded via a heated nozzle and placed in layers [186]. This technique allows for accurate regulation of the geometry and design of printed items; however, the lignin filament must have appropriate melting and flow characteristics [187]. The mechanical strength of printed components is frequently affected by the bonding degree between layers, which may be maximized by meticulously controlling printing parameters such as temperature, layer height, and scan speed [188]. FDM is a widely utilized 3D printing technique in industry. The utilization of lignin in FDM methods faces a significant issue due to the limited thermoplastic characteristics of lignin; charring at a higher temperature increases lignin viscosity, making it difficult to extrude through a 3D printer nozzle [40]. Therefore, as a composite or blending, lignin is incorporated with melt polymers such as PLA and ABS in lower concentrations (3-40 wt.%) to improve its 3D printability **Table 2.4** [189].

Table 2.4. Lignin for FDM 3D printing.

Lignin type	Lignin modification	Max. lignin con., %	Filament preparation	Ref.
Biorefinery lignin	NA	80	Blending with Polyhydroxyalkanoate	[190]
Enzymatic hydrolysis lignin	Lignin nanoparticles	1	Blending with polypropylene	[191]
Lignin	Lignin-caprolactone polymerization	5	Blending with acrylonitrile-butadiene-styrene	[192]
Organosolv lignin	NA	1	Blending with acrylonitrile-butadiene-styrene and graphene nanoplatelets	[193]
Alkali lignin	Acetylation and hexanoation	50	Blending with polylactic acid	[194]
Industrial lignin	Lignin nanosphere prepared via ethyl acetate	0.5	Blending with polylactic acid	[195]
Kraft lignin	NA	20	Blending with polylactic acid	[196]

The link between structure and rheology significantly influences the printability, performance, and application of 3D-printed materials [197]. The disparities in the printability of a polymer predominantly stem from its rheological properties in both the printing state and solid form [198]. The rheological characteristics of lignin are heavily influenced by its structure, which varies according to the source and extraction method employed [199]. Hardwood organosolv lignin demonstrated superior printability to softwood kraft lignin at an equivalent temperature [40]. The superior printability of hardwood lignin compared to softwood lignin is attributed to the more significant presence of ether linkages in hardwood, resulting in less rigid structures characterized by C_α-C_β-C_γ-OH chains [200]. In contrast, softwood lignin is abundant in inflexible segments composed of biphenyl and biphenyl ether, which are rich in guaiacyl and p-hydroxyphenyl groups, thereby restricting its mobility and leading to a higher glass transition temperature

(Tg) and melt viscosity than hardwood lignin [200]. In addition, the rheological studies of softwood and hardwood lignin revealed that hardwood lignin has a much longer elastic response with strain amplitude over 10% [182]. In contrast, softwood lignin behaves more like a solid material at a temperature between 170-190°C. This behavior of softwood lignin is further supported by a much higher storage modulus (G') than hardwood lignin, indicating a higher complex viscosity, which will cause a resistance to flow [201]. The polydispersity of the polymers influences the rheological properties of lignin; the polydispersity of lignin is typically high in the commonly available technical lignin sourced from paper or biorefinery mills, thereby complicating the regulation of printing temperatures. The polydispersity within a single lignin polymer results in complications regarding its melting behavior, as higher molecular weight molecules necessitate elevated temperatures for melting, while lower molar mass lignin degrades into a rigid char, impeding flow or deformation [181].

To optimize lignin for 3D printing, methods such as composite formulations with polymers such as ABS and carbon fibers, thermal crosslinking methods such as chemical modifications are employed, along with tailored printing methods that enhance the performance of the final printed products, particularly in terms of mechanical strength, hydrophobicity, and hydrophilicity. The modification of lignin is crucial for improving its printability and mechanical performance in 3D printing applications. Chemical modifications such as carboxylation, esterification, methacrylate, and laccase modification can introduce flexible side chains or reduce the cross-link density of lignin, enhancing its flowability and thermal properties [183, 202]. For example, grafting lignin with polycaprolactone (PCL) or polylactic acid (PLA) before blending with pure PCL or PLA polymers improves its processability [181, 183, 203]. The modifications impart lignin flexibility, which is essential for maintaining structural integrity in printed parts. Additionally, incorporating plasticizers or additives can further enhance the elasticity and ductility of lignin-based filaments, enabling the production of more resilient printed structures. These modifications ultimately allow for fine-tuning lignin's rheological properties, making it more suitable for various 3D printing techniques, such as fused deposition modeling (FDM) or selective laser sintering (SLS) [181].

Lignin-based 3D printing offers an exciting pathway for creating sustainable materials with tailored properties. Through strategic chemical modifications and various 3D printing techniques, lignin can be transformed into a versatile feedstock for producing high-performance objects and coping with advanced manufacturing techniques. The ability to adjust mechanical strength, hydrophobicity, and hydrophilicity allows for the design of lignin-based materials that meet the specific demands of a wide range of applications, contributing to the ongoing efforts to reduce reliance on fossil fuel-derived materials in the manufacturing sector. This advancement aligns with sustainability goals and paves the way for lignin to be recognized as a valuable resource in the emerging field of additive manufacturing.

2.7. Conclusions, Limitations, Challenges, and Future Perspectives

This review examined the methodologies employed by researchers for lignin utilization through fractionation, functionalization, and a combination of both processes for thermoplastics, coatings, and 3D printing composites. The functionalization of lignin via various functional groups is a successful approach for obtaining hydrophobic, superhydrophobic, and flame-retardant coatings. Incorporating functionalized lignin in composite formulations improved the compatibility of lignin with multiple polymer matrices. However, the concentration of lignin used is significantly lower, and the utilization of toxic solvents and limited durability studies are observed as a limitation of the existing literature. Higher concentrations of lignin are reported to cause phase separation and aggregation even after modifications and significantly lower the mechanical properties. It was also demonstrated that the different lignin types significantly influence the characteristics of lignin-based polymers or composite materials.

Functionalized lignin has demonstrated significant potential in various applications due to its abundant availability, biodegradability, and unique chemical properties. It enhances coatings' UV-blocking, antimicrobial, and barrier properties, offering a sustainable alternative to fossil-based polymers. In composites, lignin improves mechanical properties and thermal stability, while in 3D printing, it serves as a renewable feedstock for creating complex structures with enhanced performance. However, challenges such as variability in lignin's structure, complexity and cost of functionalization, processing difficulties, and market acceptance need to be studied.

Future perspectives should include developing advanced functionalization techniques, integrating lignin with other biopolymers, scaling up production for industrial applications, and focusing on sustainability to drive adoption in various sectors, contributing to a circular economy. Despite the challenges, the promising future of functionalized lignin in sustainable material science is evident.

2.8. References

1. Antar, M., et al., *Biomass for a sustainable bioeconomy: An overview of world biomass production and utilization.* Renewable and Sustainable Energy Reviews, 2021. **139**: p. 110691.
2. Sertolli, A., et al., *Biomass potential and utilization in worldwide research trends—a bibliometric analysis.* Sustainability, 2022. **14**(9): p. 5515.
3. Iakovou, E., et al., *Waste biomass-to-energy supply chain management: A critical synthesis.* Waste management, 2010. **30**(10): p. 1860-1870.
4. Ali, S., et al., *Recent Advances in Characterization and Valorization of Lignin and Its Value-Added Products: Challenges and Future Perspectives.* Biomass, 2024. **4**(3): p. 947-977.
5. Radhika, N.L., S. Sachdeva, and M. Kumar, *Lignin depolymerization and biotransformation to industrially important chemicals/biofuels.* Fuel, 2022. **312**: p. 122935.
6. Watkins, D., et al., *Extraction and characterization of lignin from different biomass resources.* Journal of materials research and technology, 2015. **4**(1): p. 26-32.
7. Dessbesell, L., et al., *Global lignin supply overview and kraft lignin potential as an alternative for petroleum-based polymers.* Renewable and Sustainable Energy Reviews, 2020. **123**: p. 109768.
8. Balk, M., et al., *Lignin, the lignification process, and advanced, lignin-based materials.* International Journal of Molecular Sciences, 2023. **24**(14): p. 11668.
9. Weng, C., X. Peng, and Y. Han, *Depolymerization and conversion of lignin to value-added bioproducts by microbial and enzymatic catalysis.* Biotechnology for Biofuels, 2021. **14**: p. 1-22.
10. Mishra, M., *Lignin as a Biomaterial for Bioimaging.* 2023.
11. Zhang, W., et al., *Lignin derived carbon materials: current status and future trends.* Carbon Research, 2022. **1**(1): p. 14.
12. Gellerstedt, G. and G. Henriksson, *Lignins: major sources, structure and properties.* Monomers, polymers and composites from renewable resources, 2008: p. 201-224.
13. Karthäuser, J., et al., *Lignin and lignin-derived compounds for wood applications—a review.* Molecules, 2021. **26**(9): p. 2533.
14. Crestini, C., et al., *On the structure of softwood kraft lignin.* Green Chemistry, 2017. **19**(17): p. 4104-4121.
15. Peracchi, L.M., et al., *Grass lignin: biosynthesis, biological roles, and industrial applications.* Frontiers in Plant Science, 2024. **15**: p. 1343097.
16. Radotić, K. and M. Mićić, *Methods for extraction and purification of lignin and cellulose from plant tissues.* Sample preparation techniques for soil, plant, and animal samples, 2016: p. 365-376.
17. Panamgama, L.A. and P. Peramune. *Extraction and modification of lignin biopolymer*. IEEE.

18. de la Torre, M.J., et al., *Organosolv lignin for biofuel.* Industrial crops and products, 2013. **45**: p. 58-63.
19. Al Arni, S., *Extraction and isolation methods for lignin separation from sugarcane bagasse: a review.* Industrial Crops and Products, 2018. **115**: p. 330-339.
20. Yuan, Y., et al., *Recent advances in understanding the effects of lignin structural characteristics on enzymatic hydrolysis.* Biotechnology for Biofuels, 2021. **14**: p. 1-20.
21. Wang, G. and H. Chen, *Enhanced lignin extraction process from steam exploded corn stalk.* Separation and Purification Technology, 2016. **157**: p. 93-101.
22. Vishtal, A. and A. Kraslawski, *Challenges in industrial applications of technical lignins.* BioResources, 2011. **6**(3).
23. Bandyopadhyay-Ghosh, S., S.B. Ghosh, and M. Sain, *The use of biobased nanofibres in composites*, in *Biofiber reinforcements in composite materials*. 2015, Elsevier. p. 571-647.
24. Covinich, L.G. and M.C. Area, *Trends and Limitations of Lignin as a Starting Material.* BioResources, 2024. **19**(1).
25. Prado, R., et al., *Lignin purification with green solvents.* Cellulose Chemistry and Technology, 2012. **46**(3): p. 221.
26. Argyropoulos, D.D.S., et al., *Kraft Lignin: A Valuable, Sustainable Resource, Opportunities and Challenges.* ChemSusChem, 2023. **16**(23): p. e202300492.
27. Wang, H., et al., *From lignin to valuable products–strategies, challenges, and prospects.* Bioresource technology, 2019. **271**: p. 449-461.
28. Rabelo, S.C., et al., *Organosolv pretreatment for biorefineries: Current status, perspectives, and challenges.* Bioresource Technology, 2023. **369**: p. 128331.
29. Alherech, M., et al., *From lignin to valuable aromatic chemicals: lignin depolymerization and monomer separation via centrifugal partition chromatography.* ACS Central Science, 2021. **7**(11): p. 1831-1837.
30. Pei, Z., et al., *Research Progress on Lignin Depolymerization Strategies: A Review.* Polymers, 2024. **16**(17): p. 2388.
31. Rodrigues, J.S., et al., *Lignin fractionation methods: can lignin fractions be separated in a true industrial process?* Industrial & Engineering Chemistry Research, 2021. **60**(30): p. 10863-10881.
32. Bertella, S. and J.S. Luterbacher, *Lignin functionalization for the production of novel materials.* Trends in Chemistry, 2020. **2**(5): p. 440-453.
33. Gan, M.J., et al., *Lignin to value-added chemicals and advanced materials: extraction, degradation, and functionalization.* Green Chemistry, 2022. **24**(20): p. 7705-7750.
34. Ruwoldt, J., F.H. Blindheim, and G. Chinga-Carrasco, *Functional surfaces, films, and coatings with lignin–a critical review.* RSC advances, 2023. **13**(18): p. 12529-12553.
35. Agustiany, E.A., et al., *Recent developments in lignin modification and its application in lignin‐based green composites: a review.* Polymer Composites, 2022. **43**(8): p. 4848-4865.
36. Wang, H., M. Tucker, and Y. Ji, *Recent development in chemical depolymerization of lignin: a review.* Journal of Applied Chemistry, 2013. **2013**(1): p. 838645.
37. Jiang, L., et al., *Strategies for lignin depolymerization and reconstruction towards functional polymers.* Sustainable Energy & Fuels, 2023. **7**(13): p. 2953-2973.
38. Fazeli, M., et al., *Lignin beyond the status quo: recent and emerging composite applications.* Green Chemistry, 2024. **26**(2): p. 593-630.
39. Shorey, R., et al., *Valorization of lignin for advanced material applications: a review.* RSC Sustainability, 2024.
40. Ebers, L.S., et al., *3D printing of lignin: Challenges, opportunities and roads onward.* Biopolymers, 2021. **112**(6): p. e23431.
41. Katahira, R., T.J. Elder, and G.T. Beckham, *A brief introduction to lignin structure.* 2018.

42. Lin, S.Y. and C.W. Dence, *Methods in lignin chemistry*. 2012: Springer Science & Business Media.
43. Hatfield, R. and W. Vermerris, *Lignin formation in plants. The dilemma of linkage specificity.* Plant physiology, 2001. **126**(4): p. 1351-1357.
44. Guadix-Montero, S. and M. Sankar, *Review on catalytic cleavage of C–C inter-unit linkages in lignin model compounds: towards lignin depolymerisation*. Topics in Catalysis, 2018. **61**: p. 183-198.
45. El Mansouri, N.-E. and J. Salvadó, *Analytical methods for determining functional groups in various technical lignins*. Industrial crops and products, 2007. **26**(2): p. 116-124.
46. Sun, R.C., *Lignin source and structural characterization.* ChemSusChem, 2020. **13**(17): p. 4385-4393.
47. Liao, J.J., et al., *Current advancement on the isolation, characterization and application of lignin.* International journal of biological macromolecules, 2020. **162**: p. 985-1024.
48. Pang, T., et al., *Lignin fractionation: Effective strategy to reduce molecule weight dependent heterogeneity for upgraded lignin valorization.* Ind. Crops Prod., 2021. **165**: p. 113442. 10.1016/j.indcrop.2021.113442.
49. Huang, D., et al., *The cornerstone of realizing lignin value-addition: Exploiting the native structure and properties of lignin by extraction methods.* Chemical Engineering Journal, 2020. **402**: p. 126237.
50. Kazzaz, A.E. and P. Fatehi, *Technical lignin and its potential modification routes: A mini-review.* Ind. Crops Prod., 2020. **154**: p. 112732.
51. Gierer, J., *Chemical aspects of kraft pulping.* Wood Science and Technology, 1980. **14**(4): p. 241-266.
52. Jardim, J.M., et al., *The effect of the kraft pulping process, wood species, and pH on lignin recovery from black liquor.* Fibers, 2022. **10**(2): p. 16.
53. Kienberger, M., et al., *Systematic review on isolation processes for technical lignin.* Processes, 2021. **9**(5): p. 804.
54. Tomani, P.E.R., *The lignoboost process.* Cellulose Chemistry & Technology, 2010. **44**(1): p. 53.
55. Fatehi, P. and J. Chen, *Extraction of technical lignins from pulping spent liquors, challenges and opportunities.* Production of biofuels and chemicals from lignin, 2016: p. 35-54.
56. Diaz-Baca, J.A. and P. Fatehi, *Process development for tall oil lignin production.* Bioresource Technology, 2021. **329**: p. 124891. https://doi.org/10.1016/j.biortech.2021.124891.
57. Demuner, I.F., et al., *Biorefinery Review: Wide-Reaching Products Through Kraft Lignin.* Bioresources, 2019. **14**(3). 10.15376/biores.14.3.Demuner.
58. Figueiredo, P., et al., *Properties and chemical modifications of lignin: Towards lignin-based nanomaterials for biomedical applications.* Progress in Materials Science, 2018. **93**: p. 233-269.
59. Tribot, A., et al., *Wood-lignin: Supply, extraction processes and use as bio-based material.* European Polymer Journal, 2019. **112**: p. 228-240.
60. Mousavioun, P. and W.O.S. Doherty, *Chemical and thermal properties of fractionated bagasse soda lignin*. Industrial crops and products, 2010. **31**(1): p. 52-58.
61. Wenger, J., V. Haas, and T. Stern, *Why can we make anything from lignin except money? Towards a broader economic perspective in lignin research.* Current Forestry Reports, 2020. **6**: p. 294-308.
62. Ragauskas, A.J., et al., *Lignin valorization: improving lignin processing in the biorefinery.* science, 2014. **344**(6185): p. 1246843.
63. Suota, M.J., et al., *Lignin Functionalization Strategies and the Potential Applications of Its Derivatives-A Review.* Bioresources, 2021. **16**(3): p. 6471-6511. 10.15376/biores.16.3.Suota.
64. Xu, J., et al., *Biomass fractionation and lignin fractionation towards lignin valorization.* ChemSusChem, 2020. **13**(17): p. 4284-4295.
65. Chatterjee, S. and T. Saito, *Solvent fractionation of lignin*, in *Polymer Precursor-Derived Carbon*. 2014, ACS Publications. p. 153-168.

66. Sadeghifar, H. and A. Ragauskas, *Perspective on technical lignin fractionation.* ACS sustain. Chem. Eng., 2020. **8**(22): p. 8086-8101. 10.1021/acssuschemeng.0c01348.
67. Wang, G. and H. Chen, *Fractionation of alkali-extracted lignin from steam-exploded stalk by gradient acid precipitation.* Separation and Purification Technology, 2013. **105**: p. 98-105.
68. dos Santos, P.S.B., et al., *Characterisation of Kraft lignin separated by gradient acid precipitation.* Industrial crops and products, 2014. **55**: p. 149-154.
69. Brodin, I., E. Sjöholm, and G. Gellerstedt, *Kraft lignin as feedstock for chemical products: The effects of membrane filtration.* 2009.
70. Burke, J., *Solubility parameters: theory and application.* 1984.
71. Hansen, C.M., *Hansen solubility parameters: a user's handbook*. 2007: CRC press.
72. Schuerch, C., *The solvent properties of liquids and their relation to the solubility, swelling, isolation and fractionation of lignin.* Journal of the American Chemical Society, 1952. **74**(20): p. 5061-5067.
73. Gigli, M. and C. Crestini, *Fractionation of industrial lignins: opportunities and challenges.* Green Chem., 2020. **22**(15): p. 4722-4746. 10.1039/D0GC01606C.
74. Hararak, B., I. Khan, and G.F. Fernando, *Single-Solvent Fractionation and Electro-Spinning Neat Softwood Kraft Lignin.* ACS Applied Bio Materials, 2023. **6**(8): p. 3153-3165.
75. Passoni, V., et al., *Fractionation of Industrial Softwood Kraft Lignin: Solvent Selection as a Tool for Tailored Material Properties.* ACS Sustainable Chemistry & Engineering, 2016. **4**(4): p. 2232-2242. 10.1021/acssuschemeng.5b01722.
76. Domínguez-Robles, J., et al., *Aqueous acetone fractionation of kraft, organosolv and soda lignins.* International Journal of Biological Macromolecules, 2018. **106**: p. 979-987. https://doi.org/10.1016/j.ijbiomac.2017.08.102.
77. Meng, X., et al., *Characterization of fractional cuts of co-solvent enhanced lignocellulosic fractionation lignin isolated by sequential precipitation.* Bioresource technology, 2019. **272**: p. 202-208.
78. Evstigneyev, E.I. and S.M. Shevchenko, *Structure, chemical reactivity and solubility of lignin: a fresh look.* Wood Science and Technology, 2019. **53**: p. 7-47.
79. Vermaas, J.V., M.F. Crowley, and G.T. Beckham, *Molecular lignin solubility and structure in organic solvents.* ACS Sustainable Chemistry & Engineering, 2020. **8**(48): p. 17839-17850.
80. Hong, S., et al., *Structure–function relationships of deep eutectic solvents for lignin extraction and chemical transformation.* Green Chemistry, 2020. **22**(21): p. 7219-7232.
81. Katahira, R., T.J. Elder, and G.T. Beckham, *A Brief Introduction to Lignin Structure*, in *Lignin Valorization: Emerging Approaches*, G.T. Beckham, Editor. 2018, The Royal Society of Chemistry. p. 0.
82. Akpan, E.I., *Chemistry and structure of lignin.* Sustainable Lignin for Carbon Fibers: Principles, Techniques, and Applications, 2019: p. 1-50.
83. Kazzaz, A.E., Z.H. Feizi, and P. Fatehi, *Grafting strategies for hydroxy groups of lignin for producing materials.* Green Chem., 2019. **21**(21): p. 5714-5752. https://doi.org/10.1039/C9GC02598G.
84. Hua, Q., et al., *Aqueous dispersions of esterified lignin particles for hydrophobic coatings.* Frontiers in chemistry, 2019. **7**: p. 515.
85. Alwadani, N., N. Ghavidel, and P. Fatehi, *Surface and interface characteristics of hydrophobic lignin derivatives in solvents and films.* Colloids Surf., 2021. **609**: p. 125656. https://doi.org/10.1016/j.colsurfa.2020.125656.
86. Kudanga, T., et al., *Reactivity of long chain alkylamines to lignin moieties: Implications on hydrophobicity of lignocellulose materials.* Journal of biotechnology, 2010. **149**(1-2): p. 81-87.
87. Buono, P., et al., *New insights on the chemical modification of lignin: Acetylation versus silylation.* ACS Sustainable Chemistry & Engineering, 2016. **4**(10): p. 5212-5222.

88. Shorey, R., A. Gupta, and T.H. Mekonnen, *Hydrophobic modification of lignin for rubber composites.* Ind. Crops Prod., 2021. **174**: p. 114189. https://doi.org/10.1016/j.indcrop.2021.114189.
89. Ouyang, X., et al., *Sulfonation of alkali lignin and its potential use in dispersant for cement.* Journal of Dispersion Science and Technology, 2009. **30**(1): p. 1-6.
90. Figueiredo, P., et al., *Functionalization of carboxylated lignin nanoparticles for targeted and pH-responsive delivery of anticancer drugs.* Nanomedicine, 2017. **12**(21): p. 2581-2596.
91. Podschun, J., B. Saake, and R. Lehnen, *Reactivity enhancement of organosolv lignin by phenolation for improved bio-based thermosets.* European Polymer Journal, 2015. **67**: p. 1-11.
92. Kazzaz, A.E. and P. Fatehi, *Fabrication of amphoteric lignin and its hydrophilicity/oleophilicity at oil/water interface.* Journal of colloid and interface science, 2020. **561**: p. 231-243.
93. Atifi, S., C. Miao, and W.Y. Hamad, *Surface modification of lignin for applications in polypropylene blends.* Journal of Applied Polymer Science, 2017. **134**(29): p. 45103.
94. Zadeh, E.M., S.F. O'Keefe, and Y.-T. Kim, *Utilization of lignin in biopolymeric packaging films.* ACS omega, 2018. **3**(7): p. 7388-7398.
95. Wang, T.Y., et al., *Lignin to dispersants, adsorbents, flocculants and adhesives: A critical review on industrial applications of lignin.* Industrial Crops and Products, 2023. **199**. 10.1016/j.indcrop.2023.116715.
96. Yang, H., et al., *Lignin-derived bio-based flame retardants toward high-performance sustainable polymeric materials.* Green Chem., 2020. **22**(7): p. 2129-2161.
97. Saikia, A., K. Dutta, and A. Singh, *Solvent -free grafting route to develop thin and flexible polymer film from lignin.* Polymers for Advanced Technologies, 2024. **35**(6): p. e6457.
98. Trinh, B.M., et al., *Compostable lignin grafted poly (ε-caprolactone) polyurethane biomedical materials: Shape memory, foaming capabilities, and biocompatibility.* Chem. Eng. J., 2024. **485**: p. 149845. 10.1016/j.cej.2024.149845.
99. Law, K.-Y., *Definitions for hydrophilicity, hydrophobicity, and superhydrophobicity: getting the basics right*. 2014, ACS Publications. p. 686-688.
100. Drelich, J., et al., *Hydrophilic and superhydrophilic surfaces and materials.* Soft Matter, 2011. **7**(21): p. 9804-9828.
101. Zettlemoyer, A.C., *Hydrophobic surfaces.* Journal of Colloid and Interface Science, 1968. **28**(3-4): p. 343-369.
102. Ma, M. and R.M. Hill, *Superhydrophobic surfaces.* Current opinion in colloid & interface science, 2006. **11**(4): p. 193-202.
103. Jeevahan, J., et al., *Superhydrophobic surfaces: a review on fundamentals, applications, and challenges.* Journal of Coatings Technology and Research, 2018. **15**: p. 231-250.
104. Law, K.-Y., *Water–surface interactions and definitions for hydrophilicity, hydrophobicity and superhydrophobicity.* Pure and Applied Chemistry, 2015. **87**(8): p. 759-765.
105. Musl, O., et al., *Mapping of the hydrophobic composition of lignosulfonates.* ACS Sustainable Chemistry & Engineering, 2021. **9**(49): p. 16786-16795.
106. Yu, S., et al., *Lignin self-assembly and auto-adhesion for hydrophobic cellulose/lignin composite film fabrication.* International Journal of Biological Macromolecules, 2023. **233**: p. 123598.
107. Ekeberg, D., et al., *Characterisation of lignosulphonates and kraft lignin by hydrophobic interaction chromatography.* Analytica Chimica Acta, 2006. **565**(1): p. 121-128.
108. Erfani Jazi, M., et al., *Structure, chemistry and physicochemistry of lignin for material functionalization.* SN Applied Sciences, 2019. **1**(9): p. 1094. 10.1007/s42452-019-1126-8.
109. Lisý, A., et al., *About Hydrophobicity of lignin: A review of selected chemical methods for lignin valorisation in biopolymer production.* Energies, 2022. **15**(17): p. 6213.

110. Huang, J.J., et al., *Impacts of hydrophobic, hydrophilic, superhydrophobic and superhydrophilic nanofibrous substrates on the thin film composite forward osmosis membranes.* Journal of Environmental Chemical Engineering, 2022. **10**(1): p. 106958.
111. An, L., et al., *One-step silanization and amination of lignin and its adsorption of Congo red and Cu (II) ions in aqueous solution.* International Journal of Biological Macromolecules, 2020. **159**: p. 222-230.
112. Siuda, J., et al., *Catalyzed Reaction of Cellulose and Lignin with Methyltrimethoxysilane-FT-IR, C-13 NMR and Si-29 NMR Studies.* Materials, 2019. **12**(12). 10.3390/ma12122006.
113. Devadasu, S., et al. *Development of ultra-high build self-healing coatings using amino silanized lignin nanocapsules*. in *2nd International Conference on Aspects of Materials Science and Engineering (ICAMSE)*. 2021. Chandigarh, INDIA.
114. Ding, H., et al., *High hydrophobic poly(lactic acid) foams impregnating one-step Si-F modified lignin nanoparticles for oil/organic solvents absorption.* Composites Communications, 2021. **25**. 10.1016/j.coco.2021.100730.
115. Li, S., et al., *Thermally stable and tough coatings and films using vinyl silylated lignin.* ACS Sustainable Chemistry & Engineering, 2018. **6**(2): p. 1988-1998.
116. Sun, H., et al., *Lignin-based superhydrophobic melamine resin sponges and their application in oil/water separation.* Industrial crops and products, 2021. **170**: p. 113798.
117. Nisar, S. and Z.A. Raza, *Corn straw lignin—A sustainable bioinspired finish for superhydrophobic and UV-protective cellulose fabric.* International Journal of Biological Macromolecules, 2024. **257**: p. 128393.
118. Liu, X., et al., *Preparation and Performance of Lignin-Based Multifunctional Superhydrophobic Coating.* Molecules, 2022. **27**(4): p. 1440.
119. Li, M., et al., *Preparation of lignin nanospheres based superhydrophobic surfaces with good robustness and long UV resistance.* RSC advances, 2022. **12**(18): p. 11517-11525.
120. Ma, B., et al., *Tailorable and scalable production of eco-friendly lignin micro-nanospheres and their application in functional superhydrophobic coating.* Chemical Engineering Journal, 2023. **457**: p. 141309. https://doi.org/10.1016/j.cej.2023.141309.
121. Sha, X., et al., *Preparation and properties of sustainable superhydrophobic cotton fabrics modified with lignin nanoparticles, tannic acid and Methyltrimethoxysilane.* Chemical Engineering Journal, 2024: p. 155797.
122. Zhang, Y., et al., *Functional food packaging for reducing residual liquid food: Thermo-resistant edible super-hydrophobic coating from coffee and beeswax.* Journal of colloid and interface science, 2019. **533**: p. 742-749.
123. Jeffri, N.I., et al., *Unlocking the potential: Evolving role of technical lignin in diverse applications and overcoming challenges.* International Journal of Biological Macromolecules, 2024: p. 133506.
124. Fattahi, N., et al., *Lignin: A valuable and promising bio-based absorbent for dye removal applications.* International Journal of Biological Macromolecules, 2024: p. 133763.
125. Ahadyani, N. and M. Abdollahi, *Phenolation, amination and cross-linking of lignin: synthesis and characterization of functionalized lignin.* Polymer Bulletin, 2024. **81**(10): p. 8643-8661.
126. Jia, Z., et al., *One-pot amination and carboxylation functionalization of lignin for efficient adsorption of Cr (VI) and Cd (II): influence of functional groups on adsorption equilibrium and mechanism.* Colloids and Surfaces A: Physicochemical and Engineering Aspects, 2024: p. 135278.
127. Qulatein, H.A., W. Gao, and P. Fatehi, *Carboxyalkylated Lignin as a Sustainable Dispersant for Coal Water Slurry.* Polymers, 2024. **16**(18): p. 2586.
128. Andriani, F. and M. Lawoko, *Oxidative Carboxylation of Lignin: Exploring Reactivity of Different Lignin Types.* Biomacromolecules, 2024.

129. Shomali, Z. and P. Fatehi, *Carboxyalkylated lignin nanoparticles with enhanced functionality for oil–water pickering emulsion systems.* ACS Sustainable Chemistry & Engineering, 2022. **10**(50): p. 16563-16577.
130. Wang, B., et al., *Recent advances in lignin modification and its application in wastewater treatment.* Lignin Utilization Strategies: From Processing to Applications, 2021: p. 143-173.
131. Ghavidel, N., M.K. Konduri, and P. Fatehi, *Chemical reactivity and sulfo-functionalization response of enzymatically produced lignin.* Industrial Crops and Products, 2021. **172**: p. 113950.
132. Cui, C., et al., *Toward Thermoplastic Lignin Polymers; Part II: Thermal & Polymer Characteristics of Kraft Lignin & Derivatives.* BioResources, 2013. **8**(1).
133. Parit, M. and Z. Jiang, *Towards lignin derived thermoplastic polymers.* Int. J. Biol. Macromol., 2020. **165**: p. 3180-3197.
134. Gordobil, O., et al., *Lignin-ester derivatives as novel thermoplastic materials.* RSC advances, 2016. **6**(90): p. 86909-86917.
135. Hatakeyama, T., S. Yamashita, and H. Hatakeyama, *Thermal properties of lignin-based polycaprolactones.* J. Therm. Anal. Calorim., 2021. **143**: p. 203-211.
136. Najarro, M.C., et al., *Tuning the lignin-caprolactone copolymer for coating metal surfaces.* ACS Appl. Polym. Mater., 2020. **2**(12): p. 5767-5778. 10.1021/acsapm.0c01026.
137. Santos, C.C.O., et al., *Lignin valorization through polymer grafting by ring-opening polymerization and its application in health, packaging, and coating.* J. Environ. Chem. Eng., 2023. **11**(3): p. 109691. https://doi.org/10.1016/j.jece.2023.109691.
138. Park, I.-K., et al., *Solvent-free bulk polymerization of lignin-polycaprolactone (PCL) copolymer and its thermoplastic characteristics.* Sci. Rep., 2019. **9**(1): p. 7033. s41598-019-43296-2.
139. Liang, X., et al., *Thermal kinetics of a lignin-based flame retardant.* Polymers, 2020. **12**(9): p. 2123.
140. Mandlekar, N., et al., *An overview on the use of lignin and its derivatives in fire retardant polymer systems*. Lignin-trends and applications. Vol. 9. 2018: IntechOpen, London, UK. 207-231.
141. Liang, D., et al., *Preparation of a novel lignin-based flame retardant for epoxy resin.* Materials Chemistry and Physics, 2021. **259**: p. 124101.
142. Gao, C., et al., *Phosphorylated kraft lignin with improved thermal stability.* International Journal of Biological Macromolecules, 2020. **162**: p. 1642-1652.
143. Zhang, S., et al., *Phosphorus containing group and lignin toward intrinsically flame retardant cellulose nanofibril-based film with enhanced mechanical properties.* Composites Part B: Engineering, 2021. **212**: p. 108699.
144. Illy, N., et al., *Phosphorylation of bio-based compounds: the state of the art.* Polymer Chemistry, 2015. **6**(35): p. 6257-6291.
145. Costes, L., et al., *Phosphorus and nitrogen derivatization as efficient route for improvement of lignin flame retardant action in PLA.* European Polymer Journal, 2016. **84**: p. 652-667.
146. Laoutid, F., et al., *Lignin as a flame retardant for biopolymers*, in *Micro and Nanolignin in Aqueous Dispersions and Polymers*. 2022, Elsevier. p. 173-202.
147. Schartel, B., *Phosphorus-based flame retardancy mechanisms—old hat or a starting point for future development?* Materials, 2010. **3**(10): p. 4710-4745.
148. Shukla, A., et al., *Sodium lignin sulfonate: a bio-macromolecule for making fire retardant cotton fabric.* Cellulose, 2019. **26**: p. 8191-8208.
149. Zhang, J., et al., *Flame retardant lignin-based silicone composites.* RSC advances, 2015. **5**(126): p. 103907-103914.
150. Li, J., et al., *Triple silicon, phosphorous, and nitrogen-grafted lignin-based flame retardant and its vulcanization promotion for styrene butadiene rubber.* ACS omega, 2023. **8**(24): p. 21549-21558.
151. Chen, J., et al., *Production of flocculants, adsorbents, and dispersants from lignin.* Molecules, 2018. **23**(4): p. 868.

152. Sutradhar, S., W. Gao, and P. Fatehi, *A green cement plasticizer from softwood kraft lignin.* Industrial & Engineering Chemistry Research, 2023. **62**(3): p. 1676-1687.
153. Qin, Y., D. Yang, and X. Qiu, *Hydroxypropyl sulfonated lignin as dye dispersant: Effect of average molecular weight.* ACS Sustainable Chemistry & Engineering, 2015. **3**(12): p. 3239-3244.
154. Qin, Y., et al., *Preparation and interaction mechanism of Nano disperse dye using hydroxypropyl sulfonated lignin.* International journal of biological macromolecules, 2020. **152**: p. 280-287.
155. Su, J., et al., *Sulfonated lignin modified with silane coupling agent as biodegradable shale inhibitor in water-based drilling fluid.* Journal of Petroleum Science and Engineering, 2022. **208**: p. 109618.
156. Wang, L., et al., *Tailored thermosetting wood adhesive based on well-defined hardwood lignin fractions.* ACS Sustainable Chemistry & Engineering, 2020. **8**(35): p. 13517-13526.
157. Sreejaya, M.M., et al., *Lignin-based organic coatings and their applications: A review.* Materials Today: Proceedings, 2022. **60**: p. 494-501.
158. Wang, X., et al., *Anticorrosive epoxy coatings from direct epoxidation of bioethanol fractionated lignin.* International Journal of Biological Macromolecules, 2022. **221**: p. 268-277. https://doi.org/10.1016/j.ijbiomac.2022.08.177.
159. Park, Y., W.O.S. Doherty, and P.J. Halley, *Developing lignin-based resin coatings and composites.* Industrial crops and products, 2008. **27**(2): p. 163-167.
160. Hua, Q., et al., *Aqueous dispersions of esterified lignin particles for hydrophobic coatings.* Front. Chem., 2019: p. 515.
161. Ma, X., et al., *Lignin -based polyurethane: recent advances and future perspectives.* Macromolecular Rapid Communications, 2021. **42**(3): p. 2000492.
162. Alinejad, M., et al., *Lignin-based polyurethanes: Opportunities for bio-based foams, elastomers, coatings and adhesives.* Polymers, 2019. **11**(7): p. 1202.
163. Golling, F.E., et al., *Polyurethanes for coatings and adhesives–chemistry and applications.* Polymer International, 2019. **68**(5): p. 848-855.
164. Das, A. and P. Mahanwar, *A brief discussion on advances in polyurethane applications.* Advanced Industrial and Engineering Polymer Research, 2020. **3**(3): p. 93-101.
165. Li, C., et al., *Fractionated lignin as a polyol in polyurethane fabrication.* International Journal of Biological Macromolecules, 2024. **256**: p. 128290. https://doi.org/10.1016/j.ijbiomac.2023.128290.
166. Klein, S.E., et al., *Antimicrobial activity of lignin-derived polyurethane coatings prepared from unmodified and demethylated lignins.* Coatings, 2019. **9**(8): p. 494.
167. Zhang, Y., et al., *Ozone oxidized lignin-based polyurethane with improved properties.* European Polymer Journal, 2019. **117**: p. 114-122.
168. Li, Y.J., et al., *Research and application progress of lignin-based composite membrane.* Journal of Polymer Engineering, 2021. **41**(4): p. 245-258. 10.1515/polyeng-2020-0268.
169. Petkovska, J., et al., *Flame-retardant, antimicrobial, and UV-protective lignin-based multilayer nanocoating.* ACS Applied Polymer Materials, 2022. **4**(6): p. 4528-4537.
170. Zhang, Y. and M. Naebe, *Lignin: A review on structure, properties, and applications as a light-colored UV absorber.* ACS Sustainable Chemistry & Engineering, 2021. **9**(4): p. 1427-1442.
171. Mo, J., et al., *Construction of interfacial dynamic bonds for high performance lignin/polymer biocomposites.* Frontiers of Chemical Science and Engineering, 2023. **17**(10): p. 1372-1388.
172. Patanair, B., et al., *Promoting interfacial interactions with the addition of lignin in poly (lactic acid) hybrid nanocomposites.* Polymers, 2021. **13**(2): p. 272.
173. Carlos de Haro, J., et al., *Lignin-based anticorrosion coatings for the protection of aluminum surfaces.* ACS Sustainable Chemistry & Engineering, 2019. **7**(6): p. 6213-6222.

174. Henn, K.A., et al., *Colloidal Lignin Particles and Epoxies for Bio-Based, Durable, and Multiresistant Nanostructured Coatings.* ACS Appl. Mater. Interfaces, 2021. **13**(29): p. 34793-34806. 10.1021/acsami.1c06087.
175. Shahrubudin, N., T.C. Lee, and R. Ramlan, *An overview on 3D printing technology: Technological, materials, and applications.* Procedia manufacturing, 2019. **35**: p. 1286-1296.
176. Mpofu, T.P., C. Mawere, and M. Mukosera, *The impact and application of 3D printing technology.* 2014.
177. Yan, Q., et al., *A review of 3D printing technology for medical applications.* Engineering, 2018. **4**(5): p. 729-742.
178. Kamran, M. and A. Saxena, *A comprehensive study on 3D printing technology.* MIT Int J Mech Eng, 2016. **6**(2): p. 63-69.
179. Stansbury, J.W. and M.J. Idacavage, *3D printing with polymers: Challenges among expanding options and opportunities.* Dental materials, 2016. **32**(1): p. 54-64.
180. Liu, J., et al., *Current advances and future perspectives of 3D printing natural-derived biopolymers.* Carbohydrate polymers, 2019. **207**: p. 297-316.
181. Wan, Z., et al., *Recent advances in lignin-based 3D printing materials: A mini-review.* International Journal of Biological Macromolecules, 2023. **253**: p. 126660. https://doi.org/10.1016/j.ijbiomac.2023.126660.
182. Jiang, B., et al., *Lignin -based materials for additive manufacturing: chemistry, processing, structures, properties, and applications.* Advanced Science, 2023. **10**(9): p. 2206055.
183. Hong, S.-H., et al., *Preparation of chemically modified lignin-reinforced PLA biocomposites and their 3D printing performance.* Polymers, 2021. **13**(4): p. 667.
184. Jiménez, M., et al., *Additive manufacturing technologies: an overview about 3D printing methods and future prospects.* Complexity, 2019. **2019**(1): p. 9656938.
185. Prabhakar, M.M., et al., *A short review on 3D printing methods, process parameters and materials.* Materials Today: Proceedings, 2021. **45**: p. 6108-6114.
186. Izdebska-Podsiadły, J., *Classification of 3D printing methods*, in *Polymers for 3D printing*. 2022, Elsevier. p. 23-34.
187.Böcherer, D., et al., *Decolorization of Lignin for High -Resolution 3D Printing of High Lignin -Content Composites.* Advanced Science, 2024: p. 2406311.
188. Wang, Z., M.S. Ganewatta, and C. Tang, *Sustainable polymers from biomass: Bridging chemistry with materials and processing.* Progress in Polymer Science, 2020. **101**: p. 101197.
189. Nguyen, N.A., C.C. Bowland, and A.K. Naskar, *A general method to improve 3D-printability and inter-layer adhesion in lignin-based composites.* Appl. Mater., 2018. **12**: p. 138-152. 10.1016/j.apmt.2018.03.009.
190. Vaidya, A.A., et al., *Integrating softwood biorefinery lignin into polyhydroxybutyrate composites and application in 3D printing.* Materials Today Communications, 2019. **19**: p. 286-296. https://doi.org/10.1016/j.mtcomm.2019.02.008.
191. Fan, D., et al., *Valorization of enzymatic hydrolysis lignin for the multifunctional stabilization of polypropylene.* Industrial Crops and Products, 2022. **187**: p. 115443. https://doi.org/10.1016/j.indcrop.2022.115443.
192. Kim, S.-H., et al., *Non-Einstein Viscosity Phenomenon of Acrylonitrile–Butadiene–Styrene Composites Containing Lignin–Polycaprolactone Particulates Highly Dispersed by High-Shear Stress.* ACS Omega, 2019. **4**(6): p. 10036-10043. 10.1021/acsomega.9b01043.
193. Mohan, D., et al., *Homogeneous distribution of lignin/graphene fillers with enhanced interlayer adhesion for 3D printing filament.* Polymer Composites, 2021. **42**(5): p. 2408-2421.

194. Yao, J., K. Odelius, and M. Hakkarainen, *Microwave Hydrophobized Lignin with Antioxidant Activity for Fused Filament Fabrication.* ACS Applied Polymer Materials, 2021. **3**(7): p. 3538-3548. 10.1021/acsapm.1c00438.
195. Long, H., et al., *Enhancing the performance of polylactic acid composites through self-assembly lignin nanospheres for fused deposition modeling.* Composites Part B: Engineering, 2022. **239**: p. 109968. https://doi.org/10.1016/j.compositesb.2022.109968.
196. Gkartzou, E., E.P. Koumoulos, and C.A. Charitidis, *Production and 3D printing processing of bio-based thermoplastic filament.* Manufacturing Review, 2017. **4**: p. 1.
197. Ngo, T.D., et al., *Additive manufacturing (3D printing): A review of materials, methods, applications and challenges.* Composites Part B: Engineering, 2018. **143**: p. 172-196.
198. Fritzler, K.B. and V.Y. Prinz, *3D printing methods for micro-and nanostructures.* Physics-Uspekhi, 2019. **62**(1): p. 54.
199. Sakunkittiyut, Y., et al., *Effect of kraft lignin on protein aggregation, functional, and rheological properties of fish protein -based material.* Journal of applied polymer science, 2013. **127**(3): p. 1703-1710.
200. Awal, A. and M. Sain, *Spectroscopic studies and evaluation of thermorheological properties of softwood and hardwood lignin.* Journal of Applied Polymer Science, 2011. **122**(2): p. 956-963.
201. Nguyen, N.A., et al., *A path for lignin valorization via additive manufacturing of high-performance sustainable composites with enhanced 3D printability.* Science advances, 2018. **4**(12): p. eaat4967.
202. Murillo-Morales, G., et al., *Characterization and 3D printing of a biodegradable polylactic acid/thermoplastic polyurethane blend with laccase-modified lignin as a nucleating agent.* International Journal of Biological Macromolecules, 2023. **236**: p. 123881.
203. Domínguez-Robles, J., et al., *Poly(caprolactone)/lignin-based 3D-printed dressings loaded with a novel combination of bioactive agents for wound-healing applications.* Sustainable Materials and Technologies, 2023. **35**: p. e00581. https://doi.org/10.1016/j.susmat.2023.e00581.

Chapter 3: Solvent-Free Lignin-Silsesquioxane Wood Coating Formulation with Superhydrophobic and Flame-Retardant Functionalities

Banchamlak Bemerw Kassaun[1] *and Pedram Fatehi*[1,2]*

Published in J. Chem. Eng. Volume 493, 1 August 2024, 152582

https://doi.org/10.1016/j.cej.2024.152582

[1]*Biorefining Research Institute, Lakehead University, 955 Oliver Road, Thunder Bay, Ontario, P7B 5E1 Canada.*

[2]*Laboratory of Natural Materials Technology, Åbo Akademi University, Henrikinkatu 2, Turku FI-20500, Finland*

First Author, email: bkassaun@lakeheadu.ca, address: 955 Oliver Road, Thunder Bay, ON, Canada, P7B 5E1

Corresponding author, email: pfatehi@lakeheadu.ca, address: 955 Oliver Road, Thunder Bay, ON, Canada, P7B 5E1

The contribution of Banchamlak Bemerw Kassaun to this work was the conception of the original draft, visualization, validation, formal analysis, data curation, and conceptualization.

Graphic abstract

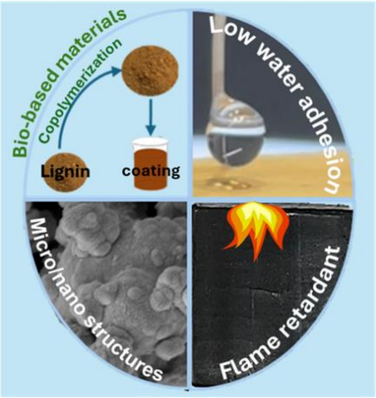

3.1. Abstract

There is a tremendous motivation to develop eco-friendly formulas for superhydrophobic and flame-retardant coatings. Presently used coating materials, particularly fluorinated compounds and their organic solvents, are potentially toxic. Here, we demonstrate that a silsesquioxane-grafted kraft lignin (WSL) and aluminum phosphate (AP) binder, i.e., an aqueous sustainable formula, can produce a flame retardant and superhydrophobic coating that is highly resistant to water and solvents. The chemical reaction of softwood kraft lignin (SKL) and aminopropyl/methyl silsesquioxane (WAPMSS) was studied comprehensively. NMR and XPS analyses confirmed the conversion of hydroxyl groups of SKL to Si-O-C via polycondensation. The product exhibited negligible wettability and was very hydrophobic. The dip coating of stain-grade pine wood species in the best formula containing WSL and AP dispersion (1/1 wt./wt.) rendered wood with superhydrophobic (with a water contact angle of (WCA) of 158°) and flame-retardant (with a limited oxygen index (LOI) of 27.2 %) functionalities. The exposure of coated wood to different liquids and high temperatures, as well as abrasion, touching, and knife-cutting analyses, confirmed the excellent durability of the coating formulation on wood. This paper demonstrates an eco-friendly pathway to produce a sustainable wood coating formulation with superhydrophobic and flame-retardant features.

3.2. Introduction

Wood is a valuable alternative to mineral and petroleum products since it requires less energy to process and stores carbon dioxide [1]. However, its hygroscopicity and flammability limit its use in many applications, such as interior furnishing, structural components, and flooring [2, 3]. There is a growing interest in developing superhydrophobic coatings for wood surfaces to inhabit the wood's moisture absorption and flammability [4]. Superhydrophobicity can be achieved by coating the surface with low surface energy molecules, such as fluorinated and polydimethylsiloxane compounds [5-7]. The uses of fluorinated compounds as superhydrophobic materials are known to cause bioaccumulation and other environmental issues. Currently, halogenated compounds are used as additives in polymer coatings to improve wood's flame-retardant application [8]. When added to a coating polymer, halogenated compounds are not chemically bonded. As a result, these compounds can gradually separate from the polymer and enter the environment. This poses a concern to the environment due to their persistent nature and toxicity [9]. Thus, strong incentives exist for fabricating sustainable superhydrophobic and flame-retardant coating materials.

Lignin can be applied for wood coating to improve its bio-resistance [10]. Interestingly, a recent study suggests that lignin can be utilized in wood coatings to impart superhydrophobic characteristics, eliminating the need for fluorine [11]. Despite the progress, the chemical modification of lignin is necessary to improve lignin's hydrophobicity for coating applications. Chemical modifications, such as methylation, demethylation, phenylation, esterification, and silanization, are among the pathways reported to improve lignin's hydrophobicity [12]. For example, one research work modified lignin using a two-step procedure involving hydroxyethylation and esterification [13]. Although the change improved the hydrophobic characteristics of the lignin-based coating, the process of modifying lignin in two steps may not be economically viable or appealing to the industry. Therefore, there is a strong incentive to identify a simple method for improving the hydrophobicity of lignin for coating formulations.

Alternatively, the incorporation of lignin in the coating formulation can offer an additional advantage to the formulation, as lignin can serve as an environmentally friendly flame retardant (FR). The FR characteristics of lignin rise from its strong charring capability due to its strong aromatic composition [14]. The FR potential of lignin was evident when it was incorporated in several polymeric matrices, such as low-density polyethylene (LDPE), polypropylene (PP), polylactic acid (PLA), acrylonitrile-butadiene-styrene copolymer (ABS), polyurethane (PU), and epoxy resins (EPs) [15]. To further improve the role of lignin as a flame retardant, the chemical modification of lignin with nitrogen and/or phosphorus-containing compounds was investigated [13]. For example, lignin was functionalized by grafting phosphorus–nitrogen and coordinating with Cu^{2+} in a two-step reaction [16]. While the impact of phosphorus–nitrogen-modified lignin incorporation on the FR of polypropylene and wood composite was positive, the effect on hydrophobicity was not reported. Therefore, the demand for a lignin-based formula imparting superhydrophobic and flame-retardant features to wood is high.

In this study, we demonstrated, for the first time, a solvent-free polymerization of softwood kraft lignin (SKL) and aminopropyl/methyl silsesquioxane (WAPMSS) to generate a sustainable coating formula with elevated flame retardancy and superhydrophobicity for wood products. A water-soluble inorganic aluminum phosphate (AP) binder was utilized in the formulation to increase the dispersion and adherence of the copolymer. Advanced techniques, such as NMR, XPS, TGA, contact angle, limited oxygen index, and smoke detector analyzers, comprehensively investigated coating formulas' physicochemical, surface, and thermal characteristics. This research demonstrates that silsesquioxane-copolymerized lignin in fluorine-free aqueous coating formulations can provide impressive superhydrophobic and flame-retardant performance.

3.3. Experimental Section

3.3.1. Materials

Softwood kraft lignin (SKL) was obtained from FPInnovations and produced via LignoForce technology. Aminopropyl/methyl silsesquioxane (WAPMSS) oligomer was purchased from Gelest Inc. USA. Sodium hydroxide (NaOH), deuterated sodium hydroxide (NaOD), deuterium oxide (D_2O-d_2), deuterated dimethyl sulfoxide (DMSO-d_6), hydrochloric acid (HCl) 37 %, 2-chloro-4,4,5,5-tetramethyl-1,3,2-dioxaphospholane (TMDP), chloroform ($CDCl_3$), ethanol (95 %), pyridine, cyclohexanol (99 %), chromium (III) acetylacetonate (97 %), aluminum hydroxide, orthophosphoric acid, toluene, and ethylene glycol were all purchased from Millipore Sigma, Oakville, Canada. Also, nylon membrane syringe filters with 0.45 µm pore openings were purchased from Fisher Scientific, Ottawa, Canada. A dialysis membrane (1,000 g/mol cut off) was obtained from spectrum labs.

3.3.2. Preparation of SKL-WAPMSS (WSL) polymers

The polymerization of SKL and WSL was conducted in an aqueous environment following the polycondensation reaction [17]. Taguchi L9 3×4 orthogonal array experimental design was used to analyze the effects of the reaction's concentration, time, temperature, and pH on the properties of induced polymers (**Table S3.1**) Appendix 3A. In this experiment, an SKL aqueous solution was prepared (25 g/L) in three-neck round bottom flasks equipped with a magnetic stirrer (200 rpm), and different concentrations of WAPMSS were added to the suspension to make different molar ratios of SKL/WAPMSS (1:0.4, 1:1.1 or 1:2.3). The pH of the system was adjusted to 10, 11, or 12 using 1 M NaOH. The system was refluxed at three different temperatures (40, 60, or 80 °C) for three periods (24, 48, or 72 h). Upon completion of the reaction, the product was centrifuged and washed three times with toluene to remove any remaining unreacted chemicals. The supernatant was resuspended in water, neutralized with 1M of HCl, followed by dialysis for 24 h, and dried in a standard oven at 60 °C for 48 h. The overall schematics are illustrated in **Figure S3.1(**a). Reaction parameters were optimized using the design expert software based on the yield and grafting ratio estimated using **Equations S**3.1 and **S**3.2. The reaction achieved the highest grafting ratio, WSL10, when conducted at pH 11, a temperature of 60 °C, and a duration of 48 hours, using a 1:1.2 mmol ratio of SKL/WAPMSS.

3.3.3. Characterization of SKL, WAPMSS and WSL copolymers

The structural analysis of SKL, WAPMSS, and copolymers was performed by proton nuclear magnetic resonance (^{1}H-NMR), heteronuclear single quantum coherence NMR (HSQC), and phosphorus nuclear magnetic (^{31}P-NMR) analysis using nuclear magnetic resonance spectroscopy (Bruker AVANCE Neo NMR-500 MHz apparatus USA) with top spin 4.02 version software. Fourier transform infrared spectroscopy (FTIR) was used to analyze the structure of the samples. In this experiment, 60-80 mg of dried, crushed lignin derivatives were deposited on the Total Reflectance (ATR) crystal of Bruker Tensor 37 (Bruker, Germany) with a PIKE MIRacle Diamond Attenuated FTIR instrument. Then, 32 scans were conducted for each sample with a resolution of 4 cm^{-1} at a wavenumber range of 500 and 4000 cm^{-1}. The chemical compositions of the samples were investigated using an X-ray photoelectron spectrometer (XPS) analyzer (Kratos AXIS Supra, Shimadzu Group Company, Japan), which was equipped with a dual anode AL/Ag monochromatic X-ray source (1486.7 eV). Oven-dried samples (60 °C) were placed on a double-sided carbon tape and fed through the XPS equipment. The number of steps, dwell, and sweep times were 230, 260, and 60 s, respectively. ESCApe^{TM} (1.4.0.1149) software (Kratos Analytical, Japan) was used to obtain the spectra and quantify the chemical bonds. The percentage of elemental compositions of the samples was determined, and the concentration of elemental silicon in the products was used to calculate the grafting efficiency of the reaction (as per **Equation S3.2**) [18].

Furthermore, after TGA analysis, the chemical compositions of WSL10 samples were analyzed using XPS following the same procedures. A static light scattering technique (SLS) was used to assess the molecular weight (MW) and radius of gyration (R_g) of SKL and copolymers [19]. In this technique, a laser light scattering instrument that was attached to a goniometer (BI-200SM, Brookhaven Instruments Corporation, NY, USA) was used for analyzing the characteristics of the polymers in solutions at the laser power of 35 mW and a wavelength of 637 nm at room temperature. The MW and R_g were determined by measuring the intensity of the scattered light at various scattering angles ranging from 20° to 155°. The same light scattering instrument analyzed the samples' hydrodynamic radius (R_h) using the dynamic light scattering technique (DLS). The wettability of SKL and WSL copolymers with water was determined following the Washburn technique and using a force tensiometer (attention sigma 700/701, Biolin Scientific, Finland) with a powder glass probe [20]. The amount of liquid absorbed by the powder bed was measured as a function of time to determine the wettability of the copolymers according to **Equation S3.3** [21]. The thermal stability analysis is an essential aspect of coating materials. The thermal stability and degradation temperature of SKL and copolymers were investigated using a thermogravimetric analysis (TGA) instrument (TGAi1000, Instrument Specialists Inc., WI, USA). For further temperature effect analysis, WSL10 copolymer samples were analyzed at six different temperature ranges (10-220, 10-360, 10-420, 10-520, 10-620, and 10-800 °C) repeatedly following a similar heating rate. The residues from each temperature range were collected for the XPS analysis. Differential scanning calorimetry (DSC) instrument

(DSC Q2000, TA Instruments, DE, USA) was employed to determine the glass transition temperature (T_g) of SKL and copolymers [22]. The supplementary material will comprehensively describe the sample preparation and experiment setup for the above analyses.

3.3.4. Coating formulation and process

The coating formula was prepared by mixing aluminum phosphate (AP) binder and the copolymer (WSL10), which was produced under the optimized conditions of 1:1.2 mmol ratio of SKL/WAPMSS, pH 11, 60 °C, and for 48 h. First, AP binder was produced by combining aluminum hydroxide ($Al(OH)_3$), 1 M, and orthophosphoric acid (H_3PO_4, 60 %), 3 M, in a three-neck round-bottom flask with magnetic stirring at 200 rpm and 100 °C for 3 h [23]. WSL10 copolymer and AP binder were mixed in water vigorously using a vortex, which was followed by magnetic stirring at 1000 rpm for one hour. The wood substrate was ultrasonically rinsed with deionized water and dried in a 60 °C oven for 2 h. The wood samples were dip-coated in the prepared dispersion for 5 minutes and cured at 100 °C for 15 minutes. The overall schematics are represented in **Figure S3.1(**b). The control samples consisted of two different formulations, one containing only the AP binder and another containing SKL and AP binder in a 1/1 wt. ratio was selected based on the stability and contact angle analysis results.

3.3.5. Stability of coating formulation

In this test, 25 mL of coating formulations were placed in cylindrical glass vials and then scanned every 30 s for six hours at 30 °C by a suspension stability analyzer, Turbiscan lab expert (Formulation, France) [20].

3.3.6. Surface analysis

An optical tensiometer (Theta Lite, Bolin Scientific, Finland) equipped with a digital camera and manual tilting stage was utilized for static contact angle and sliding angle analysis. The sessile liquid droplet method from One Attention software was applied for static contact angle analysis [24]. The measurement was replicated three times, and mean values with standard deviation were reported. The adhesion force equals the force required to remove a liquid (water) droplet from a surface [25]. This test used a force tensiometer instrument (Attention Sigma 700/701, Biolin Scientific, Finland) with an adhesion probe ring and a microbalance. The images of uncoated and coated woods with different formulas for uncoated, AP, SKL-AP, and WSL10-AP (1/1 wt. ratio) were produced using a field emission scanning electron microscope (FE-SEM, Hitachi SU-70).

3.3.7. Flame retardancy of coated wood

The limiting oxygen index (LOI) analyzer (NETZSCH TAURUS instrument, Germany) was used for determining the minimum oxygen required for the ignition of the uncoated wood, AP, KL-AP, and WSL10-AP (1/1 wt. ratio) coated wood samples following the ASTM D2863 standard. A precisely controlled environment of nitrogen and oxygen was used to burn the coated wood vertically positioned in the center of the glass column. The lowest oxygen in the carrier gas flow, known as the limiting oxygen index or LOI, was determined to be the point at which complete, blazing combustion of the material was seen [26]. The samples were prepared in a dimension of 140 mm × 20 mm × 10 mm, and five replicas were used for each sample. To assess the smoke emission characteristics of the coated wood, the ASTM D 2843-99 method was employed. This involved examining the smoke generation patterns of uncoated wood, AP, SKL-AP, and WSL10-AP (1/1 wt. ratio) coated wood samples using a smoke density test device (AIC-2843, Advanced Instrument Co., Ltd, China).

To analyze the smoke density performance of the materials, the coated samples, 42 mm × 42 mm × 4 mm in dimensions, were placed in the instrument, and then the samples were subjected to the pressure of 0.14 MPa of propane gas for 250 s after ignition [27]. The samples' smoke density rating, the SDR, and the light absorption curves were analyzed and presented. SDR measures the smoke concentration, while the light absorption curve quantifies the extent to which smoke particles absorb light during combustion. Both metrics were obtained from the light absorption data. To simulate real-life fire scenarios, samples were subjected to an intense propane gas flame to initiate ignite. Images were captured to depict the reaction of the samples visually.

3.3.8. Durability of the coating formulation

The resistance of the coating to hot water, milk, coffee, 0.1M NaOH, 0.1M HCl, and ethyl glycol was evaluated using liquid droplets through the measurement of contact angles using an optical tensiometer. The sandpaper abrasion, touching, and knifing tests were conducted on WS10-AP 1/1 wt. ratio coated wood samples to assess the bonding and durability of the coated wood. A sandpaper abrasion test was performed using a 20 g load with the coating upside down and subjected to 1500 CW sandpaper. The coating was then pushed along a straight line [2], and the contact angle of a water droplet on the surface was tested. Alternatively, the endurance of the coating was assessed through the repeated application of knife cutting and finger touching before the WCA measurement. In addition, the WCA of the coated wood was determined after six months of storage at room temperature. Furthermore, the resistance of the coating to temperature was evaluated by subjecting it to a temperature of 200 °C for 2 h, followed by WCA assessment and flame test [28].

3. 4. Result and Discussion

3.4.1. Reaction optimization of SKL and WAPMSS

Softwood kraft lignin (SKL) is rich in hydroxyl groups, and the most active sites in its structure are aliphatic and phenolic hydroxyl groups, which are the primary sites of lignin modification [29]. The SKL's phenolic and aliphatic reactive sites are used to depict possible condensation reaction between the hydroxyl groups of SKL and WAPMSS to form Si-O-C bond by releasing water as a byproduct (**Figure S3.2**(a) and **S3.2(**b)). In this reaction, an OH is lost from the silanol (-Si-OH) group of WAPMSS along with hydrogen from phenolic/aliphatic hydroxyl groups of SKL, leaving the two reactants linked via Si-O-C bond (**Figure S3.2(**a) and **S3.2(**b)). To identify the best reaction condition, the Taguchi L9 4×3 orthogonal array was utilized (**Table S3.1**). Four factors, i.e., WAPMSS concentration, pH, temperature, and time with three levels were considered for each factor. The reaction yield and grafting ratio were determined for all copolymers as described in **Equations S3.1** and **S3.2**, and results are presented in **Table S3.2**. An increase in the concentration of WAPMSS, pH, and time resulted in a higher grafting ratio of WAPMSS to SKL (**Figure S3.3(**a), **S3.3(**c)**,** and **S3.3(**d)). The increased concentration of WAPMSS likely enhanced the grafting ratio in the product by facilitating the silanization of the hydroxyl groups of SKL. This, in turn, would lead to the reaction of the remaining silanol groups with adjacent WAPMSS molecules, resulting in the formation of a multilayer WAPMSS crosslinked molecular layer on the SKL backbone. Also, at higher pH, the phenolic and aliphatic hydroxyl groups of SKL are more likely to deprotonate, making SKL more reactive [30]. Therefore, the silanol groups of WAPMSS can bind with SKL readily. On the other hand, a higher temperature (80 °C) had an insignificant effect on the grafting ratio (**Figure S3.3**(b)). This may be attributed to the tendency of SKL to undergo self-polymerization at a higher reaction temperature [31], which makes it difficult for the WAPMSS silanol group to react with SKL. Based on this analysis, the reaction conditions of 1/1.2 molar ratio of SKL/WAPMSS, pH 11, 60 °C and 48 h were determined to be optimal for generating copolymer of WSL10 with the highest yield (78 %) and grafting ratio (140 %). The sample generated under optimized conditions, WSL10, was chosen for further investigation, along with the sample with the lowest grafting ratio (WAL2), the sample with the highest grafting ratio (WSL6), and the sample with a medium grafting ratio (WSL5) to see how the resulting structural variability of the copolymer would affect the performance of the products.

3.4.2. Characterization of SKL, WAPMSS and WSL polymers

3.4.2.1. NMR analysis

NMR analyzed the chemical structures of SKL, WAPMSS, and WSL copolymers. The ^{1}H-NMR spectra of SKL, WAPMSS, and WSL copolymers and the structure of the copolymers are depicted in **Figure 3.1**(a) and **3.1**(b). The signal corresponding to DMSO-d_6 is observed at 2.5 ppm for SKL, and the signal corresponding to D_2O in the WAPMSS and WSL copolymers spectra is assigned at 5 ppm. In the ^{1}H NMR spectrum of SKL, aromatic protons are characterized by a signal between 6.0 and 7.5 ppm (h), while methoxy protons are in the 3-4 ppm (g) zone. Aliphatic protons can be detected in the area between 0 and 3.2 ppm [32]. For WAPMSS, the strong peaks observed at 2.7 ppm are associated with the -OH peaks (e) linked to Si, signals around 1.5 ppm on the spectra of the copolymers are related to the protons of NH_2 (c), signals at 0.5 ppm are associated with the propyl structure of the protons of $-CH_2-CH_2-CH_2$ (b), and very distinctive peaks at 0 ppm are assigned to the proton of CH_3 linked to Si (a) [33, 34].

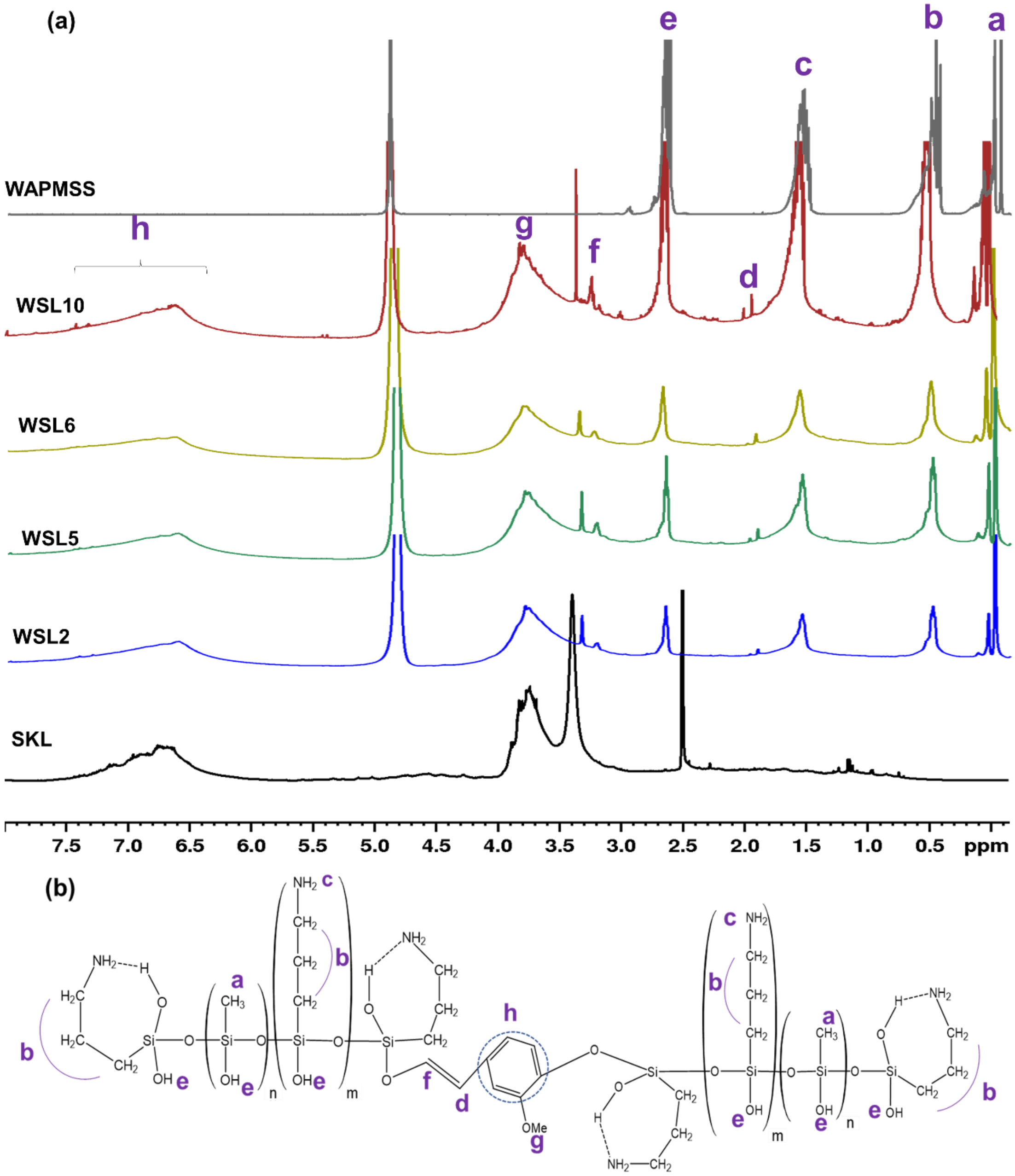

Figure 3.1. H-NMR spectra for SKL, WAPMSS, and WSL copolymers (a) and WSL copolymers (b) structure.

The ^{1}H-NMR spectra of the WSL copolymers reveal the inheritance of aromatic (h) and methoxy (g) protons from SKL. Similarly, the signals of a, b, c, and e in **Figure 3.1** are inherited from WAPMSS. However, the appearance and intensity of the signals are different between the copolymers, and WSL10 has stronger signals of a, b, c, and e among the copolymers **Figure 3.1**(a). Furthermore, new peaks appearing in the spectra of the copolymer around 1.8-1.9 ppm (d) and 3-3.2 ppm (f) correspond to the new aliphatic linkage created by the condensation of SKL aliphatic and WAPMSS hydroxyl group.

The HSQC NMR analysis was conducted on SKL, WAPMSS, and WSL copolymers to identify primary linkages and constituent units, as depicted in **Figure 3.2** and listed in **Table S3.3**. Significant lignin interunit structures, such as aromatic units of SKL (δ_C/δ_H 110.6-122.9/6.7-7.5 ppm), C-C aliphatic area (δ_C/δ_H of 5−50/ 0.5−3 ppm) and C−O aliphatic area (δ_C/δ_H of 50−95/2.75−6 ppm), were identified and marked with hexagon, elliptical and rectangular shapes, respectively, in **Figure 3.2(a).**

The correlation signals of guaiacyl (G) units G_2 (C_2-H_2), G_2' (C_2-H_2), G_5 (C_5-H_5), G_6 (C_6-H_6), and G6' (C_6-H_6) in SKL were observed at 110.6/6.7, 108.8/7.04, 115.9/6.7, 119.1/6.7, and 122.9/7.5, respectively, in **Figure S3.4**(a). The prominent interunit linkages in β-O-4 (A_β), phenylcoumaranan β-5 (B_β), and resinol β-β (C_β) were identified for SKL at the cross peak signals of δ_C /δ_H 71.4/4.7 ppm, δ_C /δ_H of 53.29/3.44 ppm and δ_C /δ_H of 53.6/3.0 ppm, respectively, in **Figure S3.5**(a) [35]. Furthermore, the methoxy (-OCH_3) functional group characteristic signal was identified at δC/δH of 55.5/3.70 in **Fig**ure **S3.4**(a). On the other hand, WAPMSS only had strong aliphatic C-C linkages that appeared in the cross-peak signals δ_C/δ_H of 0-22/0-3.2 in **Figure 3.2(b)**. The copolymers' HSQC spectra reveal the unambiguous aromatic and methoxy structures in **Figure 3.2(c-f)**. This result confirms that the WSL copolymers inherited the aromatic units and methoxy groups from SKL, aligning with H-NMR analysis (**Figure 3.1**). The robust aliphatic structures in the copolymer structure are inherited from WAPMSS in **Figure 3.2(c-f)**.

Compared with SKL, the WSL copolymer samples had the same intensity of the β-β linkage. The β-O-4 and β-5 linkages were detected only for WSL10 in **Figure 3.2**(f). The Cα-Hα in phenylcoumaran substructures, Cγ-Hγ in resinol units, and C_Υ-H_Υ in β-O-4' were prominent in all samples (except for WSL6) in **Figure S3.5** (b-e). It is possible that β-O-4 and β-5 linkages were cleaved due to the higher temperature and prolonged reaction conditions for generating WSL6. A new cross-peak signal was identified for all the copolymers in the C-O linkages region at the δ_C /δ_H of 46.2/3.21 ppm, which is assigned to the new linkage created by the condensation of the hydroxyl group of WAPMSS and SKL. The aliphatic C-C linkages in the copolymers exhibit higher strength compared to SKL and bear a resemblance to WAPMSS, thus offering more support for the occurrence of copolymerization **Figure S3.6** and **Figure S3.7**.

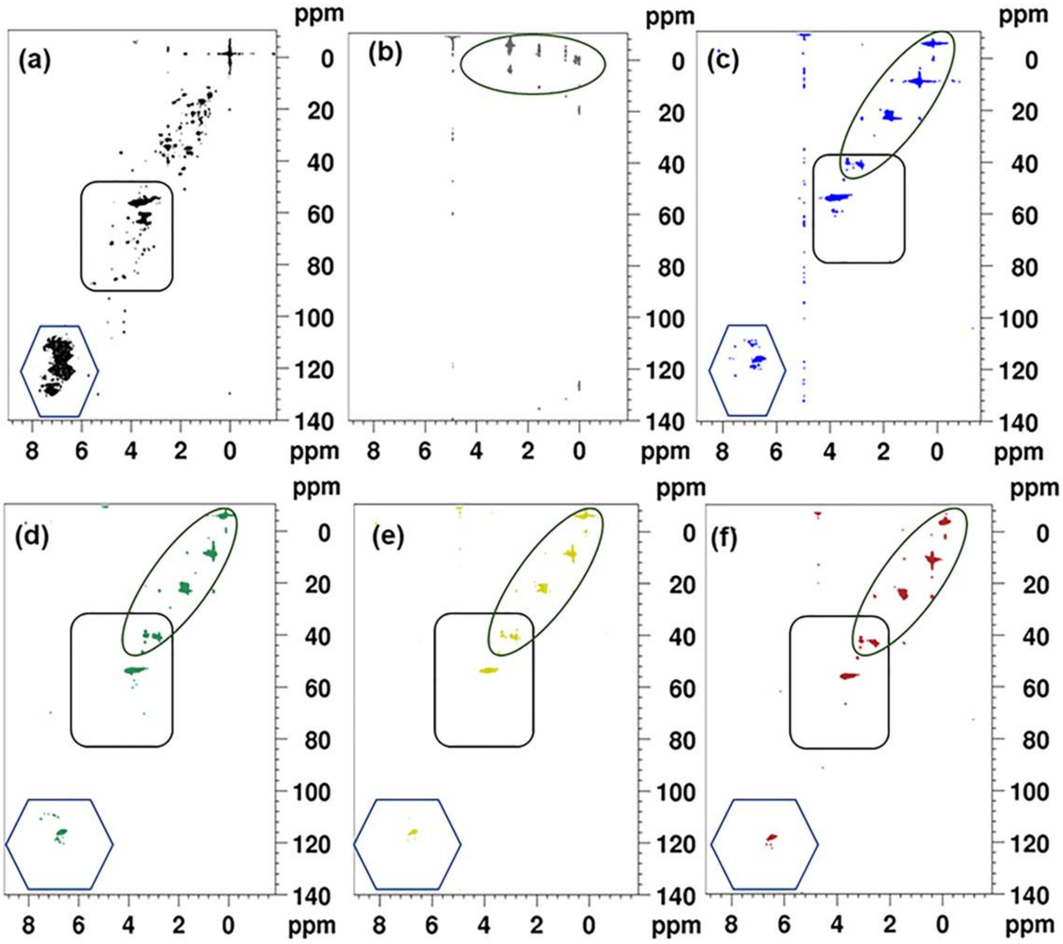

Figure 3.2. HSQC NMR spectra δC/δH 10-145/-2-8 of SKL (a), WAPMSS (b), WSL2 (c), WSL5 (d), WSL6 (e), and WSL10 (f).

The ^{31}P-NMR spectra of SKL, WSL2, WSL5, WSL6, and WSL10 are displayed in **Figure 3.3**(a) to quantify the aliphatic, phenolic (C-5 substituted and guaiacyl), and carboxylate OH group content of the samples [36]. The hydroxyl groups of the copolymers were reduced significantly relative to that of SKL, as indicated in **Figure 3.3**(a). In addition, the aliphatic, total phenolic, and carboxylate OH contents of SKL were higher than those of WSL. The quantification of SKL and WSL2 spectra peaks reveal the proportionate decreases in the concentration of phenolic, aliphatic, and carboxylic groups, indicating that the condensation process was not selective.

3.4.2.2. FTIR analysis

The FTIR spectra of SKL, WAPMSS, and WSL copolymers are shown in **Figure 3.3**(b). The transmittance at 1600, 1510, and 1425 cm^{-1} are the distinctive peaks of aromatic ring vibrations for SKL [37]. These distinctive peaks are present in copolymers, confirming ^{1}H NMR and HSQC results (**Figure 3.1** and **Figure 3.2**). The transmittance peak at 3340 cm^{-1} is attributed to the aliphatic and phenolic OH stretching of SKL [38]. The intensity of the hydroxyl stretching group is significantly lower in the copolymer's spectra than SKL's. This information can support ^{31}P-NMR results, as it confirms that all OH groups of lignin are occupied due to salinization via polycondensation. The transmittance at 3005 cm^{-1} corresponds to sp^{2}, which is the contribution of C-H associated with silicon [39]. In addition, the high transmittance at 835 and 785 cm^{-1} is the characteristic of Si-CH$_{3.}$ The siloxanes (Si-O-Si) have more intense infrared bands between 1008 and 1000 cm^{-1}.

The inheritance of transmittance signals for WAPMSS is detected in the copolymers, aligning with the H-NMR and HSQC results. The strong transmittance signals at 1240 and 975 cm^{-1} are assigned to the phenoxy group attached to silicon in the copolymer spectra [33]. Relative to WSL2, the increased intensity of Si-O-Si and Si-O-C bonds in WSL6 can be attributed to increased WAPMSS concentration. The sample produced under optimized conditions, WSL10, displayed a relatively high intensity in the Si-O-C bond, which XPS analysis will further quantify.

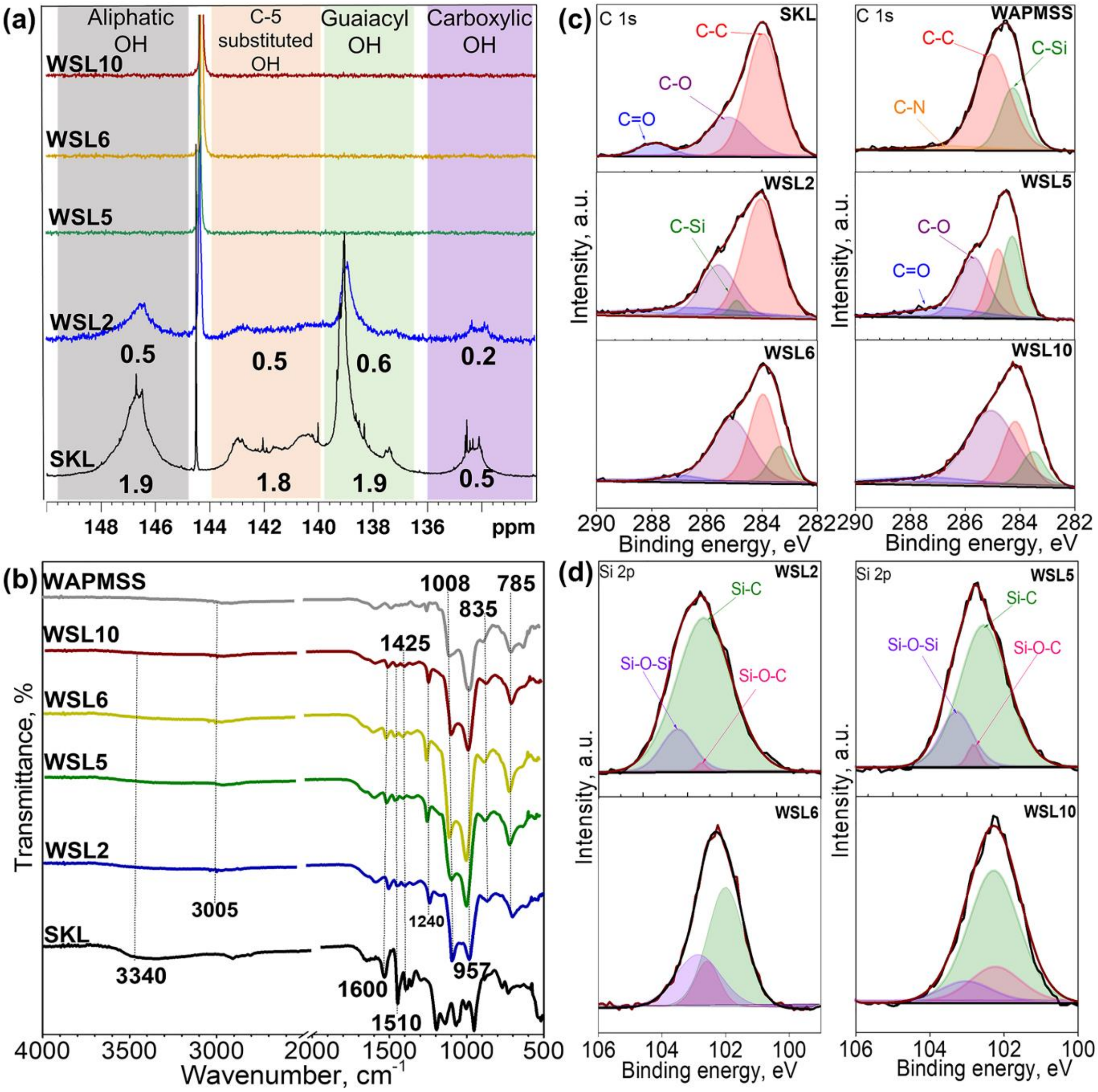

Figure 3.3. ^{31} P-NMR (a), FTIR spectra analysis (b), XPS C1s deconvoluted spectra (c) of SKL, WAPMSS, and WSL copolymers and (d) XPS Si 2p deconvoluted spectra of WSL copolymers (c), The concentrations indicated are in Fig. 3a is in mmol/g.

3.4.2.3. XPS analysis

Surface elemental compositions and chemical bonds of SKL, WAPMSS, and WSL copolymers were studied by XPS. The elemental compositions of SKL were carbon (285 eV) and oxygen (532 eV) [40]. Additional elements, nitrogen (400 eV) and silicon (152.9 eV and 101 eV) were also detected for the WAPMSS and WSL copolymers in **Figure S3.8**(a) [41, 42]. The core level spectra of C1s with fitting analysis for the peaks related to carbon linkages are observed in **Figure 3.3**(c). SKL Cls peak deconvolution resulted in three major components of C-C (284.8 eV), C=O (~ 288 – 290 eV), and C-O (~286 eV) in **Figure 3.3**(c). Likewise, the C1s spectrum of WAPMSS was analyzed, and the significant carbon linkages were C-Si (283 eV), C-C (284.8 eV), and traces of C-N (286 eV) [43]. In the copolymers' C1s envelope, the C-C, C-O, C-Si, and traces of C=O linkages were identified. The O=C-O bond concentration decreased significantly for all copolymers compared to SKL, while the O-C bond concentration increased, as detailed in **Table S3.4**. WSL2 had the highest concentration of O=C-O bonds between the copolymers, followed by WSL5 and WSL6, while WSL10 had the lowest concentration. These results confirm that all the possible OH reactive sites could participate in the reaction, consistent with ^{31}P-NMR and FTIR studies. Furthermore, the copolymers had a higher concentration of C-O bonds than SKL. This is due to the formation of a novel Si-O-C linkage between SKL and WAPMSS due to the polycondensation reaction, which agrees with the HSQC NMR analysis showing an increase in C-O aliphatic linkages.

Similar Si 2p peaks were deconvoluted for WAPMSS and WSL copolymers, and results are presented in **Figure S3.8**(b) and **Figure S3.8**(d). The Si 2p spectra for WAPMSS show two deconvoluted components of Si-C (101.34 eV) and Si-O-Si/Si-OH (103.76 eV). However, the WSL copolymers showed a third new component of Si-O-C (102.5) [44], which is in good alignment with FTIR analysis. The presence and concentration of Si-O-C linkages confirm the copolymerization of SKL and WAPMSS. From the results of WSL2, it can be observed that only 10 % of the Si concentration is linked to the O-C bond (**Table S3.4**). However, WSL10 had 60% Si in its structure related to the O-C, showing that the optimization helped create more Si-O-C linkages, which aligns well with FTIR and NMR results.

3.4.2.4. Molecular weight (MW), radius of gyration (Rg), and hydrodynamic radius (Rh)

The MW, R_g, R_h, and shape factor, R_g/R_h, of SKL and the copolymer macromolecules in NaOH solution were analyzed with SLS and DLS techniques, and the results are presented in **Table 3.1** and **Table S3.5**. It is seen that the MW, R_g, and R_h of the copolymers were much greater than those of SKL. The copolymerization of WAPMSS and SKL increased the MW of copolymers. After the reaction, there was a noticeable increase in the MW of the copolymers compared to SKL. The highest MW was for WSL10, which could be ascribed to the amine group from WAPMSS, inducing a side reaction on the lignin backbone, such as the condensation crosslinking reaction, which NMR, FTIR, and XPS confirmed. WSL2 had the lowest MW, owning to the lowest WAPMSS content due to mild reaction conditions (time, temperature, and pH). The R_g and R_h of the copolymer were also higher than those of SKL. In general, the increase in the R_g and R_h of the copolymer can be attributed to the introduction of WAPMSS molecules to the SKL structure, which increased the adequate size of the copolymers.

The shape factor of the polymers can determine the shape and compactness of polymer aggregates in a solution, R_g/R_h [45]. For anisotropic geometry, R_g/R_h of 1.5-1.8 implies an extended random coil particle, 1.0-1.3 a hyperbranched cluster, 1.0 a hollow sphere (1.0), and 0.77 a uniform sphere (dense center ornamented by long, sparse chains) [46]. In general, the shape factor of the copolymers was less than that of SKL (~1.7), which indicates the random coil aggregates formed when SKL was dissolved in a robust alkali solution [47]. The smaller shape factor value of the copolymers can be explained by forming more extensive self-assembly characteristics of silsesquioxane-containing molecules in an aqueous environment resulting from the hydrophobic end chains [48]. However, among the copolymers, WSL10 had a shape factor of ~0.775, indicating a spherical micelle geometry with a higher density at the center, which the crosslinking silsesquioxane molecules on the backbone of SKL can explain [49]. The crosslinking density of silsesquioxane on the backbone of SKL is supported by the higher concentration of Si-O-Si linkage from XPS (**Fig**ure 3.**3**(d)) and FTIR (**Figure 3.3**(b)) results for WSL10.

Table 3.1**.** Molecular weight (MW), radius of gyration (R_g), and hydrodynamic radius (R_h) of WSL and SKL.

Copolymers	**MW (g/mol)**	**R_g (nm)**	**R_h (nm)**	**~R_g/R_h**
SKL	$(7.59 \pm 0.89)\times 10^4$	17.1 ± 9.1	10 ± 0.002	1.7
WSL2	$(1.14 \pm 0.14)\times 10^5$	17.1 ± 8.1	9.6 ± 0.004	1.7
WSL5	$(1.40 \pm 0.18)\times 10^5$	30.3 ± 17.1	20 ± 0.002	1.5

WSL6	$(1.80 \pm 0.12)\times 10^5$	36.2 ± 7.41	30.4± 0.004	1.1
WSL10	$(2.14 \pm 0.23)\times 10^5$	58.0 ± 8.4	78 ± 0.04	0.74

± in MW and R_g for standard deviation, relative variance R_h

3.4.2.5. Powder wettability analysis

The wetting process involves an exchange of solid/gas particles for solid/water particles [21]. The Washburn method examines the ability of a liquid to penetrate a powder bed over time to assess wettability. The wettability of SKL and WSL copolymers is shown in **Figure 3.4**(a). SKL absorbs water slowly but extensively compared to the copolymers. Among the copolymers, WSL2 exhibited the highest water uptake in the first 50 min, followed by WSL5 and WSL6 in descending order. The WSL2's highest water absorption can be justified by the presence of free hydroxyl groups in the structure, as discussed in ^{31}P-NMR (**Figure 3**.**3**(a)) and XPS results (**Figure 3.3**(c)). Conversely, the WSL5 has less COOH and more Si-C groups in its structure, contributing to its limited water uptake. However, WSL10 showed no sign of water absorption, indicating that the copolymers have superhydrophobic properties [50]. The superhydrophobicity of WSL10 is a result of a higher concentration of Si-O-C and Si-O-Si bonds in the structure, which was confirmed by FTIR (**Figure 3.3**(b)) and XPS (**Figure 3.3**(c)) [51].

3.4.2.6. Thermal analysis

The thermal stability of SKL, WSL2, WSL6, WSL5, and WSL10 was investigated by TGA and DSC analyses, and the results are shown in **Figure 3.4**(b-c). The TGA and DTG curves are depicted in **Figure 3.4**(b) and **3.4**(c), respectively. The onset temperature (T_o), the temperature of 50% weight loss ($T_{50\%}$), and the maximum decomposition temperature (DTG_{max}) were utilized to characterize the thermal sensitivity of the copolymers. SKL displayed a rapid weight loss at approximately 290 ± 2 °C with a 50 % weight loss at approximately 500 ± 4 °C. Due to the intricacy of lignin biomacromolecules, its complete breakdown occurred between 500 and 520 °C [52]. The copolymers displayed distinctive decomposition behavior compared to SKL in **Figure 3.4**(b) and **Figure 3.4**(c). The decomposition of WSL polymers starts at higher temperatures, at approximately 300 °C, and the maximum decomposition occurs at higher than 600 °C. The improvement in the decomposition temperature for the copolymers resulted from the condensation or crosslinking reaction of WAPMSS in the SKL macromolecules. In addition, the DTG_{max} of WSL10 was 120° larger than that of SKL, and the char residue of WSL10 was 33 % greater than that of SKL. Adding Si to the copolymer's macromolecular structure increases DTG_{max} and weight residue [53]. Differences in T_o and DTG_{max} were noticed among the copolymers. The decomposition temperature of WSL2 was lower than that of WSL6, WSL5, and WSL10. An enhanced substitution occurred in a greater quantity of WAPMSS, resulting in a more compact structure (**Table 3.1**), which can explain the higher thermal stability of WSL6, WSL5, and WSL10.

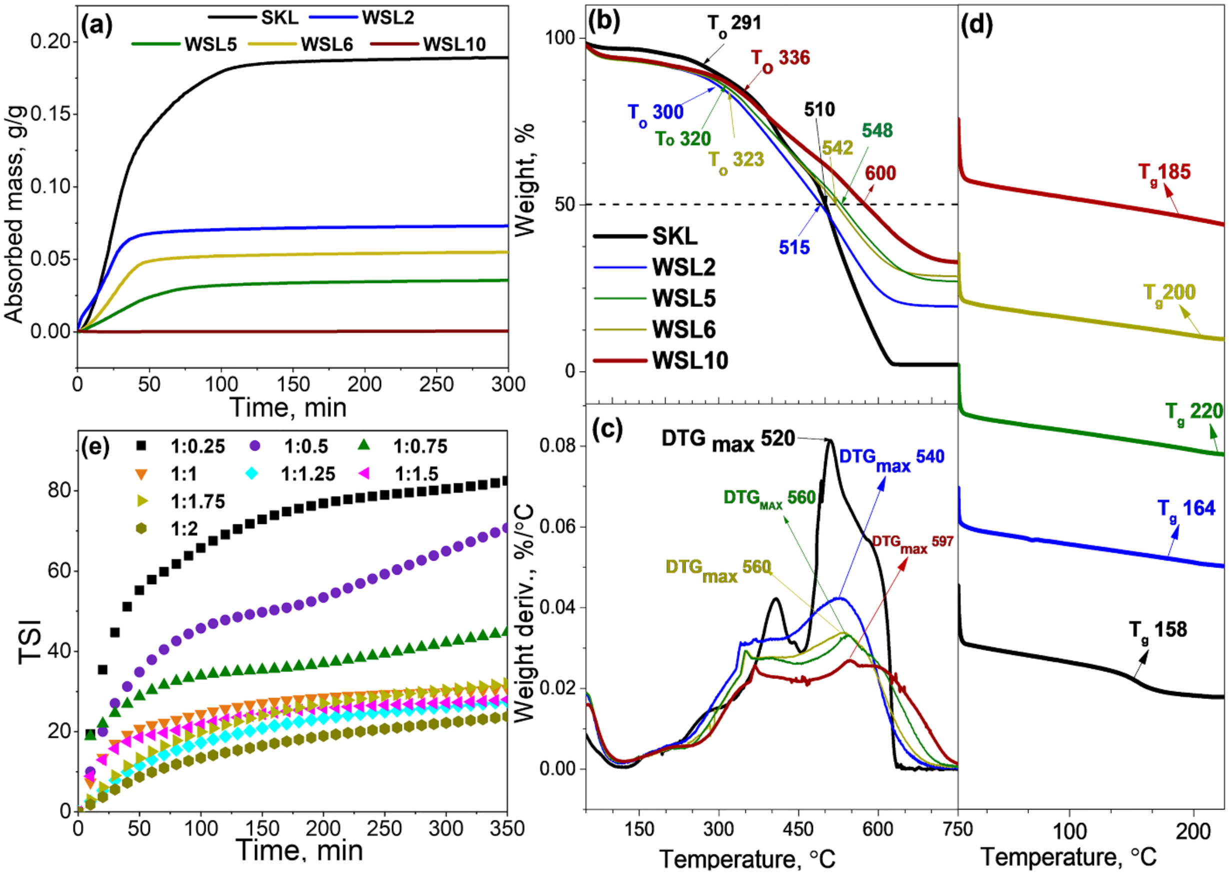

Figure 3.4. Water absorption of SKL and WSL copolymers (a) TGA curve showing T_o and $T_{50\%}$ (b), DTG curve indicating DTG_{max} (c) and T_g on the DSC curve (d) of SKL and WSL copolymers, and TSI variation of coating formulations over 6h (legends indicate the wt. ratio) (e).

To understand the structural changes of the copolymers caused by temperature, residues obtained at different temperatures of TGA analysis were subjected to XPS analysis. The C1s and Si2p deconvoluted XPS spectra are presented in **Figure S3.9(**a-f) and **Figure S3.10(**a-f), respectively. **Table S3.6** shows the concentration of C1s and Si2p deconvoluted bonds after different temperature exposures of WSL10. The C-C bond in **Figure S3.9**(a-f) only decreased by 4 % from its initial concentration, indicating that the polymerization of WAPMSS safeguards the aromatic rings within the lignin structure up to 420 °C. Also, Si detected in the copolymer at > 700 °C is linked to the Si-O-C (55 %) and Si-O-Si (40 %) structures, as confirmed in the XPS analysis in **Figure S3.9**(f). Interestingly, the residues of an aromatic ring connected to Si are still detectable in the residual of the samples after TGA analysis in **Figure S3.10**(f). This can be attributed to forming a heat shield composed of a silicon-oxygen network structure that protects the organic structure.

The glass transition temperature, T_g, of SKL and WSL copolymers, is depicted in **Figure 3.4**(d). T_g strongly relies on a polymer's molecular structure and crosslinking density. In general, the T_g of the copolymers was higher than that of SKL. This indicates that the copolymerization of WAPMSS and SKL resulted in a crosslinked structure, reducing the free volume of the chain's mobility and increasing T_g. The effective improvement in the T_g was attributed to the increase in the molecular weight (**Table 3.1**), the rigid cage structure of silsesquioxane, and the SKL crosslinking network [53]. As the proportion of WAPMSS increased in the copolymer, the T_g of the copolymers also increased. While WSL2 had the lowest concentration of WAPMSS, its T_g was lower than that of the other copolymers, but WSL6's greater WAPMSS concentration resulted in a higher T_g. This would directly be linked to the influence of a silsesquioxane crosslinked structure on the backbone of SKL, which would shield the molecular structure of lignin. This shielding effect would reduce the mobility of the copolymer chain and increase its T_g [54, 55].

3.4.3. Coating formulation stability

The dispersion stability of a coating formulation reveals information about its constituents' interactions and shelf life [56]. WSL10 was chosen for coating formulation with AP binder because of its notable water resistance (**Figure 3.4**(a)) and thermal stability (**Figure 3.4**(b-c)). Eight coating formulations were created by mixing WSL10 and AP at different ratios, as displayed in **Table S3.7**. The dispersion stability defined by the TSI global over 6 h of the eight formulations is shown in **Figure 3.4**(e). The higher the stability of a coating formulation, the lower the TSI value. It was observed that when the amount of WSL10 was higher than AP in the aqueous dispersion, the TSI value increased. This suggests that the WSL10 particles exhibited increased self-interaction, resulting in aggregation and settling [57]. Interestingly, the formula containing 50 % WSL10 had a reasonable TSI value of 24, and further reducing its content did not remarkably improve the suspension's stability. The AP binder used in the formulation improved the stability of the WSL10 particles in water to a greater extent in **Figure 3.4**(e). In this case, the phosphonate group from AP and the available silanol group from WSL10 could create intermolecular hydrogen-bond formation [58].

3.4.4. Surface characterization of coated wood

The surface morphology and water contact angle of four samples, comprising uncoated wood, wood coated with the formulations of AP binder, SKL-AP with 1/1 wt./wt. ratio and WSL10-AP with 1/1 wt./wt. ratios were evaluated, and the findings are shown in **Figure 3.5**. The uncoated wood surface had a smooth surface where the grains, pits, and grooves could be observed (**Figure 3.5**(a) and **3.5**(b)) with a hydrophilic property (WCA = 34°), as seen in **Figure 3.5**(c). AP-coated wood had a rough surface, where the visible grooves and pits were covered with a water contact angle of 87° (**Figure 3.5**(d)**, 3.5**(e)**,** and **3.5**(f)). The hydrophilic properties of AP are the reason for its limited application for wood coating [59]. When SKL was added to the coating formula, the wood's surface exhibited complex aggregated and agglomerated structures (**Figure 3.5**(g) and **3.5**(h)), and the water contact angle increased to 92° (**Figure 3.5**(i)). The introduction of rough surface morphology enhanced the water-repellency of the formulation on the coated surface [27]. Wood surfaces covered with a formulation containing WSL10 displayed more distinct patterns, with spherical large particles connected to smaller particles with a water contact angle of 158° (**Figure 3.5**(j)**, 3.5**(k)**,** and 3.**5**(l)). In this case, WSL10 imparted superhydrophobicity to wood surfaces because of its chemical structure, as discussed earlier.

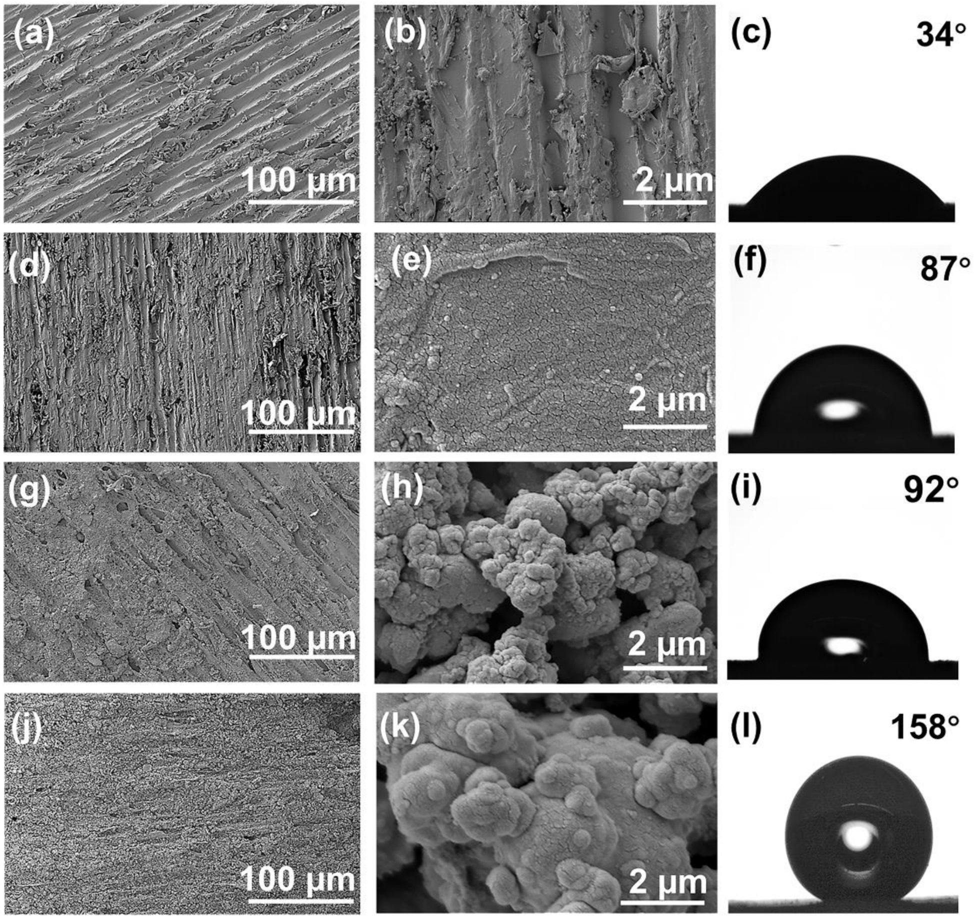

Figure 3.5. SEM image(a) and (b), and water contact angle of uncoated wood (c), SEM image (d) and (e), water contact angle of AP coated wood (f), SEM image (g) and (h), water contact angle of SKL-AP (1/1 wt./wt. of SKL/AP) coated wood (i), SEM image (J) and (k), water contact angle of WSL10-AP (1/1 wt./wt. of WSL/AP) coated wood (i).

The static contact angle of water droplets on the wood coated with different formulas is shown in **Figure 3.6**(a). The variation in the ratio of WSL10 and AP did not affect the contact angle significantly, and a contact angle of >150° was observed for all samples. The increment in the AP content reduced the sliding angle for the water droplet on the coated surface. This phenomenon may be attributed to the improved roughness on the wood substrate because of the enhanced dispersion of the WSL10 in the AP binder system, as demonstrated by the stability study (**Figure 3.4**(e)). The air-trapping surface structure is essential for the development of low-sliding-angle surfaces [60, 61]. Similar to the stability analysis, the formula with the mixing ratio of 1/1 wt. for WSL10/AP generated the coated surface with acceptable hydrophobicity while keeping the coating formula green. The better surface properties of this formulation follow the same trend of suspension stability (**Figure 3.4**(e)), implying that the stability of the suspension might have contributed to the development of a uniform coated wood surface because of a low sliding angle.

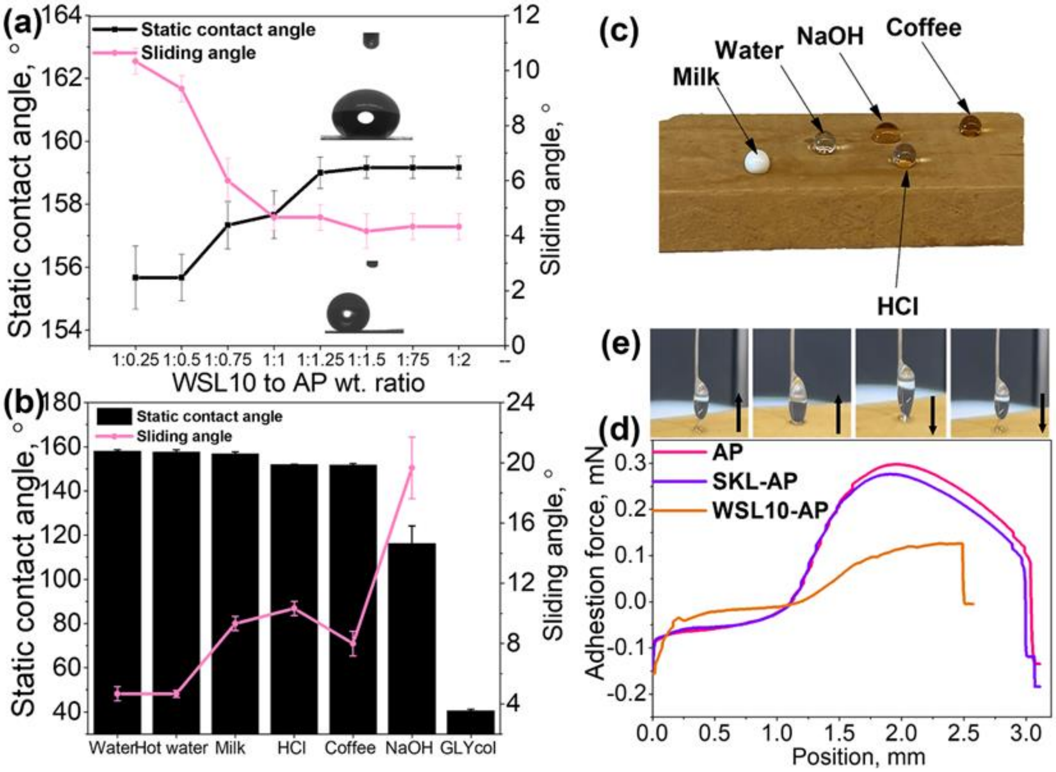

Figure 3.6. Water contact angle analysis for different ratios of WSL10 and AP (a), the contact angle of various chemicals on the wood surface with WSL10-AP 1/1 wt./wt. (b and c), droplets of different solutions deposited on the wood surface coated with WSL10 and AP 1/1 wt./wt. (d and e)

The force required for removing a liquid droplet from the surface it encounters is known as the adhesion force of a liquid droplet on the surface [25]. The adhesion force measurement efficiently quantifies the interactions between liquid and solid surfaces. **Figures 3.6**(d) and **3.6(**e) show the adhesion force of water droplets on the coated wood surface as a function of its position. This analysis was performed on the AP, SKL-AP, and WSL10-AP coated surface, and the results are shown in **Figure 3.6**(d). Three steps are involved in this process: spreading, maximal adhesion, and separation (pull-off) of the water droplets from the coated surface. AP and SKL-AP coated wood had hydrophobic surfaces where the water droplet was attached to the surface, and the pull-off force required for extracting a water droplet from the surface was 0.28 mN and 0.25 mN, respectively. On the other hand, the wood surfaces coated with WSL10-AP (1/1 wt./wt.) exhibited less droplet spreading and a pull-off force of 0.025 mN. The droplet left no water residue on the surface after contacting the coated surface for WSL10-AP, confirming its superhydrophobicity (**Figure 3.6**(e)). These results are consistent with the contact angle analysis of coated wood surfaces (**Figure 3.6**(a)) and the surface morphology confirming that the micro and nano hierarchical structure of coated wood surfaces improved the superhydrophobicity of wood (**Figure 3.5**(k)) [62].

3.4.5. Flame retardancy of coated wood

The flame retardance capabilities of the coatings were evaluated by limiting oxygen index (LOI), smoke density, and flame test. The findings can be shown in **Figures 3.7**. The coated sample with WSL10-AP (1/1 wt./wt.) had a 27.4 % LOI value, higher than other samples in **Figure 3.7**(a). Such an improvement may be attributed to the integration of silsesquioxane into the structure of WSL10, making it more flame-resistant [63]. The increased LOI value of the coating formulation containing WSL10 (in comparison with that containing SKL) is due to the superior charring ability of WSL10 because the homogenous silsesquioxane on the backbone of SKL functions as a heat shield layer at a higher temperature, resulting in decreased flammability [64]. This phenomenon results from the structural and thermal properties of WSL10, as discussed in (**Figure 3.4**). This delayed ignition characteristic is also reported when silsesquioxane is integrated into different polymer matrices, such as polyolefins, polyester, and polycarbonate, due to the creation of a specific architectural structure [65].

Light absorption and smoke density rating of wood are essential characteristics of wood ignition. **Figure 3.7**(b) and 3.**7(**d) depict the light absorption curves for the coatings and smoke density ratings (SDR). It is observable that wood coated with the WSL10-AP (1/1 wt.) formula had the lowest light absorption and smoke density, indirectly inferring that this sample was less ignited and took longer for decomposition than other samples. The lowest rate of combustion obtained for WSL10-AP is attributable to the possibility of producing a crosslinked ceramic phase upon heating, which might operate as a barrier to limit the spread of the flame, thereby allowing the wood to retain its structural integrity (**Figure S3.11**). AP did not significantly increase the igniting performance of wood, while SKL improved it less than WSL10 did.

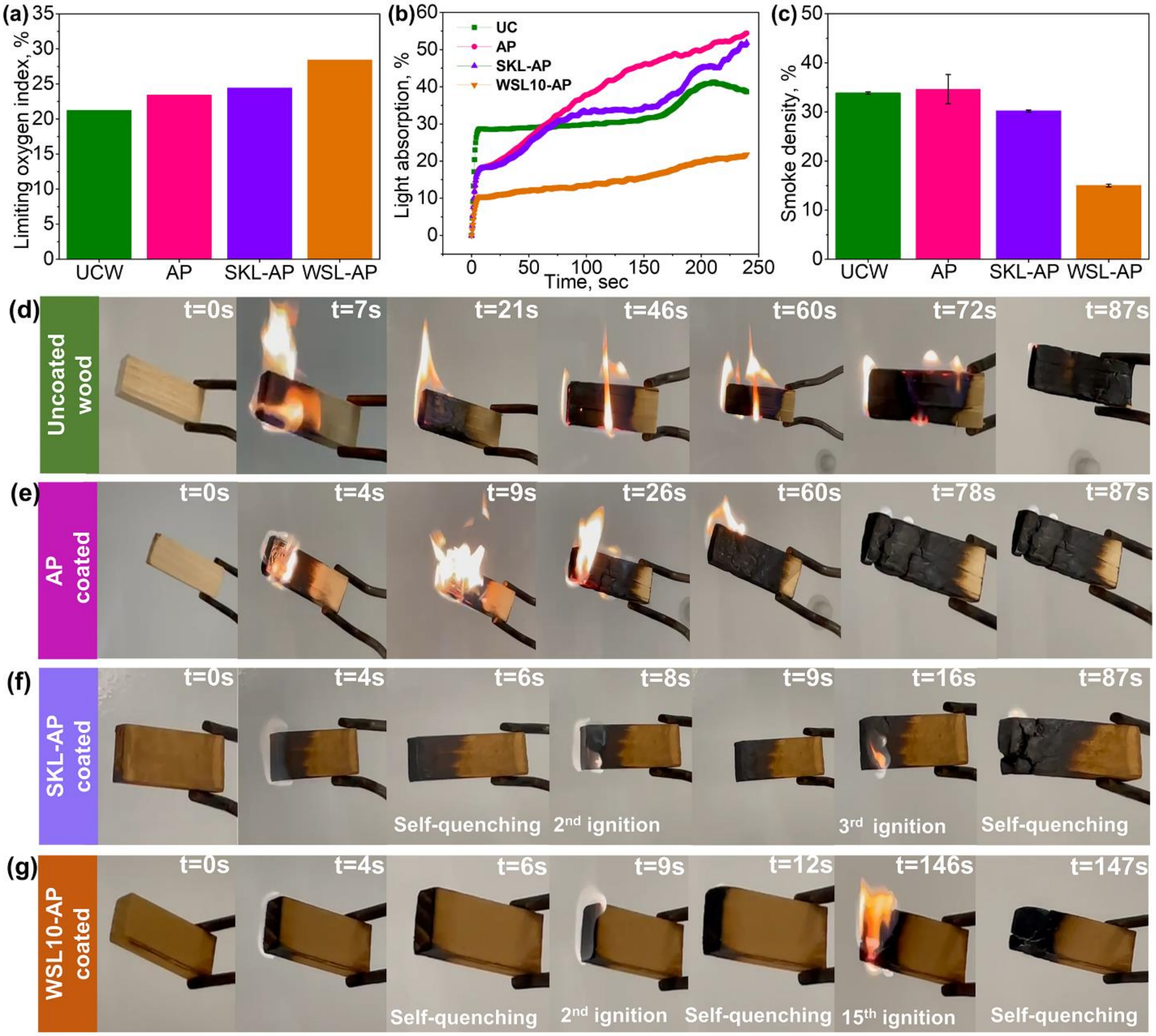

Figure 3.7. Limiting oxygen index (LOI) (a), light absorption (b), smoke density rating values (c), and images of the flame test for uncoated wood (d), AP-coated (e), SKL-AP (f), and WSL10-AP (1/1 wt./wt.) (g).

The flame test was conducted to replicate a real-life fire, and the outcome is illustrated in **Figure 3.7**(d-g). Uncoated wood, when exposed to propane gas, underwent a consistent and sustained igniting, with a flame that persisted for 72 seconds to burn the sample completely until extinguishing at 87 seconds. The AP-coated wood exhibited comparable properties to uncoated wood. However, the SKL-AP-coated wood demonstrated self-quenching properties. After the third ignition, the flame on the SKL-AP-coated wood remained steady for 87 seconds. The wood coated with WSL10-AP exhibited a significantly reduced inclination for igniting. It required 15 ignition attempts before a noticeable flame was observed on the coating, and the flame extinguished before almost one-third of the wood had burned.

3.4.6. Durability of superhydrophobic and flame-retardant properties of wood

Superhydrophobic coatings are useful for applications that require water resistance. Still, these surfaces can be subjected to other chemical environments, requiring the analysis of the coated surface in different chemical environments. The static contact angle and sliding angle of various solutions on the wood sample coated with 1/1 wt./wt. of WSL10 and AP are shown in **Figure 3.6**(b) and **3**.**6(**c). It is seen that only ethylene glycol and NaOH solution droplets had small contact angle values on the coated wood surface. The strong alkaline solution (NaOH) may develop a non-oxidation reduction reaction between the silanol group of WSL10 and NaOH, leading to the decomposing of silanol groups of WSL10 [66]. On the other hand, two organic CH_3 groups in the WSL10 structure (**Figure 3.1**(b)) caused the coating to be wetted to ethylene glycol droplets. Hence, the strong attraction force between the ethylene glycol (having a hydrophobic nature) droplet and the coated surface would lead to surface wetting [67]. The analysis shows a higher contact angle for acidic droplets, implying good chemical resistance and superhydrophobicity. The stability of high contact angle results at high water temperatures and in various chemical conditions, demonstrating the surface's durability.

The bonding between the coated layer and the surface, as well as the durability of the coated layer, were assessed by sand abrasion, touching, and knife-cutting experiments on the wood coated with WSL10-AP (1/1 wt. ratio), which was followed by WCA analysis. The outcomes are depicted in **Figure S3.12**. The sand abrasion test result followed by WCA shows that the coated layer could maintain the superhydrophobic characteristics until 90 cm abrasion. However, beyond 90 cm, the WCA starts to reduce. The WCA remained above 140° until a friction distance of 150 cm, after which the WCA declined dramatically. The finger-touching and knife-cutting test on the coating exhibited a WCA of larger than 150° and a sliding angle of smaller than 10°. These results demonstrate a strong adherence of the coated layer to wood and confirm its durability, as shown in **Figure S3.12**. The strong adhesion of the coating to the wood surface is due to the penetrating properties of AP beyond the wood surface and the potential covalent link between AP and wood, resulting in a robust interface between the adhesive and wood cell wall [68, 69].

Furthermore, results in **Figure S3.13** indicate that the coating maintained its superhydrophobic properties even after a prolonged period of storage (i.e., 6 months) at room temperature. In addition, the resistance of the superhydrophobic coating to temperature was verified by observing a WCA greater than 150° even after subjecting it to a temperature of 200 °C for 2 hours, as shown in **Figure S3.14**. Furthermore, the coating's flame retardancy after temperature exposure was demonstrated by its ability to withstand ignition three times and self-quench after the fourth ignition [70]. After 88 seconds, one-third of the wood remained unaffected, as determined by the flame test.

3.5. Conclusions

A novel superhydrophobic sustainable coating material was fabricated from kraft lignin polymerized with silsesquioxane through a polycondensation reaction in an aqueous system. The reaction experiment was modeled via Taguchi L9 4×3 and optimized for grafting ratios. The reaction under pH 11, 60 °C, and 48 hours, and a 1:1.2 mmol ratio of SKL/WAPMSS was the optimum for obtaining the polymer, WSL10, with the highest Si content. NMR, XPS, and FTIR measurements confirmed the presence of Si-O-C/Si-O-Si bonds in the induced copolymer and, thus, the success of copolymerization. DSC, TGA, and SLS revealed increases in the thermal stability and T_g of the material ascribable to the abundance of the aromatic ring from lignin to the copolymer, an increase in the molecular weight after polymerization, and a more rigid structure due to the presence of the inorganic phase (i.e., Si-O-Si). The powder wettability analysis confirmed that the product (WSL10) demonstrated superhydrophobicity with null mass gain. The copolymer possessed this attribute because of the substitution of the hydroxyl groups of lignin with Si-O-C linkages and the prevalence of Si-O-Si bonds. In line with the Turbiscan stability index, adding an AP binder to the coating formulation enhanced the stability of the suspension. In contrast, the hydrophobic properties of the formulation were improved with the addition of WSL10. Based on the examination of static contact angle, a mixture of WSL10 and AP (in a 1/1 wt. ratio) had a higher contact angle of 158° than pure AP binder (87°) and SKL-AP (92°) binder formulations. When WSL10 was included in the formulation for coating wood, the water sliding angle was around 4° on coated wood, and only 0.05 mN pull-off force was required for removing water droplets from the surface horizontally, which confirmed the superhydrophobicity of the coating formulation. The LOI value of 27 % and the SDR of 15 % indicated the flame-retardant characteristics of the WSL10-derived coatings. The exposure to different liquids and high temperatures, as well as abrasion, touching, and knife-cutting experiments, confirmed the excellent durability of the coating layer on wood. This study reveals that lignin can produce sustainable, functional coatings as a renewable precursor. Additionally, the findings highlight that the induced materials can be considered for superhydrophobic and flame-retardant applications.

3.6. References

1. Ramage, M.H., et al., *The wood from the trees: The use of timber in construction.* Renew. Sust. Energ. Rev., 2017. **68**: p. 333-359. 10.1016/j.rser.2016.09.107.
2. Lowden, L.A. and T.R. Hull, *Flammability behaviour of wood and a review of the methods for its reduction.* Fire science reviews, 2013. **2**: p. 1-19. 10.1186/2193-0414-2-4.
3. Bartlett, A.I., R.M. Hadden, and L.A. Bisby, *A review of factors affecting the burning behaviour of wood for application to tall timber construction.* Fire Technology, 2019. **55**: p. 1-49. 10.1007/s10694-018-0787-y.
4. Jia, S., et al., *A new insight into the design of robust superhydrophobic and fire retardant wood: Breaking the conflicting requirement on adhesives.* Chem. Eng. J., 2023. **475**: p. 146240. 10.1016/j.cej.2023.146240.
5. Hooda, A., et al., *A review on fundamentals, constraints and fabrication techniques of superhydrophobic coatings.* Prog. Org. Coat, 2020. **142**: p. 105557. 10.1016/j.porgcoat.2020.105557.
6. Vazirinasab, E., R. Jafari, and G. Momen, *Application of superhydrophobic coatings as a corrosion barrier: A review.* Surf. Coat. Technol., 2018. **341**: p. 40-56. 10.1016/j.surfcoat.2017.11.053.
7. Liu, S., et al., *A nature-inspired strategy towards superhydrophobic wood.* Journal of Materials Chemistry A, 2023. **11**(47): p. 25875-25886.
8. Li, F.-F., *Comprehensive Review of Recent Research Advances on Flame-Retardant Coatings for Building Materials: Chemical Ingredients, Micromorphology, and Processing Techniques.* Molecules, 2023. **28**(4): p. 1842. 10.3390/molecules28041842.
9. Morgan, A.B. and J.W. Gilman, *An overview of flame retardancy of polymeric materials: application, technology, and future directions.* Fire and Materials, 2013. **37**(4): p. 259-279. 10.1002/fam.2128.

10. Chirkova, J., et al., *Lignins as agents for bio-protection of wood: 11th EWLP, Hamburg, Germany, August 16–19, 2010*. Holzforschung, 2011. 10.1515/hf.2011.092.
11. Ma, B., et al., *Tailorable and scalable production of eco-friendly lignin micro-nanospheres and their application in functional superhydrophobic coating.* Chemical Engineering Journal, 2023. **457**: p. 141309. https://doi.org/10.1016/j.cej.2023.141309.
12. Thébault, M., et al., *Effect of phenolation, lignin-type and degree of substitution on the properties of lignin-modified phenol-formaldehyde impregnation resins: Molecular weight distribution, wetting behavior, rheological properties and thermal curing profiles.* J. Renew. Mater., 2020. **8**(6): p. 603-630. 10.32604/jrm.2020.09616.
13. Hua, Q., et al., *Aqueous dispersions of esterified lignin particles for hydrophobic coatings.* Front. Chem., 2019. **7**: p. 515. 10.3389/fchem.2019.00515.
14. Mandlekar, N., et al., *An overview on the use of lignin and its derivatives in fire retardant polymer systems*. Lignin-trends and applications. Vol. 9. 2018: IntechOpen, London, UK. 207-231.
15. Yang, H., et al., *Lignin-derived bio-based flame retardants toward high-performance sustainable polymeric materials.* Green Chem., 2020. **22**(7): p. 2129-2161.
16. Liu, L., et al., *Fabrication of green lignin-based flame retardants for enhancing the thermal and fire retardancy properties of polypropylene/wood composites.* ACS Sustainable Chemistry & Engineering, 2016. **4**(4): p. 2422-2431. 10.1021/acssuschemeng.6b00112.
17. Tronc, F., L. Lestel, and S. Boileau, *Polycondensation using hydrosilylation: a tool for preparing tailor-made polysiloxanes with anchoring groups.* Polym. J., 2000. **41**(13): p. 5039-5046. 10.1016/S0032-3861(99)00566-2.
18. Fang, R., et al., *Research on the graft copolymerization of EH-lignin with acrylamide.* Nat. sci., 2009. **1**(01): p. 17. 10.4236/ns.2009.11004.
19. Tolbert, A., et al., *Characterization and analysis of the molecular weight of lignin for biorefining studies.* Biofuel Bioprod. Biorefin, 2014. **8**(6): p. 836-856. 10.1002/bbb.1500.
20. Alwadani, N., N. Ghavidel, and P. Fatehi, *Surface and interface characteristics of hydrophobic lignin derivatives in solvents and films.* Colloids Surf. A Physicochem. Eng. Asp., 2021. **609**: p. 125656. 10.1016/j.colsurfa.2020.125656.
21. Alghunaim, A., S. Kirdponpattara, and B.-m.Z. Newby, *Techniques for determining contact angle and wettability of powders.* Powder Technol., 2016. **287**: p. 201-215. https://doi.org/10.1016/j.powtec.2015.10.002.
22. Sen, S., S. Patil, and D.S. Argyropoulos, *Thermal properties of lignin in copolymers, blends, and composites: a review.* Green Chem., 2015. **17**(11): p. 4862-4887. 10.1039/C5GC01066G.
23. Liu, M., et al., *An all-water-based system for robust superhydrophobic surfaces.* J. Colloid Interface Sci., 2018. **519**: p. 130-136. 10.1016/j.jcis.2018.02.055.
24. Park, J., et al., *Shape of a large drop on a rough hydrophobic surface.* Phys. Fluids, 2013. **25**(2). 10.1063/1.4789494.
25. Sun, Y., et al., *Direct measurements of adhesion forces of water droplets on smooth and patterned polymers.* Surf. Innov., 2017. **6**(1–2): p. 93-105. 10.1680/jsuin.17.00049.
26. Tomak, E.D. and A.D. Cavdar, *Limited oxygen index levels of impregnated Scots pine wood.* Thermochim. Acta., 2013. **573**: p. 181-185. 10.1016/j.tca.2013.09.022.
27. An, S.J., et al., *Long-term lithium-ion battery performance improvement via ultraviolet light treatment of the graphite anode.* J. Electrochem. Soc., 2016. **163**(14): p. A2866. 10.1149/2.0171614jes.
28. Jia, S., et al., *Efficiently texturing hierarchical epoxy layer for smart superhydrophobic surfaces with excellent durability and exceptional stability exposed to fire.* Chemical Engineering Journal, 2018. **348**: p. 212-223. 10.1016/j.cej.2018.04.195.

29. Kazzaz, A.E., Z.H. Feizi, and P. Fatehi, *Grafting strategies for hydroxy groups of lignin for producing materials.* Green Chem., 2019. **21**(21): p. 5714-5752. https://doi.org/10.1039/C9GC02598G.
30. Lancefield, C.S., et al., *Identification of a diagnostic structural motif reveals a new reaction intermediate and condensation pathway in kraft lignin formation.* J. Chem. sci., 2018. **9**(30): p. 6348-6360. 10.1039/C8SC02000K.
31. Jardim, J.M., et al., *Insights into the potential of hardwood kraft lignin to be a green platform material for emergence of the biorefinery.* Polym. J., 2020. **12**(8): p. 1795. 10.3390/polym12081795.
32. Nagy, M., et al., *Characterization of CO 2 precipitated Kraft lignin to promote its utilization.* Green Chem., 2010. **12**(1): p. 31-34. 10.1039/B913602A.
33. Li, S., et al., *Thermally stable and tough coatings and films using vinyl silylated lignin.* ACS Sustain. Chem. Eng., 2018. **6**(2): p. 1988-1998. 10.1021/acssuschemeng.7b03387.
34. Gnanasekaran, D., et al., *Ring opening metathesis polymerization of polyoctahedral oligomeric silsesquioxanes (POSS) incorporated oxanorbornene-5, 6-dicarboximide: synthesis, characterization, and surface morphology of copolymers.* Aust. J. Chem., 2011. **64**(3): p. 309-315. 10.1071/CH10367.
35. Zhao, C., et al., *Revealing Structural Differences between Alkaline and Kraft Lignins by HSQC NMR.* Ind. amp; Eng. Chem. Res., 2019. **58**(14): p. 5707-5714. 10.1021/acs.iecr.9b00499.
36. Abdelkafi, F., et al., *Structural Analysis of Alfa Grass (Stipa tenacissima L.) Lignin Obtained by Acetic Acid/Formic Acid Delignification.* Biomacromolecules, 2011. **12**(11): p. 3895-3902. 10.1021/bm2008179.
37. An, L., et al., *One-step silanization and amination of lignin and its adsorption of Congo red and Cu (II) ions in aqueous solution.* Int. J. Biol. Macromol., 2020. **159**: p. 222-230. 10.1016/j.ijbiomac.2020.05.072.
38. Gwon, J.G., Lee, S. Y., Doh, G. H., & Kim, J. H. , *Characterization of chemically modified wood fibers using FTIR spectroscopy for biocomposites.* J. Appl. Polym. Sci, 2010. **116**(6): p. 3212-3219. 10.1002/app.31746.
39. Carlos de Haro, J., et al., *Lignin-based anticorrosion coatings for the protection of aluminum surfaces.* ACS Sustain. Chem. Eng., 2019. **7**(6): p. 6213-6222. 10.1021/acssuschemeng.8b06568.
40. Chen, X., X. Wang, and D. Fang, *A review on C1s XPS-spectra for some kinds of carbon materials.* Fullerenes, 2020. **28**(12): p. 1048-1058. 10.1080/1536383X.2020.1794851.
41. Stańczyk, K., et al., *Transformation of nitrogen structures in carbonization of model compounds determined by XPS.* Carbon, 1995. **33**(10): p. 1383-1392.
42. Deng, Z.W. and R. Souda, *XPS studies on silicon carbonitride films prepared by sequential implantation of nitrogen and carbon into silicon.* Diam. Relat. Mater., 2002. **11**(9): p. 1676-1682. 10.1016/S0925-9635(02)00143-7.
43. Arefmanesh, M., et al., *Bromide-based ionic liquid treatment of hardwood organosolv lignin yielded a more reactive biobased polyol.* Industrial & Engineering Chemistry Research, 2020. **59**(42): p. 18740-18747. 10.1021/acs.iecr.0c03718.
44. Ye, H., et al., *Simple spray deposition of a water-based superhydrophobic coating with high stability for flexible applications.* J. Mater, 2017. **5**(20): p. 9882-9890. 10.1039/C7TA02118F.
45. Kim, D., et al., *Direct synthesis of polymer nanocapsules: self-assembly of polymer hollow spheres through irreversible covalent bond formation.* J. Am. Chem. Soc, 2010. **132**(28): p. 9908-9919. 10.1021/ja1039242.
46. Zhang, Y., et al., *A novel route to thermosensitive polymeric core–shell aggregates and hollow spheres in aqueous media.* Adv. Funct. Mater, 2005. **15**(4): p. 695-699. 10.1002/adfm.200400378.

47. Li, H., et al., *Preparation of nanocapsules via the self-assembly of kraft lignin: A totally green process with renewable resources.* ACS Sustain. Chem. Eng., 2016. **4**(4): p. 1946-1953. 10.1021/acssuschemeng.5b01066.
48. Loman-Cortes, P., D.J. Jacobs, and J.L. Vivero-Escoto, *Molecular dynamic simulation of polyhedral oligomeric silsesquioxane porphyrin molecules: Self-assembly and influence on morphology.* Mater. Today Commun., 2021. **29**: p. 102815. 10.1016/j.mtcomm.2021.102815.
49. Chen, L., et al., *Structure, bioactivity and applications of natural hyperbranched polysaccharides.* Carbohydr. Polym., 2019. **223**: p. 115076. 10.1016/j.carbpol.2019.115076.
50. Yan, Y.Y., N. Gao, and W. Barthlott, *Mimicking natural superhydrophobic surfaces and grasping the wetting process: A review on recent progress in preparing superhydrophobic surfaces.* Adv. Colloid Interface Sci., 2011. **169**(2): p. 80-105. https://doi.org/10.1016/j.cis.2011.08.005.
51. Foorginezhad, S. and M.M. Zerafat, *Fabrication of superhydrophobic coatings with self-cleaning properties on cotton fabric based on Octa vinyl polyhedral oligomeric silsesquioxane/polydimethylsiloxane (OV-POSS/PDMS) nanocomposite.* J. Colloid Interface Sci., 2019. **540**: p. 78-87. 10.1016/j.jcis.2019.01.007.
52. Zhang, J., et al., *A modified lignin adsorbent for the removal of 2, 4, 6-trinitrotoluene.* Chem. Eng. J., 2011. **168**(3): p. 1055-1063. 10.1016/j.cej.2011.01.083.
53. Lan, Z., et al., *Transparent, high glass-transition temperature, shape memory hybrid polyimides based on polyhedral oligomeric silsesquioxane.* Polym. J., 2019. **11**(6): p. 1058. 10.3390/polym11061058.
54. Chung, H.-J., K.-S. Woo, and S.-T. Lim, *Glass transition and enthalpy relaxation of cross-linked corn starches.* Carbohydr. polym., 2004. **55**(1): p. 9-15. 10.1016/j.carbpol.2003.04.002.
55. Schwab, J.J. and J.D. Lichtenhan, *Polyhedral oligomeric silsesquioxane (POSS) -based polymers.* Appl. organomet. chem., 1998. **12**(10‐11): p. 707-713. 10.1002/(SICI)1099-0739(199810/11)12:10/11%3C707::AID-AOC776%3E3.0.CO;2-1.
56. Pomeroy, M.J., *Coatings for gas turbine materials and long term stability issues.* Mater. Des., 2005. **26**(3): p. 223-231. 10.1016/j.matdes.2004.02.005.
57. Luo, L. and I. Tomac, *Experimental investigation of particle agglomeration effects on slurry settling in viscous fluid.* Transp. Porous Media, 2018. **121**: p. 333-352. 10.1007/s11242-017-0956-3.
58. Murashov, V.V. and J. Leszczynski, *Adsorption of the phosphate groups on silica hydroxyls: an ab initio study.* J. Phys. Chem. A., 1999. **103**(9): p. 1228-1238. 10.1021/jp981996r.
59. Chen, T., et al., *Constructing hydrophobic interfaces in aluminophosphate adhesives with reduced graphene oxide to improve the performance of wood-based boards.* Compos. B. Eng., 2020. **198**: p. 108168. 10.1016/j.compositesb.2020.108168.
60. Pan, A., et al., *In-situ deposition of oxidized porous metal nanoparticles on the surface of picosecond laser-induced micro/nano structures: A new kind of meta-surface equipped with both super-hydrophobicity and anti-reflectivity.* Chem. Eng. J., 2023. **460**: p. 141582. 10.1016/j.cej.2023.141582.
61. Ma, P., et al., *Super-hydrophobic Cs4PbBr6@PDB composites with water-driven photoluminescence enhancement and dehydration recovery.* Chem. Eng. J., 2022. **436**: p. 135077. 10.1016/j.cej.2022.135077.
62. Wang, Z., et al., *Mechanically durable and self-healing super-hydrophobic coating with hierarchically structured KH570 modified SiO2-decorated aligned carbon nanotube bundles.* Chem. Eng. J., 2021. **408**: p. 127263. 10.1016/j.cej.2020.127263.
63. He, Q., et al., *Synergistic effects of polyhedral oligomeric silsesquioxane (POSS) and oligomeric bisphenyl A bis (diphenyl phosphate)(BDP) on thermal and flame retardant properties of polycarbonate.* J. mater. sci., 2009. **44**: p. 1308-1316. 10.1007/s10853-009-3266-5.

64. Qian, Y., et al., *Synthesis of a novel hybrid synergistic flame retardant and its application in PP/IFR*. Polym. Degrad. Stab., 2011. **96**(6): p. 1134-1140. 10.1016/j.polymdegradstab.2011.02.017.
65. Zhang, W., G. Camino, and R. Yang, *Polymer/polyhedral oligomeric silsesquioxane (POSS) nanocomposites: An overview of fire retardance*. Prog. Polym. Sci., 2017. **67**: p. 77-125. 10.1016/j.progpolymsci.2016.09.011.
66. Wang, M., et al., *A contrastive investigation on the anticorrosive performance of stearic acid and fluoroalkylsilane-modified superhydrophobic surface in salt, alkali, and acid solution.* Langmuir, 2020. **36**(34): p. 10279-10292. 10.1021/acs.langmuir.0c02080.
67. Qi, X., et al., *Super-hydrophobic graphene-based high elastic sponge with superior photothermal effect for efficient cleaning of oil contamination.* Chemical Engineering Journal, 2023. **476**: p. 146317. 10.1016/j.cej.2023.146317.
68. Wu, Z., et al., *Eco-benign PVA/aluminum phosphate as an alternative to formaldehyde-based adhesives in wood-based panels.* RSC advances, 2021. **11**(54): p. 34416-34423. 10.1039/D1RA05552F.
69. Ülker, O., *Wood adhesives and bonding theory.* Adhesives–applications and properties, 2016. 10.5772/65759.
70. Hussain, S.S., et al., *Self-extinguishable, intumescent poly (urethane-triazole) s as halogen-free flame retardant materials via bulk polymerization of azide-alkynes.* Progress in Organic Coatings, 2024. **188**: p. 108228. 10.1016/j.porgcoat.2024.108228.

Chapter 4: Superhydrophobic Lignin Incorporated Natural Rubber Film for Oil-Water Separation

*Banchamlak Bemerw Kassaun, Pedram Fatehi**

Under review in Polymer

Biorefining Research Institute, Lakehead University, 955 Oliver Road, Thunder Bay, Ontario, P7B 5E1 Canada.

First Author, email: bkassaun@lakeheadu.ca, address: 955 Oliver Road, Thunder Bay, ON, Canada, P7B 5E1

Corresponding author, email: pfatehi@lakeheadu.ca, address: 955 Oliver Road, Thunder Bay, ON, Canada, P7B 5E1

The contribution of Banchamlak Bemerw Kassaun to this work was the conception of the original draft, visualization, validation, formal analysis, data curation, conceptualization.

Graphic abstract

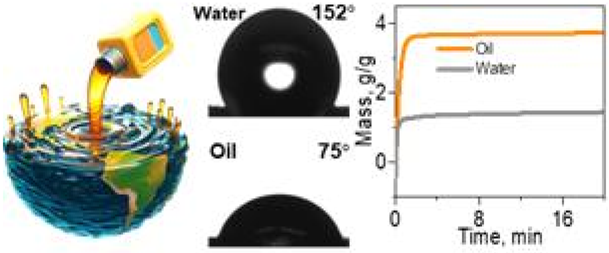

4.1. Abstract

Natural rubbers (NR) are used widely in industry, yet they exhibit diminished tensile strength and deteriorate under high temperature and moisture conditions. Thus, additional substances are needed to improve their mechanical properties and thermal stability. In this study, we examined a hypothesis that the incorporation of lignin derivative, which was fabricated via aqueous-based copolymerization of kraft lignin (SKL) and aminopropyl/ flurosilsesquioxane (WAPFSS), into the NR matrix would improve the hydrophobic, thermal and mechanical characteristics of NR. The findings of this study revealed that 20 wt.% inclusion of lignin-silsesquioxane copolymer (WSF) in the NR formulation (W20) improved the mechanical properties of induced films by 81%, which was 58% higher than its counterpart containing unmodified kraft lignin in the NR matrix (K20 sample). Interestingly, the W20 sample was more mechanically durable after heat treatment and water exposure than K20 and pure NR. W20's 150° water contact angle and 10° slide angle confirmed its superhydrophobicity, which survived after high-temperature exposure and sandpaper wear tests. The W20 absorbed oil at a higher rate than water. The superior performance of WSF-containing NR films was attributed to the interaction of WSF and NR, which resulted from a reduced hydroxyl group and the addition of hydrophobic Si-O-Si and Si-C groups to the lignin backbone. The present study provides fundamentals for fabricating sustainable lignin-based superhydrophobic natural rubber materials with potential applications as an oil and water separator.

Keywords: Lignin, natural rubber, oil-water separation, superhydrophobic

4.2. Introduction

Natural rubber (NR) is an important industrial raw material extensively utilized in applications such as tires, seals, damping systems, soft robotics, wearable electronics, and stretchable sensors [1]. NR-based products can be made by mixing vulcanizing agents, accelerators, and other ingredients into the NR matrix, followed by shaping and vulcanization [2]. The use of NR latex in NR-based films presents two grand challenges: achieving high strength (including modulus, hardness, and wear resistance) and desirable surface qualities (such as hydrophobicity) [3]. NR demonstrates enhanced modulus, hardness, and wear resistance when fillers, such as carbon black and silica, are used along with NR [4-6]. However, the utilization of such fillers faces limitations, such as poor dispersion in the latex matrix, some health and environmental concerns, and impaired sustainability [7]. The hydrophobicity of such films has been reported to improve via coating with silica-based superhydrophobic nanomaterials [8]. However, this process would require additional steps to coat the film after formation, and the coatings could be damaged under abrasion. Moreover, using environmentally unsustainable materials to coat rubber films is unattractive.

Green functional materials like lignin have received attention in the rubber industry due to their abundance, low production cost, biodegradability, thermal stability, and antioxidant properties [9-11]. However, incorporating lignin in a rubber matrix is not straightforward due to the polarity of lignin molecules, which contributes to strong self-interactions (i.e., aggregation), leading to lower mechanical properties and hydrophobicity of films [12]. On the other hand, lignin nanoparticles [13], nano hybridization [14], and chemically modified lignin [15] were reported to improve the mechanical properties of NR films by improving the interfacial adhesion between lignin and the rubber matrix. Jiang et al. reported the fabrication of lignin nanoparticles (LPCs), which enhanced NR's mechanical characteristics, thermal stability, and thermo-oxidative stability [13]. In another study, Qiu et al. reported that a nanohybrid of aminated soda lignin and SiO_2 resulted in a uniform nanosphere, whose incorporation in NR had improved NR's mechanical properties similar to carbon black. However, no information was provided regarding the surface characteristics of the rubber sheet [14]. Another study by Shorey et al. reported using hydrophobic-modified lignin as a reinforcing agent for natural rubber [16]. In this work, kraft lignin was silanized with an organosilane compound in dimethyl sulfoxide solvent and incorporated into NR. The resultant film exhibited improved mechanical properties and reduced water absorption. However, such modification was solvent-based, a low proportion (10%) of silylated lignin was utilized, and the mechanical performance of the film after exposure to water was poor. Due to the current challenges, exploring a suitable water-based modification of KL that could enhance the thermomechanical and water-repellent properties of NR films is necessary.

Environmental conditions, such as constant exposure to extreme temperatures and humidity, affect the durability of natural rubber-based material [17]. Thermo-oxidative, hydrolytic, and photo-oxidative degradation of natural rubber films is caused by the breakdown of chemical bonds in the isoprene rubber, reducing the life span of rubber-based materials [18-21]. Chemicals, such as amines and phenolics, are effective and powerful antioxidants protecting against aging by scavenging the free radicals during the oxidative chain reaction. Phenolic structures that reach biopolymers (e.g., lignin) can improve the durability of lignin-containing natural rubber materials [22, 23]. Furthermore, the amination of lignin would improve its radical scavenging effect. Therefore, it is important to study how incorporating lignin can improve the durability of NR-based films.

Superhydrophobic materials are proposed to be an ideal absorbent for separating oil and water and cleaning oil spills [24]. The use of such materials is growing due to the ever-growing contamination of marine habitats by oil spills [25-27]. Superhydrophobic rubber films exhibit water contact angles of >150° and oil of ~ 0°, designed with hydrophobic characteristics and frequently composed of micro or nanostructures [28]. Rubber materials' inherent malleability and resilience provide a diverse and recyclable foundation for separating oil and water from many sources [29]. One popular technique for creating superhydrophobic surfaces involves the application of hydrophobic substances, such as fluoroalkyl silanes or perfluorinated compounds, onto the surface of natural rubber. This would lead to the creation of a hydrophobic layer [30]. In addition, the surface roughness may be improved by utilizing nanostructuring techniques, such as roughening the surface [28, 31, 32]. These processes provide a rough surface texture that traps air pockets, decreasing the surface area that encounters water and resulting in the superhydrophobic effect. The work presented herein focused on the fabrication of a novel superhydrophobic, thermally stable, and moisture-resistant sustainable natural rubber film by incorporating lignin-derived polymers into NR. The study is composed of a simple water-based modification of kraft lignin to generate superhydrophobic lignin with improved thermal and oil adsorption characteristics. A water-based Aminopropyl/flurosilsesquioxane oligomer was selected as a silsesquioxane agent for polymerizing with kraft lignin (WSF). The changes in the chemical, structural, and thermal properties of lignin were assessed comprehensively by NMR, XPS, FTIR, and TGA. The modified lignin (WSF) was used in natural rubber latex as a functional filler following the latex mixing method. The mechanical, thermal, and surface properties of the prepared NR-lignin films were investigated before and after exposure to heat and water. The impact of the dosage of WSF on NR's physicochemical properties was investigated, and the resulting superhydrophobic films' oil and water absorption were comprehensively assessed. The results of this work provide a method to generate a sustainable superhydrophobic and strong NR-based oil and water separator.

4.3. Experimental Section

4.3.1. Materials

Kraft lignin (SKL) was acquired from FPInnovations and manufactured using the LignoForce technique. Aminopropyl/flurosilsesquioxane (WAPFSS) oligomer was obtained from Gelest Inc.USA. Sodium hydroxide (NaOH), potassium hydroxide (KOH), deuterated sodium hydroxide (NaOD), deuterium oxide (D_2O), deuterated dimethyl sulfoxide (DMSO-d_6), hydrochloric acid (HCl) 37%, 2-chloro-4,4,5,5-tetramethyl-1,3,2-dioxaphospholane (TMDP), chloroform ($CDCl_3$), ethanol (95%), pyridine, cyclohexanol (99%), chromium (III) acetylacetonate (97%), toluene, zinc oxide (ZnO), sulfur (99.5%), zinc (II) dibutyl Di thiocarbamate (ZDBC) and soyabean oil were all bought from Millipore Sigma in Oakville, Canada. Additionally, nylon membrane syringe filters with a pore size of 0.45 µm were purchased from Fisher Scientific in Ottawa, Canada. A dialysis membrane with a molecular weight cut-off of 1,000 g/mol was purchased from Spectrum Labs. A natural rubber latex (NR, 60 wt. %) was purchased from Amazon.

4.3.2. Lignin Copolymerization

Softwood kraft lignin (SKL) and WAPFSS polymerization was conducted in an aqueous environment following the polycondensation reaction. To prepare a lignin suspension in deionized water, 1 g of SKL was dispersed in 40 mL of deionized water in a three-neck flask (i.e., SKL concentration of 25 g/L). The suspension was continuously agitated for 1 h. Afterward, the solution of WAPFSS (20 vol% in water) was added to the SKL solution at a 1:1 molar ratio. The mixture was relocated in a three-neck flask and heated in a water bath at 60°C. After 48 h, the product was cooled to ambient temperature. The system's pH was neutralized using a 1M sodium hydroxide solution. A 24-

hour dialysis and freeze-drying of the sample followed this step. The resulting sample was labeled as WSF.

4.3.3. Lignin Rubber Sheet Formulation and Film Casting

A solution casting method was followed to produce composite films of NR, WSF, or SKL. The mass proportion of the rubber compounds was calculated by parts per hundred rubber (phr) consisting of NR (100 phr), crosslinking agent sulfur (1.5 phr), activator ZnO (1.3 phr), and accelerator ZDBC (0.7 phr) with the addition of WSF at 10, 20, and 30 wt.%. WSF was initially added to 20 mL of deionized water, the pH was raised to 11 with 0.3 M KOH, and the mixture was left to agitate for 1 h at 250 rpm using a magnetic stirrer. Afterward, the suspension was supplemented with sulfur powder as a crosslinking agent, ZnO as an activator, and ZDBC as an accelerator. The mixture was stirred for 10 minutes at ambient temperature, followed by an additional 3 minutes of ultrasonication (Omni-Ruptor 4000 from Omni International Inc). A certain quantity of NR latex was introduced to a beaker and agitated for 2h at 250 rpm and room temperature to start the maturation process . Ultimately, the matured rubber formulations were carefully poured into silicon molds and subjected to a 48-hour drying period at ambient temperature. The sheets were separated from the silicon mold and underwent a 2-hour curing at a temperature of 100°C. The samples were labeled as Wx (x being 10, 20, or 30 wt.% of WSF). Control samples for the present work were developed, which consisted of an NR sheet without lignin (NR) and an NR sheet with 20% unmodified lignin, K (K20).

4.3.4. Characterization

4.3.4.1. Characterization of K and W powders

The reaction yield was calculated by measuring the product before and after the Silsesquioxation modification **Equation 4.1**.

$$\%\,Yield = \frac{dry\ mass\ of\ A}{dry\ mass\ of\ SKL+B} \times 100 \qquad (4.1)$$

“A” stands for W, and “B” refers to WAPMSS (Aminopropyl/flurosilsesquioxane (WAPFSS)) for the process of Silsesquioxation.

Nuclear Magnetic Resonance (NMR) of SKL and WSF were structurally investigated using proton nuclear magnetic resonance (^{1}H-NMR) and heteronuclear single quantum coherence NMR (HSQC) by top spin 4.02 software (Bruker AVANCE Neo NMR-500 MHz apparatus USA). For this investigation, 60-70 mg of oven-dried WSF sample were dissolved in 1 mL of D_2O and 2 µL of 40% NaOD, while 60-70 mg of SKL was mixed in 1 mL of DMSO–d_6 at room temperature for 12 h. ^{1}H NMR test parameters were 16 scans, 3.28-sec acquisition, 1s relaxation, and 90° pulse at room temperature. Bruker pulse hsqcetgpsisp2.3 software assessed HSQC analysis using 13 ppm spectra width in the F2 (^{1}H) dimension and 2048 data points (155 ms acquisition time), 165 ppm in the F1 (^{13}C) dimension with 256 data points (6.2 ms acquisition time), a 1.5 s pulse delay, and sixteen scans at room temperature. To quantify the change in phenolic, aliphatic, and carboxylic hydroxyl groups, indirect ^{31}P NMR analysis was performed after the phosphorylation reaction of lignin. First, 50-60 mg of pre-dried samples (60°C) were mixed with 1 mL of a solution containing chloroform-d ($CDCl_3$) and pyridine at a ratio of 1:1.6 (v/v). Then, 52 µL (5 g/L) of a relaxing agent, i.e., chromium (III) acetylacetonate, was added to the mixture. The mixture was stirred at 120 rpm for 12 h. After adding 200 µL of phosphorylating reagent (TMDP) to the sample solutions, the mixture was agitated at 120 rpm for 1 h. Afterward, 50 µL internal standard (cyclohexanol, 20 g/L) was added, and the system was stirred for 30 min. After that, the solutions were placed in NMR tubes and analyzed with 1024 scans per sample, 90° pulse width, and 5-sec relaxation delay [33]. The compositions of SKL and WSF were examined using an X-ray photoelectron spectrometer (XPS) analyzer (Kratos AXIS Supra, Shimadzu Group Company, Japan) with a dual anode AL/Ag monochromatic X-ray source (1486.7 eV). Samples were put through XPS on double-sided carbon tape after oven-drying at 60°C. Steps, dwell, and sweep times were 230, 260, and 60 s. ESCApe^{TM} (1.4.0.1149) software (Kratos Analytical, Japan) was used to obtain spectra and quantify the chemical bonds of the samples [34]. Fourier Transform Infrared Spectroscopy (FTIR) was conducted using a Bruker Tensor 37 (Bruker, Germany) equipped with a PIKE MIRacle Diamond Attenuated Total Reflectance (ATR) accessory to examine the materials' structure. 32 scans were conducted for each sample with a resolution of 4 cm^{-1} at a wavenumber range of 500 and 4000 cm^{-1}. Similar conditions were employed for the structural characterization of NR and NR-lignin films before and after heat treatment.

Powder wettability analysis of WSF and SKL was performed via the Washburn method using a force tensiometer (Attention Sigma 700/701, Biolin Scientific, Finland) with a powder glass probe . Washburn measures the capillary rise of liquid into particles. The resultant curve conveys data on absorption amount and kinetics, contingent upon the contact angle of the powder and the characteristics of the liquid. This study placed 200 mg of samples in a cylindrical metal tube with an open base bottom and taped three times to guarantee adequate packing [35]. **Equation 4.2** was used to test the samples' wettability by immersing the powder holder in liquid and measuring the powder bed's liquid absorption over time.

$$W^2 = \frac{C\rho\gamma l\cos\theta\, t}{2\eta} \qquad (4.2)$$

Where WSF is the weight of absorbed water (g), C is a geometric constant (0.04), ρ is the liquid density (0.998 g/mL), γ is surface tension (for water is 72.8 mN/m and for oil is 34 mN/m), L is the length of the powder glass probe (5.5 mm), η is the viscosity of the liquid (for water is 0.01 g/cm. s, and oil is 1.72 g/cm), and t is measurements time. The same analysis was utilized to assess the water and oil adsorption of NR and NR-lignin films.

5.3.4.2. Characterization of NR and NR-Lignin Films

The mechanical properties of NR-lignin films were examined using universal testing equipment with a 200 N load cell (Shimadzu Instrone-6800 series, Japan). Samples were cut from solution cast sheets with a dog bone-shaped die, measuring 27 cm long, 3.12 cm wide (ASTM D638 type V), and 0.5–1.2 mm thick. Three specimens from each film were evaluated at 50 mm/min at room temperature, and the average value with an error bar was reported [36]. Thermal stability and degradation temperature of SKL and WSF powders and NR and NR-lignin films were investigated by thermogravimetric analysis (TGA) instrument (TGAi1000, Instrument Specialists Inc., WI, USA). The instrument was loaded with 10-10.36 mg of dried samples in a Tzero® aluminum pan. The analysis was conducted in a nitrogen environment with a 10 mL/min flow rate and a heating rate of 10°C/min from 25°C to 800°C [37]. Curated sheets were examined using SEM to assess the morphology of NR and NR-lignin films. The film's SEM photos were captured via a scanning electron microscope (Zeiss FESEM 1530) with an accelerating voltage of 10.00 kV accelerating voltage in a vacuum (10^{-4}-10^{-3} Pa with 100× to 10,000× magnifications. In this analysis, the non-conductive samples underwent a process of gold-coating using a sputter coater. The contact angle of NR and NR-lignin films untreated, thermally aged, and abrased (W20) with a liquid (water or oil) was measured using an optical tensiometer (Theta Lite, Bolin Scientific, Finland) with a digital camera and manual tilting stage. The experiment involved placing a liquid droplet with 6-10 μL volume onto the surface of a film and coated glass. The contact angle of the droplet was visually measured using a camera for 50 seconds. The water sliding angle was determined using a tilting stage. The experiment involved applying a water droplet (6-10 μL) onto the treated wood surface at a 180° angle on the tilting stage. The stage was then gradually tilted until the droplet began to slide. The measurement was replicated thrice and presented as the average and standard deviation. The measurement was conducted using the sessile liquid droplet technique and one-attention software. ASTM D570 standards were followed according to **Equation 5.3** to evaluate the water diffusion coefficient. Three bone-shaped specimens of dogs were cut from each sample of NR and NR-lignin films; each specimen was submerged in 50 mL of water. Weight change after removing excess surface water was monitored over 72 h, and the diffusion coefficient was calculated according to ASTM D5229 in **Equation 4.3**.

$$D = \frac{\Pi}{16}\left(\frac{M_n - M_{n-1}}{M_{max}}\right)^2 \left(\frac{d}{\sqrt{t_n} - \sqrt{t}_{n-1}}\right)^2 \qquad (4.3)$$

Where M_{max} is the saturated (maximum) moisture content, Mn is the moisture content at t_n, M_{n-1} is the moisture content at t_{n-1}, and d is the thickness of the composite. Furthermore, the samples' mechanical properties were assessed using the method stated in the mechanical properties section.

The mechanical stability of NR and NR-lignin samples was assessed by subjecting dog bone-shaped specimens to water absorption for 72 hours at room temperature or thermal exposure in a convection oven at 120°C for 24 hours. Subsequently, the specimens were analyzed for their mechanical properties [38]. Samples were cut from each cured sheet and placed in a conventional oven for 24 hr at 120 °C to evaluate the affinity of NR and NR-lignin films to withstand thermal aging. Subsequently, they were cooled at room temperature for another 24 hours. The mechanical properties of the thermally aged specimens were assessed using the previously reported unaged rubber tensile test method [39]. A sandpaper abrasion test was conducted by applying a downward force of 20 grams on the W20 film and subjecting it to 1500 CW sandpaper. The film was pushed along a linear trajectory, and the water contact angle was measured after each cycle. One cycle is equivalent to a 30 cm abrasion [40].

4.4. Results and Discussion

4.4.1. Lignin Derivative Analysis

4.4.1.1. Chemical Structure and Reaction Analysis

The ^{1}H-NMR, ^{31}P-NMR, and HSQC NMR were used to investigate the changes in the chemical structure of SKL before and after the modification, and the results are presented in **Figure 4.1**a-d. The DMSO-d_6 signal was detected at 2.5 ppm in the SKL spectrum, while the D_2O signal in the WSF spectrum was identified at 5 ppm. The ^{1}H-NMR spectrum of K shows that aromatic protons exhibited a signal within the chemical shift range of 6.0 to 7.5 ppm, and methoxy protons were observed in the 3-4 ppm region. Aliphatic protons were detectable at 0 and 3.2 ppm **Figure 4.1**a [41]. WSF exhibited all the protons identified in SKL. Additionally, copolymerization caused extra peaks. The firm peaks in WSF observed at 2.7 ppm, 1.5 ppm, and 0.5 ppm were associated with the -OH peaks linked with Si, protons from NH_2, and the protons from the propyl structure of $-CH_2-CH_2-CH_2$, respectively, resulting from WAPFSS chains as shown in **Figure S4.1** Appendix 5A [42]. The HSQC analysis of SKL and WSF was carried out to identify the primary linkages of lignin prominent interunit linkages in β-O-4 (A_β), phenylcoumaranan β-5 (B_β), and resinol β-β (C_β), and the methoxy ($-OCH_3$) functional group at cross peak signals of δ_C/δ_H 83.6/4.27 ppm, 53.29/3.44 ppm, 53.6/3.0 ppm and 55.5/3.70, respectively **Figure 4.1**b [43]. In addition to the similar signals inherited from SKL, WSF had strong $-OCH_2$ linkages in the cross-peak signals δ_C/δ_H of 42-45/3.2-3.4. The aromatic linkage signals of guaiacyl (G) units were identified for G_2, G_5, and G_6 in both SKL and WSF samples at 110/6.7, 115.9/6.7, and 122.9/7.5, respectively, in **Figure 4.1**c. The presence of the aromatic units along with lignin primary linkages in WSF confirmed that the reaction did not alter the original structure of lignin significantly. The ^{31}P-NMR spectra and quantification of the aliphatic, phenolic (C-5 substituted, and guaiacyl) and carboxylate OH group content of the samples after phosphorylation are presented in **Figure 4.1**d and **Table S4.1**. Compared to SKL, the decrease in phenolic, aliphatic, and carboxylic groups in WSF suggests that the hydroxyl group was the site of reaction for SKL and WAPFSS through a condensation process **Figure S4.**2 [44]. Furthermore, FTIR analysis was conducted, and the results are presented in **Figure 4.1**e. The band at around 3404 cm^{-1} in SKL and WSF was attributed to the hydroxyl groups in lignin's aliphatic and phenolic structures [45]. However, the strength of this peak was comparatively lower in WSF. This indicates the copolymerization at this specific functional group in conjunction with ^{31}P-NMR (**Figure 4.1a-**d). The peaks observed at 2840 and 2928 cm^{-1} resulted from the stretching vibrations of the C−H bonds in the methylene and methyl groups, respectively [46]. After copolymerization, there was a considerable increase in the intensity of the peaks corresponding to the methyl group structures [47]. Along with ^{1}H-NMR, FTIR results indicate the effective incorporation of molecular chains with several methyl groups during copolymerization. Due to the copolymerization taking place at the aromatic parts of K, the peaks corresponding to the C−H vibrations of the aromatic skeleton at 1603, 1506, and 812 cm^{-1} and the C−O vibrations of the guaiacol ring at 1269 cm^{-1} of K significantly decreased in the spectrum of WSF, which is consistent with the HSQC analysis. The presence of a new peak at 835 cm^{-1} and the heightened intensity between 1008 and 1000 cm^{-1} can be attributed to the presence of Si-CH$_3$ and siloxanes (Si-O-Si) in the WSF spectrum, which are a direct outcome of the copolymerization [48]. The copolymer spectrum exhibited prominent transmittance signals at 1240 and 975 cm^{-1}, corresponding to a phenoxy group connected to silicon. Additionally, the peak observed at 1162 cm^{-1} was attributed to the stretching vibration of the C-F bond resulting from copolymerization [49, 50]. Also, the alteration in the chemical composition of SKL and WSF was validated using XPS **Figure 4.1**f-i. When comparing the broad spectra of SKL and WSF, the presence of C1s (285.1 eV) and O1s (533 eV) [51] peaks was detected in both samples.

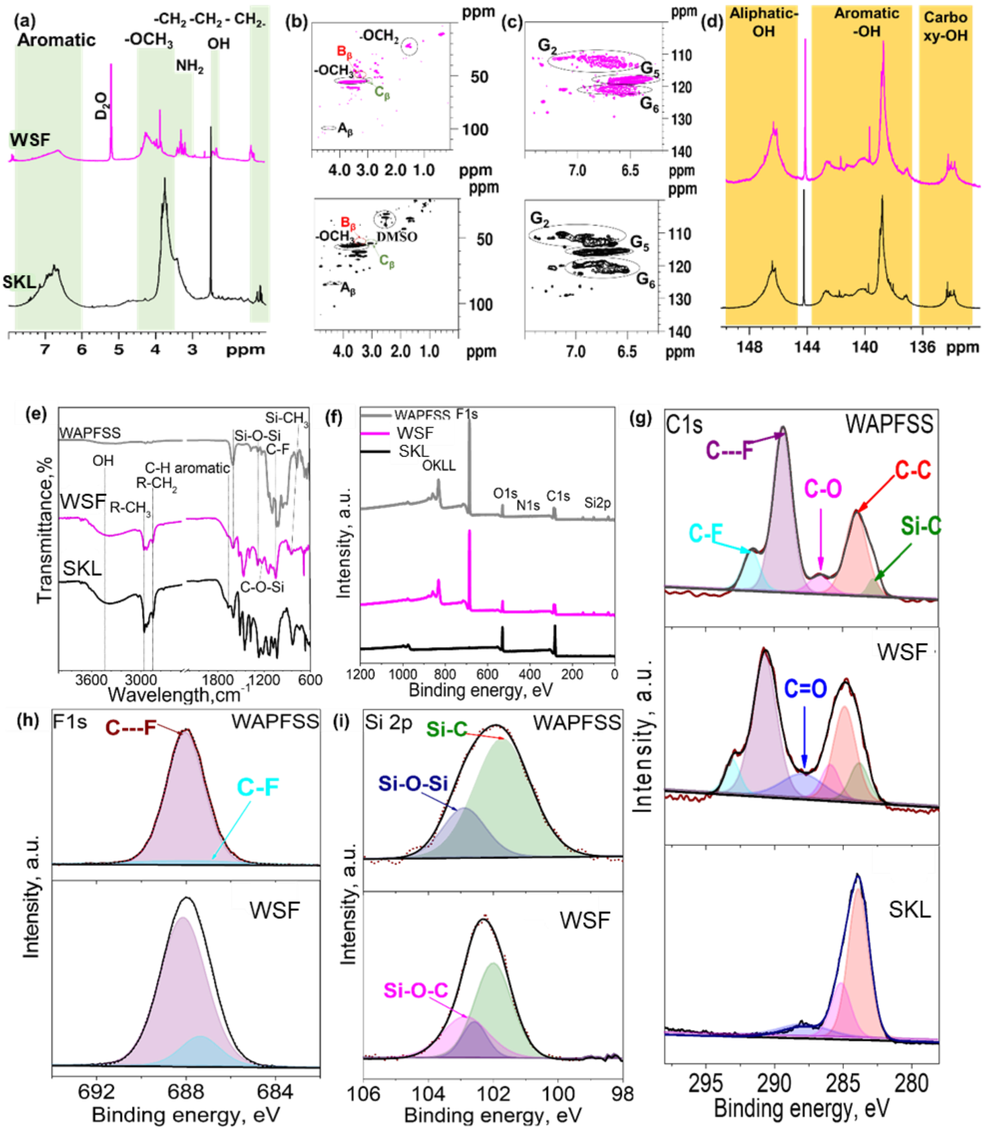

Figure 4.1. 1H-NMR (a), HSQC NMR (b) and 31P-NMR (c) of SKL and WSF, (A) β-aryl ether (β-O-4) linkages: (B) phenyl-coumaran structure (β-5′/α-O-4′); (C) secoisolariciresinol substructure; (D) resinol substructure (β-β); (E) guaiacyl propanol unit. FTIR (d), XPS wide specC1s deconvoluted spectra of SKL (e), C1s spectra of SKL, WSF, and WAPFSS (f) F1s deconvoluted spectra of WSF and WAPFSS (g), and Si2p of WSF and WAPFSS deconvoluted (h and i).

Additionally, novel F1s (689 eV) and Si2p (152.9 eV and 101 eV) peaks were observed for WSF, as illustrated in **Figure 4.1**f. Notably, WSF exhibited a substantial F/C ratio of 3.26, which was about 1500 times larger than that of SKL (0.0021). Furthermore, there was a significant reduction in the C/O area ratio from SKL (4.25) to WSF (2.07), suggesting that silsesquioxane groups were incorporated into the carbon chains of WSF. This led to a drop in the carbon content due to the rise in the inorganic content. For more details, the C1s core-level spectra of SKL and WSF were deconvoluted, and the results are shown in **Figure 4.1g.** SKL C1s peak deconvolution resulted in three major components of C-C (284.8

eV), C=O (~ 288 – 290 eV), and C-O (~286 eV). Similarly, the C1s spectrum of WSF exhibited similar components as SKL, but it also revealed additional components, namely C-Si (283 eV), C---F (292 eV), and C-F (283 eV) [52]. The O=C bond concentration showed a slight decrease for WSF compared to SKL. This implies that the condensation copolymerization led to the decrease in the C=O-H site of lignin, which is consistent with ^{31}P-NMR studies. The F1 peaks of WSF were deconvoluted in two components, C---F (688.5 eV) and C-F (686.5 eV), as illustrated in **Figure 4.1**h. This fluorine component came from the oligomer WAPFSS. It can be assumed that mainly the carbon atom of the open edge of lignin planes was bound with fluorine, and the bond between carbon and fluorine can be attributed to the semi-ionic type (C---F) and covalent bonding (C-F) in these samples [53]. Similarly, Si2p peaks were deconvoluted for WSF; the results are presented in **Figure 4.1**i. The Si2p spectra for WSF show three deconvoluted components of Si-C (101.34 eV), Si-O-Si/Si-OH (103.76 eV), and Si-O-C (102.5) [54]. Based on NMR, XPS, and FTIR analyses, it can be concluded that the copolymerization took place in the hydroxyl group of SKL. This reaction occurred by converting the hydroxyl group into Si-O-C linkages between lignin and the copolymer. The reduction in the total hydroxyl content further supports this conclusion.

5.4.1.2. Hydrophobicity of Lignin Derivatives

The wetting process involves an exchange of solid/gas particles for solid/water particles. When determining wettability, the Washburn method looks at the liquid's ability to infiltrate a powder bed over time [55]. The wettability of SKL and WSF copolymers is shown in **Figure 4.2**a. SKL absorbed water slowly but extensively. However, WSF showed no sign of water absorption. The SKL's higher water absorption can be justified by the presence of free hydroxyl groups in its structure, as discussed in the P-NMR (**Figure** 4.**1**d) and XPS analyses (**Figure 4.1**g). On the other hand, the WSF has less hydroxyl and more Si-C and F end groups in its structure, contributing to its limited water uptake [56]. The superhydrophobicity of WSF arises from its low surface energy, which is achieved through copolymerization with WAPFSS. The copolymerization process altered the hydrophilic properties of the hydroxyl groups in lignin, converting them into Si-O-C groups (**Figure 4.1**g). The copolymerization also resulted in abundant Si-O-Si bonds and C-F end groups on the lignin, as confirmed by the FTIR and XPS (**Figure 4.1**f-i) analyses. Si and F electronegativity in the material created a low surface energy environment, which enhanced its affinity to attract electrons. Consequently, the material's surfaces exhibited a reduced interaction with water molecules, leading to its superhydrophobicity [57-61].

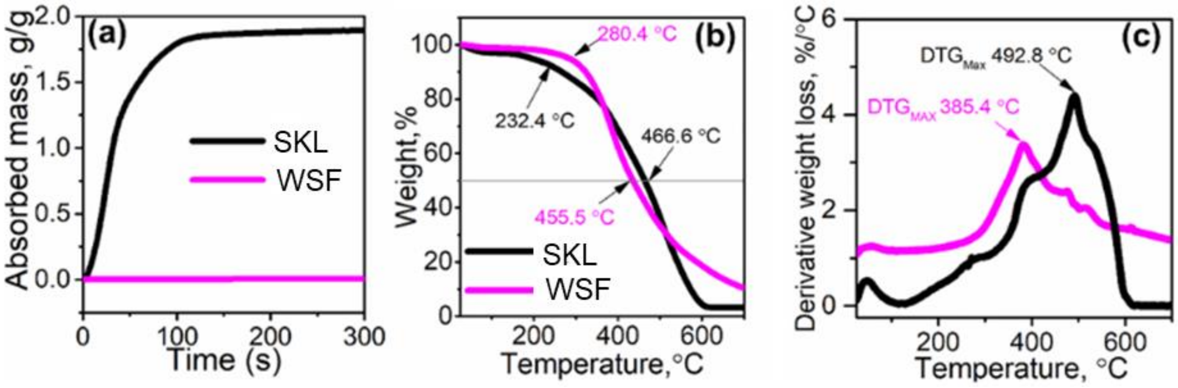

Figure 4.2. Powder water wettability (a), thermogravimetric curves (b), and differential thermogravimetric curves(c) of SKL and WSF.

4.4.1.3. Thermal Properties of Lignin Derivatives

The thermal characteristics of SKL and WSF were examined using TGA, and the findings are displayed in **Figure 4.2**b and 4.**2**c. The temperature at which thermal deterioration begins (onset temperature, T_o), the temperature at which 50% of the weight is lost ($T_{50\%}$), and the highest temperature at which maximum degradation occurs (DTG_{max}) are important parameters to consider for the thermal analysis of the material. The T_o of WSF was 24°C higher than that of SKL, whereas the $T_{50\%}$ and DTG_{max} of SKL were 11°C and 107.4°C higher than those of WSF, respectively. Following the DTG_{max}, the degradation of SKL occurred quicker than that of WSF. Additionally, the final ash content of SKL was negligible, whereas WSF contained 18% ash. The increase in T_o and percentage weight residue can be attributed to an inorganic component (Si) originating from the lignin macrostructure, as demonstrated by NMR, XPS, and FTIR analysis (**Figure 4.1**).

4.4.2. Properties of Lignin-Rubber Films

4.4.2.1. Mechanical Properties

The change in the mechanical properties of NR and NR-lignin films is examined, and the results are shown in **Figure 4.3**a-b. Incorporating WSF polymers up to 20 wt.% in the NR films showed a significant increase in tensile strength and percentage elongation compared with pure NR. However, further increases in the WSF (W30) concentration showed a decrease in strain. This is attributed to an aggregation of WSF particles in the NR structure at this concentration. W20 samples show a higher strain than K20. The deficiency of SKL is attributed to the polar functional moiety in the SKL structure, yielding its poor dispersion in the hydrophobic rubber matrix [62]. Similarly, W20 in the rubber matrix showed a significant improvement in tensile strength to ~13 MPa (**Figure 4.3**b), i.e., an 81% increase compared to the pure NR sheet and a 58% increase compared to K20. Such results confirm better dispersibility of modified lignin samples, which imparts superior mechanical properties to the elastomeric matrix because the copolymerization results in strong hydrophobic interactions between WSF and NR (**Figure 4.4**).

4.4.2.2. Surface Morphology

The morphology of pure NR and NR-lignin film was investigated using SEM, and the results are presented in **Figure S4.3**. In the micrograph of the surface of the NR sample, it is observed that the surface is planar with some cavities. The samples of W10 and W20 showed denser surfaces without holes and cavities. This analysis indicates better compatibility of WSF (i.e., hydrophobic particles) than the K20 sample dispersed throughout the NR matrix.

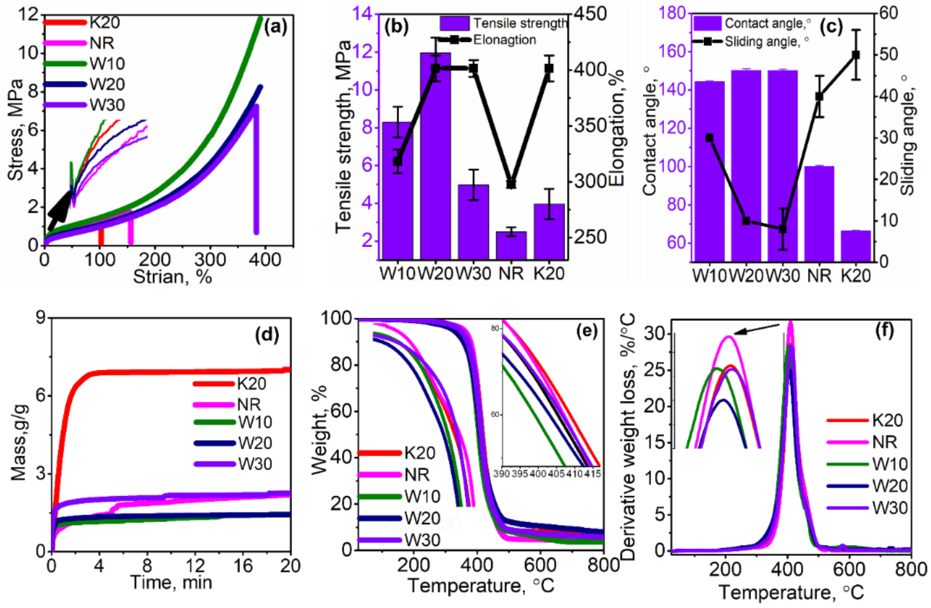

Figure 4.3. Stress-strain curve (a), tensile strength and percentage elongation (b), water contact angle (c), water absorption (d), FTIR transmittance spectra (e), TGA (g), and DTGA (h) of NR and NR-lignin films at different concentrations of WSF (W10-30) and SKL (K20).

However, the W30 sample showed a very rough surface with holes and smaller particles on the surface. The results confirmed that the smooth surface of the NR film had transformed into a rough surface due to the incorporation of WSF, which met the condition for achieving superhydrophobicity [63].

4.4.2.3. Water Contact Angle and Water Absorption Performance

The static contact angle and sliding angle of water droplets on the NR and NR-lignin films were measured, and the results are presented in **Figure 4.3**c. The contact angle of NR was around 100°, and the sliding angles were around 40°. The introduction of 10% WSF showed a drastic increase in contact angle by 45° and a sliding angle by 20°. Furthermore, the increased concentration of WSF to 30% resulted in a superhydrophobic surface with a contact angle of >150°and a sliding angle of <10°. This property is attributable to the hydrophobic nature of WSF, as seen by its limited water absorption (**Figure 4.2**a). The reduction in the hydroxyl group of WSF (**Table S4.1**) and the presence of lower surface energy structures, like Si-O-Si and C-F, would make the WSF-containing films superhydrophobic [64]. On the contrary, K20 showed a reduced contact angle value of 55°, attributed to the presence of hydroxyl, carboxyl, and phenolic groups in SKL (**Table S4.1**) that would increase the polarity and hydrophilicity of rubber films [65].

The water absorption of NR and NR-lignin films is recorded by tensiometer, and the absorbed water mass is depicted in **Figure 4.3**d. NR film absorbed around 24% of its weight in the first 15h of immersion in water. The introduction of up to 20 % WSF in NR films reduced water uptake. This is correlated with the hydrophobicity imparted by the WSF samples to the composite (**Figure 4.2**a). The lowest water absorption was for the W20 sample, as hydrophobic WSF particles may have occupied microvoids, leaving less free volume for water to contact the rubber molecules (**Figure 4.3)**. This is also supported by the lower diffusion coefficient value of 0.001 mm^2/s in **Table 4.1**. For W30 samples, the increased water uptake was followed by the improved water diffusion coefficient (**Table 4.1)**, which might be attributed to the capillary diffusion of water molecules to the NR matrix activated by the presence of voids presented in the W30 morphology of the films (**Figure S4.3**). On the other hand, K20 showed the highest water uptake value (7 g/g), which is consistent with the lowest water contact angle value (**Figure 4.3**c) and attributed to the hydrophilicity of the SKL sample (**Figure 4.2**a).

4.4.2.4. Structural Analysis

FTIR was used to analyze the NR and NR-lignin film structure (**Figure S4.4**a). The strong peaks with the highest intensity at 2960, 2918, and 2850 cm^{-1} correspond to the stretching vibration of the CH_3, CH_2, and CH groups in the cis-1,4-polyisoprene macromolecules [66]. However, the lignin particles also revealed a small shift in this wavenumber range for the samples containing SKL and WSF. This is due to the presence of methylene and methyl molecular compounds in the lignin structure (**Figure 4.1**e). The strong peak around 1640 and 1594 cm^{-1} is attributed to C=C in the rubber chain and the symmetric aromatic skeletal vibration indicated by lignin macromolecules, respectively. The signals for CH_3 deformation at 1450 cm^{-1}, C-O-C deformation at 1350 cm^{-1}, and CH deformation at 1200–900 cm^{-1} were observed. The vibration of the CH wagging band appeared at 835 cm^{-1} in the rubber chains [67]. Moreover, the peaks between 3600 and 3150 cm^{-1} associated with OH stretching were noticed.

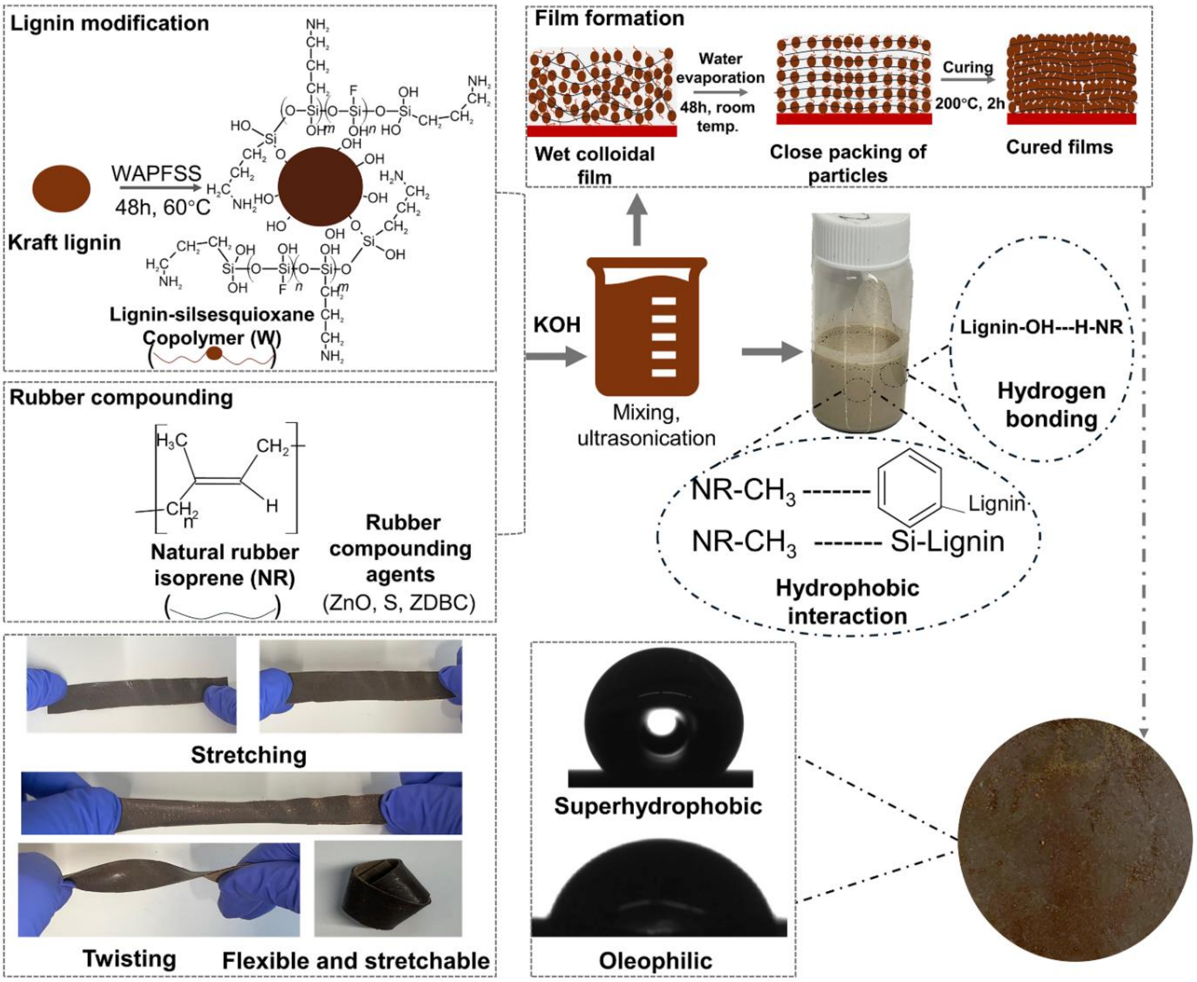

Figure 4.4. Schematic illustration of the process for lignin-silsesquioxane-natural rubber film fabrications.

The appearance and intensity of those bonds increased with the concentration of the WSF polymer in the NR composite. The FTIR spectra of all the samples demonstrated similar profiles, given that a higher concentration of rubber molecules exists in each film. The major difference in the FTIR spectra of the samples is the presence of aromatic skeletal vibration in samples containing WSF and SKL, while those peaks are not present in pure NR. Additional differences were associated with the varying intensity and slight shift in the characteristic's peaks. The WSF-containing samples show a distinctive peak around 1200 cm^{-1} and 1162 cm^{-1}, identified as the Si-O-Si and C-F vibrating bonds, like WSF (**Figure 4.1**e). Furthermore, the intensity of the OH stretching vibration decreased when the concentration of WSF increased. The interaction between the lignin units and the natural rubber chain can be explained in the FTIR results. The intensive peak at 1603 cm^{-1} and strong peak at 1515 cm^{-1} were related to the symmetric aromatic skeletal vibration and aryl ring stretching indicated by lignin molecules, respectively, which were shifted to 1594 cm^{-1} and 1506 in the NR-lignin spectra. This shift indicates a non-covalent interaction between the NR chains and lignin due to the interaction of NR and lignin molecules.

4.4.2.5. Thermal Stability

The thermal stability of the NR and NR-lignin film was assessed by TGA and presented in **Figure 4.3**e-f. The T_o, $T_{50\%}$, and DTG_{max} are shown in **Table 4.1**. The thermal degradation profile of all the samples closely resembles that of the NR film. This is anticipated because NR maintained the largest concentration in all the films. As seen in **Table 4.1**, upon careful examination of the data, it is evident that the incorporation of WSF increased the T_o, $T_{50\%}$, and DTG_{max} values compared to pure NR. This increase in the thermal stability followed the concentration increase of WSF in the films. The improved thermal stability of WSF-containing NR films is attributed to the incorporation of lignin, with its rich aromatic structure and higher thermal stability (**Figure 4.2**b-c) [68]. Similarly, the $T_{o,}$ $T_{50\%,}$ and DTG_{max} of K20 were much higher than those of NR between K20 and W20. Except T_o, other thermal properties, such as $T_{50\%}$ and DTG_{max}, were higher for K20 than W20, which is consistent with the thermal characteristics of SKL and WSF, as discussed in section 5.4.1.3 (**Figure 4.2**b-c).

Table 4.1. Onset temperature (T_o), the temperature at which 50 wt.% is lost ($T_{50\%}$), the highest temperature at which degradation occurs (DTGmax), wt.% of residue at 800°C, and diffusion coefficient.

Samples	**T_o,°C**	**$T_{50\%}$,°C**	**DTG_{max},°C**	**Residue weight, wt.% at 800°C**	**D, mm^2/s**
K20	325.3	401.6	410.8	6.6	0.005
NR	273.3	400.6	409.9	3.5	0.001
W10	313.1	391.3	402.9	3.6	0.001
W20	327.8	394.5	406.8	7.9	0.001
W30	354.3	398.7	411.4	5.8	0.075

4.4.3. Durability of Lignin-Rubber Films

The mechanical properties and surface hydrophobicity of NR and NR-lignin films after water and thermal treatment were assessed and the results are presented in **Figure 4.5**a-e. The mechanical properties of pure NR films deteriorated after exposure to water (**Figures 4.5**a and **4.5**c).

This could be caused by hydrolysis, swelling, and leaching of the rubber components when immersed in water. The reaction of water with rubber molecules, breaking the polymer chains and reducing the rubber's molecular weight and crosslink density, decreases mechanical properties [69].

The tensile strength of W10 samples dropped by 60% after water immersion, which was 10% better than that of pure NR. The increase in the WSF concentration in the NR films reduced the impact of the water treatment on mechanical properties, as can be seen by only a 10% drop in tensile strength for the W30 sample. This result is attributed to the hydrophobic nature of WSF present in NR films (**Figure 4.2**a and **Figure 4.3**c). The hydrophilic nature of SKL would lead to the wetting of the films and the leakage of SKL into water. The leakage of SKL would form voids in the structure of the NR film and the disassociation of rubber molecules.

On the other hand, swelling increases the volume and decreases the density and tensile strength of the rubber, while leaching facilitates the loss of soluble components [70]. As a result, the film becomes fragile and exhibits poor mechanical properties. On the other hand, water swelling can cause rubber's physical expansion due to water absorption by comparatively hydrophilic polymers, such as SKL, which can increase the volume and weight of rubber but decrease the elongation at break. As a result, using highly hydrophobic polymers, such as WSF, reduced water absorption in the NR matrix, resulting in lower swelling and higher elongation at break when compared to its SKL counterpart and pure NR. The mechanical characteristics of the NR and NR-lignin films are presented after thermal treatment in **Figure 4.5**b-d. In general, subjecting the NR and NR-lignin films to heat treatment significantly reduced the mechanical characteristics of all the samples. Pure NR films' tensile strength and elongation at break after thermal treatment decreased by 80% and 96%, respectively, compared to untreated counterparts. In contrast, W20 tensile strength and elongation at break were reduced by 63% and 86%, respectively (**Figure 4.3**b). This indicates that incorporating WSF in the NR films would help resist thermal aging. The negative influence of thermal aging on the mechanical properties of the NR films decreased with the increase in the WSF concentration (**Figure 4.5**b-d). Conversely, the heat treatment caused significant decreases of 94% and 95% in the tensile strength and elongation percentage of K20 film, respectively, compared to the untreated counterpart. This reduction is even greater than the impact of thermal treatment on NR properties.

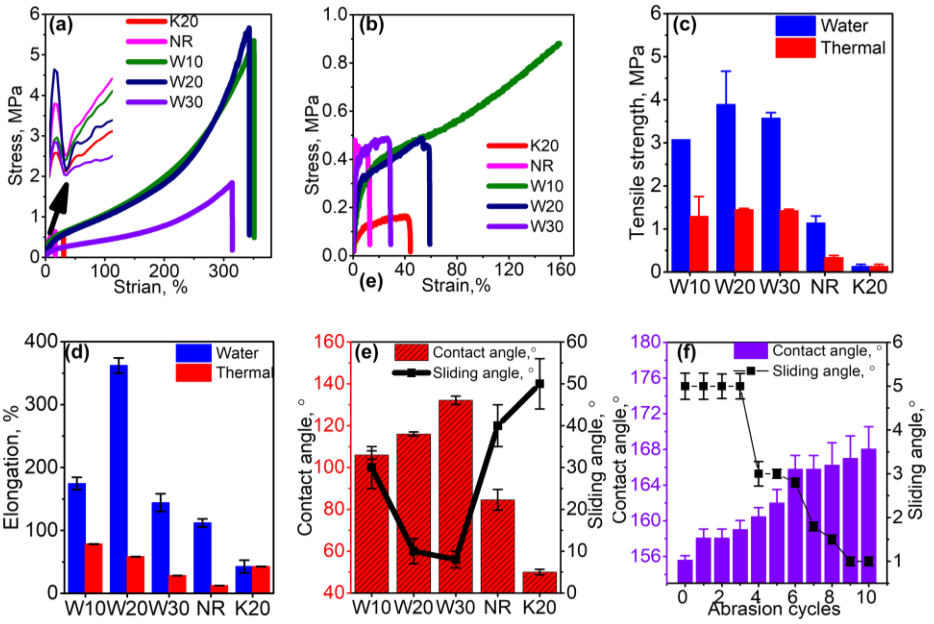

Figure 4.5. Stress versus strain of samples after water treatment (a), thermal treatment (b), tensile strength (c), percentage elongation after water (72h) and thermal treatment (120°C for 24 h) (d), water contact angle after thermal treatment (e) and water contact angle after sandpaper abrasion (g).

The heat resistance of NR films is likely due to the restricted distribution of SKL inside the NR matrix, causing it to aggregate within the NR structure. This aggregation creates a surface susceptible to thermal damage (**Figure S4.3**). The elongation at the break following heat treatment appears to be impacted more significantly than the tensile strength. The decrease in elasticity is attributed to the decreased mobility of the elastomeric components caused by the strong interactions between fillers and the inclusion of the stiff lignin component in the matrix. In addition, the interconnected chains of natural rubber (NR) cannot separate, resulting in premature rupture when subjected to tensile force and reduced elongation at the fracture point [71]. The young modulus for NR films increased slightly with the addition of WSF, attributed to the incorporation of higher amounts of rigid lignin in soft elastomeric matrix and stronger filler-filler interactions (**Figure S4.4**b) [72].

When the concentration of WSF increased to 30%, the young modulus dropped. After thermal treatment, the modulus of the composite’s films decreased drastically, implying the rubber molecules' chemical degradation. On the contrary, the modulus of all the films increased after water absorption treatment. The water contacts and sliding angles were analyzed on the thermally aged samples (**Figure 4.5**e). The water contact angle decreased for all the samples following thermal treatment. Thermal treatment is reported to introduce polar functional groups, such as carbonyl groups, during the thermal treatment due to oxidation, increasing the surface energy and leading to higher wettability [73].

The chemical structure of the NR and NR-lignin film change after thermal treatment was investigated using FTIR. Results are presented in **Figure S4.4**c. The chemical bond of C=C and OH stretching transmittance between the isoprene units showed a significant reduction in the intensity for the NR films thermally treated compared to prepared samples (**Figure S4.4**a). The C=C bond breaks and rearranges at high temperatures, forming shorter chains with oxygen-containing functional groups. This change creates a broader peak of the carbonyl band in the region of 1679-1800 cm^{-1}. There is an apparent formation of carbonyl functionality in the thermally treated films. The FTIR spectra of pure NR and W10 film show a very broad and deep peak after thermal treatment, while W20 and K20 show smaller peaks.

In contrast, the higher concentration of WSF prevents the conversion of C=C to C-O by acting as a radical scavenger and a thermal stabilizer for the natural rubber matrix. The presence of phenolic hydroxyl groups and aromatic rings in SKL and WSF (**Figure 4.1**d and **Table S4.1**) can donate hydrogen atoms or electrons to quench the free radicals generated during the thermal oxidation of natural rubber. This can prevent chain scission and crosslinking reactions leading to the deterioration of the natural rubber films [74]. The OH stretching reduction can be explained by the degradation process involving the OH radicals that react with isoprene molecules of the rubber structure.

To investigate the durability of the superhydrophobicity of the film, the W20 samples, as the best samples, were subjected to abrasion, and the film's water contact angle was measured. The results are presented in **Figure 4.5**f. The water contact angle increased with the increase in the abrasion cycle while the sliding angle decreased. The durability of superhydrophobic natural rubber surfaces is always indicated as a bottleneck for applications such as coating, and with the abrasion cycle increasing, the water contact angle generally drops. However, these reports are only concerned with superhydrophobic surfaces achieved by surface coating [75, 76]. In our case, the superhydrophobic films were generated by incorporating a highly hydrophobic polymer (WSF) inside the NR matrix. Therefore, when the abrasion removes/breaks the NR matrix, the WSF polymer particle will be more exposed on the surfaces. Thus, a higher water contact angle and lower sliding angle were achieved. This can be further supported by the decreased water contact angle when pure NR was subjected to abrasion (**Figure S4.5)**.

The cyclic tensile experiment was conducted on W20 films to quantify the stretchable and twistable characteristics of the film (**Figure 4.4**) by investigating the mechanical hysteresis behavior of the W20 sample at different strains, as shown in **Figure 4.6**a.

The composite exhibited increased stress with increasing strain, followed by rapid recovery to the initial value upon decreasing strain. The stress-strain curve shows minimal changes even after 10 cycles, indicating excellent repeatability and stability of the composite. The stability of W20 superhydrophobicity under stress was investigated, as shown in **Figure 4.6**b, to determine possible applications for these films. The films remained superhydrophobic at different strain percentages of 10, 20, 40, and 60 % elongation, as evidenced by the droplet profiles in **Figure 4.6**b.

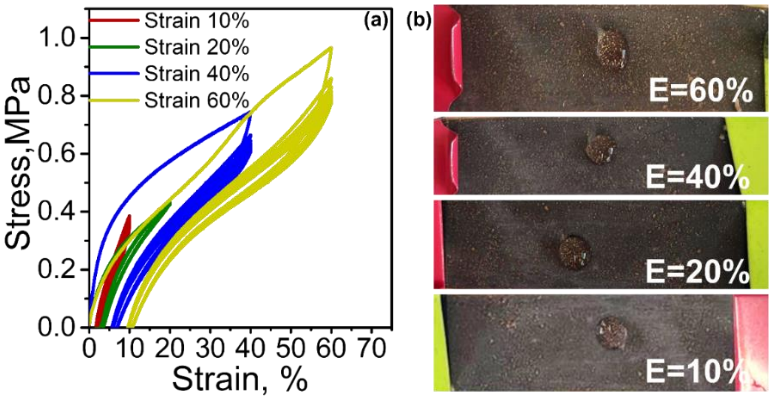

Figure 4.6. The tensile recovery curves (a), and water droplet profile at difference percentage elongation (b), of W20 films.

The water droplet stands on the W20 surface, keeping its aspherical shape even after 60% elongation. It exhibited excellent water repellence, further corroborating the robust superhydrophobicity of W20. The cyclic tensile experiment and the superhydrophobicity at different elongation percentages indicated that the film could withstand repetitive strains while maintaining its hydrophobic characteristics.

4.4.4. Oil Adsorption and Oil and Water Separation Efficiency

The oil contact angle on NR and NR-lignin film surfaces was measured and reported in **Figure 4.7**a. The film's oil contact angle values in **Figure 4.7**a were lower than the water contact angle values (**Figure 4.3**c). NR films exhibited an oil contact angle of around 40°, while W10 films had a lower contact angle of 21°. This is attributed to the robust nonpolar characteristic of incorporating silane-grafted lignin (WSF sample) in NR film, which facilitates its interaction with oil. Nevertheless, the rise in WSF concentration reduced the contact angle however not lower than NR.

This result may be attributed to the morphology of the films. This superhydrophobic but lipophilic characteristic of WSF films is ideal for separation and purification, especially for oil and water separation. On the other hand, the K20 sample had an oil contact angle of 32°, close to that of the water contact angle value (**Figure 4.3**c), making this sample challenging for oil and water separation applications. The oil adsorption by the NR and NR-lignin films was assessed using a tensiometer, and reports are depicted in **Figure 4.7**b. The oil adsorption capacity of K20 was significantly greater than that of NR and W20.

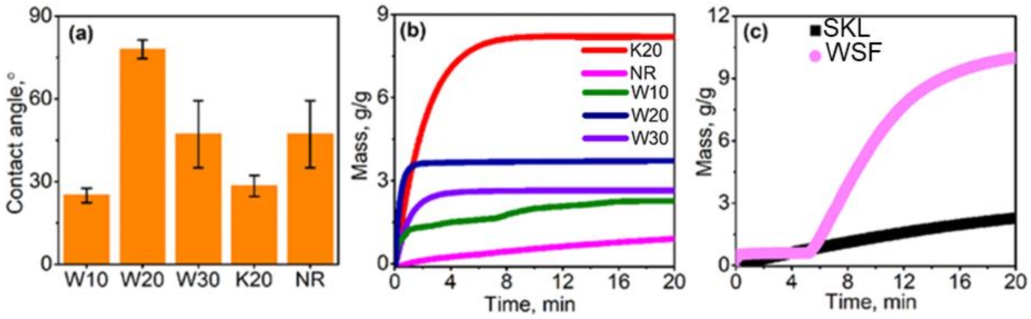

Figure 4.7. Oil contact angle (a), oil adsorption from tensiometer analysis of the films (b), and oil adsorption by SKL and WSF powders (c).

The WSF powders exhibited a markedly greater oil adsorption capacity than SKL (**Figure 4.7**c), attributed to more robust aliphatic chains of WSF than SKL (**Figure 4.1**a-b). Therefore, increased oil adsorption by K20 compared to W20 can be due to the morphology of films and not related to the hydrophobicity of samples (**Figure 4.3**f). Perhaps the larger aggregates of K in NR resulted in greater exposure to the oil interphase. In contrast, the well-dispersed WSF was exposed to a lesser extent. It is also worth recalling that K20 films absorbed more water than W20 (**Figure 4.3**d), which makes K20 applications in oil-water separation ineffective since the selective absorption ratio of oil/water is critical. This ratio was 2.85 wt./wt. for W20, 1.0 wt./wt. for NR and 1.05 wt./wt. for SKL20%, suggesting that W20 was suitable for oil-water separation while other samples were unsuitable (**Figure 4.7**b and **4.7**c).

4.5 Comparison

The W20 sample shows superior water contact angle, oil contact angle, and oil adsorption capacity compared to natural rubber-based oil adsorbents reported in the literature, as shown in **Table 4.2**. Furthermore, W20 surpasses the performance of other lignin-containing natural rubber-based films in terms of lignin concentrations, water contact angle, water absorption, and tensile strength (**Table 4.2)**. According to **Equation 4.1,** the percentage of pure lignin in the lignin polymer was approximately 50%, resulting in a 10 wt.% pure lignin in W20. These results are far better than those of the previously documented natural rubber films **(Table 4.2)** that included lignin because they contained more lignin in the formulation, and the formulation contained more natural materials and functioned more effectively. In addition, the stability and repeatability of the W20 sample (**Figure 4.6**a) exhibiting minimal changes in stress-strain values after 10 cycles confirm the durability of this sustainable NR film. Thus, the results demonstrated a promising method for generating superhydrophobic natural rubber specifically for oil-water separation.

Table 4.2. Summary of existing literature on natural polymers-based oil adsorbents compared to this study

Material	**Preparation method**	**Water contact angle, °**	**Maximum lignin concentration wt.%**	**Oil contact angle, °**	**WCA (°) after abrasion (ab, no)**	**Oil adsorption mass, g/g**	**Water uptake, %**	**Tensile strength change, %**	**Reference**
Graphene oxide, natural rubber	Graphite oxidation, latex mixing	83°	×	×	×	12	×	×	[77]
Chitosan, epoxidized natural rubber	Natural rubber epoxidation, latex mixing	×	×	×	×	1.5	×	×	[78]
Silica-lignin hybrid, natural rubber	Precipitation method from rice husk waste	133°	0.15	×	×	1.36	×	×	[79]
Silane-kraft lignin, natural rubber	Lignin modification, latex mixing	×	10	×	×	×	9	8.3	[16]
Amine-kraft lignin, carbon black, natural rubber	Lignin modification, Sheet formulation	×	4	×	×	×	×	-5.0	[39]
Carboxylate lignin, natural rubber	Lignin fractionation, latex mixing	95	15	×	×	×	×	5.9	[80]
Silsesquioxane-kraft lignin, natural rubber film	Lignin polymerization, latex mixing	155°	20	60°	168°, ab>10	3.2	14	81	This work

"×" denotes the values not reported in the papers discussed.

4.6. Conclusion

The incorporation of kraft lignin (SKL) copolymerized with aminopropyl/flurosilsesquioxane (WAPFSS) into natural rubber (NR) to improve its mechanical and water-repellence was investigated in this study. The copolymerized sample (WSF) was generated in an aqueous medium via polycondensation reaction, and some of the hydroxyl groups of lignin were converted to Si-O-C linkages as confirmed by NMR, XPS, and FTIR. The ^{31}P-NMR results also indicated the hydroxyl group of lignin dropped from 6.83 mmol/g in K to 3.47 mmol/g in WSF. The copolymerization reduced the water absorption tendency of WSF, as confirmed by the tensiometer. The tensile strength and Young's modulus measurements suggest that the reinforcing potential of WSF was significantly larger than that of SKL. The NR films' water contact angle increased as the WSF concentration increased. Additionally, the tensile strength of the films increased with concentrating WSF up to 20 wt.% (W20). Moreover, the W20 sample had superior mechanical and water-repellent characteristics before and after thermal and water treatments to pure NR and KL20% samples. This was attributed to the more homogeneous dispersion and interaction of hydrophobic WSF and NR matrix as observed by SEM. The W20 film was superhydrophobic with a water contact angle of >150° and a sliding angle of <10°. The superhydrophobic characteristics of W20 remained unaffected even after thermal exposure and sandpaper abrasion. WSF-containing NR films had a low contact angle for oil and a higher oil/water adsorption tendency. Due to its low water absorption, high oil adsorption, high thermomechanical properties, and durability, which were better than other those reported in previous studies, the lignin-incorporated NR can be used as a sustainable oil-water separator and oil spillage cleaning material.

4.7. References

1. Watari, T., et al., *Performance evaluation of the pilot scale upflow anaerobic sludge blanket – Downflow hanging sponge system for natural rubber processing wastewater treatment in South Vietnam*. Bioresour. Technol., 2017. **237**: p. 204-212. https://doi.org/10.1016/j.biortech.2017.02.058.
2. Onsri, P., et al., *Dual-functional natural rubber latex foam composites for solar-driven clean water production and heavy metal decontamination*. International Journal of Biological Macromolecules, 2024. **273**: p. 133056. https://doi.org/10.1016/j.ijbiomac.2024.133056.
3. Sisanth, K.S., et al., *General introduction to rubber compounding*, in *Progress in rubber nanocomposites*. 2017, Elsevier. p. 1-39.
4. Bokobza, L. and O. Rapoport, *Reinforcement of natural rubber*. J. Appl. Polym. Sci., 2002. **85**(11): p. 2301-2316. https://doi.org/10.1002/app.10858.
5. Zhang, G., et al., *Influence of a novel coupling agent on the performance of recovered carbon black filled natural rubber*. Compos. B. Eng., 2023. **255**: p. 110614. https://doi.org/10.1016/j.compositesb.2023.110614.
6. Parulekar, Y. and A.K. Mohanty, *Biodegradable toughened polymers from renewable resources: blends of polyhydroxybutyrate with epoxidized natural rubber and maleated polybutadiene*. Green Chem., 2006. **8**(2): p. 206-213. https://doi.org/10.1039/B508213G.
7. Stickney, P.B. and R.D. Falb, *Carbon black-rubber interactions and bound rubber*. Rubber Chem.Technol., 1964. **37**(5): p. 1299-1340. https://doi.org/10.5254/1.3540401.

8. Chang, B.P., et al., *Bioresourced fillers for rubber composite sustainability: current development and future opportunities*. Green Chem., 2021. **23**(15): p. 5337-5378. https://doi.org/10.1039/D1GC01115D
9. Liu, R., et al., *Lignin -based micro -and nanomaterials and their composites in biomedical applications*. ChemSusChem, 2020. **13**(17): p. 4266-4283. https://doi.org/10.1002/cssc.202000783.
10. Zhang, G., et al., *Mechanically Robust, Self-Repairable, Shape Memory and Recyclable Ionomeric Elastomer Composites with Renewable Lignin via Interfacial Metal–Ligand Interactions*. ACS Appl. Mater. Interfaces, 2022. **14**(33): p. 38216-38227. https://doi.org/10.1021/acsami.2c10731.
11. Wu, R.-L., et al., *Green composite films prepared from cellulose, starch and lignin in room-temperature ionic liquid*. Bioresour.Technol., 2009. **100**(9): p. 2569-2574. https://doi.org/10.1016/j.biortech.2008.11.044.
12. Argyropoulos, D.D.S., et al., *Kraft Lignin: A Valuable, Sustainable Resource, Opportunities and Challenges*. ChemSusChem, 2023. **16**(23): p. e202300492. https://doi.org/10.1002/cssc.202300492.
13. Jiang, C., et al., *Nano-lignin filled natural rubber composites: Preparation and characterization*. Express Polym. Lett., 2013. **7**(5). https://doi.org/10.3144/expresspolymlett.2013.44.
14. Qiu, J., et al., *Study on lignin amination for lignin/SiO2 nano-hybrids towards sustainable natural rubber composites*. Int. J. Biol. Macromol., 2023. **233**: p. 123547. https://doi.org/10.1016/j.ijbiomac.2023.123547.
15. Zhao, Z.M., et al., *Emerging strategies for modifying lignin chemistry to enhance biological lignin valorization*. ChemSusChem, 2020. **13**(20): p. 5423-5432. https://doi.org/10.1002/cssc.202001401.
16. Shorey, R., A. Gupta, and T.H. Mekonnen, *Hydrophobic modification of lignin for rubber composites*. Ind. Crops Prod., 2021. **174**: p. 114189. https://doi.org/10.1016/j.indcrop.2021.114189.
17. Mente P, M.T., Hlangothi and SP, *Natural rubber and reclaimed Rubber composites–A Systematic Review*. Polymer, 2016. **2**(7). https://doi.org/10.4172/2471-9935.100015.
18. Azhar, N.N.H., et al., *Thermal and photo oxidative degradation of natural rubber film in the presence of iron (III) stearate*. J. Polym. Res., 2022. **29**(11): p. 476. https://doi.org/10.1007/s10965-022-03316-8.
19. Ibrahim, S., et al., *Preparation and characterization of low-molecular-weight natural rubber latex via photodegradation catalyzed by nano TiO2*. Polymers, 2018. **10**(11): p. 1216. https://doi.org/10.3390/polym10111216.
20. Flaifel, M.H., et al., *Thermal conductivity and dynamic mechanical analysis of NiZn ferrite nanoparticles filled thermoplastic natural rubber nanocomposite*. Compos. B. Eng., 2013. **52**: p. 334-339. https://doi.org/10.1016/j.compositesb.2013.04.021.
21. Lizundia, E., et al., *Multifunctional lignin-based nanocomposites and nanohybrids*. Green Chem., 2021. **23**(18): p. 6698-6760. https://doi.org/10.1039/D1GC01684A.
22. Gregorova, A., B.K. Kosikova, and R. Moravcik, *Stabilization effect of lignin in natural rubber*. Polym. Degrad. Stab., 2006. **91**(2): p. 229-233. https://doi.org/10.1016/j.polymdegradstab.2005.05.009.
23. Zhao, W., et al., *Use of lignin-based crude carbon dots as effective antioxidant for natural rubber*. International Journal of Biological Macromolecules, 2023. **253**: p. 126594. https://doi.org/10.1016/j.ijbiomac.2023.126594.
24. Wang, T., et al., *Development of biomass aerogels with aligned channels: For continuous treatment of oily wastewater and solar-powered oil evaporation*. Bioresour. Technol., 2024. **412**: p. 131344. https://doi.org/10.1016/j.biortech.2024.131344.

25. Mohammadiun, S., et al., *Intelligent computational techniques in marine oil spill management: A critical review.* J. Hazard. Mater., 2021. **419**: p. 126425. https://doi.org/10.1016/j.jhazmat.2021.126425.
26. MacIntosh, A., et al., *Ecotoxicological effects of decommissioning offshore petroleum infrastructure: A systematic review.* Crit. Rev. Environ. Sci. Technol. , 2022. **52**(18): p. 3283-3321. https://doi.org/10.1080/10643389.2021.1917949.
27. Gupta, R.K., et al., *Oil/water separation techniques: a review of recent progresses and future directions.* J. Mater. Chem. A, 2017. **5**(31): p. 16025-16058. https://doi.org/10.1039/C7TA02070H
28. Zhang, J., et al., *Hierarchical bio-inspired design and fabrication of all-dimensional superhydrophobic ultra-lightweight high-volume fly ash cement foams using novel ultrasonic-assisted siloxane-encapsulated pickering emulsions.* Compos. B. Eng., 2024. **282**: p. 111581. https://doi.org/10.1016/j.compositesb.2024.111581.
29. Ghamarpoor, R. and M. Jamshidi, *Synergistic effect of microwave assisted devulcanization of waste NBR rubber and using superhydrophobic/superoleophilic silica nanoparticles on oil-water separation.* Alex. Eng. J., 2023. **69**: p. 67-84. https://doi.org/10.1016/j.aej.2023.02.002.
30. Saengkaew, J., et al., *Superhydrophobic coating from fluoroalkylsilane modified natural rubber encapsulated SiO2 composites for self-driven oil/water separation.* Appl. Surf. Sci., 2018. **462**: p. 164-174. https://doi.org/10.1016/j.apsusc.2018.08.059.
31. Ghamarpoor, R. and M. Jamshidi, *Silanizing nano SiO2 and its application in recycled nitrile rubber to prepare super oil resistant/superhydrophobic/superoleophilic oil/water separator.* J. Environ. Chem. Eng., 2022. **10**(3). https://doi.org/10.1016/j.jece.2022.107971.
32. Tao, J., et al., *Fabrication of room temperature self-healing, robust superhydrophobic coatings via spraying dual cross-linking supramolecular silicone polymer/SiO2 composite.* Composites Part B: Engineering, 2024. **273**: p. 111245. https://doi.org/10.1016/j.compositesb.2024.111245.
33. Meng, X., et al., *Determination of hydroxyl groups in biorefinery resources via quantitative 31P NMR spectroscopy.* Nat. Protoc., 2019. **14**(9): p. 2627-2647. https://doi.org/10.1038/s41596-019-0191-1.
34. Johansson, L.-S., et al., *Evaluation of surface lignin on cellulose fibers with XPS.* Appl. Surf. Sci., 1999. **144**: p. 92-95. https://doi.org/10.1016/S0169-4332(98)00920-9.
35. Alwadani, N., N. Ghavidel, and P. Fatehi, *Surface and interface characteristics of hydrophobic lignin derivatives in solvents and films.* Colloids Surf., 2021. **609**: p. 125656. https://doi.org/10.1016/j.colsurfa.2020.125656.
36. Rostami, M., M. Mohseni, and Z. Ranjbar, *An attempt to quantitatively predict the interfacial adhesion of differently surface treated nanosilicas in a polyurethane coating matrix using tensile strength and DMTA analysis.* Int. J. Adhes. Adhes., 2012. **34**: p. 24-31. https://doi.org/10.1016/j.ijadhadh.2011.12.005.
37. Deng, Y., et al., *Preparation and relationship between structure and properties of PTMEG based polyurethane acrylate UV cured films.* J. Macromol. Sci. , 2023. **60**(1): p. 63-70. https://doi.org/10.1080/10601325.2022.2149340.
38. Yang, Y., et al., *Renewable vanillin-based thermoplastic polybutadiene rubber: high strength, recyclability, self-welding, shape memory, and antibacterial properties.* ACS Appl. Mater. Interfaces, 2022. **14**(41): p. 47025-47035. https://doi.org/10.1021/acsami.2c13339.
39. Chung, J.-Y., et al., *Amine-functionalized lignin as an eco-friendly antioxidant for rubber compounds.* ACS Sustain. Chem. Eng., 2023. **11**(6): p. 2303-2313. https://doi.org/10.1021/acssuschemeng.2c05878.
40. Wang, J.W., et al., *Preparation strategy and evaluation method of durable superhydrophobic rubber composites.* Adv. Colloid Interface Sci., 2022. **299**. https://doi.org/10.1016/j.cis.2021.102549.

41. Nagy, M., et al., *Characterization of CO 2 precipitated Kraft lignin to promote its utilization.* Green Chem., 2010. **12**(1): p. 31-34. https://doi.org/10.1039/B913602A.
42. Riehle, N., et al., *Data on the synthesis and mechanical characterization of polysiloxane-based urea-elastomers prepared from amino-terminated polydimethylsiloxanes and polydimethyl-methyl-phenyl-siloxane-copolymers.* Data in brief, 2018. **18**: p. 1784-1794. https://doi.org/10.1016/j.dib.2018.04.083.
43. Zhao, C., et al., *Revealing Structural Differences between Alkaline and Kraft Lignins by HSQC NMR.* Ind. Eng. Chem. Res., 2019. **58**(14): p. 5707-5714. https://doi.org/10.1021/acs.iecr.9b00499.
44. Kazzaz, A.E., Z.H. Feizi, and P. Fatehi, *Grafting strategies for hydroxy groups of lignin for producing materials.* Green Chem., 2019. **21**(21): p. 5714-5752. https://doi.org/10.1039/C9GC02598G.
45. An, L., et al., *Fractionation of enzymatic hydrolysis lignin by sequential extraction for enhancing antioxidant performance.* Int. J. Biol. Macromol., 2017. **99**: p. 674-681. https://doi.org/10.1016/j.ijbiomac.2017.03.015.
46. Zhong, B., et al., *Surface modification of halloysite nanotubes by vulcanization accelerator and properties of styrene-butadiene rubber nanocomposites with modified halloysite nanotubes.* Appl. Surf. Sci., 2016. **366**: p. 193-201. https://doi.org/10.1016/j.apsusc.2016.01.084.
47. An, L., et al., *Fractionation of enzymatic hydrolysis lignin by sequential extraction for enhancing antioxidant performance.* Int. J. Biol. Macromol., 2017. **99**: p. 674-681. https://doi.org/10.1016/j.ijbiomac.2017.03.015.
48. Du, Y. and H. Liu, *Triazine‐Functionalized Silsesquioxane‐Based Hybrid Porous Polymers for Efficient Photocatalytic Degradation of Both Acidic and Basic Dyes under Visible Light.* ChemCatChem, 2021. **13**(24): p. 5178-5190. https://doi.org/10.1002/cctc.202101231.
49. Simon, S., A. Malik, and B. Kandasubramanian, *Hierarchical Electrospun Super-Hydrophobic Nanocomposites of Fluoroelastomer.* Mater. Focus, 2018. **7**(2): p. 194-206. https://doi.org/10.1166/mat.2018.1499.
50. Chen, W.-H., et al., *Silanization of solid surfaces via mercaptopropylsilatrane: a new approach of constructing gold colloid monolayers.* RSC Adv., 2014. **4**(87): p. 46527-46535. https://doi.org//10.1039/C4RA05583G
51. Chen, X., X. Wang, and D. Fang, *A review on C1s XPS-spectra for some kinds of carbon materials.* Fuller. Nanotub. Car. N. , 2020. **28**(12): p. 1048-1058. https://doi.org/10.1080/1536383X.2020.1794851.
52. Arefmanesh, M., et al., *Bromide-based ionic liquid treatment of hardwood organosolv lignin yielded a more reactive biobased polyol.* Ind. Eng.Chem. Res., 2020. **59**(42): p. 18740-18747. https://doi.org/10.1021/acs.iecr.0c03718.
53. Nikolenko, Y.M., et al., *Hydrolytic Lignin: It's Activated and Fluorinated Forms.* Key Eng. Mater., 2019. **806**: p. 100-105. https://doi.org/10.1016/j.matpr.2018.08.020.
54. da Silva Carvalho, V.A., et al., *A Metallo‐Silsesquioxane Synthesized from Cu (II) via a Cyanide Fe (III) Bridge: Synthesis and Application as an Electrochemical Sensor.* ChemistrySelect, 2024. **9**(30): p. e202401702. https:/doi.org./10.1002/slct.202401702.
55. Alghunaim, A., S. Kirdponpattara, and B.-m.Z. Newby, *Techniques for determining contact angle and wettability of powders.* Powder Technol., 2016. **287**: p. 201-215. https://doi.org/10.1016/j.powtec.2015.10.002.
56. Yan, Y.Y., N. Gao, and W. Barthlott, *Mimicking natural superhydrophobic surfaces and grasping the wetting process: A review on recent progress in preparing superhydrophobic surfaces.* Adv. Colloid Interface Sci., 2011. **169**(2): p. 80-105. https://doi.org/10.1016/j.cis.2011.08.005.
57. Ge, Q. and H. Liu, *Rational design and preparation of superhydrophobic photo-cured hybrid epoxy coating modified by fluorocarbon substituted silsesquioxane-based nanoparticles.* Prog. Org. Coat., 2022. **172**: p. 107089. https://doi.org/10.1016/j.porgcoat.2022.107089.

58. Foorginezhad, S. and M.M. Zerafat, *Fabrication of superhydrophobic coatings with self-cleaning properties on cotton fabric based on Octa vinyl polyhedral oligomeric silsesquioxane/polydimethylsiloxane (OV-POSS/PDMS) nanocomposite.* JCIS, 2019. **540**: p. 78-87. https://doi.org/10.1016/j.jcis.2019.01.007.
59. Kim, K., J.D. Lichtenhan, and J.U. Otaigbe, *Facile route to nature inspired hydrophobic surface modification of phosphate glass using polyhedral oligomeric silsesquioxane with improved properties.* Appl. Surf. Sci., 2019. **470**: p. 733-743. https://doi.org/10.1016/j.apsusc.2018.11.181.
60. Zheng, Z., et al., *Magnetic superhydrophobic polymer nanosphere cage as a framework for miceller catalysis in biphasic media.* ChemCatChem, 2014. **6**(6): p. 1626-1634. https://doi.org/10.1002/cctc.201400009.
61. Meng, L.-Y. and S.-J. Park, *Effect of fluorination of carbon nanotubes on superhydrophobic properties of fluoro-based films.* JCIS, 2010. **342**(2): p. 559-563. https://doi.org/10.1016/j.jcis.2009.10.022.
62. Intapun, J., et al., *The Characteristics of Natural Rubber Composites with Klason Lignin as a Green Reinforcing Filler: Thermal Stability, Mechanical and Dynamical Properties.* Polymers, 2021. **13**(7). https://doi.org/10.3390/polym13071109.
63. Latthe, S.S., et al., *Superhydrophobic surfaces developed by mimicking hierarchical surface morphology of lotus leaf.* Molecules, 2014. **19**(4): p. 4256-4283. https://doi.org/10.3390/molecules19044256.
64. Liu, Y., et al., *Preparation of a superhydrophobic coating based on polysiloxane modified SiO2 and study on its anti-icing performance.* Surf. Coat.Technol., 2022. **437**: p. 128359. https://doi.org/10.1016/j.surfcoat.2022.128359.
65. Notley, S.M. and M. Norgren, *Surface energy and wettability of spin-coated thin films of lignin isolated from wood.* Langmuir, 2010. **26**(8): p. 5484-5490. https://doi.org/10.1021/la1003337.
66. Ali, A.M.M., et al., *Grafted natural rubber-based polymer electrolytes: ATR-FTIR and conductivity studies.* Ionics, 2008. **14**: p. 491-500. https://doi.org/10.1007/s11581-007-0199-3.
67. Agrebi, F., et al., *Study of nanocomposites based on cellulose nanoparticles and natural rubber latex by ATR/FTIR spectroscopy: The impact of reinforcement.* Polym. Compos., 2019. **40**(5): p. 2076-2087. https://doi.org/10.1002/pc.24989.
68. Cao, Q., et al., *Novel lignin-cellulose-based carbon nanofibers as high-performance supercapacitors.* ACS Appl. Mater. Interfaces, 2019. **12**(1): p. 1210-1221. https://doi.org/10.1021/acsami.9b14727.
69. Gurjar, A.K., et al., *Investigation of mechanical properties of luffa fibre reinforced natural rubber composites: Implications of process parameters.* J. Mater. Res.Technol., 2024. **29**: p. 4232-4244. https://doi.org/10.1016/j.jmrt.2024.02.133.
70. Chen, Z.H., et al. *The effect of crosslink and reinforcement of hydroxymethylated kraft lignin on bromobutyl rubber II. Effect of the degree of lignin hydroxymethylation*. in *2nd International Symposium on Emerging Technologies of Pulping and Papermaking*. 2002. Guangzhou, Peoples R China.
71. Kim, D.Y., et al., *Correlation between the crosslink characteristics and mechanical properties of natural rubber compound via accelerators and reinforcement.* Polymers, 2020. **12**(9): p. 2020. https://doi.org/10.3390/polym12092020.
72. Mostafa, A., et al., *Rubber-filler interactions and its effect in rheological and mechanical properties of filled compounds.* J. Test. Eval., 2010. **38**(3): p. 347-359. https://doi.org/10.1520/JTE101942.
73. Do Nascimento, R.M., et al., *Thermal annealing of natural rubber films controls wettability and enhances cytocompatibility.* Surf. Coat. Technol., 2022. **31**: p. 102048. https://doi.org/10.1016/j.surfin.2022.102048.

74. Zhao, X., et al., *Melanin-inspired design: preparing sustainable photothermal materials from lignin for energy generation.* ACS Appl. Mater. Interfaces, 2021. **13**(6): p. 7600-7607. https://doi.org/10.1021/acsami.0c21256.
75. Zou, L., et al., *Superhydrophobic and superoleophilic polyethylene aerogel coated natural rubber latex foam for oil-water separation application.* Polym.Test., 2020. **85**. https://doi.org/10.1016/j.polymertesting.2020.106451.
76. Wimalasiri, V.K., et al., *Silica Based Superhydrophobic Nanocoatings for Natural Rubber Surfaces.* J. Nanomater., 2017. **2017**. https://doi.org/10.1155/2017/2102467.
77. Songsaeng, S., P. Thamyongkit, and S. Poompradub, *Natural rubber/reduced-graphene oxide composite materials: Morphological and oil adsorption properties for treatment of oil spills.* J. Adv. Res., 2019. **20**: p. 79-89. https://doi.org/10.1016/j.jare.2019.05.007.
78. Mosaku, A.M., et al., *Adsorptive remediation of oil spill contaminated water using chitosan modified natural rubber as adsorbent.* Chemistry Africa, 2021. **4**(3): p. 535-543. https://doi.org/10.1007/s42250-021-00243-x.
79. Mardiyati, Y., et al., *A Silica-Lignin Hybrid Filler in a Natural Rubber Foam Composite as a Green Oil Spill Absorbent.* Polymers, 2022. **14**(14). https://doi.org/10.3390/polym14142930.
80. Li, M., et al., *Design of a lignin-based versatile bioreinforcement for high-performance natural rubber composites.* ACS Sustain. Chem. Eng., 2022. **10**(24): p. 8031-8042. https://doi.org/10.1021/acssuschemeng.2c02113.

Chapter 5: Superhydrophobic, flame-retardant recyclable, and biodegradable lignin-polyurethane composite films

Banchamlak Bemerw Kassaun,[1] *Yu Liu,*[2] *Fangong Kong,*[2] *Pedram Fatehi**[1]

Under review in Chemical Engineering Journal

[1]Green Processes Research Center and Chemical Engineering Department, Lakehead University, 955 Oliver Road, Thunder Bay, ON P7B5E1, Canada

[2]State Key Laboratory of Biobased Material and Green Papermaking, Qilu University of Technology, Shandong Academy of Sciences, Jinan 250353, China

First Author, email: bkassaun@lakeheadu.ca, address: 955 Oliver Road, Thunder Bay, ON, Canada, P7B 5E1

Corresponding author, email: pfatehi@lakeheadu.ca, address: 955 Oliver Road, Thunder Bay, ON, Canada, P7B 5E1

The contribution of Banchamlak Bemerw Kassaun to this work was the conception of the original draft, visualization, validation, formal analysis, data curation, and conceptualization.

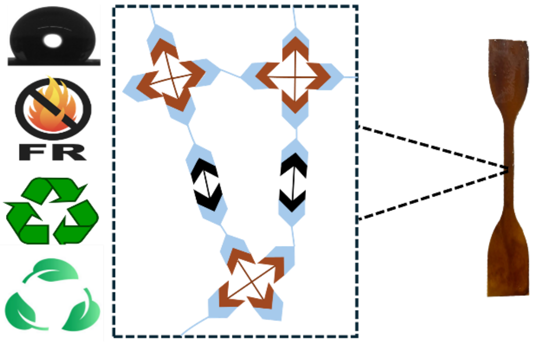

Keywords: Lignin, superhydrophobicity, flame retardancy, polyurethane, coatings

5.1. Abstract

Polyurethane (PU) is widely used in adhesive, foam, and coating applications. There is an urgent need to improve PU's hydrophobic, thermal, and flame-retardant performance while lowering its environmental footprints. Herein, we introduce a new recyclable PU composite film with improved biodegradability, superhydrophobicity, and flame retardancy. The coating formulation contained 50 wt.% of water-based silsesquioxane lignin (WL) as a superhydrophobic constituent and 0.12 wt.% sulfoethylated lignin (SL) as a dispersant. The aqueous-based PU film showed superhydrophobic performance (164° ± 2 water contact angle and 4° ± 2 low sliding angle) when coated. Flame retardant analysis indicated a limiting oxygen index improvement from 18.5% in pure PU to 25.5% in PU-containing 50 wt.% WL and 0.12 wt.% SL. The formulation demonstrated superhydrophobic and flame-retardant qualities when placed as coated over a wood, metal, and paper surface. The superhydrophobic characteristics of coated surfaces resisted sandpaper abrasion, UV ozone exposure, and thermal exposure. In addition, the film containing lignin exhibited better biodegradability than pure PU films. This aqueous phase PU formulation would be suitable for many surfaces with environmentally benign features.

5.2. Introduction

Polyurethane (PU) is a polymer made of isocyanate, a hard segment, and polyol, a soft segment, to form a repeating urethane group [1]. Due to its high substrate adhesion and mechanical properties, PU is used in many applications [2], e.g., adhesives, coatings, adsorbents, and elastomers [3]. Nevertheless, PU exhibits poor waterproofing and thermal stability performance [4]. In PU formulations, polar groups and hydrophilic components affect water repellency, yielding poor hydrophobicity [2, 5]. In addition, PU's urethane linkages are susceptible to oxidation and hydrolysis, making it thermally unstable [6, 7]. Due to its significant flammability and limited hydrophobic properties, PU application is limited for wood coatings [8]. Moreover, using non-renewable petroleum-based ingredients in PU fabrication is known to be environmentally unfriendly [9]. The hydrophobic properties of PU materials can be improved by decreasing surface energy and generating rough surfaces utilizing silicide and fluoride

[10]. Despite its acceptable flame retardancy, fluoride in PU may have adverse environmental implications and, thus, not suitable for this application [11]. Currently, the PU industry seeks ways to reduce its environmental impact while improving PU products' hydrophobicity and thermal properties [9].

Lignin is a natural polymer and can be utilized in PU composites to enhance their properties and reduce their environmental impact [12]. Lignin is highly favorable for PU composites due to its abundance, biodegradability, functionality, and multi-functionality [13]. Adding lignin to PU composites improves PU material's resistance to heat and flammability by promoting the formation of char layers [12]. In addition, due to the strong interaction between lignin and the PU matrix, lignin would improve the tensile strength, modulus, and elongation at break [14-16]. However, lignin-based PU composites still face challenges. The reasons include poor compatibility of lignin with PU matrix (due to poor dispersion) and the composite's reduced hydrophobicity and mechanical properties at a higher lignin content (e.g., 5%) [17]. Some common strategies to improve the interfacial adhesion and dispersion of lignin in the PU matrix are lignin nanoparticle production [18, 19], chemical modification of lignin [20-22], and the addition of compatibilizers in the PU-lignin matrix [23]. For example, wheat straw-based lignin nanoparticles were utilized as a nanofiller for PU film production [18], and its 5 wt.% inclusion improved the water contact angle of the PU film by 49° and increased tensile strength by 36%. However, the tensile strength dropped at a higher concentration due to lignin aggregation creating structural defect spots in the PU matrix. In another study, Wang et al. fractionated and alkylated lignin and its 30 wt.% inclusion improved the corrosion resistance of coated aluminum surfaces, achieving a twofold increase [20]. However, two-step modification of lignin may be economically unviable for larger scale implementation of this strategy. In another investigation, adding 0.5 wt.% of 3-aminopropyltriethoxy silane (APTES) functionalized lignin in PU films led to a 9% boost in tensile strength and improved thermal stability [22]. At a higher dosage, the strength and thermal properties of the PU film dropped due to poor dispersion and agglomeration of lignin in the formulation. Hence, it is necessary to determine a pathway to incorporate kraft lignin in the production of PU film at a higher concentration while improving the mechanical, thermal, and hydrophobic characteristics of PU films.

Enhancing the recyclability and biodegradability of PU material offers an additional approach to mitigate its environmental effect [24-26]. The recyclability and biodegradability of PU materials are greatly affected by their diisocyanates and polyols components. Furthermore, certain additives and fillers can improve or impede the recyclability and biodegradability of PUs by impacting their resistance to heat and deterioration [27, 28]. Hence, meticulous choice and enhancement of polyurethane components are essential for improving their potential recyclability and sustainability. The introduction of lignin in PU materials is reported to improve the re-process ability [29] and impart the material's biodegradability [30]. In this work, we aim to produce advanced PU materials that are highly functional, recyclable, and biodegradable.

In this study, we present a concise and environmentally conscious approach for synthesizing water-based PU coating materials incorporating softwood kraft lignin. This approach exploits two separate lignin modifications of a water-based silsesquioxane lignin copolymer (WL) obtained through the copolymerization of lignin with aminopropyl/methyl silsesquioxane (WAPMSS) and a sulfoethylated lignin (SL) achieved via sulfoethylation of lignin with 2-bromoethanesulfonate. The WL was utilized as a superhydrophobic and flame-retardant component, while the SL served as a dispersant in the PU formulation. In opposition to traditional PU/lignin composites, the composite manufacturing process was solvent- and catalyst-free. The resultant materials with high lignin incorporation (up to 50%) showed superior water repellency, high thermal stability, excellent processability, flame-retardancy, recyclability and better biodegradability. Further investigations showed that the resultant material can be utilized in high abrasive environment while maintaining its superhydrophobicity.

5.3. Experimental Section

5.3.1. Materials

Kraft lignin (SKL) was obtained from FPInnovations and produced via LignoForce technology. Aminopropyl/methyl silsesquioxane (WAPMSS) was purchased from Gelest Inc. USA. Sodium 2-bromoethanesulfonate, sodium hydroxide (NaOH), deuterated sodium hydroxide (NaOD), deuterium oxide (D_2O-d_2), deuterated dimethyl sulfoxide (DMSO-d_6), hydrochloric acid (HCl) 37%, sodium hydroxide (NaOH), 2-chloro-4,4,5,5-tetramethyl-1,3,2-dioxaphospholane (TMDP), chloroform ($CDCl_3$), ethanol (95%), pyridine, cyclohexanol (99%), chromium (III) acetylacetonate (97%), dimethylformamide (DMF), poly tetrahydrofuran (PTMG, Mw of 2000 g mol^{-1} with hydroxyl value of 204 mmol g^{-1}), isophorone diisocyanate (IPDI), monopotassium phosphate (KH_2PO_4), disodium phosphate (Na_2HPO_4), ammonium chloride (NH_4Cl), sodium chloride (NaCl), potassium hydroxide (KOH) and calcium chloride ($CaCl_2$) were all purchased from Millipore Sigma, Oakville, Canada. Also, nylon membrane syringe filters with 0.45 µm pore openings, filter papers were purchased from Fisher Scientific, Ottawa, Canada. A dialysis membrane (1,000 g mol^{-1} cut-off) was obtained from spectrum labs. Stain grade pine wood, and metal sheet were purchased from Home Depot, Canada.

5.3.2. Preparation of SKL-WAPMSS (WL) Polymer

The polymerization of SKL and WL was conducted in an aqueous environment following the polycondensation reaction [31]. SKL (1 g, 5.5 mmol) was dispersed in deionized water (40 mL) in a three-neck flask to make a 25 gL^{-1} of lignin suspension in deionized water. The suspension was kept stirring for 1 h. Then, WAPMSS solution, 20% in water (9 mL, 5.5 mmol), in a 1:1 molar ratio with WL, was fed into the reaction medium. The reaction was initiated by transferring the three-neck flask to a preheated water bath at 60 °C, mixing at 250 rpm. Upon reaction completion, after 48 h, the reaction medium was cooled to room temperature. The product was centrifuged and washed three times with toluene to remove any remaining unreacted chemicals. The supernatant, i.e., copolymerized lignin, was resuspended in water, and the suspension was neutralized with 1M of HCl, followed by dialysis for 24 h, and dried in a standard oven at 60 °C for 48 h.

5.3.3. Preparation of Sulfoethylated Lignin (SL)

The sulfoethylation of SKL was carried out following the literature [32]. To synthesize sulfoethylated lignin, SKL (1.5 g, 5.5 mmol) was dispersed in a mixture of isopropyl alcohol (45 mL) and NaOH (12 mL, 30 wt.%) at room temperature and stirred (250 rpm) for 30 min in a three-neck flask. Then, a sulfoethylation reagent (1:0.6 mmol ratio of SKL: sodium 2-bromoethanesulfonate) was added to the mixture and refluxed in continuous cold water at 80 °C for 2 h. Afterward, the reaction product was washed several times with ethanol/water (40:10 vol vol^{-1}) and recovered by centrifugation at 3000 rpm for 5 min. The precipitates were dissolved in deionized water (50 mL) and purified using dialysis for 2 days. After purification, the collected products were dried in a conventional oven at 60 °C until a constant weight was obtained.

5.3.4. Synthesis of PU emulsion

The synthesis of PU was conducted by the procedure outlined in the literature [18]. Initially, PTMG (20 g) and IPDI (11.04 g) were introduced into a desiccated three-neck flask. Subsequently, the flask was immersed in an oil bath and subjected to mechanical stirring at 200 rpm. At 85 °C, acetone (5 mL), DMBA (2.03 mL), and DBTDL (20 μL) were introduced into the flask, and the system was kept for 1 h. Subsequently, 1,4-butanediol (BDO) (1.42 g) was introduced to the system, and the mixture was stirred at 200 rpm using a mechanical stirrer for 3 h. Every hour, acetone (5 mL) was introduced to the reaction system to maintain the system's viscosity low. Subsequently, the mixture was subjected to cooling until it reached a temperature of 60 °C. Afterward, a quantity of triethylamine (1.38 g) was introduced to the flask, and the reaction proceeded for 0.5 h. After the reaction, the mixture was emulsified by adding deionized water at a concentration of 40 g L^{-1} and agitating it with a magnetic stirrer at 250 rpm for 4 h.

5.3.5. Formulation

A specific quantity of WL powder and PU emulsion was introduced to a dried vial. Then, the blend was vortexed at a high speed for 5 min, followed by magnetic stirring at 500 rpm for 5 h at room temperature. The mixture was named PWLx, where x represents the weight percentage of WL (3%, 5%, 10%, 25%, and 50%) in the formulation. Control samples were prepared using SKL and pure PU emulsion following the same procedure.

In a different set of experiments, SL was utilized as a dispersant, and it was added directly to the prepared blend of PWL50, vortexed at high speed for 5 min, and followed by homogenization using ultrasonic machine (Omni-Ruptor4000, Omni International Int.) at room temperature, 240 W power, and 30 sec with 3 sec intervals. A varied amount of SL (0.12 wt.%, 0.18 wt.%, 0.25 wt.%, 0.5 wt.%

based on the total weight of the formulation) was added to the system to study the effect of dispersant concentrations in the formulation. The optimal concentration of SL in the formulation was determined by conducting a suspension stability test using a Turbiscan lab expert following Turbiscan stability index (TSI) and water contact angle analysis, and this concentration was subsequently utilized in all the samples. The samples were labeled as PWLxS, where x denotes the weight percentage of WL (3%, 5%, 10%, 25%, and 50%).

5.3.6. Film casting and coating

For film generation, the formulation mixture was poured into a silicon mold, cured into a film at 55 °C, and then dried at 120 °C for 2 h. On the other hand, a formulated solution was applied onto a wooden, metal, and filter paper substrate. Before applying, the wood and metal surfaces were thoroughly cleaned with deionized water and then dried in an oven at 60 °C for 2 h. The wood, metal and filter paper samples were immersed in the prepared coating solution for 5 min and then subjected to a curing process at 120 °C for 2 h. The control samples consisted of uncoated samples, and PU.

5.3.7. Recycling

The recyclability of the films was evaluated by inserting the cured films into a vial containing a DMF solvent and subjecting them to magnetic stirring at 250 rpm for 24 h. Subsequently, the films were produced following the procedures outlined in section 4.2.6.

5.3.8. Characterization

5.3.8.1. Structural analysis of SKL, WL and SL

SKL, WL, and SL were investigated for their chemical structures using proton nuclear magnetic resonance (^{1}H-NMR), heteronuclear single quantum coherence NMR (HSQC) and ^{31}P-NMR [33], using top spin 4.02 software (Bruker AVANCE Neo NMR-500 MHz apparatus USA). The analysis details, conditions, and sample preparation are stated in supporting information. The chemical compositions of lignin polymers (SKL, WL, and SL), PU films and PU composite films were examined using an XPS analyzer (Kratos AXIS Supra, Shimadzu Group Company, Japan) with a dual anode AL/Ag monochromatic X-ray source (1486.7 eV). Samples were put through XPS on a double-sided carbon tape after being oven-dried at 60 °C. Steps, dwell, and sweep times were 230, 260, and 60 s. ESCApeTM (1.4.0.1149) (Kratos Analytical, Japan) was utilized to obtain spectra and quantify chemical bond [34, 35],

5.3.8.2. Formulation stability analysis.

The stability of the formulation were analyzed by taking 25 mL of coating formulations of PU were deposited in cylindrical glass vials. The vials were then scanned by a suspension stability analyzer called a Turbiscan lab expert (Formulation, France) every 30 s for a period of 12 h at 30 °C [36].

5.3.8.3. Mechanical and thermal properties analysis of the films

The mechanical properties of PU and PU composite films were examined using universal testing equipment with a 200 N load cell (Shimadzu Instrone-6800 series, Japan). Samples were cut from composite sheets with a dog bone-shaped die, measuring 27 cm long, 3.12 cm wide (ASTM D638 type V), and 0.5–1 mm thick. Three specimens from each film were evaluated at 50 mm min^{-1} and room temperature, and average values with error bars were reported [37]. The thermal stability and degradation temperature of SKL, WL, SL, PU, and PU composite films were investigated by thermogravimetric analysis (TGA) instrument (TGAi1000, Instrument Specialists Inc., WI, USA). The instrument was loaded with 10-10.36 mg of dried samples in a Tzero® aluminum pan. The analysis was conducted in a nitrogen environment with a flow rate of 10 mL min^{-1} and a heating rate of 10 °C min^{-1} from 25 °C to 800 °C [38, 39]. The glass transition (T_g) and melt temperature (T_m) for as synthesized and recycled PU, PS, and PWL50S films were investigated via a differential scanning calorimeter (DSC) (DSC Q2000, TA Instruments, DE, USA). 3-4 mg sample was placed in a Tzero pan (T 140829, Switzerland), sealed with a Tzero lid (T 140826, Switzerland), fed to the instrument and heated from 20 °C to 200 °C in three heating cycles. The last heating cycle was used to find the T_g and T_m [40].

4.3.8.4. Liquid contact angle, water absorption and UV transmittance analysis

The static liquid (water, 0.1 M NaOH and 0.1 M HCl) contact angle investigation utilized an optical tensiometer (Theta Lite, Bolin Scientific, Finland) with a digital camera and manual tilting stage. The sessile liquid droplet approach from one attention program was utilized for the static contact angle analysis. The test involved placing a 6-10 µL liquid droplet on the PU films, coated wood, metal and paper surface and measuring the contact angle visually using a camera for 50 s. A tilting stage test was processed for the water sliding angle on the surfaces. The test involved placing a water droplet (6-10 µL) on the surfaces at 180° on the tilting stage and slowly tilting it until the droplet started to slide. The measurement was repeated three times and reported as a mean with the standard deviation. The films water absorption characteristics were assessed by a force tensiometer (attention sigma 700/701, Biolin Scientific, Finland) with a metal probe. The study was conducted by immersing a cylindrical metal tube with an open bottom base containing 0.01 mg of the films into a liquid. The amount of liquid absorbed by the films was determined using the Washburn technique **Equation 5.1**.

$$W^2 = {}^{C\rho\gamma l cos\theta\ t}/_{2\eta} \qquad (5.1)$$

Where W is the weight of absorbed water (g), C is a geometric constant (0.04), ρ is the liquid density (0.998 g mL^{-1}), γ is surface tension (72.8 mN m^{-1}), L is the length of the powder glass probe (5.5 mm), η is the viscosity of the liquid (0.01 g cm.s^{-1}), and t is measurements time (300 s). The UV transmittance of the films was evaluated using a UV-Vis spectrophotometer (UV-2600i, SHIMADZU, Japan). The transmittance in the wavelength range of 200-800 nm was analyzed.

4.3.8.5. Durability of samples for abrasion, thermal and UV-Ozone

A wood, paper, and metal sample, which had been coated with PWL50S previously, was sandpapered with 1500 mesh sandpaper. A 20 g weight was then placed on top of the samples, and they were pushed down a straight line. Water contact angle analysis was conducted after each 30 cm length of abrasion. To analyze the superhydrophobicity of coated wood after thermal exposure, the wood samples, which had been coated previously, were subjected to a temperature of 200 °C in an oven. The water contact angle of the samples was then measured at different time intervals. Similarly, the wood samples coated with a protective layer were also subjected to UV-ozone exposure for varying durations. Subsequently, the water contact angle of the samples was evaluated.

4.3.8.6. Ignition performance of films and coated samples

An ASTM D 2843-99 method was utilized to determine the smoke emission parameters of coated wood by investigating the smoke production profile with a smoke density test apparatus (AIC-2843, Advanced Instrument Co., Ltd., China). The coated samples (42 mm × 42 mm × 4 mm) were placed in the instrument and subjected to 0.14 MPa propane gas pressure for 250 seconds after ignition. The light absorption curves and smoke density ratings (SDRs) of the samples were analyzed and reported [41]. The limiting oxygen index (LOI) analyzer (NETZSCH TAURUS apparatus, Germany) determined the lowest oxygen needed to ignite film samples according to ASTM D2863. The films and coated wood samples were tested using this method. The glass column's center was burned in a controlled nitrogen and oxygen environment. Sample dimensions were 140 mm × 20 mm × 10 mm for wood and 120 mm × 35 mm × 2.5 mm for films, and the test was conducted in five replicates [42]. The flame test was performed to simulate real-life fire scenarios, films, coated wood and papers were subjected to an intense propane gas flame to initiate ignite. Images were captured to depict the reaction of the samples visually.

4.3.8.7. Biodegradability

PU, PS, and PWL50S biodegradability analysis was conducted under aerobic conditions in a mineral salt aqueous environment via a respirometer instrument (AER-800S respirometer system). The nutrition culture medium contained KH_2PO4 (3 g L^{-1}), Na_2HPO4 (6 g L^{-1}), NH_4Cl (1 g L^{-1}), NaCl (0.5 g L^{-1}), and $CaCl_2$ (0.003 g L^{-1}). For the aquatic biodegradation test, microbial inoculum sourced from polished NX comprised a specialized blend of non-pathogenic Bacillus bacteria of soil origin. In a spore form, these bacteria required rehydration with nutrient buffer water to initiate sporulation. To initiate biodegradation, 5 mL of microbial inoculum was introduced to each 500 mL sterilized mineral salt medium bioreactor. Subsequently, the released CO_2 was collected via 30% KOH adsorption during biodegradation. The evaluation process involved monitoring the consumption of oxygen. The control samples for the study were SKL, SL, WL, blank control (a mineral with a microbial inoculum), and starch as a reference sample. The biodegradability of the samples (R) was determined following **Equation 5.2**.

$$R = \frac{Q_T - Q_b}{C_T \times ThOD_T} \times 100 \qquad (5.2)$$

Q_T and Q_b represented the oxygen consumption values of the test substance and the blank, respectively, in mg L^{-1}. C_T and $ThOD_T$ represent the concentration of the test substance in mg L^{-1} and the theoretical oxygen demand of the test substance expressed as mgO_2 mg^{-1}.

5.4. Result and Discussion

5.4.1. Nuclear magnetic resonance (NMR) analysis

SL and WL were derived from SKL through the substitution of phenolic hydroxyl groups with 2-bromoethansulfonate and the replacement of the hydroxyl group with a siloxane bond using aminopropylmethyl silsesquioxane, respectively (**Figure S5.1**a-b) Appendix 4A [43]. NMR study was conducted on SKL, SL, and WL to ascertain their respective chemical structures. **Figure S5.2** illustrates the NMR spectra of the biopolymers, along with the structural representation of a monomeric unit. The resonance attributed to DMSO-d_6 is detected at a chemical shift of 2.5 ppm in both SKL and SL spectra. Conversely, the resonance associated with D_2O is ascribed to a chemical shift at 5 ppm in the WL spectrum. In the ^{1}H-NMR spectrum of SKL, the aromatic protons exhibit a resonance signal ranging from 6.0 to 7.5 ppm (**Figure S5.2**a), the methoxy protons display a resonance signal ranging from 3 to 4 ppm (**Figure S5.2**a) [44, 45]. Aliphatic protons can be detected within the chemical shift range of 0 to 3.2 ppm [46]. A novel peak emerged in the oxygenated region at around 3.2 ppm (-O-CH_2) for the SL polymer [43]. A novel peak emerged in the oxygenated region at around 3.2 ppm (-O-CH_2) for the SL polymer. The prominent peaks observed at 2.7 ppm in WL are attributed to the -OH peaks originating from silicon (**Figure S5.2**a). The signals observed at 1.5 ppm in the spectrum of WL are associated with protons originating from NH_2 groups (**Figures S5.2**a). The signals observed at a chemical shift of 0.5 ppm are associated with the propyl structure of protons originating from the CH_2-CH_2-CH_2 group (**Figures S5.2**a and **S5.3**). The signals detected at 0 ppm are attributed to the proton of CH_3 that is coupled with Si (a) [47]. The ^{1}H-NMR spectra of the SL and WL polymers exhibit the presence of the aromatic (h) and methoxy (g) protons derived from SKL (**Figure S5.2**a). Nevertheless, the prevalence of aliphatic-H is more pronounced in WL than in SL, which is the result of long aliphatic chains originating from WAPMSS in WL, while SL only had one ethyl group (**Figure S5.3**).

The HSQC NMR analysis was conducted on SKL, SL, and WL samples to reveal interconnections and identify the primary group constituents, as depicted in **Figure S5.2**b. The cross-peak signals of δC/δH at 71.4/4.7 ppm, δC/δH at 53.29/3.44 ppm, and δC/δH at 53.6/3.0 ppm were observed in SKL, SL, and WL polymers, indicating the presence of substantial interunit linkages in β-O-4 ($A_β$), β-5 ($B_β$), and β-β ($C_β$) (**Figure S5.2**d), respectively[48]. In addition, the distinctive signal corresponding to the methoxy ($-OCH_3$) functional group was observed at the chemical shift of δC/δH 55.5/3.70 in **Figure S5.2**b [49]. The HSQC spectra offer distinct evidence of major linkages (β-O-4′, β-5′, and β-β) and major units (secoisolariciresinol substructure, resinol substructure, and guaiacyl propanol unit) and methoxy structures in SKL, WL, and SL. This finding is consistent with the results obtained from ^{1}H-NMR analysis, indicating that both WL and SL kept the original structure of SKL. In the context of the SL structure, the cross-peak signals seen at the δC/δH of 50.7/2.8 and 32.2/1.8 ppm correspond to the functional groups of $-OCH_2$ and CH_2, respectively [50]. This further confirms the presence of strong ethyl groups in the structure of SL because of sulfoethylation. The WL spectrum exhibited aliphatic linkages, which could be attributed to the silsesquioxane inherited from the WAPMSS (**Figure S5.1**). A novel cross-peak signal was also detected in the WL within the C-O linkage region at the δC/δH of 46.2/3.2 ppm. This signal represents the formation of a new chemical bond (C-O-Si) between SKL and WAPMSS. This bond is produced through a condensation reaction involving WAPMSS and SKL [51].

The quantitative ^{31}P-NMR spectra of SKL, SL, and WL following phosphorylation are depicted in **Figure S5.2**c. The proportions of aliphatic, aromatic (C-5 substituted and guaiacyl), and carboxylate hydroxyl (OH) groups present in the samples are quantified and depicted in **Table S5.1**. The hydroxyl group content of the SL polymers was lower than that of SKL, whereas no hydroxyl groups were discernible for WL (**Figure S5.2**c). The decrease in the overall number of hydroxyl groups in SL provides evidence for the successful transformation of the hydroxyl groups of SKL, which is further corroborated by the presence of C-O-C connections in HSQC NMR analysis. Similarly, the silanization process led to the complete conversion of hydroxyl groups of SKL for WL production (**Figure S5.2**).

5.4.2. X-ray photoelectron spectroscopy (XPS) analysis

XPS investigation revealed the elemental compositions and chemical bonding characteristics of SKL, SL, and WL. The elemental compositions of SKL consisted of carbon (285 eV) and oxygen (532 eV), and impurity traces of sulfur (166.5 eV) [52]. **Figure S5.4**(a) revealed the presence of sulfur (166.5 eV) in SL, as well as nitrogen (400 eV) and silicon (152.9 eV and 101 eV) in WL [53, 54]. **Figure S5.4**(b) displays the core level spectra of C1s, along with a fitting analysis for the peaks associated with carbon bonds. The deconvolution of the Cls peaks for SKL yields three primary components of C-C (284.8 eV), C=O (288–290 eV), and C-O (286 eV) [55]. Similarly, an examination was conducted on the C1s spectrum of SL, resulting in the identification of a new C-S peak at 284.8 eV.[50] In examining WL's C1s, the carbon links of particular significance involved carbon and silicon (C-Si) at an energy level of 283 eV. In contrast to SKL, a notable reduction in the concentration of O=C-O bonds was observed in the WL, but the concentration of O-C bonds exhibited an increase in the WL. This observation implies that the reaction involves the possible OH reactive sites, which aligns with the findings from P-NMR (**Figure S5.2**b) and FTIR (**Figure S5.4**) studies. Furthermore, it can be observed that the WL exhibited higher C-O bonds than the SKL. The formation of a new C-O-Si connection between SKL and WAPMSS can be attributed to the polycondensation reaction. This observation aligns with the findings of the HSQC NMR investigation, which revealed a notable augmentation in aliphatic C-O bonds.

In addition, the S2p peaks of SL were subjected to deconvolution, and the outcomes are presented in **Figure S5.4**(c). The three components under consideration are denoted as S=O (168 eV), S-H (163 eV), and S-O (165 eV). This finding, along with the FTIR (**Figure S5.5**), H NMR, and HSQC NMR, confirms the successful sulfoethylation of SKL to produce SL. The deconvolution of Si 2p peaks for WL is illustrated in **Figure S5.4**(d). The Si 2p spectrum of WL exhibits distinct components corresponding to Si-C (101.34 eV), Si-O-Si/Si-OH (103.76 eV), and Si-O-C (102.5 eV) [56]. The results align with the outcomes derived from FTIR analysis (**Figure S5.5**), where the WL spectrum show higher transmittance peaks of Si-C, Si-O-Si, and Si-O-C. The identification of Si-O-C bonds on the XPS and FTIR spectra, along with the detection of C-O linkages in the HSQC spectrum and the reduction in hydroxyl groups observed in the ^{31}P-NMR spectrum, provide conclusive evidence of the copolymerization and conversion of lignin's hydroxyl groups (due to silanization) for WL production (**Table S5.1**).

5.4.3. WL-containing PU Emulsion Formulation Stability

The assessment of coating formulation's stability provides insights into the interactions of its constituents and shelf life of the formulation [57]. The formulation was prepared by combining a PU water emulsion with varying proportions of WL or SKL. The appearance of dispersion stability (i.e., TSI global index) of the five samples for over 12 h is shown in **Figure S5.6** and **Figure S5.7**a. There exists an inverse relationship between the stability of a coating formulation and the TSI value, whereby an increase in stability corresponds to a decrease in the TSI value [58]. The PU emulsion was stable as evidenced by a TSI value of 2. Adding SKL led elevated the TSI value, suggesting a less stable system. Similarly, the inclusion of WL polymer in the PU emulsion system led to a significant rise in the TSI value. The comparative dispersibility of SKL and WL in a PU system is notably better for SKL, as demonstrated by the TSI result and verified through visual examination. This suggests that the WL particles possess greater hydrophobic interaction, resulting in their aggregation and sedimentation.

5.4.4. Performance of Films

The examination conducted by XPS focused on analyzing the elemental compositions and chemical bonding characteristics of the films, specifically those of PU, PKL10, and PWL10 in **Figure 5.1**a. The deconvolution of the C1s peaks corresponding to the PU and PKL10 results in the identification of four main components: C-C (284.8 eV), C-N (286.2 eV), C=O (288–290 eV), and C-O (286 eV) [59]. The percentage area concentration of the C=O bond on PU is 2.10, whereas PKL10 has a concentration of 3.82. A considerable number of C=O bonds may indicate the existence of carboxylic-OH groups, which are notably abundant in the SKL structure (**Figures S5.2**b and **5.2**b). An extra component, C-Si (283 eV), was observed in the deconvolution of PWL10. The presence of a C-Si bond in PWL10 indicates the existence of Si-CH_2 structural components originating from WL due to copolymerization (**Figure S5.3**b). **Figure 5.1**b and **Figure S5.7**b displays the stress-strain curves for the films, and data for tensile strength and elongation at break are illustrated in **Figure S5.7**c-d. The SKL sample with more than 10 wt.% proportion in PU displayed disintegration and fragility, making it impossible to analyze the mechanical properties, as depicted in **Figure S5.8**. Insufficient film formation of SKL at a greater concentration is caused by agglomeration due to significant self-interaction [60]. Compared to PU, the WL and SKL composite films exhibited reduced tensile strength and elongation at break. However, incorporating lignin polymer resulted in an increased modulus, indicating that the produced film was more rigid.

PU films when the proportion of SKL surpassed 3% in the film [18]. Water contact angle (WCA) and sliding angle (SA) analysis was carried out to determine the superhydrophobic and hydrophobic characteristics of the films in **Figure 5.1**c. The WCA and SA values of the pure PU were measured to be 90° and 40°, respectively. By including 10 wt.% SKL in the PU matrix, the films exhibited a reduction in their WCA value by 35°.

Compared to PU film, the hydrophilicity of PKL10 films may be attributed to a free carboxylic group inside PKL10 film structure (**Figure 5.1**a). However, the water contact angle of PWL10 composites exhibited a 30° increase compared to pure PU. Furthermore, when the content of WL increased in the PU film, the water contact angle increased while the SA decreased progressively. The PWL50 film exhibited the maximum WCA value of 163° and a low SA of 8°.

To enhance comprehension and establish a connection between the surface morphology of the films, SEM imaging analysis of the samples was conducted (**Figure 5.1**d). PU film surfaces were relatively smoother than those of PKL10 or PWL10. When SKL particles were introduced to the PU matrix, the film surface exhibited microscopic clusters and clumps of particles. However, a more detailed examination reveals that these clusters were spherical aggregates. Conversely, PWL10 films exhibited higher polymer aggregation than PKL10. The decreased dispersibility of the WL within the PU matrix is the cause of this discrepancy (**Figure S5.7**a). The PWL10 and PWL50 films contained spherical macroscopic particles associated with smaller particles and air pockets. This can be ascribed to the film's heightened hydrophobic nature and coating. Incorporating 50 wt.% of WL into the PU matrix led to a smoother surface than incorporating 10 wt.% in **Figure 5.1**d. Particle aggregates arranged diagonally on the PWL50 film were detected at reduced resolution, potentially contributing to the film's decreased mechanical characteristics (**Figure 5.1**b).

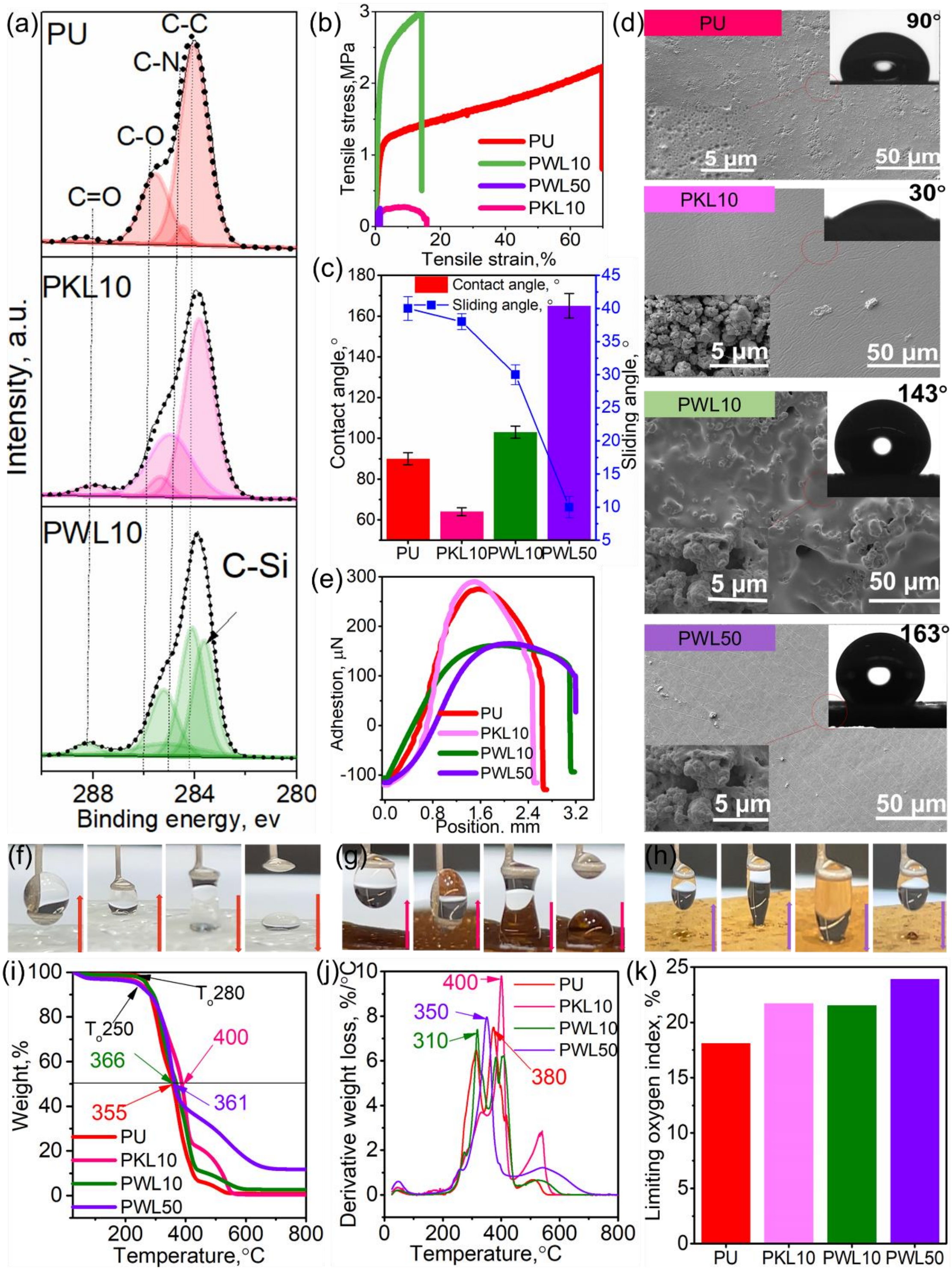

Figure 5.1. C1s deconvoluted XPS spectra of the films (a), stress-strain curves (b), water contact, and sliding angle (c) SEM images at 50 µm and 5 µm scales (d), water droplet adhesion force study (e), droplet attachment and detachment steps on PU (f) and PKL10 (g) and PWL50 (h), and TGA (i), DTG (j) and limiting oxygen index (LOI) (f) of PU, PKL10, PWL10 and PWL50 films.

Poor dispersion of WL in the PU matrix suggests inadequate interfacial adhesion between the polymer matrix (PU) and WL, leading to reduced mechanical load transfer from the polymer matrix to WL and consequently resulting in poor mechanical characteristics of the overall film [61].

Tensiometer measurements of water adhesion force was utilized to quantify the coatings' water adhesion force in **Figure 5.1**e. The droplet profile was captured by digital camera and presented in **Figure 5.1**f-h. The instrument stage supports the suspended droplet when it contacts the sample on the stage, resulting in a considerable decrease in force. As the stage drops, the force rapidly increases until it peaks. The PU and PKL10 films had detachment peaks at 1.5 and 2 mm, with pull-off forces of 250 and 285 μN. Like PWL50, the superhydrophobic film exhibits a detachment peak of 0.12 mm and a pull-off force of 80 μN. Hydrophobic surfaces, once separated, show a notable decrease in the adhesion force, indicating that half of the droplet remains on the surfaces [62], as shown with PU and PKL10. Conversely, PWL50 restored their water adhesion force to zero. This shows such surfaces' extraordinary water-repellent and low water adhesion properties [63]. The water droplet exhibited a strong adhesion to the surface of the PU (f) and PKL10 (g) films. However, the droplets could quickly detach from the PWL50 film (h). Films incorporated with WL exhibited high water repellency and resistance to water adhesion. This phenomenon may occur due to the copolymerization process, which would replace the hydrophilic hydroxy groups of lignin with hydrophobic silsesquioxane groups (**Figure S5.2**). The WCA and SA (**Figure 5.1**c) and SEM (**Figure 5.1**d) revealed the presence of a hierarchical structure at both the micro and nano levels, contributing to enhanced superhydrophobic characteristics.

The thermal stability of PU, PKL10, PWL10, and PWL50 were investigated by TGA analyses, as shown in **Figures 5.1**i and **5.2**j. The films' thermal stability was assessed by the onset temperature (T_o), 50% weight loss temperature ($T_{50\%}$), and maximum decomposition temperature (DTGmax). PU showed T_o at 280 °C and $T_{50\%}$ at 355 °C. PKL10 had a $T_{50\%}$ and DTGmax that were 45 and 20 °C higher than PU, respectively. Incorporating SKL in the PU matrix significantly enhanced the thermal stability of the film. Adding more hard segments (aromatic structures of lignin) could result in the formation of crosslinks, leading to higher char production and enhanced interaction between the PU matrix and SKL polymer [1, 6]. The $T_{50\%}$ value of PWL10 decreases by 10 °C, whereas the DTGmax occurred 40 °C lower than PU. Poor WL dispersion (**Figure S5.7**a) causes aggregation in the PU matrix (**Figure 5.1**d). Agglomerations or clusters may cause film flaws or voids, and faults or voids in the PWL10 and PWL50 layer may cause thermal deterioration [64]. The poor dispersion of WL (**Figure S5.7a**) may reduce the contact area and interaction between the WL and the PU matrix, reducing WL thermal barrier characteristics. Similarly, PWL50 film had a DTGmax of 350°C, i.e., 20 °C lower than PU film in **Figure 5.2**j. Due to WL's inorganic component, PWL50's ultimate weight residue was 17% greater than PU's.

The LOI values of the films are illustrated in **Figure 5.2**k. The pure PU had the lowest LOI value of 18.4%, while the PWL50 had the highest LOI value of 25.4%, exceeding the values of the other samples. The WL -containing PU films had a higher LOI than PU and PKL10 due to enhanced charring properties of WL, as shown by TGA analysis in **Table S5.2**. A silsesquioxane structure on the SKL backbone provides thermal protection to charring, lowering flammability at high temperatures. When incorporated into PU polymer, silsesquioxane would delay ignition and strengthen the PU matrix [65]. The WL polymer in water-based PU emulsion exhibited superior hydrophobicity, thermal stability, and flame-retardant features when utilized in a high concentration (50%), surpassing the performance of pure PU or PKL10 coating materials. Nevertheless, the mechanical characteristics of this film were significantly inferior to those of PU or PKL10 due to the inadequate dispersibility of WL in the PU matrix. Hence, an attempt was made to enhance the dispersibility of WL in the PU matrix by utilizing SL as a dispersant in the following section.

5.4.5. Effect of SL on the Stability and Surface Chemistry of PWL50 Formulations

The effect of SL on the stability and surface properties of PWL50 formulation was investigated, and the results are shown in **Figure 5.2**a-d. **Figure 5.2**a shows that the lack of SL in the PWL50 sample led to instability with the TSI value 55. The high molecular weight (**Table S5.2**) and hydrophobic character of WL particles may interfere with their dispersion in PU due to their agglomeration. Adding 0.12 wt.% SL to PWL50 increased dispersion stability by 25% and adding more SL to the dispersion improved its stability further. However, the surface became more hydrophilic.

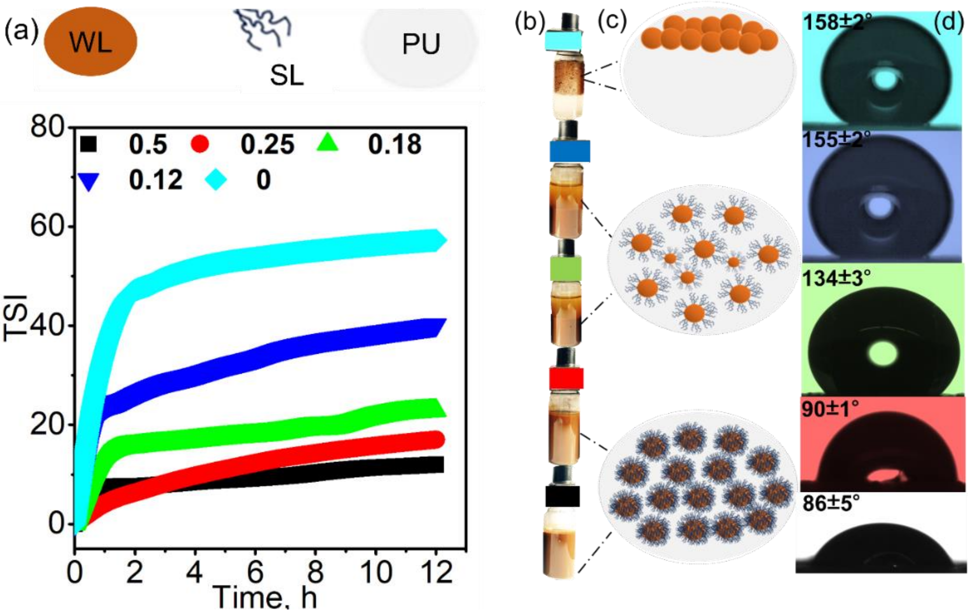

Figure 5.2. Coating formulation stability (TSI) for 12h every 30 sec scans legend showing the concentration of SL (a), visual of the formulations after 12 h preparation (b), possible illustration of hydrophobic/hydrophilic effect of SL molecules in PWL50 dispersion (c) and water contact value of the films (d).

These effects have also been found in previous investigations involving the utilization of sulfonated lignin as a dye dispersant [66]. Dispersants reduce particle agglomeration by introducing steric hindrance and electrostatic forces. Due to its high surface charge density (2.1 mmol/g), SL adsorption onto WL particles could prevent WL agglomeration by electrostatic repulsion (**Figure 5.2**c). Introducing SL at lower concentrations (e.g., 0.12 wt.%) resulted in sustained superhydrophobicity with a contact angle of 155° (**Figure 5.2**d). As a result, 0.12 wt.% concentration of SL was selected as a dispersant for the following section.

5.4.6. Effect of SL on the Properties of PU Films

The effect of SL dispersant on the surface morphology, mechanical properties, and thermal properties of WL and SKL-containing films were investigated, and results are presented in **Figure 5.3**. **Figure 5.3**a illustrates the appearance and the surface morphology of films generated with the addition of 0.12 wt.% SL. The addition of SL in a pure PU (PS) water emulsion changes the color from clear to brown, and the appearance of small aggregates was detected in the film, and the WCA remained 90°. Similarly, SL was incorporated in the SKL and WL containing formulas, where its addition improved the film's appearance while not affecting the water contact angle values crediting the optimization of SL in **section**

5.3.5 (**Figure 5.3**a). The overall water absorption of the films were also analyzed by tensiometer as shown in **Figure 5.3**b. PKL10S and PS exhibit the most water absorption, with values of 12.8 g/g and 11.8 g/g, respectively. PU has a lower water absorption compared to PKL10S and PS. On the other hand, PWL10S and PWL50S had the lowest water absorption, with values of 1g/g and 2.1 g/g, respectively. The reduced water absorption of PWL10S and PWL50S can be ascribed to the films' higher water contact angle (WCA) values (**Figure 5.1**a and **Figure 5.3**a) and the hydrophobic characteristics of WL. The greater water absorption of PWL50S, as opposed to PW10S, can be attributed to the exposure of the PU matrix in PWL50S, which is caused by the porous nature of the film.

Figure 5.3c shows the UV-transmittance spectra of the films; the PU films show more than 68% in the UVC (190-275 nm) regions, 78% transmittance in the UVB (275-320 nm) regions, and 90% transmittance in the UVA (320-380 nm) regions. The films containing lignin, show 100 percent protection in the UVA, UVB, and UVC as shown by 0% transmittance in the regions. The superior UV-shielding property resulted from the abundant phenolic hydroxyl, methoxy and carbonyl groups concentrated in the outer surface of SKL, SL and WL particles (**Figure S5.2** and **Figure S5.3**). Additionally, the complex structure of lignin allows for the scattering and absorption of UV light that penetrates the film, resulting in reduced transmittance [67].

The stress-strain curve, tensile strength, and percentage elongation of PS, PKL10S, PWL10S, and PWL50S composite films are presented in **Figure 5.3**d and **Figure S5.7**c-e, respectively. Compared with films prepared without SL, the films generated with SL had a higher modulus and tensile strength. Incorporating SL in the pure PU film improved the tensile strength by 2.5 MPa. The structural component of SL consists of many aromatic structures (**Figure S5.2**) that strengthen the films as rigid segments. PKL5S showed the highest tensile strength (35 MPa). Similarly, the PWL5S films improved tensile strength by 8 MPa compared to PWL5. This improvement in the tensile strength is attributed to the improved dispersion of WL and SKL particles in the PU system in the presence of SL (**Figure 5.4**a). The mechanical strength of PU films is enhanced when they contain a higher concentration (5% and 10%) of SKL in the presence of SL, as compared to a similar concentration with WL. There could be a possible reaction between SKL hydroxyl groups (**Figure S5.2**c), with isocyanate groups to generate urethane bonds and be the reason for the improved mechanical strength [68]. This phenomenon is not true for WL since siloxane groups occupy the hydroxyl groups (**Figure S5.2**c). However, when the concentration of SKL increased more than 10%, the tensile strength dropped even in the presence of SL. Consequently, producing a PU film with a concentration exceeding 10% in SKL material was deemed unattainable (**Figure S5.8**). Nevertheless, it was possible to produce a film with higher concentrations of WL (25% and 50%) despite the subsequent reduction in mechanical properties.

According to the data presented in **Figure S5.7**d, it can be observed that the elongation at the break of PS containing film was comparatively lower than that of PKL10S and PWL10S. Additionally, the elongation at the break of SKL and WL-containing films with SL films exhibited a steady drop as the SKL or WL content concentration increased. The increase in SKL or WL in the PU matrix would increase the PU composite matrix's hard segment, reducing the PU film's ability to deform under stress and making it more brittle with a decrease in elongation at break [68, 69].

The thermal stability of PS, PKL10S, PWL10S, and PWL50S was investigated, and their TGA and DTG curves are depicted in **Figures 5.3**e-f, respectively. Except PWL50S, which exhibited a 60 °C rise in the T_o compared to PWL50 (**Figure 5.1**i-j), the remaining samples did not demonstrate an increase in the T_o. This result indicates that the introduction of SL had no impact on the thermal resistance of PKL10 or PWL10 but had a notable effect on PWL50 where the concentration of WL was higher (50%). This enhanced T_o is directly related with the dispersion of WL in the PU system because of SL (**Figure 5.2**a). Notably, in the absence of SL in the formulation, the T_o was significantly lower (**Figure 5.1**a). The SL films demonstrated elevated temperatures at $T_{50\%}$ compared to the formulation without SL.

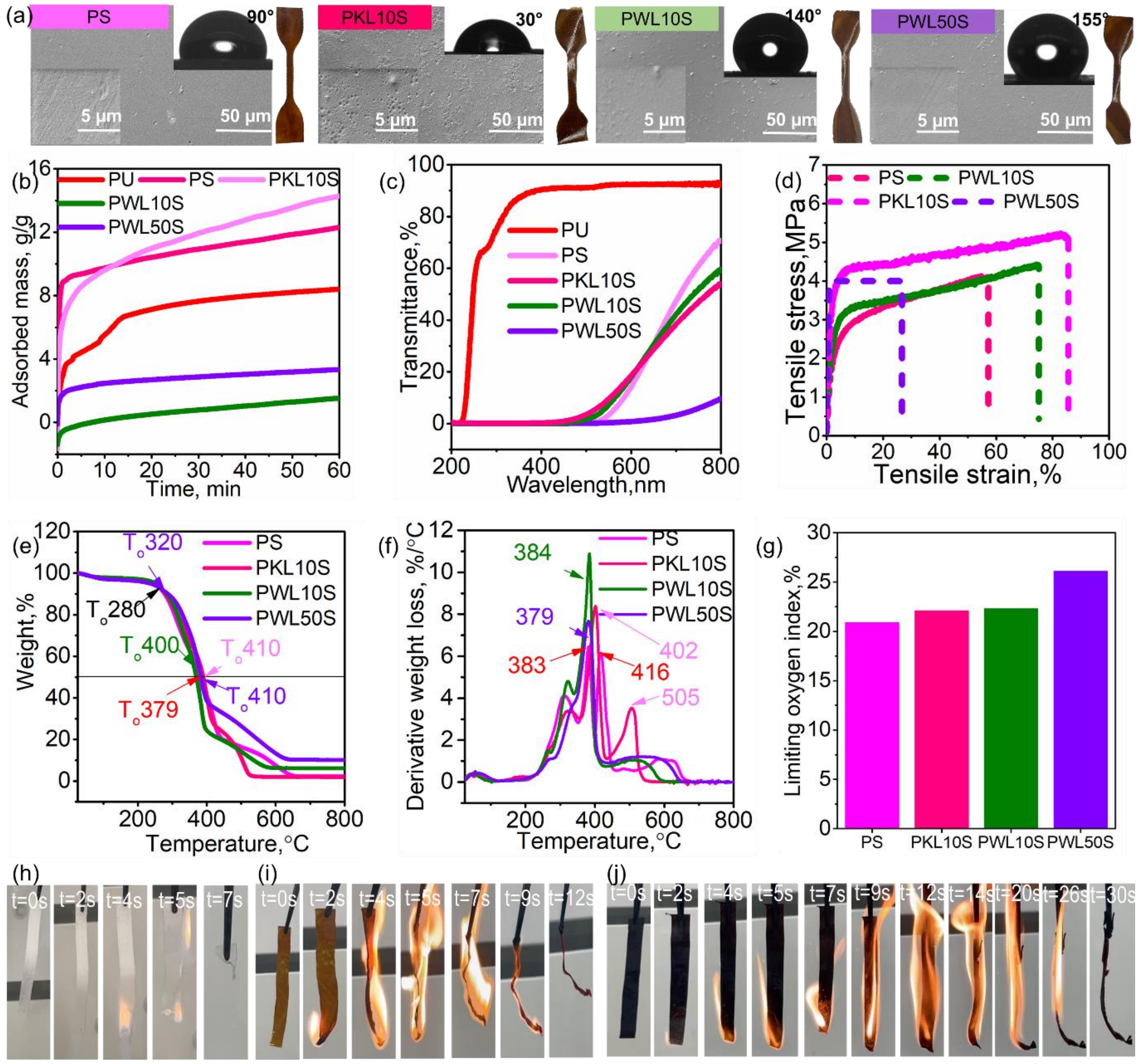

Figure 5.3. Surface morphology, contact angle and appearance of films (a), water absorption (b), UV-Vis transmittance spectra (c) stress-strain curve (d), TGA (e) and DTG (f), limiting oxygen index (LOI) (g) of PS, PKL10S, PWL10S and PWL50S, digital images for the flame test PU (h), PS(i), and PWL50S of the films.

The experimental findings demonstrated 24, 10, 44, and 54 °C temperature enhancements for PS, PKL10S, PWL10S, and PWL50S. This indicates that more energy was needed to break SKL or WL's interaction with PU chemical chains in the presence of SL. The inclusion of SL also improved the DTG_{max} for all the films. Nevertheless, the DTG_{max} of PKL10S exhibited a higher increase than PWL10S and PWL50S. In this case, SL in the PU matrix increased the composite film's SKL and WL dispersion and increased the presence of the stiff phenylpropane aromatic rings. This improved thermal stability by increasing char formation. Typically, the dense organization of lignin inside the PU matrix can significantly improve the heat resistance of films [70]. It is worth mentioning that WL particles were also beneficial for increasing the residual weight of the PU films, as expected.

After SL was incorporated into the PU films, the LOI value was investigated for samples of PS, PKL10S, PWL10S, and PWL50S. The PS film demonstrates a 2.8% increase in LOI compared to pure PU. The LOI value for PWL50S showed a 2.2% improvement compared to the sample without SL. This improvement in the LOI value is attributed to well-dispersed SL in the PU matrix structure (**Figure 5.2**a). This finding can also be supported by the improved thermal stability resulting from TGA analysis (**Figure 5.3**e-f). The flame test was conducted to replicate a real-life fire on PU, PS, and PWL50S, and the outcome is illustrated in **Figure 5.3**h-j. When exposed to propane gas, PU underwent a consistent and sustained igniting, with a flame that burned the sample entirely within 7 seconds. PS samples took 12 s for the flame to propagate and reach the end of the film, but unlike PU, the PS samples left the structure of the film intact after the flame was extinguished in 12 s.

This indicates that the introduction of SL in the PU matrix, even in a concentration as low as 0.12 wt.% improved the stability of the film when burned, as also indicated in the TGA and LOI analysis (**Figure 5.3**e-g). The PWL50S films, on the other hand, took 30 seconds for the flame to reach the end of the film from the ignited tip on the 2nd ignition, and after the flame reached the top, the film still hung without losing its structural integrity. This stability of PWL50S for flame is attributed to the highest concentration (50%) of WL, which has a high thermal stability (**Table S5.2**).

5.4.7. Coating Performance of PU-based formulations on different surfaces

The formulation exhibiting superhydrophobic properties (PWL50S) was coated in wood, metal, and paper, and the contact angle was measured and reported with different liquids (**Figure 5.4**a). The coated surfaces all show a contact angle > 150° exhibiting the superhydrophobic characteristics of the formulation. The contact angle exhibited reduced when a droplet of 0.1M NaOH was applied. However, the variation in contact angle was less pronounced with a droplet of 0.1M HCl. The reduced contact angle with NaOH droplets could be a result of the ionization of lignin's acidic groups (phenolic hydroxyl groups for SL) and the reduced ether bonds resulted from the presence of higher alkyl chains on WL

(**Figure S5.2**) [71, 72]. A superhydrophobic coating's durability depends on its abrasion resistance [73]. To enhance practical applicability, the superhydrophobic (PWL50S) coated wood, metal, and paper underwent sandpaper abrasion testing, and the water contact angle after abrasion is reported in **Figure 5.4**b. The coating withstood up to 160 cm of abrasion before the contact angle dropped for wood and metal while the coated paper failed after 60 cm. The potential cause for stability of the superhydrophobicity on wood and metal is attributed to the strong adhesion of the coating formulation as a result of sticky nature of PU on metal and wood while the paper itself lacks mechanical strength [74]. Following the 160 cm abrasion, the contact angle decreased for wood, but the superhydrophobicity remained unchanged on the metal surface until 320 cm. This phenomenon can be explained by the separation of the coating from the underlying wood substrate, which then exposes the wood surface directly to water droplets. The presence of the coating on the metal surface may be attributed to the metal's superior mechanical qualities compared to wood. The coated wood exhibits excellent stability of its superhydrophobic qualities even after being subjected to heat deterioration at 200 °C and exposure to UV-ozone for up to 200 min **Figure 5.4**c. The WCA remind higher than 130° even after 600 min of UV ozone and thermal exposure. The stability of the superhydrophobic coating on wood, when exposed to thermal and UV radiation, is attributed to the thermal stability of WL and its ability to absorb 100% of UV rays. This conclusion is based on the findings of TGA and UV-Vis transmittance analysis. These properties enable the coating to retain its superhydrophobicity and shield the coated wood from thermal and UV degradation.

Additionally, the fire-resistant properties of the formulations were evaluated by applying them to a wooden surface and measuring the LOI and smoke density. The LOI, SDR, and light absorption curves for uncoated wood, PS, PKL10S, PWL10S, and PWL50S coated wood are shown in **Figure 5.4**d-e. Concentrated smoke reduces perceptibility, limiting egress and injuring those trying to evacuate [75]. The smoke generation level of materials is a significant focal point in assessing fire safety risks [76]. **Figure 5.4e** shows how light absorption in uncoated wood increased when lit and stabilized as it burned. Peak light absorption was 50%, and smoke density was 18 at 250 s (**Figure 5.4**d).

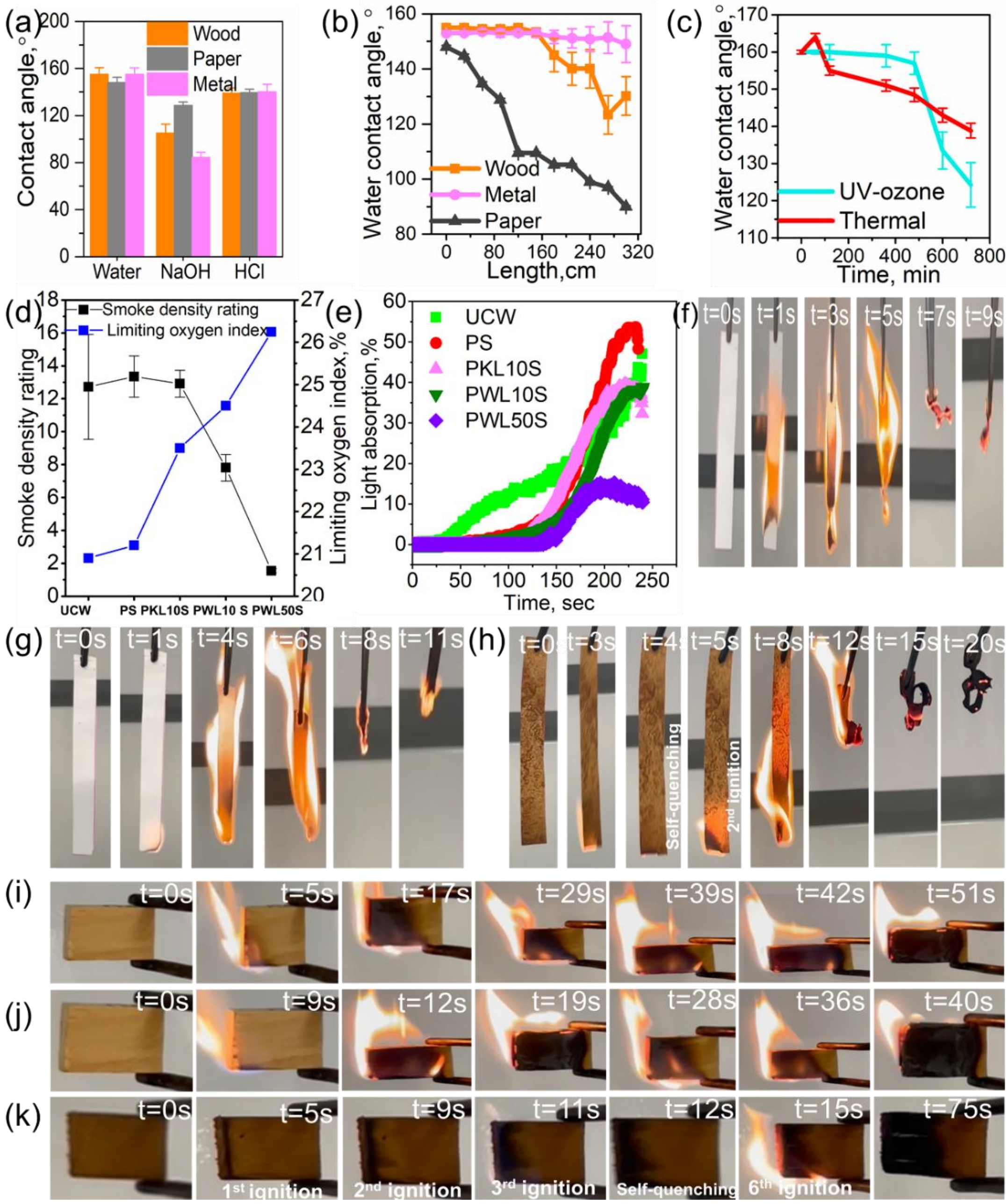

Figure 5. 4. Liquid contact angle (a) water contact angle after abrasion (b) of PWL50 coated wood, metal and paper, stability of water contact angle on PWL50S coated wood after thermal exposure at a 200 °C oven and UV-Ozone exposure (c), limiting oxygen index and smoke density rating (d) and light absorption (e) of PS, PKL10S, PWL10S and PWL50S, flame test on uncoated (f), PU coated (g), and PWL50S coated filter paper (h), uncoated (i), PU coated (j) and PWL50S coated wood (k).

Wood coated with PU had a peak light absorption of 55% and a smoke density of 15. Due to their high flammability, PU coatings are unsuitable for naturally flammable wood coatings. Utilizing PWL10S or PKL10S did not increase smoke production in the coated wood. Smoke output decreased when WL was increased to 50. This was supported by 29% light absorption and 4 smoke density. The results indicate that WL greatly reduced wood combustion. WL50 may create a crosslinked ceramic phase during burning, reducing the combustion rate. This phase prevents the fire from spreading and preserves the wood's structure.

Flame tests were performed on uncoated paper and wood samples with PU and PWL50S. The results of these tests are available in **Figure 5.4**f-k. Uncoated and PU-coated paper burned rapidly, with the flame consuming the paper in around 9 and 11 s, respectively. In contrast, PWL50S-coated paper self-extinguished upon first ignition, and it took 20 s for the flame to spread and reach the end of the paper. Additionally, there was a noticeable paper residue remaining at the end. Uncoated and PU-coated wood immediately caught fire and burned entirely at 51 and 40 seconds of ignition, respectively (**Figure 5.4**i-k). However, due to its self-quenching properties, the PWL50S coated wood required a 6th ignition. Even after the 6th ignition and 75 s of burning, the flame did not devour half of the coated wood. The self-quenching property exhibited by both paper and wood may be attributed solely to the flame retardant and thermal stability of the PWL50S coating formulation, as demonstrated in the film and flame test (**Figure 5.3**j), as well as the higher thermal stability of WL and the charring characteristics of lignin (**Table S5.**2).

5.4.8. Recyclability of PU films

The manufacture of PU is criticized for generating non-biodegradable waste in landfills, primarily because of the permanent interconnected structure of PU crosslinks. Nevertheless, the hydroxyl and carbamate groups from separate polymer chains can engage in transcarbamoylation processes, creating dynamic covalent networks. These networks can undergo reversible formation and cleavage, providing PU with excellent solvent reprocessing ability [77]. The recyclability of the PU films was examined by cutting the cured samples into smaller pieces and dissolving them in DMF. The dissolved material was cast and cured, as seen in **Figure S5.9**. The tensile stress-strain curve of the reprocessed samples is assessed (**Figure S5.7**f). **Table 5.1** shows the original and recycled films' tensile strength, elongation at break, modulus, and water contact angle. The films are often recyclable due to the advantageous presence of a significant amount of hydroxyl groups in lignin. The hydroxyl groups quickly engage in transcarbamoylation interactions with carbamate groups in a suitable solvent, leading to the swift restoration of covalent cross-linking networks. Furthermore, the findings demonstrated that recycled films enhanced tensile strength and modulus. Enhanced mechanical characteristics of the films after reprocessing, as opposed to the first synthesized samples, may be attributed only to the improved compatibility of the dispersion medium DMF, in contrast to the original water used during the initial synthesis. The structural analysis of the films before and after reprocessing via FTIR revealed that the characteristics peaks of the carbamate (C=O) vibrational band (1700-1730 cm^{-1}), the crosslink stretching vibrations (C-O-C), and N-H stretching bands were intact in the reprocessed films as can be seen in **Figure S5.10**a-b. Furthermore, the DSC graph of PU, PS, and PWL50S before and after reprocessing is depicted in **Figure S5.11**a-b**.** The samples' melt temperature (T_m) didn't change significantly, while a significant glass transition temperature (T_g) shift was observed for all the samples.

Table 5.1. PU films' elongation, tensile strength, and modulus as prepared and recycled.

Sample	**Elongation, %**		**Tensile strength, MPa**		**Modulus, MPa**		**Contact angle, °**	
	Virgin	Recycled	Virgin	Recycled	Virgin	Recycled	Virgin	Recycled
PS	50±3.6	59.1±0.6	4.5±0.1	9.64±0.4	209±149	796.9±151	90±2	90±0.5
PKL10S	85±3.9	56.1±10	14.9±3	47.35±5	584.5±123	2006.3±22	30±2	29±5
PWL10S	74.3±8.4	9.3±0.5	3.9±0.7	39.8±2	350±166	592.6±157	140±3	142±3
PWL50S	20.4±9.5	10.7±4.5	2.4±0.2	10.2±0.1	92.7±41	447.1±2.6	158±2	160±3

The term "virgin" refers to the specimens in their as-prepared state.

The T_g of the initially manufactured PU varies between -34.9° and 0.61° in the reprocessed samples. Similarly, the T_g of PS changed from -41.6° to 0.53°, and the T_g of PWL50S changeds from -35.1° to -15.5°. The rise in T_g signifies an augmentation in crystallinity and crosslinking after reprocessing the films, potentially arising from a more organized structure in the PU polymer that would restrict molecular movement [78]. This alteration is noteworthy in PU and PS, however the modification in PWL50S is comparatively less pronounced. Including DMF in the recycling process might impede the movement of polymer chains because of intensified solvent-polymer interactions, resulting in an elevated T_g [79, 80]. In contrast, the original synthesis formulation used water, which might not facilitate strong interaction, leading to decreased T_g. The improved higher crystallinity, as indicated by higher T_g

after reprocessing, is consistent with the improved mechanical properties of the films (**Table 5.1** and **Figure S5.7**f).

5.4.9. Biodegradability

The biodegradability of PU, PS, and PWL50S films was assessed in compost media at room temperature. SKL, WL, and SL polymer's degradability was also evaluated to understand the biodegradability of the films (**Figure 5.5**). The control sample for this test was starch, and the results are presented in **Figure S5.13**, showing a 20% degradability after 5 days, which is consistent with previous reports [81]. PU films were not biodegradable at all (i.e., almost zero biodegradability), while PWL50S and PS had better biodegradability. The non-degradability of PU films is a well-established fact owing to their synthetic composition, hydrolysis resistance, and high durability[82]. The improved degradability of the lignin-containing films (PWL50S and PS) is a result of its biodegradable component SL (9%) and WL (8%) in the film, as can be seen in **Figure 5.5**.The slight improvement in the degradability of PU films after the inclusion of lignin is encouraging and comparable with other studies where biopolymer such as cellulose were coated with PU the degradability of the material were around 12.5% for the 5 days of the test run [83].

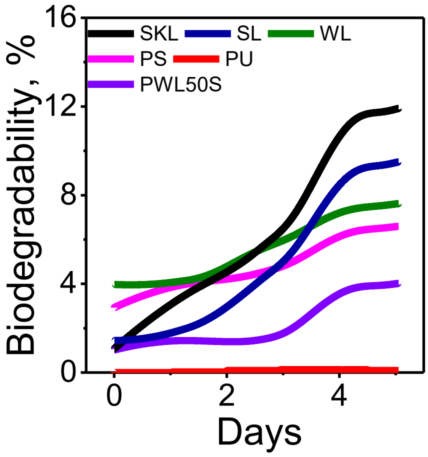

Figure 5.5. Biodegradation analysis of SKL, WL, and SL polymers and PU, PS, and PWL50S films.

The FTIR spectra of the samples after the biodegradability test were conducted and presented in **Figure S5.12**a-b.

When compared to the samples before biodegradable analysis (**Figure S5.5**), the samples undergone the biodegradation had a significant increase in 3340 cm^{-1}, indicating an increase in the hydroxyl group in WL, SL, and SKL. Also, the decreasing intensity in 1600 cm^{-1}, 1510 cm$^{-1,}$ and 1425 cm^{-1} bands indicate the breakdown of the aromatic C=C in the samples after biodegradability test (**Figure S5.12**a). Furthermore, increased intensity of C=O stretching bands in 1700 cm^{-1} was observed for the samples SKL, WL, and SL, indicating degradation of C=C bonds because of oxidation, consistent with the higher degradation of the samples (**Figure 5.5**). On the other hand, the PU films show similar FTIR peaks to those before degradation which is consistent with almost 0% degradation (**Figure 5.5**). In contrast, PS and PWL50S films, after the degradation test, show an increase in the hydroxyl groups and the C=O vibrational bands consistent with the increase of the bonds in SL and WL. The later change was significantly higher for PS (**Figure S5.12)** than the other ones before the biodegradation (**Figure S5.10)**. The FTIR analysis after biodegradation tests for the samples reveling the change in the hydroxyl, C=O and C=C bonds is consistent with the degradability results (**Figure 5.5**).

5.4.10. Implications

The primary focus of research on PU polymers revolves around the following problems. 1. Increasing the use of bio-based polymers in PU synthesis. 2. Enhancing thermal stability, biodegradability, and recyclability of PU. Increasing the hydrophobicity of PU materials [11]. One of the significant issues of including biopolymers in PU is that the performance of the final material, such as hydrophobicity, drops significantly [84]. Similar to the current study, in another study PU films' water contact angle values was improved, but the formulation included non-bio-based ingredients, such as silicide and fluoride [85-87]. In the past, lignin was used as a filler in the production of PU film with limited quantity due to the negative impact of lignin on PU qualities (**Table 5.2)**. The current study described in this paper employed 50.12% of modified lignin (WL and SL) in PU formulation. Based on the yield for both WL and SL (as shown in supporting information), the overall proportion of lignin in the PU formulation was 25.06%, which is significantly more significant than, and a much more superior hydrophobicity, thermal stability, and flame retardancy to, the previously reported results with (**Figure 5.6**). A Further noteworthy finding of this study is that SKL at a concentration of 10% was integrated into a PU film in the presence of lignin-based dispersant, SL. This indicates that the affinity of lignin, and its incorporation, in PU formulation would be improved not only by its functionalization but also by employing its derivative as a dispersant.

Table 5.2. Comparing lignin concentration, tensile strength, water contact angle, and limiting oxygen index value from this work and existing work.

Composition	Method of lignin modification	Maximum lignin concentration, %	Tensile strength, MPa	WCA, °	LOI, %	Reference
Industrial alkali lignin,ZnO, PU	Quaternization (QAL) QAL/ZnO composite	1.2	25	×	×	[20]
Kraft lignin, 29.45 μm particle size and WPU	Silanization with 3-aminopropyltriethoxy silane 99%	2	7	×	×	[21]
Lignin, PU, DMAc	Unmodified	3	57	110.3	×	[67]
kraft lignin, TiO_2, water-based PU	Sulfonation	2.8	9.9	85.9	×	[68]
Lignin, Isocyanate	Lignin urethane modification	30	13.3	×	×	[69]
Lignin, amine-modified silica, and isocyanate	Lignin liquefaction	3	9.2	73.2	×	[88]
Lignin, WPU	Lignin nanoparticles	5	58	114	×	[18]
Softwood kraft lignin, WPU	Silanization, Sulfoethylation	50.12	2.6	155	26	This work

Note, “×” means not reported.

5.5. Conclusion

A novel water-based superhydrophobic, flame-retardant, and recyclable PU film was prepared using lignin and PU water emulsion. In two different pathways, SKL was utilized to generate a superhydrophobic and flame-retardant material and a dispersant for a single use in the PU formulation. The polymerization of SKL and aminopropyl/methyl silsesquioxane (WAPMSS) and the existence of C-O-Si linkage were confirmed by NMR, XPS, and FTIR techniques. Introducing WL (50 wt.%) to an aqueous PU emulsion improved WCA and SA values by 60° and 4°, respectively. In the PU matrix, WL particles formed nano and micro air pockets (as observed via SEM), promoting surface superhydrophobicity. However, due to poor dispersion and aggregation of WL particles, the PWL50 film had lower mechanical strength than pure PU. Incorporating SL (0.12 wt.%) as a dispersant in the PU formula increased tensile strength and elongation while maintaining the superhydrophobicity of

PWL50S with a water contact angle of 158±2° and a sliding angle lesser than 10°. SL also enhanced the thermal stability of PWL50S by a 31° rise in the T50% compared to PWL50. In addition, the LOI value increased from 18.5 to 21% when 0.12 wt.% SL was incorporated in PU, and from 24.5 to 25.5 when SL was incorporated in PWL50. PWL50S coated wood, metal, and filter paper exhibited superhydrophobic characteristics for water, NaOH (0.1 M), and HCL (0.1 M) droplets. Moreover, wood coated with PWL50S had a higher LOI and a lower SDR than PU and PKL10. In addition, the films exhibit exceptional recyclability when re-processed and cured by a solvent, maintaining mechanical strength and water contact values. The superhydrophobic characteristics of the coated wood stood sandpaper abrasion (160 cm), UV-ozone exposure (600 min), and thermal exposure (200 °C for 500 min). The film also showed better biodegradability compared to pure PU, indicating that the introduction of lignin improved the material's environmental footprint. The findings of this study demonstrate that lignin can be integrated into PU films at a significant proportion (>25 wt.%). Incorporating lignin imparts unique superhydrophobicity, thermal stability, and flame retardancy to the films and wood coatings. This, in turn, reduces the environmental impact of PU-based materials and opens possibilities for using this lignin-incorporated PU in other applications beyond coating.

5.6. References

[1] J. O. Akindoyo, M. Beg, S. Ghazali, M. Islam, N. Jeyaratnam, A. Yuvaraj, *Rsc Advances* **2016**, 6, 114453.

[2] U. Meier-Westhues, E. Squiller, *KG: Hannover, Germany* **2019**.

[3] F. E. Golling, R. Pires, A. Hecking, J. Weikard, F. Richter, K. Danielmeier, D. Dijkstra, *Polymer International* **2019**, 68, 848.

[4] N. Qiu, L. Wang, S. Wu, D. S. Likhachev, *Engineering Failure Analysis* **2015**, 55, 208.

[5] D. Yang, S. Wang, R. Zhong, W. Liu, X. Qiu, *Frontiers of Chemical Science and Engineering* **2019**, 13, 59.

[6] J. C. Q. Amado, in *Thermosoftening Plastics*, Vol. 2019, IntechOpen London, UK, 2019.

[7] D. J. Lyman, *Journal of Polymer Science* **1960**, 45, 49.

[8] H. W. Engels, H. G. Pirkl, R. Albers, R. W. Albach, J. Krause, A. Hoffmann, H. Casselmann, J. Dormish, *Angewandte Chemie International Edition* **2013**, 52, 9422.

[9] C. O. Adetunji, O. T. Olaniyan, O. A. Anani, A. Inobeme, J. T. Mathew, *Polyurethane Chemistry: Renewable Polyols and Isocyanates* **2021**, 393.

[10] R. H. Bean, T. E. Long, *Polymer International* **2024**, 73, 5.

[11] H. Zhao, W.-C. Gao, Q. Li, M. R. Khan, G.-H. Hu, Y. Liu, W. Wu, C.-X. Huang, R. K. Y. Li, *Advances in Colloid and Interface Science* **2022**, 303, 102644.

[12] X. Ma, J. Chen, J. Zhu, N. Yan, *Macromolecular Rapid Communications* **2021**, 42, 2000492.

[13] C. Liu, P. Luan, Q. Li, Z. Cheng, P. Xiang, D. Liu, Y. Hou, Y. Yang, H. Zhu, *Advanced Materials* **2021**, 33, 2001654.

[14] D. Zhang, J. Zeng, W. Liu, X. Qiu, Y. Qian, H. Zhang, Y. Yang, M. Liu, D. Yang, *Green Chemistry* **2021**, 23, 5972.
[15] M. R. Ridho, E. A. Agustiany, M. Rahmi Dn, E. W. Madyaratri, M. Ghozali, W. K. Restu, F. Falah, M. A. Rahandi Lubis, F. A. Syamani, Y. Nurhamiyah, *Advances in Materials Science and Engineering* **2022**, 2022, 1.
[16] Y. Chen, S. Fu, H. Zhang, *Colloids and Surfaces A: Physicochemical and Engineering Aspects* **2020**, 585, 124164.
[17] H. Li, Y. Liang, P. Li, C. He, *Journal of Bioresources and Bioproducts* **2020**, 5, 163.
[18] L. Wu, S. Liu, Q. Wang, Y. Wang, X. Ji, G. Yang, J. Chen, C. Li, P. Fatehi, *Industrial Crops and Products* **2022**, 177, 114526.
[19] G. Qi, W. Yang, D. Puglia, H. Wang, P. Xu, W. Dong, T. Zheng, P. Ma, *Materials & Design* **2020**, 196, 109150.
[20] X. Wang, R. O. Nayanathara, W. Leng, E. B. Caldona, L. Liu, R. C. Advincula, Z. Zhang, X. Zhang, *Journal of Agriculture and Food Research* **2022**, 10, 100452.
[21] H. Wang, X. Qiu, W. Liu, F. Fu, D. Yang, *Industrial & Engineering Chemistry Research* **2017**, 56, 11133.
[22] Q. Y. Ng, J. H. Low, M. M. Pang, C. I. Idumah, *Journal of Polymers and the Environment* **2023**, 31, 688.
[23] M. Shi, X. Wang, J. Yang, *Polymer Bulletin* **2023**, 80, 5553.
[24] G. Rossignolo, G. Malucelli, *Green Chemistry* **2024**.
[25] R. Guo, Q. Zhang, Y. Wu, H. Chen, Y. Liu, J. Wang, X. Duan, Q. Chen, Z. Ge, Y. Zhang, *Advanced Materials* **2023**, 35, 2212130.
[26] X. Wang, S. Zhan, Z. Lu, J. Li, X. Yang, Y. Qiao, Y. Men, J. Sun, *Advanced Materials* **2020**, 32, 2005759.
[27] D. dos Santos Rosa, D. M. Lenz, *Biodegrad. Eng. Technol. Intech Rij. Croat* **2013**, 433.
[28] M. Cregut, M. Bedas, M. J. Durand, G. Thouand, *Biotechnology advances* **2013**, 31, 1634.
[29] D. Wang, Y. Shan, L. Liu, M. Diao, J. Yao, *Industrial Crops and Products* **2024**, 208, 117905.
[30] X. Chen, T. Guo, X. Mo, L. Zhang, R. Wang, Y. Xue, X. Fan, S. Sun, *International Journal of Biological Macromolecules* **2023**, 231, 123334.
[31] B. Bemerw Kassaun, P. Fatehi, *Chemical Engineering Journal* **2024**, 493, 152582.
[32] K. Bahrpaima, P. Fatehi, *ChemSusChem* **2018**, 11, 2967.
[33] X. Meng, C. Crestini, H. Ben, N. Hao, Y. Pu, A. J. Ragauskas, D. S. Argyropoulos, *Nat. Protoc.* **2019**, 14, 2627.
[34] L.-S. Johansson, J. Campbell, K. Koljonen, P. Stenius, *Applied surface science* **1999**, 144, 92.
[35] N. M. Stark, D. J. Yelle, U. P. Agarwal, *Lignin in polymer composites* **2016**, 49.
[36] J. Zhang, H. Cui, J. Qiu, X. Wang, Y. Zhong, C. Yao, L. Yao, Q. Zheng, C. Xiong, *Food Chemistry* **2023**, 410, 135364.
[37] M. Rostami, M. Mohseni, Z. Ranjbar, *International journal of adhesion and adhesives* **2012**, 34, 24.
[38] Y. Deng, S. Huang, Y. Liu, J. Xu, Z. Li, S. He, J. Zhang, *Journal of Macromolecular Science, Part A* **2023**, 60, 63.
[39] L. A. Riddell, F. J. Enthoven, J.-P. B. Lindner, F. Meirer, P. C. Bruijnincx, *Green Chemistry* **2023**, 25, 6051.
[40] X. Peng, J. Zhang, P. Xiao, *Advanced Materials* **2024**, 2400178.
[41] B. Mamatha, D. Sujatha, S. Nath, D. Uday, A. Nandanwar, presented at *Wood is Good: Current Trends and Future Prospects in Wood Utilization*, **2017**.
[42] K. Sykam, S. S. Hussain, S. Sivanandan, R. Narayan, P. Basak, *Progress in Organic Coatings* **2023**, 179, 107549.
[43] N. Ghavidel, P. Fatehi, *ChemSusChem* **2020**, 13, 4567.
[44] M. Nagy, M. Kosa, H. Theliander, A. J. Ragauskas, *Green Chemistry* **2010**, 12, 31.
[45] N. Mahmood, Z. Yuan, J. Schmidt, C. C. Xu, *Bioresource technology* **2013**, 139, 13.

[46] D. Ibarra, L. García-Fuentevilla, G. Domínguez, R. Martín-Sampedro, M. Hernández, M. E. Arias, J. I. Santos, M. E. Eugenio, *International Journal of Molecular Sciences* **2023**, 24, 2359.
[47] N. Riehle, S. Thude, A. Kandelbauer, G. E. Tovar, G. Lorenz, *JoVE (Journal of Visualized Experiments)* **2019**, e58590.
[48] C. Zhao, J. Huang, L. Yang, F. Yue, F. Lu, *Industrial & Engineering Chemistry Research* **2019**, 58, 5707.
[49] L. An, G. Wang, H. Jia, C. Liu, W. Sui, C. Si, *International journal of biological macromolecules* **2017**, 99, 674.
[50] N. Ghavidel, M. K. Konduri, P. Fatehi, *Industrial Crops and Products* **2021**, 172, 113950.
[51] H. Schmidt, H. Scholze, A. Kaiser, *Journal of Non-Crystalline Solids* **1984**, 63, 1.
[52] X. Chen, X. Wang, D. Fang, *Fullerenes* **2020**, 28, 1048.
[53] S. Liu, W. Cao, Y. Wang, W. Wei, L. Li, H. Jin, L. Guo, *Waste Management* **2022**, 153, 240.
[54] A. Miletić, P. Panjan, M. Čekada, L. Kovačević, P. Terek, J. Kovač, G. Dražič, B. Škorić, *Ceramics International* **2021**, 47, 2022.
[55] M. Arefmanesh, T. V. Vuong, J. K. Mobley, M. Alinejad, E. R. Master, M. Nejad, *Industrial & Engineering Chemistry Research* **2020**, 59, 18740.
[56] A. Kaur, P. Chahal, T. Hogan, *IEEE Electron Device Letters* **2015**, 37, 142.
[57] M. Pomeroy, *Materials & design* **2005**, 26, 223.
[58] N. A. Miele, S. Volpe, E. Torrieri, S. Cavella, *Journal of Food Engineering* **2022**, 331, 111123.
[59] A. K. Mishra, D. Chattopadhyay, B. Sreedhar, K. Raju, *Progress in organic coatings* **2006**, 55, 231.
[60] C. Jiang, H. He, X. Yao, P. Yu, L. Zhou, D. Jia, *Journal of Applied Polymer Science* **2018**, 135, 45759.
[61] Z. Wu, H. Wang, X. Tian, M. Xue, X. Ding, X. Ye, Z. Cui, *Polymer* **2014**, 55, 187.
[62] M. A. Kashfipour, N. Mehra, J. Zhu, *Advanced Composites and Hybrid Materials* **2018**, 1, 415.
[63] M. Jamali, A. Moghadam, H. V. Tafreshi, B. Pourdeyhimi, *Applied Surface Science* **2018**, 456, 626.
[64] B. Samuel, H. Zhao, K.-Y. Law, *The Journal of Physical Chemistry C* **2011**, 115, 14852.
[65] A. Bansal, H. Yang, C. Li, K. Cho, B. C. Benicewicz, S. K. Kumar, L. S. Schadler, *Nature materials* **2005**, 4, 693.
[66] G. Dias, M. A. Prado, C. Carone, R. Ligabue, A. Dumas, F. Martin, C. Le Roux, P. Micoud, S. Einloft, *Polymer Bulletin* **2015**, 72, 2991.
[67] X. Xiao, J. Jiang, Y. Wang, B. Wang, T.-Q. Yuan, Q. Shi, X. Liao, B. Shi, R.-C. Sun, *ACS Sustainable Chemistry & Engineering* **2021**, 9, 9053.
[68] X. Li, Y. Liu, X. Ren, *International Journal of Biological Macromolecules* **2022**, 216, 86.
[69] B. M. Kim, J. S. Choi, S. Jang, H. Park, S. Y. Lee, J. Jung, J. Park, *Polymers* **2023**, 15, 3987.
[70] J. Huang, H. Wang, W. Liu, J. Huang, D. Yang, X. Qiu, L. Zhao, F. Hu, Y. Feng, *International Journal of Biological Macromolecules* **2023**, 225, 1505.
[71] E. A. Agustiany, M. Rasyidur Ridho, M. Rahmi DN, E. W. Madyaratri, F. Falah, M. A. R. Lubis, N. N. Solihat, F. A. Syamani, P. Karungamye, A. Sohail, *Polymer Composites* **2022**, 43, 4848.
[72] E. I. Evstigneev, *Russian Journal of Applied Chemistry* **2011**, 84, 1040.
[73] W. G. Glasser, *Frontiers in chemistry* **2019**, 7, 565.
[74] Y. Liu, Y. Shao, Y. Wang, J. Wang, *Colloids and Surfaces A: Physicochemical and Engineering Aspects* **2022**, 648, 129335.
[75] S. Rabbani, E. Bakhshandeh, R. Jafari, G. Momen, *Progress in Organic Coatings* **2022**, 165, 106715.
[76] E. Pearce, *Flame-retardant polymeric materials*, Springer Science & Business Media, **2012**.
[77] L. Imhof, K. Stueben, *Polymer Engineering & Science* **1973**, 13, 146.
[78] C. Bakkali-Hassani, D. Berne, V. Ladmiral, S. Caillol, *Macromolecules* **2022**, 55, 7974.
[79] S. Kim, K. Li, A. Alsbaiee, J. P. Brutman, W. R. Dichtel, *Advanced Materials* **2023**, 35, 2305387.

[80] M. I. León-Campos, J. A. Claudio-Rizo, D. A. Cabrera-Munguía, L. E. Cobos-Puc, M. Caldera-Villalobos, M. O. González-Díaz, F. J. Enríquez-Medrano, *Journal of Polymer Research* **2024**, 31, 213.
[81] F. M. de Souza, P. K. Kahol, R. K. Gupta, in *Polyurethane chemistry: Renewable polyols and isocyanates*, ACS Publications, 2021.
[82] S. Park, J. Kim, J.-H. Choi, J.-C. Kim, J. Kim, Y. Cho, S. Jung, H. W. Kwak, I.-G. Choi, *International Journal of Biological Macromolecules* **2023**, 253, 127472.
[83] A. Magnin, E. Pollet, V. Phalip, L. Avérous, *Biotechnology Advances* **2020**, 39, 107457.
[84] L. Zhang, J. Zhou, J. Huang, P. Gong, Q. Zhou, L. Zheng, Y. Du, *Industrial & engineering chemistry research* **1999**, 38, 4284.
[85] D. Macocinschi, D. Filip, S. Vlad, *Polymer Composites* **2010**, 31, 1956.
[86] J. Wu, X. Wu, C. Mu, C. Wang, W. Lin, *Progress in Organic Coatings* **2024**, 188, 108174.
[87] S. Dai, F. Yan, J. Ma, J. Guo, H. Hu, Y. Liu, L. Liu, Y. Ao, *Composites Science and Technology* **2024**, 245, 110328.
[88] H. Zheng, M. Pan, J. Wen, J. Yuan, L. Zhu, H. Yu, *Industrial & Engineering Chemistry Research* **2019**, 58, 8050.
[89] B. Xue, Y. Yang, R. Tang, Y. Sun, S. Sun, X. Cao, X. Li, *BioResources* **2019**, 14, 6100.

Chapter 6: 3D printable lignin-caprolactone copolymer

Banchamlak Bemerw Kassaun[1,2], *Luyao Wang*[2], *Oskar Backman*[2], *Chunlin Xu*[2], *Pedram Fatehi**[1,2]

[1]*Department of Chemical Engineering, Lakehead University, 955 Oliver Road, Thunder Bay, ON P7B 5E1, Canada,*

[2]*Laboratory of Natural Materials Technology, Faculty of Science and Engineering, Åbo Akademi University, Henrikinkatu 2, Turku, FI-20500, Finland.*

Under review in Green Chemistry

The contribution of Banchamlak Bemerw Kassaun to this work was the conception of the original draft, visualization, validation, formal analysis, data curation, and conceptualization.

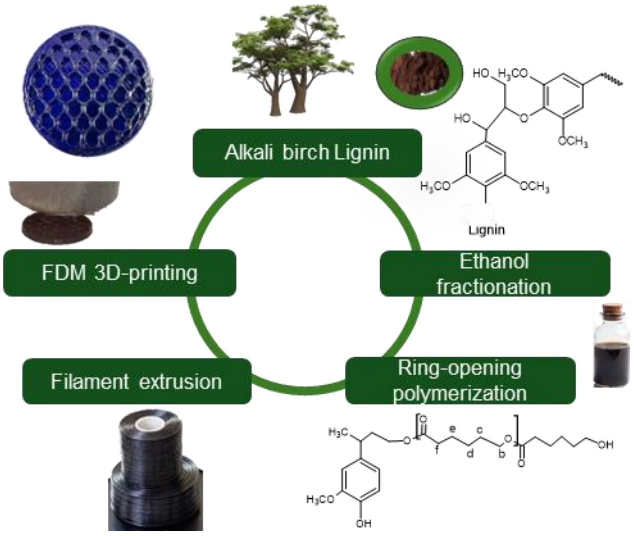

6.1. Abstract

The use of lignin in three-dimensional (3D) printing materials has been considered a viable strategy to generate sustainable 3D printing objects. However, complex molecular structures, high viscosity, and charring of lignin impair its 3D printability. This study investigated the synthesis of lignin-caprolactone (CL) polymer and its fused deposition modeling (FDM)-3D printing performance. Lignin-caprolactone polymerization was carried out with ethanol-soluble fractionated birch alkali lignin (BL_E) and caprolactone. Results showed that ethanol fractionation reduced lignin's average molecular weight from 22870 to 3827 g mol^{-1} and increased its hydroxyl group concentration. The melt temperature, viscosity, and polymerization degree were considered in the Box-Behnken surface approach to obtain lignin-caprolactone, BLPO, with the best results. Compared to unfractionated lignin caprolactone (BLPO), fractionated lignin-caprolactone polymer (BL_EPO) had a 10.9% higher grafting ratio, 69.43% rise in melt temperature (T_m), and 85.71% increase in glass transition temperature. The melt rheological investigation showed that BL_EPO's lower viscosity (160.9 Pa.s) and shear-thinning behavior than those of BLPO made it more suitable for the 3D printing application. The 15 °C delay in G' and G'' cross-over points of BL_EPO compared to BLPO improved 3D printing adhesion layers. Furthermore, BL_EPO exhibited superior mechanical characteristics and a greater water contact angle (92°) than BLPO. The reduction in molecular weight distribution of lignin (due to ethanol fractionation) prior to copolymerization facilitated the production of a 3D-printable polymer containing 75% lignin. By tailoring the melt and viscosity parameters of the lignin-caprolactone copolymer, lignin-copolymer exhibited improved 3D printing techniques, which offers advantages over lignin composite 3D printing.

Keywords: lignin, caprolactone, three-dimensional printing, sustainable polymers

6.2. Introduction

Fused deposition modeling (FDM) is a widely used extrusion-based technique for fabricating 3D printing materials [1, 2]. Generally, rheological properties, thermal conductivity, and shear rate influence polymeric materials' printability via FDM [3]. Currently, acrylonitrile butadiene styrene, polyethylene terephthalate, polycarbonate, polyether ether ketone, polypropylene, polylactic acid, and nylon are commonly used in FDM-3D printing [4]. Despite their high efficiency, they are environmentally unfriendly and expensive [2]. Thus, the incentive for generating sustainable 3D printing material is high.

The use of various biomass materials in 3D printing, such as cellulose and hemicellulose, has gained attention due to their renewable nature and potential to reduce environmental impacts [5]. These materials have been utilized to produce biodegradable composites for fabricating 3D printed components, which provide advantages for sustainable manufacturing [6]. Nevertheless, the usability of cellulose and hemicellulose in 3D printing in the FDM technique is limited owing to their low-temperature stability, moisture sensitivity, weak mechanical properties, and challenges in extrusion caused by their fibrous nature [7]. Thanks to its higher thermal stability, moisture resistance, higher mechanical properties, antioxidant, antibacterial, and biodegradable properties, lignin, i.e., a plentiful and sustainable biopolymer, has gained attention for fabricating sustainable 3D printing materials [8, 9].

Lignin has traditionally been underutilized and dominantly burnt as an energy source [10]. Its rich aromatic structure makes it suitable for creating valuable products, such as bio-adhesives, bioplastics, and carbon fibers [11]. Nevertheless, the complex structure of lignin, its undesired thermal properties (e.g., its ability to char at high temperatures), and rheological properties (e.g., shear thickening behavior, which causes increased resistance to flow or deformation) have hindered its application in 3D printing applications [12-14]. For this reason, the application of lignin in 3D printing via FDM is limited to lignin being blended at a low quantity (e.g., 2-40 %) with other polymers, such as acrylonitrile-butadiene-styrene (ABS), polylactic acid (PLA) and polyamide (PA) [14-17]. For example, Nguyen et al. mixed hardwood lignin and thermoplastic nylon 12 and reported improved rigidity and decreased melting viscosity of lignin for use as a 3D printing material [14]. In another study, an organosolv hardwood lignin exhibited high compatibility with polylactic acid (PLA), and its 15 wt.% lignin-loaded composition exhibited outstanding printability via the FDM process [12]. While incorporating lignin into polymer blends offers advantages, the exceptional properties (e.g., mechanical stability, UV protection, and antioxidant) of lignin in the blend are constrained by the percentage of lignin (40 wt.%

max) in the matrix [18, 19]. Additionally, the blending process frequently results in phase separation, further restricting the ultimate characteristics of the printed material. One way to widen the use of lignin in a 3D printable formulation is to crosslink lignin and other thermoplastic polymers to improve their thermal and rheological properties. The performance of polymerized lignin in 3D printing applications has yet to be explored. This presented herein examined polymerizing lignin with caprolactone (CL) to generate sustainable 3D printing material as the first objective.

Polycaprolactone (PCL) is a biodegradable polyester with a low melting point of approximately 60 °C and a glass transition temperature of roughly -60 °C [20, 21]. PCL is a favorable thermoplastic polymer for producing FDM scaffolds for tissue engineering applications due to its biocompatibility, biodegradability, low melting temperature, low glass transition temperature, and high thermal stability [22, 23]. Generally, carbon nanotubes, pristine graphene, and tricalcium phosphate are included in the PCL matrix to improve the mechanical properties and structural integrity of PCL materials [24-26]. However, these fillers would limit their biodegradability and biocompatibility [27]. In the past, caprolactone (CL), the monomer for PCL, was polymerized with kraft lignin to produce thermoplastic materials by compression molding with PCL [28]. However, the report did not elaborate on the reaction fundamentals and the molding characteristics of the lignin-caprolactone polymer. As the characteristics of such polymers would significantly impact their 3D printing affinity, the second objective of this study was to understand the polymerization reaction system to achieve a sustainable polymer with the best printing performance.

In this study, the lignin was fractionated by ethanol to reduce its average molecular weight before polymerizing with CL [29, 30]. Ethanol fractionation is chosen for upgrading lignin properties (e.g., molecular weight distribution) due to its simplicity, less severe process conditions, and the specific solubility of lignin in ethanol, as opposed to other techniques, such as lignin depolymerization and acid catalytic upgrading [31-35]. This study presents a ring-opening polymerization of birch alkali lignin (BL) and CL to produce a 3D printable polymer with exceptional flow characteristics. The properties of BL were improved using ethanol fractionation, and the ethanol soluble fractionated lignin (BL_E) resulted in a lower average molecular weight than BL, which was then used to fabricate lignin-caprolactone polymer with best properties (BL_EPO) following the Box-Behnken (BBD) response surface method (RSM). The printability of the selected sample was assessed by running melt rheology. Then, the 3D printing methods of FDM were employed to study the 3D printing performance of the generated sustainable material. The mechanical strength, surface properties, and appearance of 3D-printed structures were evaluated comprehensively. This work demonstrated a promising approach to utilizing polymerized lignin for a microstructurally well-organized 3D printed material fabrication.

6.3. Experimental Section

6.3.1 Materials

Birch alkali lignin (BL) was supplied by CH-Bioforce Oy (Espoo, Finland), ethanol (96%), hexane (99%), ε-caprolactone (CL), dibutyltin dilaurate (DBTDL, 95%), methanol (95%), dimethyl sulfoxide (DMSO-d_6), chloroform ($CDCl_3$), anhydrous pyridine, endo-N-hydroxy-5-norbornene-2,3-dicarboximide, chromium (III) acetylacetonate ($Cr(acac)_3$, 2-chloro-4,4,5,5-tetramethyl-1,3,2-dioxaphospholane (Cl-TMDP), dimethyl sulfoxide-d_6 (DMSO-d_6), chloroform-d containing 0.03%, tetramethylsilane (TMS), and polycaprolactone (PCL, 80,000 g/mol) were purchased from Sigma Aldrich.

6.3.2. Ethanol fractionation of birch alkali lignin

Birch alkali lignin (BL) was fractionated using ethanol. The amount of solvent and lignin was set to 7:1 wt/wt. After stirring for 2 h, the insoluble and soluble parts of lignin were separated using a vacuum filter. The ethanol-soluble part of lignin (BL_E) was taken and treated by a rotary evaporator to separate lignin from ethanol. Subsequently, samples were collected, washed with hexane, and dried in a 60°C oven for 48 hours. **Equation S6.**1 (Appendix 6A) was used to measure the yield of the lignin fractionation process.

6.3.3. Experimental design by Box-Behnken (BBD)- response surface method (RSM) for lignin-caprolactone (BL_EP) polymerization

The experiments for the polymerization of lignin and caprolactone (BL_EP) were designed using response surface methodology (RSM) based on a box-Behnken design (BBD). The BBD-RSM approach was used to evaluate the impact of three independent factors on the BL_EP polymer's viscosity and melt temperature. To accomplish this goal, the influence of three experimental factors (the ratio of caprolactone monomer to the hydroxyl group of lignin (CL/OH), the concentration of catalyst, and the reaction duration) was assessed. These factors were evaluated at three levels: low, medium, and high, represented by coded values of -1, 0, and +1, respectively, in **Table S6.1**. To achieve this objective, 17 experiments were devised using the Box-Behnken Design (BBD) methodology. All second-order regression coefficients were determined by the statistical analysis of the findings using the ANOVA technique. Afterward, the best reaction conditions were determined by merging the acquired outcomes and graphing an equation for each response variable. The statistical analysis of multivariable equations, derivation of coefficients for a second-order regression model, and the examination of the impacts of factors on variables were conducted using design expert statistical software (Version 12, State-Ease Inc, USA). All BBD-RSM equations are listed in **Equations S6.**2-**S6.**5.

6.3.4. Polymerization of lignin and caprolactone

Lignin and caprolactone polymerization generates lignin caprolactone polymer (BL_EP) without needing a solvent [28]. Caprolactone was used as a monomer for ring-opening polymerization (ROP), lignin was used as a micro initiator, and DBTDL was used as a catalyst. The BL_E was mixed with CL based on the CL/OH ratio of lignin (as listed in **Table S6.1**) at 50°C under nitrogen and stirred for 30 min. DBTDL (based on the wt.% ratio of lignin listed in **Table S6.1**) was added slowly to the mixture, which was heated to 150 °C under magnetic stirring (250 rpm). ROP is a form of chain-growth polymerization in which the terminal end of a polymer chain acts as a reactive center where further cyclic monomers (CL) can react by opening its ring structure and forming a longer polymer chain. The -COO- group is formed via the opening of the CL ring and reacts with the OH group of lignin to form an ester linkage, leaving -OH at the end of the CL chain, which subsequently reacts with CL monomers to grow a PCL

(**Figure S6.1**b). When the reaction was complete (for the durations listed in **Table S6.1**), the product was cooled to room temperature, and the mixture was washed several times with cool methanol to remove impurities. The overall schematics of the reaction are described in **Figure S6.1**a. The optimized conditions were a CL/OH ratio (mmol/g) of 1.1, a reaction time of 420 min, and a catalyst concentration of 1wt.% based on lignin amount (**Table S6.2**), which generated the sample labeled as BL_EP. A control sample with unfractionated lignin (BL) was produced under the same conditions as BL_EP and labeled as BLP.

6.3.5. Lignin filament extrusion

Samples prepared under the optimization conditions were used to generate filaments. The lignin caprolactone polymer filament was generated using ethanol-fractionated lignin copolymer under optimized conditions (BL_EP), and the control sample was generated by unfractionated lignin under the same conditions and labeled as BLP. The BL_EP and BLP were extruded using a compounding twin extrusion machine (Xplore MC15HT). The extrusion was conducted at 100°C for BLPO and 80°C for BL_EPO at a speed of 5 rpm to generate filaments with a 1.5 -1.7 mm diameter.

6.3.6. 3D printing of BLPO and BL_EPO polymers

The printability of BLPO and BL_EPO was assessed by the fused deposition modeling (FDM) method using extrusion-based 3D printing (Printer One, BRINTER Ltd., Finland) equipped with a 0.55 mm nozzle diameter. The samples were prepared as a pallet by chopping the prepared filaments and fed to a granular tool printhead with the temperature set at 100°C for BLPO and 80°C for BL_EPO. The print bed was prepared by coating a tin PCL layer for better grip throughout the study. An eight-layered honeycomb structure was printed at a speed of 8 mm/s, pressure of 200 mbar, layer height of 0.2 mm, and shell thickness of 0.5 mm.

6.3.7. Characterization of lignin and lignin-caprolactone polymers

*6.3.*7.1. Molecular weight analysis

The molecular weight of lignin derivatives (BL and BL_E) and the copolymers (BL_EP2, BL_EP5, BL_EP6, BL_EPO, and BLPO) was assessed with a size exclusion chromatography (SEC) equipped with a multiangle light scattering detector and differential refractive index concentration detector (MALLS(IR)). Vacuum oven-dried (40°C) samples were prepared in a clean HPLC vial at 10 mg/mL concentration in DMSO/0.05M LiBr eluent, followed by filtration using 0.2 μm Nylon filters before SEC analysis. The separation was performed on a Jordi Gel glucose mixed-bed guard column (50 mm×10 mm i.d) and a Jordi Gel GBR mixed-bed column (250 mm×10 mm i.d). The molecular weight analysis was performed using the following parameters: 0.5 mL min^{-1} flow rate, 60 °C column temperature, 100 μL injection volume, and 0.15 mL g^{-1} dn/dc value. The data was evaluated by Astra software, version 7.3.3 [36].

6.3.7.2. NMR analysis

The hydroxyl groups of BL, BL$_E$, BL$_E$P2, BL$_E$P5, and BL$_E$P6 (reaction conditions available in **Table S6.1** and **Table S6.3**), BL$_E$PO, and BLPO were quantified by ^{31}P NMR [37]. The samples were prepared by dissolving 20 mg vacuum oven-dried (40°C) samples in the solvent mixture of 0.55 mL of anhydrous pyridine and $CDCl_3$ (1.6:1, v/v) that contained relaxation reagent of chromium (III) acetylacetone (Cr(acsac)$_3$, 1.3 μmol) and internal standard of endo-N-hydroxy-5-norbornene-2-3-dicarboximide (12 μmol). The ratio of internal standard to lignin was set to 0.6 mmol g^{-1}. The hydroxyl groups were phosphorylated with 0.1 mL of 2-chloro-4,4,5,5-tetramethyl-1,3,2-dioxaphospholane for 30 min before ^{31}P-NMR measurement. The concentration of Cr(acac)$_3$ was 0.002 M to ensure the complete relation of the phosphorus nuclei before applying the radiofrequency pulse. Spectrum acquisition parameters were a 10 s pulse delay, 2.0 s acquisition time, and 64 scans. The hydroxyl group was used to calculate the grafting percentage of CL on the hydroxyl group of lignin according to **Equation S6.**6.

^{1}H-NMR and HSQC NMR analyses were performed on BL, BL$_E$, BL$_E$P, BLPO, and BL$_E$PO samples. The ^{1}H-NMR setup was set to 16 scans, 3.28 s acquisition, 1s relaxation, and 90° pulse at room temperature. BL and BL$_E$ samples were prepared by dissolving the vacuum oven-dried (40°C) samples in 80 mg/mL DMSO, while BL$_E$P and BLPO were prepared by dissolving 80 mg samples in 0.75 mL of $CDCl_3$ (0.03v/v% of TMS). The HSQC NMR spectra were acquired using the HSQCEDETGPSISP2.3 pulse sequence with a relaxation delay of 2.0s and an acquisition time of 0.15s, recording 256 increments of 80 scans per increment. The results were assessed using Top Spin 4.02 software. The ^{1}H-NMR spectra of the BL$_E$PO and BLPO were used to quantify the degree of polymerization (n) in the PCL chain segments, following **Equation S6.**7. While the quantification of major linkages of BL and BL$_E$ were performed according to **Equation S8-S9**.

6.3.7.3. Thermal analysis

The thermal stability of BL, BL$_E$, BL$_E$P (17 samples), BL$_E$PO, and BLPO samples was assessed by a Q500 thermogravimetric analyzer (TA Instrument, USA). Around 10 mg of vacuum oven-dried (40 °C) samples were weighed into an alumina disposable crucible (T 2101127, China) and heated from 30°C to 800°C at a 10°C min^{-1} under a nitrogen atmosphere at the flow rate of 15 mL min^{-1}. The samples' glass transition temperature (T_g) and melt temperature (T_m) were assessed using a Discovery DSC 250 calorimeter in a heating-cooling-heating cycle under continuous nitrogen at the flow rate of 15 mL min^{-1}. The vacuum oven-dried (40°C) samples were weighed into a Tzero pan (T 140829, Switzerland) sealed with a Tzero lid (T 140826, Switzerland) and then transferred to the calorimeter containing a reference, i.e., an empty sealed Tzero pan. TRIOS v5.5.5.1.5 software was used to determine the T_g and T_m of the samples.

6.3.7.4. Rheology

The viscosity of BL$_E$P (17 samples) was assessed by the BBD-RSM design at each melting temperature using an MCR 702 MultiDrive rheometer (Anton Paar GmbH), a PP25 parallel plate (diameter: 25 mm and gap: 0.5 mm) at a shear rate of 0.1 to 100 s^{-1}. Melt rheological properties of the BLPO and BL$_E$PO samples were assessed by temperature ramp experiment at a 1°C min^{-1} heating rate starting from 130°C and going to a temperature where the first sight of crossover between storage modulus and loss modulus was detected. The data acquisition time was 10 seconds per data point. In addition, the rheological study was conducted on BLPO at a temperature of 100°C and BL$_E$PO at 80°C with a hybrid rotational rheometer (Discovery HR-2, TA Instruments, DE, USA). The analysis included a flow ramp test at a shear rate ranging from 0.01 to 1000 s^{-1} and a frequency sweep test of 1 to 100 rad s^{-1}, with a strain of 63% in the viscoelastic zone.

6.3.7.5. Mechanical Properties

The BL$_E$PO films were prepared by molding, and the mechanical properties of the films were examined using universal testing equipment with a 200 N load cell (Shimadzu Instrone-6800 series, Japan). Samples were cut from cast sheets with a rectangular shape die, measuring 27 cm long, 3.12 cm wide (ASTM D638 type V), and 1.2 mm thick. Five specimens from BL$_E$PO film were evaluated at 50 mm min^{-1} and room temperature, and an average value with a standard error was reported. The BLPO sample cured faster before the film was prepared correctly, and the prepared sample was too brittle to be tested.

6.3.7.6. Contact Angle Analysis and Imaging

Using the sessile drop method, an optical tensiometer assessed the surface wettability of BLPO and BL$_E$PO 3D-printed parts (Theta Lite, Bolin Scientific, Finland). The experiment was conducted by placing a liquid droplet (6-10 µL) onto the flat side of the 3D-printed samples. The contact angle of the droplet was visually measured using a camera for 10 seconds. The contact angle was analyzed using one-attention software, the measurement was performed in three places, and the mean value was reported. An optical microscope (specifically, a Nikon ECLIPSE E200) was used to capture microscopic photographs of the printed samples.

6.4. Result and discussion

6.4.1. Ethanol fractionation of birch alkali lignin

The chemical structure of lignin substantially impacts the characteristics of the material incorporating it [38]. Therefore, the chemical structure, molecular weight, and thermal properties of birch alkali lignin, unfractionated (BL) and ethanol fractionated (BL$_E$), were assessed and reported in **Figure 6.1**. The molar mass distributions of BL and BL$_E$ are illustrated in **Figure 6.1**a, and the average molecular weight (Mw) and polydispersity (ĐM) values are displayed in **Table 6.1**. The BL$_E$ exhibited a significantly lower Mw and ĐM than BL. The reduced Mw and ĐM result from ethanol fractionation, which solubilized part of lignin fragments, reducing lignin's Mw and molar mass dispersibility [30, 39, 40].

The ^{1}H NMR spectra of BL and BL_E polymers are presented in **Figure 6.1**b. The spectra revealed that aromatic protons appeared in the 6.0-7.5 ppm region, methoxy proton at 3.75 ppm, aliphatic proton at 0.85-2.2 ppm, and DSMO solvent at 2.5 ppm [34]. BL_E showed stronger aliphatic signals that belonged to ethanol residues [41]. The quantity of aliphatic, guaiacyl, C5-substituted, and carboxylic hydroxyl groups in BL and BL_E was determined by quantitative ^{31}P NMR analysis (**Figure 6.1**c), and the hydroxyl group concentration of BL and BL_E are listed in **Table 6.1.** Phenolic hydroxyl groups were substantially risen compared to aliphatic and carboxylic hydroxyl groups for BL_E than BL. The C_5-substituted hydroxyl groups exhibited the most significant rise from the constituents of phenolic hydroxyl groups. In addition, the interunit linkages and substructures of BL and BL_E were analyzed by HSQC NMR to understand the changes in lignin structure further. The spectra are presented in **Figure 6.1**(d-g), and the δ_C/δ_H ppm are presented in **Table S6.3**. Quantitative HSQC was used for evaluating the inter-unit linkages in BL and BL_E using the guaiacol (G2) and syringyl (S2,6) signals as an internal standard described according to **Equation** (**S6.5-S6.6**), and values are listed in **Table 6.1** [42]. The oxygenated aliphatic region (δC/δH 40-120/2.5-6.0) of BL and BL_E showed signals presented in **Figure 6.1**(d-e). The dominant interunit linkages in BL and BL_E were the diacylglycerol-β-aryl ether link (β-O-4′) followed by pinoresinol (β–β′) and minor amounts of phenylcoumaran (β-5′). Relative to BL, the BL_E interunit linkages showed a 165% reduction, which was prominent for β-O-4 (**Table 6.1)**. This reduction could result from the breakage of β-O-4 linkages due to the ethanol fractionation [43]. This is further supported by the increased phenolic hydroxyl group content from ^{31}P NMR analysis (**Figure 6.1**c). Furthermore, the aromatic linkages (δ_C/δ_H 100-140/6.0-8) were analyzed, and the results are presented in **Figure 6.1**(f-g). The results showed a vigorous intensity of the S units in BL_E compared to BL. The increase in the S units is consistent with the result of P-NMR, where the phenolic hydroxyl group showed an increase.

The thermal properties of BL and BL_E were assessed using TGA and DSC to understand the thermal alteration of lignin after ethanol fractionation. The TGA and DTG curves are presented in **Figure 6.1(**h-i). The results indicated that the BL_E had a lower T_o (onset temperature) and $T_{50\%}$ (the temperature at which 50% of the weight was lost) than BL (**Table 6.1)**. However, the DTG_{max} of BL_E was 20 °C higher than BL. The lower average molecular weight of BL_E than BL could be the reason for the lower T_o and $T_{50\%}$. The increased phenolic hydroxyl group of BL_E contributed to the higher DTG_{max} due to the higher frequency of intermolecular hydrogen bond interactions of phenolic hydroxyl groups [44]. The glass transition (T_g) of BL and BL_E were analyzed using DSC, and results are presented in **Table 6.1**. In general, the T_g of BL_E was lower than BL, which is attributed to the reduced molecular weight, narrower molecular weight distribution (**Table 6.3**), and change in the hydroxyl group of BL_E, which would increase the chain mobility and thus reduce T_g.

6.4.2. Lignin and caprolactone polymerization via ring opening polymerization (ROP)

The fractionated lignin (BL_E) and caprolactone (CL) polymerization were designed using BBD-RMS. Lignin-(OH) served as a macroinitiator with $Sn(Oct)_2$ catalyst and CL as a monomer [24]. ROP is a polymerization process where the reactive center of a polymer chain is the terminal end. This reactive center allows for the opening of cyclic monomers (CL) and forms a more extended polymer chain (**Figure S6.1**b) [14, 24]. The impact of reaction conditions on the response variables (viscosity, melt temperature, and degree of polymerization) is thoroughly discussed in the supporting information, with detailed Figures (**Figure S6.5-S6.7**) and Tables (**Table S6.5-S6.7**). This document places particular emphasis on the selected polymers (BL_EP2, BL_EP5, and BL_EP6) and the optimized polymer (BL_EPO) and control polymer (BLPO).

6.4.2.1. ^{31}P NMR analysis

According to ^{31}P NMR (**Figure 6.1**b), the total hydroxyl group of BL_E was 4.85 mmol g^{-1}. This indicates that about 4.85 mmol/g of initiating sites are available on the lignin structure, corresponding to 0.64 mmol/g carboxylic, 1.44 mmol/g aliphatic, and 2.77 mmol/g phenolic groups (**Table 6.1)**. The amount of the hydroxyl group on the lignin-caprolactone polymers after polymerization was assessed by ^{31}P NMR in **Figure 6.2**a. BL_EPO, BLPO, and 3 selected samples based on the CL/OH ratio (BL_EP2, BL_EP5, and BL_EP6) were analyzed for ^{31}P-NMR spectra in **Figure 6.2**a. The total grafting ratio (substitution) was calculated using the hydroxyl groups of the polymers from ^{31}P-NMR (**Equation S6.6),** and the results are presented in **Table 6.1**. The spectra of lignin-caprolactone polymers showed aromatic and methoxy peaks similar to those of BL_E and BL. However, the quantification of each peak showed a decrease in all the hydroxyl groups in the lignin-caprolactone polymers compared to BL$_E$ and BL in **Table 6.1**, confirming the success of polymerization and lignin's hydroxyl group participation in the polymerization.

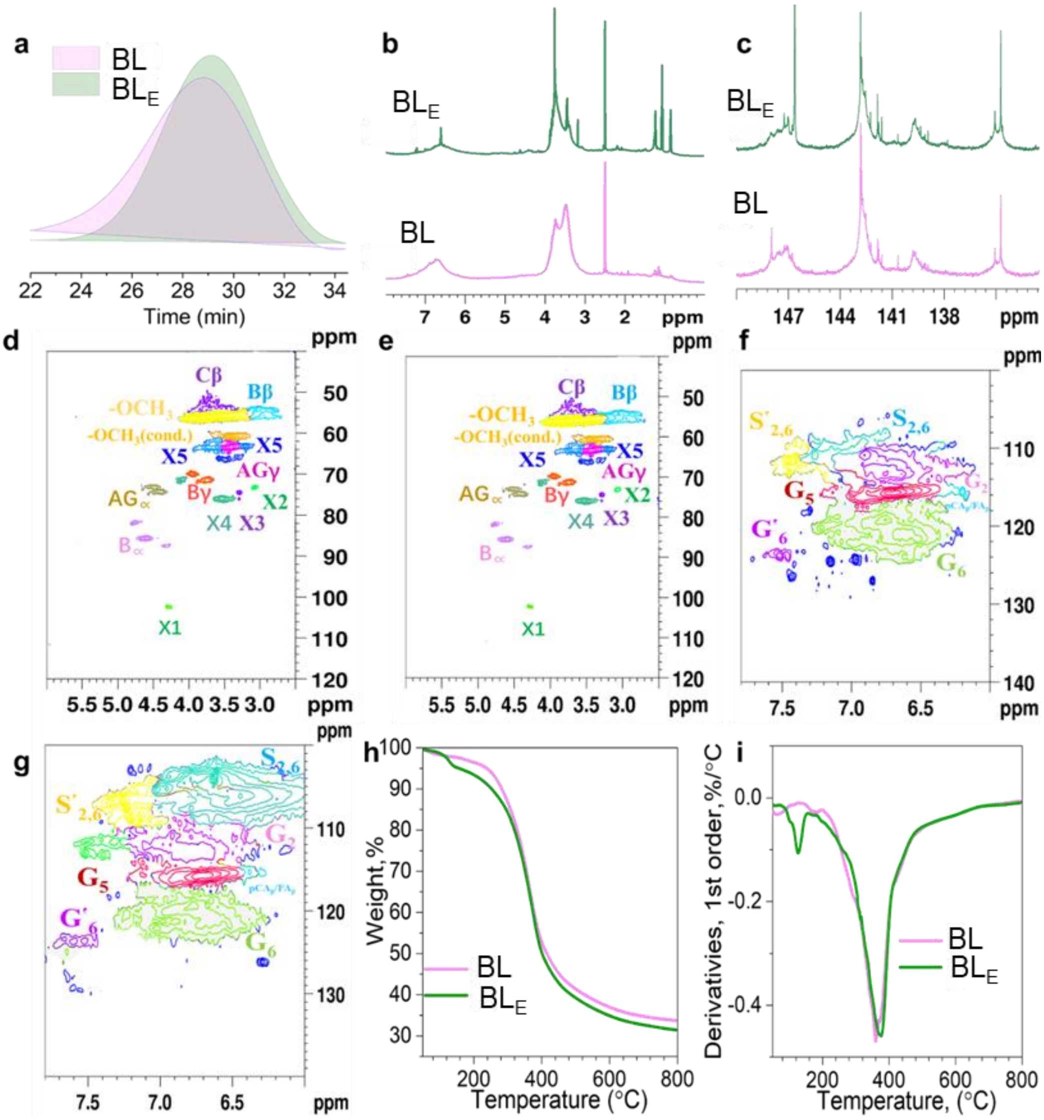

Figure 6. 1. Molar mass distribution (a),^{1}H NMR (b), ^{31}P NMR (c), HSQC spectra of oxygenated aliphatic linkages (d-e), aromatic linkages (f-g) of BL and BL$_E$, and TGA (h) and DTG (i) of BL and BL$_E$.

The BL$_E$P2, BL$_E$P5, and BL$_E$P6 samples were chosen from 17 samples to investigate the effect of CL/OH and catalyst concentration on the structure of the polymers. Also, BL$_E$PO (optimized) and BLPO (control) were assessed to understand how the structural variations in lignin-caprolactone polymers (due to ethanol fractionation) would impact the performance of the copolymer in 3D printing.

Table 6. 1. Yield, grafting ratio (substitution) based on hydroxyl group, molar mass characteristics, hydroxyl group distribution, quantification of major linkages, thermal characteristics, and degree of polymerization (DP) based on H-NMR linkage quantification of lignin and lignin caprolactone polymers.

	Yield %	Graft %	Molar mass characteristics		Lignin hydroxyl group amount mmol g^{-1}			The concentration of interunit linkages % C9 units			Thermal characteristics °C					DP
			Mw g mol^{-1}	$Đ_M$	Phenolic	Aliphatic	Carboxyl	β-O-4	B-β	B-5	T_o	$T_{50\%}$	DTG_{max}	T_g	T_m	
BL	100	-	22870	3	2.6	1.4	0.6	13.9	7.8	12.8	239	416	360	120	-	-
$\mathrm{BL_E}$	54	-	3827	1	2.7	1.4	0.6	3.6	4.4	1.9	123	398	380	111	-	-
$\mathrm{BL_EP}$	-	27	402300		2.1	0.9	0.5	-	-	-	292	397	396	-26	49	4.9
BLPO	-	16	728800		2.1	0.9	0.7	-	-	-	287	392	396	-14	47	5.2

Interestingly, lignin's hydroxyl groups are present in $\mathrm{BL_E}$PO, BLPO, $\mathrm{BL_E}$P2, $\mathrm{BL_E}$P5, and $\mathrm{BL_E}$P6, indicating that not all their hydroxyl groups reacted with caprolactone. **Table 6.1** shows the total grafting %, and **Figure S6.2** shows the substitution percentage for each functional hydroxyl group. $\mathrm{BL_E}$PO had a higher grafting and degree of substitution than BLPO, as seen in **Table 6.1** and **Figure S6.2**, respectively. The increase in the grafting percentage in $\mathrm{BL_E}$PO (compared with BLPO) is attributed to the increased hydroxyl groups of $\mathrm{BL_E}$ due to ethanol fractionation (**Table 6.1** and **Figure 6.1**b), creating more initiation sites for the CL ring opening and subsequent grafting. Previous research indicated that the CL monomers would mainly react with the aliphatic hydroxyl groups of kraft lignin, and this reactivity would be dependent on the CL/OH ratios [42]. However, the reactivity of phenolic hydroxyl was higher when the ratio of CL/OH was higher [45].

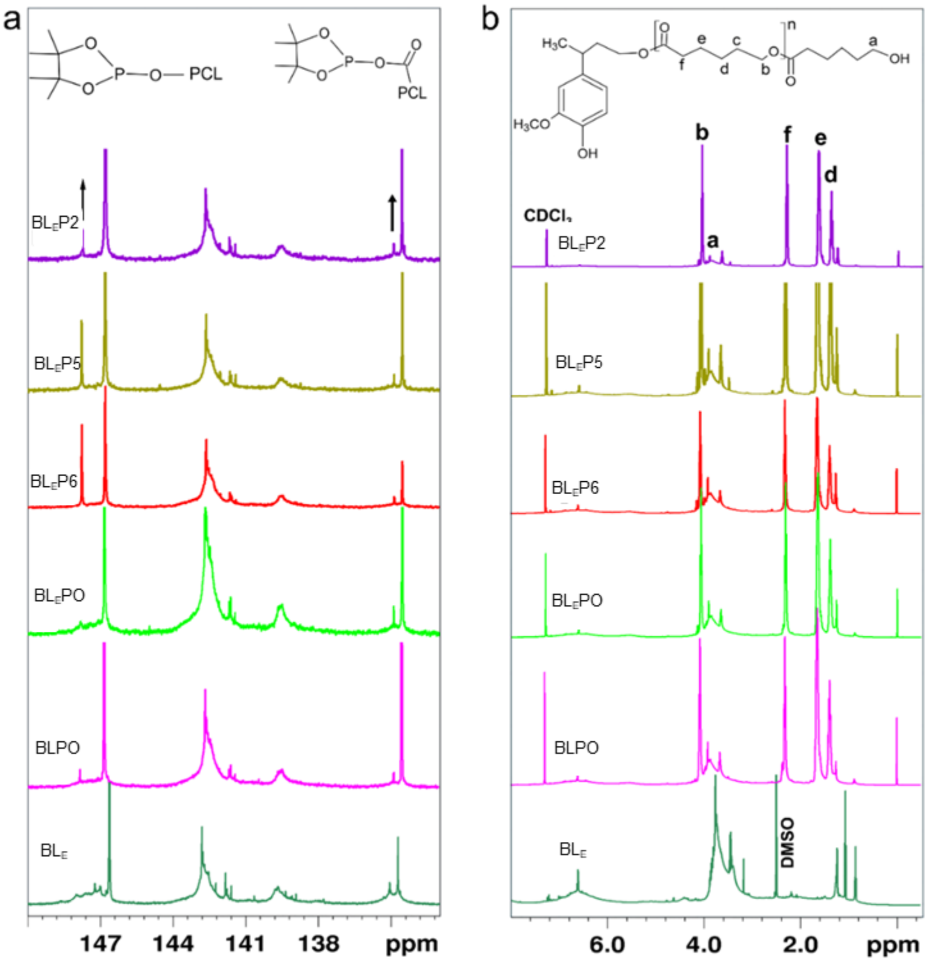

Figure 6.2. ^{31}P-NMR (a) and ^{1}H-NMR (b) spectra of BL$_E$, BL$_E$P's, and BLPO polymer.

Similarly, BL$_E$P2 had the highest grafting percentage and substitution of phenolic hydroxyl groups (54%), followed by BL$_E$P5 with phenolic hydroxyl groups (38%) between the three samples. This behavior could be due to the higher CL concentration in BL$_E$P2 than in BL$_E$P5, which would provide an advantage in reacting with lignin's hydroxyl sites. BL$_E$P6 had the lowest grafting percentage and the highest hydroxyl group substitution (30%).

6.4.2.2. ^{1}H NMR analysis

The ^{1}H-NMR spectra of the polymers are depicted in **Figure 6.1**b and **Figure S6.3**. The degree of polymerization (DP) was calculated according to **Equation S6.7**, and the results are presented in **Table S6.4** and **Table 6.1**. The ^{1}H-NMR spectra for all BL$_E$PO, BLPO, BL$_E$P2, BL$_E$P5, and BL$_E$P6 samples showed a peak at 7.24 ppm, corresponding to CDCl$_3$, while that at 2.5 ppm corresponded to DMSO in BL$_E$. Due to the chloroform used as the solvent of NMR [46], the BL$_E$P spectra shifted to the left slightly, moving the methoxy peak from 3.3–3.9 ppm in BL_E to 4-4.5 ppm in the lignin-caprolactone polymers. The aliphatic-H of BL_E appeared in the 0.5-1.2 ppm range, while that in copolymers was observed at 1.9-2.9 ppm. The aliphatic-H in the copolymers is a result of $-CH_2-$ (d), $-CH_2-$(e), and $-COCH_2-$ (f) appearing in 1.32, 1.57, and 2.24 ppm, respectively, as they aligned with pure PCL's ^1H NMR spectra in **Figure S6.**3. The signals corresponding to the $-CH_2O-$ (a), -COH (b), the repeating and end-group of the PCL chain at 3.9-4.1 ppm and 3.6-3.7 ppm, respectively, were identified and assigned in the copolymer's spectra. The groups described from ^1H-NMR and ^{31}P-NMR spectra (**Figure 6.2**a) and the decrease in the total hydroxyl groups of the lignin (**Table 6.1**) confirm the polymerization of CL into PCL on the lignin backbone. Furthermore, the degree of polymerization (DP) calculation following **Equation S6.**7 revealed that BLPO's degree of polymerization (DP) was higher than BL_EPO's. This could be related to the fact that the PCL chain in BLPO was larger than that in BL_EPO, which might be caused by the competing hydroxyl groups in BL_E preventing the chain growth. In contrast, the scarcity of hydroxyl groups in BL helps the development of the PCL chain. BL_EP2 had the highest DP within the three samples, whereas BL_EP6 had the lowest (**Table S6.4** and **Figure S6.3**). This indicates that the CL/OH ratio and catalyst concentration influenced the DP of lignin caprolactone polymers, which was consistent with the grafting percentage for BL_EP2 (**Table 6.1**).

6.4.2.3. HSQC NMR analysis

The aromatic and aliphatic regions' C-H correlation signals were assessed by HSQC NMR spectra for BL_EP2, BL_EP5, BL_EP6, BL_EPO, and BLPO; and the results are presented in **Figure 6.3**. The BL_EP2, BL_EP5, BL_EP6, and BL_EPO polymers share similar linkages with BL_E in the oxygenated aliphatic region δC/δH 50-100/2.5-5 ppm (**Figure 6.1d**). The aliphatic region (δC/δH 10-80/0.5-2.5) resulting from the PCL chain appeared dominant in the lignin-caprolactone polymers, which did not appear in BL_E (**Figure 6.1**d). The strong aliphatic signals dominating the HSQC NMR spectra (**Figure 6.3**) caused shielding, making the identification of some aliphatic linkage signals hard. The aromatic linkages of $S_{2,6}$, $S'_{2,6}$, G_2, G_5, and G_6 are depicted in **Figure 6.3**b. The BLPO's aliphatic oxygenated region and aliphatic regions had similar linkages to that of BL_EPO. Aromatic linkage signals in BL_EP2, BL_EP5, BL_EP6, and BL_EPO

results showed strong aromatic linkages, like BL$_E$ (**Figure 6.1**e-f). This indicated that the lignin caprolactone polymers gained strong aliphatic signals due to CL grafting and polymerization while maintaining the lignin's aromatic structure. There is a decrease in the strength of the signal in BLPO compared to BL$_E$PO,

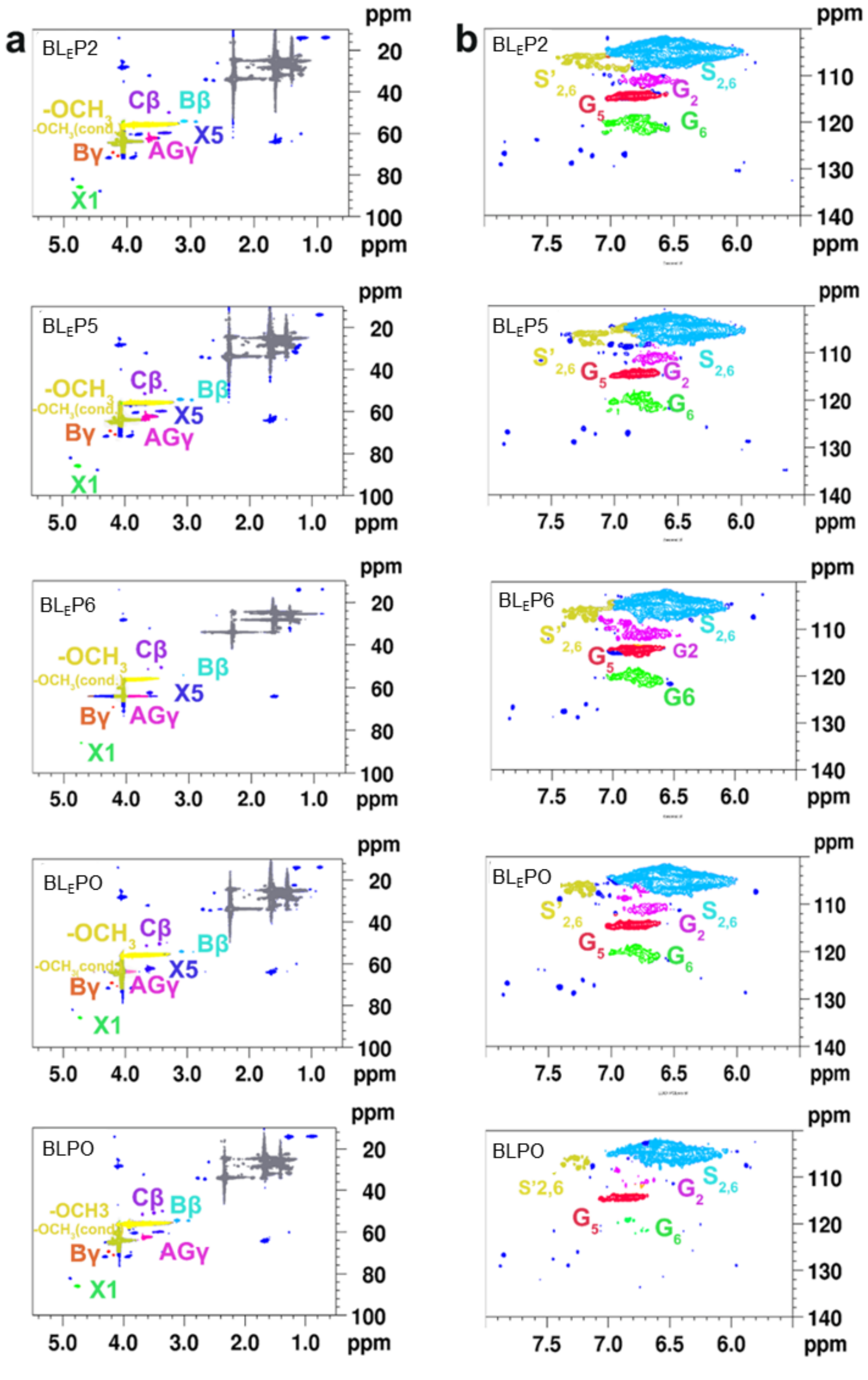

Figure 6. 3. HSQC NMR spectra, aliphatic region (a), and aromatic linkage regions (b) of BL$_E$P2, BL$_E$P5, BL$_E$P6, BL$_E$PO, and BLPO.

notably for signals $S_{2,6}$, G_2, and G_6. The variation in the intensity of $S_{2,6}$, G_2, and G_6 may be attributed to the disparity in BL and BL_E (**Figure 6.1**f-g). Furthermore, the $S_{2,6}$, G_2, and G_6 signals in BLPO exhibit lower intensities than in BL. The decreased intensity can be related to potential shielding caused by PCL grafted on the neighboring aliphatic hydroxyl group of $S_{2,6}$, G_2, and $G_{6,}$ as evidenced by ^{31}P NMR and the higher chain length of PCL in BLPO as evidenced by higher DP (**Table 6.1**).

6.4.2.4. Molecular weight analysis

The Mw was investigated for BL_EP2, BL_EP5, BL_EP6, BL_EPO, and BLPO samples (**Table 6.1)**. The BLPO polymer showed a higher average molecular weight than BL_EPO, which could have originated from the higher average molecular weight of the pristine lignin (BL). The average molecular weight of the BL_EP2, BL_EP5, BL_EP6, and BL_EPO polymers increased significantly compared to BL_E (**Table 6.1**), which further confirmed the introduction of an aliphatic polyester chain covalently bonded to the lignin structure (**Figure 6.2**b). This indicated that there was a more significant reaction of lignin's hydroxyl (OH) groups and(ε-caprolactone) (CL) chains, which led to an increase in the Mw of the copolymers.

6.4.2.5. Thermal Analysis Outcomes

The thermal properties of BL_EP2, BL_EP5, BL_EP6, BL_EPO, and BLPO polymers were analyzed using TGA and DSC (**Figure 6.4**a). The TGA analysis for BL_EP2, BL_EP5, BL_EP6, and BL_EPO polymers showed a higher T_o, $T_{50\%}$, and DTG_{max} than BL_E (**Table 6.1)**. The thermal properties showed improvement by an elevated T_o for BL_EPO and BLPO compared to BL_E and BL. This is due to the higher average molecular weight of the polymers after lignin-caprolactone polymerization, which resulted in the grafting of PCL chains to the lignin backbone, improving its thermal stability (**Table 6.1** or **Figure 6.4**a). Similarly, the T_m of BL_EP polymers was analyzed and reported in **Table 6.1**. It is crucial to note that the T_m was recorded during the initial heating cycle of the DSC analysis due to the disappearance of the T_m in the last heating cycle. The disappearance of the T_m could result from the lower concentration of CL/OH (0.8-2.6 mmol), leading to a short PCL chain length (DP from **Table 6.1**) in the lignin molecular structure. Also, the shorter chain of PCL in lignin would experience restricted molecular mobility due to the random and rigid structure of lignin [47]. All the samples exhibited lower T_g (obtained from the second heating cycle of DSC) than BL and BL_E (**Table S6.4)**.

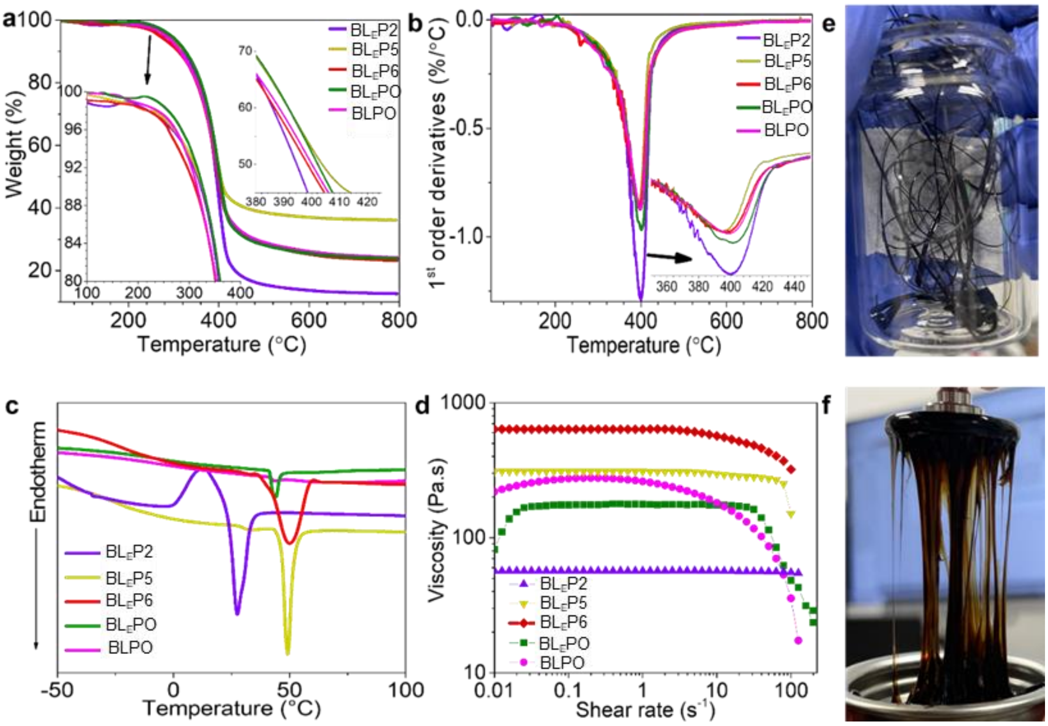

Figure 6. 4. TGA curve (a) and 1st order derivatives of TGA (b), T_m (c) and viscosity at melt temperatures (d) and appearance of the sample L_EPO at room temperature (e), and the melt temperature (f).

The decreased T_g in the polymers is attributed to the enhancement in polymers' free volume, allowing molecular movement due to the grafting of PCL on the lignin backbone [47]. Also, the difference in T_g and T_m between BL$_E$P2, BL$_E$P5, and BL$_E$P6 is insignificant due to the greater lignin concentration in all the samples and the short chain length of PCL, as shown in **Table 6.1**.

6.4.2.6. Rheological assessments

The viscosity of lignin-caprolactone polymers at melt temperature as a function of shear rate was recorded in ramp-up experiments, as presented in **Figure 6.4**b and **Figure S6.4.** The shear-thinning property is an essential characteristic of ink required for extrusion-based 3D printing. This feature was detected in BL$_E$P6, BL$_E$P5, BL$_E$PO, and BLPO (**Figure 6.4**b). However, the BL$_E$PO shows a lower viscosity at a lower shear rate, followed by BLPO, BL$_E$P5, and BL$_E$P6. BL$_E$PO's lower viscosity than BLPO is attributed to the lower M_W and $Đ_M$ of BL$_E$ than BL (**Table 6.1**). There is extensive evidence that greater Mw and a higher ĐM would result in more entanglements, a greater degree of intermolecular contacts, and the formation of a complex interplay of diverse flow behavior, leading to enhanced flow resistance [48-50]. During the ramp-up experiment at the melt temperature, BL$_E$P2 exhibited a consistently low viscosity profile. The constant viscosity against a shear rate seen during the ramp-up experiment of BL$_E$P2 may be attributed to the polymer's higher DP and Mw (**Table 6.1**). These factors contribute to a polymer without shear-thinning properties, which is not typical for a polymer suitable for 3D printing [51]. BL$_E$P6 and BL$_E$P5 exhibit shear-thinning behavior, making them attractive for 3D printing. Nevertheless, the notably elevated viscosity, even when subjected to a greater shear rate, may obstruct the nozzle, impeding the process of 3D printing by extrusion, making them undesirable for the FDM 3D printing process [52, 53]. Therefore, BL$_E$P6 and BL$_E$P5 were not used for further rheology analysis and 3D printing.

BLPO and BL$_E$PO were selected for further rheological analysis and 3D printing due to lower viscosity with a more shear-thinning behavior than the other samples, making them suitable candidates for FDM 3D printing. Temperature ramp and frequency sweep analysis provide information on molecular entanglement, molecular relaxation, layer stability, and guidelines of layer adhesion for FDM 3D printability [54]. The printability of BL$_E$P and BLPO was assessed using a temperature ramp experiment. The complex viscosity, storage (G’), and loss modulus (G”) decreased with reducing temperature for both polymers (**Figure 6.5**a-b). The complex viscosity, G’, and G”, of BLPO were higher than those of BL$_E$PO, which might be related to the higher Mw of BLPO (**Table 6.3**). Furthermore, the point at which G’ and G” intersect (i.e., cross-over point) appears at a lower temperature (55°C) for BLPO than for BL$_E$PO (40°C). This provides an insight into the material's behavior during printing, implying that BLPO behaved more like a solid at a faster rate than BL$_E$PO with the temperature decreasing. The loss modulus (G”) and storage modulus (G’) of a polymer imply the layer adhesion and quality of 3D printable materials [55]. Strong interfacial bonding between layers is crucial for strong printing. An increment in the storage modulus often correlates with improved stiffness and better layer adhesion. Conversely, decreasing loss modulus may enhance printability by reducing energy dissipation during extrusion [56]. In this regard, BL$_E$PO had a much more printable behavior than BLPO. In addition, the ratio between G’ and G” (Tan delta) of BL$_E$PO was lower than that of BLPO and closer to 1 (**Figure 6.5**c). This indicates that BL$_E$PO had more balanced viscous and elastic properties, i.e., an ideal balance for FDM printing where a balanced flow during extrusion and shape retention after printing would be necessary [57]. In addition, the complex viscosity from the frequency sweep analysis in **Figure 6.5**d exhibited that both polymers had similar flow behavior, indicating that they could flow at their melting temperature in the printing nozzle in the extrusion step. However, the significantly higher viscosity of BLPO could cause filament buckling during nozzle extrusion, which is typical for materials with a higher viscosity [58]. The final mechanical properties of the printed parts are directly dependent on the interlayer adhesion between the layers deposited subsequently. The adhesion between layers is determined by the diffusion of polymer chains across the interface and the reorganization of macromolecules to their initial state [59]. This process is directly influenced by the molten material's elastic or viscous properties and the polymer's relaxation time [59, 60]. The frequency sweep analysis for both polymers shows that G”>G’ indicating an interlayer adhesion (**Figure** 6.5e-f). In comparison, the BLPO had a higher G’ and G” than BL$_E$PO, indicating that BLPO possessed more solid-like properties than BL$_E$PO. The filaments were extruded using a filament extrusion machine, and the appearance of BL$_E$PO and BLPO is displayed in **Figure 6.5**g and **Figure S6.7**a.

6.4.2.7. Mechanical and surface properties

The tensile strength of BL$_E$PO was analyzed after the film was cast in a mold (**Figure** 6.5h); however, the BLPO film dried quickly, which hindered the film formation process (**Figure S6.7**b), and it became too brittle to be tested for tensile analysis. The poor mechanical properties of BLPO can be attributed to several factors. Firstly, BLPO has a higher average molecular weight (**Table 6.1**), which leads to BLPO having a higher viscosity at the melt temperature (**Figure 6.4**d). Furthermore, BLPO loses its elastic behavior and behaves more like a solid at a temperature higher than BL$_E$PO, as evidenced by an earlier cross-over point in the temperature ramp experiment (**Figure 6.5**b). That leads to faster drying and higher flow resistance at the melt temperature. The tensile strength of BL$_E$PO was 0.9±0.02 MPa, while its elastic modulus was 277±119 %, and young modulus was 2774±1756 MPa.

The water contact angle of BL$_E$PO (92°) was higher than BLPO (62°), indicating the higher hydrophobicity of BL$_E$PO, which could result from the higher percentage substitution of the hydrophilic hydroxyl groups in BL$_E$PO (67%) with PCL than BLPO (51%) (**Figure S6.**2).

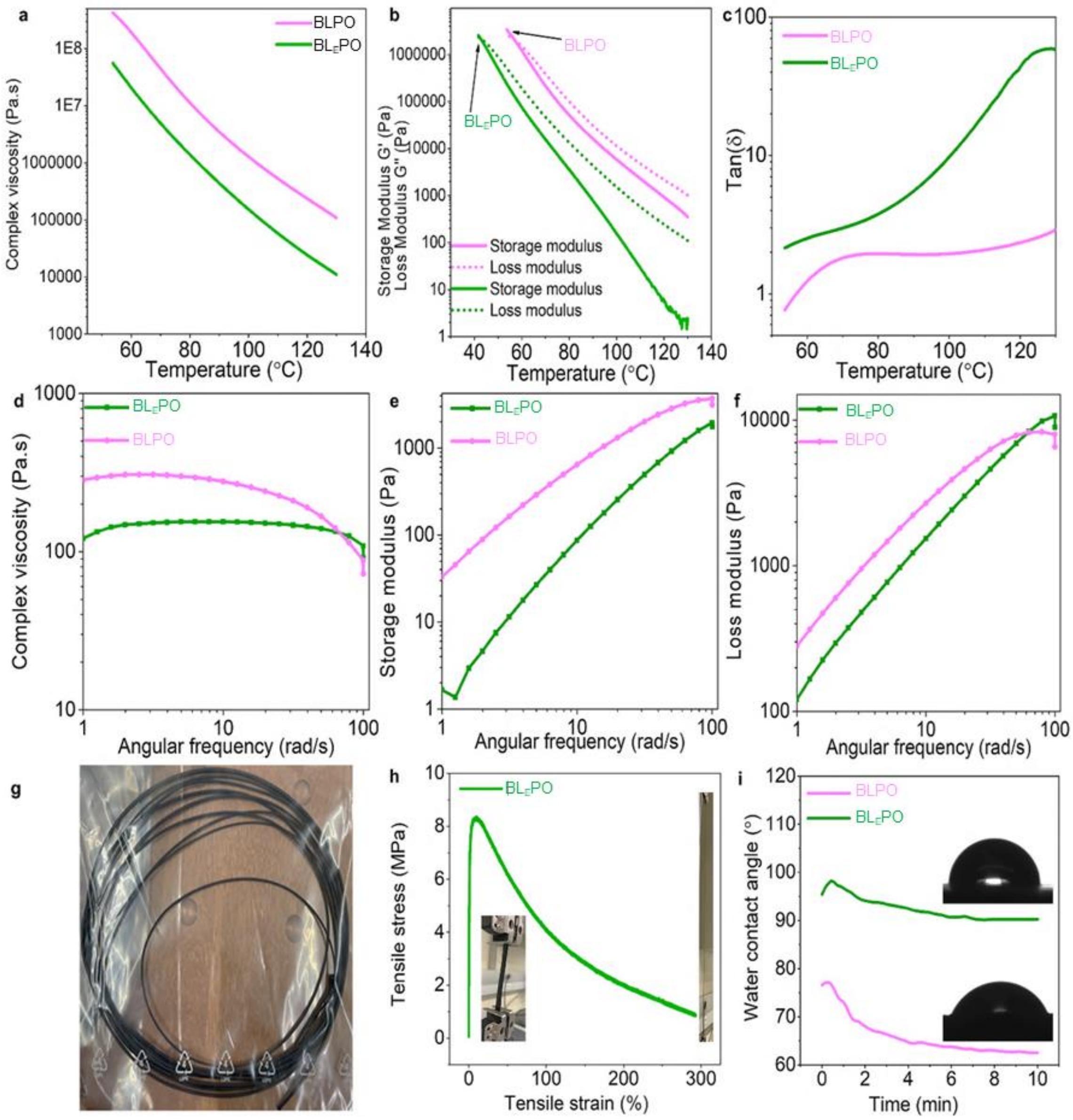

Figure 6. 5. Complex viscosity (a), storage and loss modulus (b), tan **δ** (c), of BLPO and BL$_E$PO from temperature ramp experiment, complex viscosity (d), storage modulus (e), loss modulus (f) from frequency sweep analysis: of BLPO and BL$_E$PO polymers and, extruded filament of (f), BL$_E$PO polymer (g), tensile stress vs strain curve (h), and water contact angle of BL$_E$PO and BLPO (i).

Overall, using several characterization methods clearly showed that ethanol fractionation had a noticeable effect on the physicochemical properties of the lignin-caprolactone polymer, as stated in the overall performance of BLPO and BL$_E$PO. The molecular weight, molecular weight distribution, and hydroxyl group content were altered due to ethanol separation, resulting in a lower average molecular weight and increased hydroxyl groups. This led to BL$_E$ having a more significant advantage than BL in interacting with CL, as seen by a higher grafting in the hydroxyl groups (**Figure S6.2**). BL$_E$PO had a lower viscosity and better rheological, mechanical, and hydrophobic properties than BLPO because it had a lower average molecular weight (**Table 6.1**), originating from improved free volume for molecular chain mobility and conformational rearrangement.

6.4.3. 3D printability of lignin-caprolactone polymer

The 3D printability of BLPO and BL_EPO was assessed using FDM, and images of the 3D printed parts are displayed in **Figure 6.7**. The pallets for both polymers were rolled, loaded, and printed using a 3D printer; however, as seen from the printed parts, a visible gap between layers indicates low interlayer diffusion and adhesion between deposited layers in the BLPO samples (**Figures 6.7**a' and 6.7b'). Conversely, BL_EPO showed no gaps between printed layers, indicating better interlayer adhesion and filling. This behavior could be attributed to the very high viscosity (**Figure** 6.**6**g-h) and average molecular weight of BLPO (**Table 6.3**), inducing thermal crosslinking and reducing molecular mobility interfacial diffusion, thus reducing adhesion between deposited layers [17].

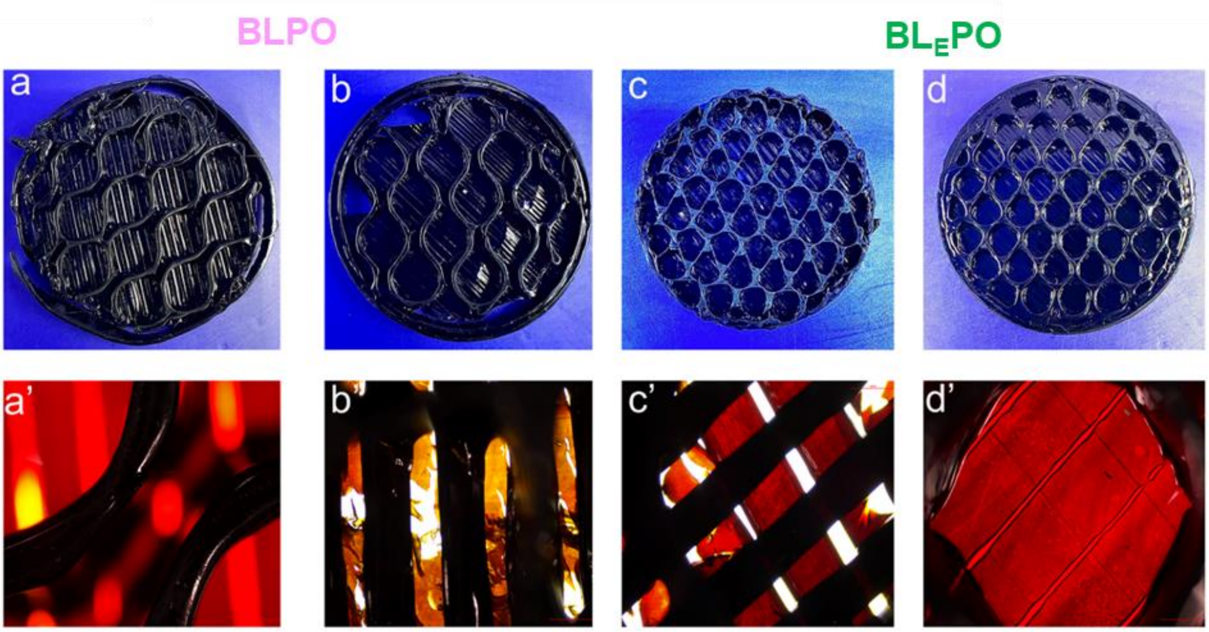

Figure 6. 6. FDM printed honeycomb structure of BLPO photograph images of trial 1 (a) and trial 2(b), light microscope image showing layer adhesions (a') and (b'), BL_EPO photograph images of trial 1 (c), and trial 2 (d) and light microscope magnification showing layer adhesion (c') and (d').

Furthermore, the intersection point observed during the melt rheology investigation **(Figure 6.6**e) of BLPO occurred at higher temperatures (55 °C), indicating that the sample might lose its ability to melt more quickly when exposed to lower temperatures. This could hinder the bonding of layers, as seen in

Figure 6.6a’-b’. The higher 3D printability of BL_EPO than BLPO might be ascribed to improved layer adhesion originating from the lowered average molecular weight and viscosity of BL_EPO due to BL_E's lower average molecular weight achieved by ethanol fractionation (**Table 6.1**). Therefore, we can conclude that the ethanol fractionation of alkali lignin improved the 3D printability of lignin-caprolactone polymers.

6.5. Comparison

In the past, lignin polymers were used in 3D printing in polymer blends alongside other polymers, such as acrylonitrile-butadiene-styrene, polycaprolactone, cummin, polycaprolactone/polyurethane, and polylactic acid following the FDM-3D printing technique, as indicated in **Table 6.2**. The addition of lignin-caprolactone polymer (15 wt.%) to acrylonitrile-butadiene-styrene led to a decrease in viscosity (2130 Pa.s) compared to the formulations without lignin-caprolactone polymer (4270 Pa.s) under similar temperature and shear rates [61]. In another study, incorporating lignin-caprolactone polymer (40 wt.%) into polycaprolactone and curcumin improved the blend's thermal stability even though the rheological properties were not reported [62]. **Table 6.2** shows that earlier publications have identified interfacial incompatibility between lignin and other polymers in the system. This incompatibility has restricted lignin's presence in the final products. Utilizing a homogeneous copolymer would facilitate the manufacturing process. The current study is unique compared to the existing literature since the lignin-caprolactone polymer was used solitarily for 3D printing after mimicking the characteristics of lignin polymer via solvent fractionation (ethanol). The total concentration of lignin present in the lignin-caprolactone matrix was 75 wt.% (i.e., a truly sustainable material) based on the calculation in (**Equation S6.1)** with much lower viscosity (160.9 Pa.S) and ease of printing. Considering the ethanol fractionation, the overall use of lignin in the produced 3D printing material would be 40.12 wt.% of the original pristine lignin. The results imply that almost 60% of pristine lignin is still available for other uses and can be incorporated into other value-added applications if collected after filtration. This study also conducted an analysis of variance (ANOVA) on the responses (viscosity, melt temperature, and degree of polymerization) of lignin-caprolactone polymer, considering three variables: CL/OH ratio, reaction time, and catalyst concentration **Tables S6.5-S6.7**. The results indicate that all reaction parameters significantly affect the response variables, with p-values less than 0.05. Additionally, suitable models for predicting the response variables are presented, as outlined in **Equations S6.10-S6.12**, using the BBD-RSM. This work provides an excellent insight into the use of lignin polymer for FDM-3D printing, which would reduce the use of inorganic and synthetic polymers in 3D printed materials, tackling the problem of sustainability.

Table 6.2. Lignin-caprolactone-containing materials for FDM-3D printing.

Materials	**Solvent**	**Filament preparation method**	**Lignin amount, wt.%**	**Other components con. %**	**Viscosity, Pa.S**	**Advantages**	**Shortcomings**	**Reference**
Lignin-caprolactone and acrylonitrile-butadiene-styrene	Solvent-free	Blending	5	ABS, 90 PCL, 5	2130	Lignin-PCL improved the processability of the composite	-Stability of composite material not reported -Lower concentration of lignin - Still used	[61]
Lignin, Polycaprolactone, and curcumin	Solvent-free	Blending	10	Curcumin, 5 PCL, 85	NR	Lignin improved the antibacterial and antimicrobial properties	-Mechanical properties not reported - Lower concentration of lignin	[62]
Enzymatic lignin, polycaprolactone and polyurethane	Solvent-free	Blending	20	PCL, 30 PU, 55	100	Lignin enhanced the rigidity of the composite	Interface incompatibility between lignin and other components	[63]
Polylactic acid, polycaprolactone, and lignin	Solvent-free	Blending	2	PCL, 24 PLA, 65	NR	Lignin improved the thermal recovery and mechanical properties	Lower concentration of lignin	[64]
Lignin and caprolactone	Solvent-free	Copolymerization	75	Caprolactone, 25	160.9	- Higher concentration of lignin -Ease of use - Superior mechanical properties	Application of 3D printed material needs investigation	This work

NR, not reported, PCL, polycaprolactone, PLA, polylactic acid and ABS, acrylonitrile-butadiene-styrene.

6.6. Conclusion

This work aimed to reduce the average molecular weight and molecular weight distribution of birch alkali lignin (BL) via ethanol fraction before polymerization of the fractionated lignin (BL_E) with caprolactone for FDM-3D printing. BL_E showed a higher hydroxyl group content, lower molecular weight, and lower poly dispersibility than BL. The increase in hydroxyl groups created more reactive sites on the lignin structure for caprolactone grafting. The copolymerization of BL_E and caprolactone was optimized by considering the melt temperature (T_m), degree of polymerization (DP), and viscosity as the primary factors of its printability. The results confirmed that the optimized sample (BL_EPO), produced by a CL/OH ratio of 1.15 mmol/g, a reaction duration of 420 minutes, and a catalyst concentration of 1 wt.% showed better printability with a melt temperature of 48°C, shear-thinning behavior, low viscosity (160.9 Pa.S) and better thermal stability with an onset temperature 292.2 °C. The melt rheology results demonstrated that BL_EPO exhibited superior interlayer adhesion during printing and mechanical capabilities to unfractionated lignin-caprolactone (BLPO) polymer. BL_E's decreased average molecular weight and narrower molecular weight distribution contributed to BL_EPO's reduced viscosity. Furthermore, the occurrence of the cross-over points between G' and G'' appearing 15 °C higher than BLPO provided BL_EPO with a favorable condition for improved layer formation and enhanced bonding between layers. BL_EPO's water contact angle value was higher than those of BLPO by 30°, which is consistent with the higher grafting percentage of CL (11% higher) to the hydroxyl groups of BL_EPO than BLPO. Based on this study's findings, the reduced variability in the lignin structure after ethanol fractionation of lignin is a viable approach for producing lignin-caprolactone polymer for 3D printable materials, where 75% of the fractionated lignin (representing 40.12 % unfractionated pristine alkali birch lignin) was part of the lignin-caprolactone polymer. Further research is required to explore the usefulness of this 3D-printed lignin-caprolactone polymer in areas such as bio-medical applications.

6.7. Reference

1. Yao, T., et al., *Tensile failure strength and separation angle of FDM 3D printing PLA material: Experimental and theoretical analyses.* Compos. B: Eng., 2020. **188**: p. 107894. https://doi.org/10.1016/j.compositesb.2020.107894.
2. chey, *A continuum constitutive model for FDM 3D printed thermoplastics.* Compos. B. Eng., 2020. **201**: p. 108373. https://doi.org/10.1016/j.compositesb.2020.108373.
3. Fu, Z., et al., *Printability in extrusion bioprinting.* Biofabrication, 2021. **13**(3): p. 033001. 10.1088/1758-5090/abe7ab.
4. Madhu, N.R., et al., *Fused deposition modelling approach using 3D printing and recycled industrial materials for a sustainable environment: a review.* Int. J. Adv. Manuf. Technol., 2022. **122**(5): p. 2125-2138. 10.1007/s00170-022-10048-y.
5. Bozkurt, Y. and E. Karayel, *3D printing technology; methods, biomedical applications, future opportunities and trends.* J. Mater. Res. Technol., 2021. **14**: p. 1430-1450. 10.1016/j.jmrt.2021.07.050.

6. Shariatnia, S., et al., *Atomization of cellulose nanocrystals aqueous suspensions in fused deposition modeling: A scalable technique to improve the strength of 3D printed polymers.* Compos. B. Eng. , 2019. **177**: p. 107291. https://doi.org/10.1016/j.compositesb.2019.107291.
7. Yapar, Ö., *3D Bioprinting of Cellulosic Structures for Versatile Applications*, in *Additive Manufacturing in Multidisciplinary Cooperation and Production*. 2023, Springer. p. 79-102.
8. Bajwa, D.S., et al., *A concise review of current lignin production, applications, products and their environmental impact.* Ind. Crops. Prod., 2019. **139**: p. 111526. 10.1016/j.indcrop.2019.111526.
9. Wasti, S., et al., *Influence of plasticizers on thermal and mechanical properties of biocomposite filaments made from lignin and polylactic acid for 3D printing.* Compos. B. Eng., 2021. **205**: p. 108483. https://doi.org/10.1016/j.compositesb.2020.108483.
10. Kazzaz, A.E., Z.H. Feizi, and P. Fatehi, *Grafting strategies for hydroxy groups of lignin for producing materials.* Green Chem., 2019. **21**(21): p. 5714-5752. https://doi.org/10.1039/C9GC02598G.
11. Yu, O. and K.H. Kim, *Lignin to materials: A focused review on recent novel lignin applications.* Appl. Sci., 2020. **10**(13): p. 4626. 10.3390/app10134626.
12. Mimini, V., et al., *Compatibility of kraft lignin, organosolv lignin and lignosulfonate with PLA in 3D printing.* J. Wood Chem. Technol., 2019. **39**(1): p. 14-30. 10.1080/02773813.2018.1488875.
13. Zhang, X., et al., *Three-dimensional printed cell culture model based on spherical colloidal lignin particles and cellulose nanofibril-alginate hydrogel.* Biomacromolecules, 2020. **21**(5): p. 1875-1885.
14. Nguyen, N.A., et al., *A path for lignin valorization via additive manufacturing of high-performance sustainable composites with enhanced 3D printability.* Sci. Advances, 2018. **4**(12): p. eaat4967. 10.1126/sciadv.aat4967.
15. Domínguez-Robles, J., et al., *Antioxidant PLA composites containing lignin for 3D printing applications: a potential material for healthcare applications.* Pharmaceutics, 2019. **11**(4): p. 165. 10.3390/pharmaceutics11040165.
16. Wasti, S., et al., *Influence of plasticizers on thermal and mechanical properties of biocomposite filaments made from lignin and polylactic acid for 3D printing.* Composites Part B: Engineering, 2021. **205**: p. 108483. 10.1016/j.compositesb.2020.108483.
17. Nguyen, N.A., C.C. Bowland, and A.K. Naskar, *A general method to improve 3D-printability and inter-layer adhesion in lignin-based composites.* Appl. Mater., 2018. **12**: p. 138-152. 10.1016/j.apmt.2018.03.009.
18. Adithyamol, V.V., S. Gupta, and B. Kandasdubramanian, *Revolutionizing 3D Printing: Harnessing the Power of Lignin-Based Ink for Versatile Applications.* Biomed. Mater. Devi., 2024: p. 1-13. 10.1007/s44174-024-00193-1.
19. Ye, H., et al., *3D-Printed polylactic acid/Lignin films with great mechanical properties and Tunable functionalities towards superior UV-shielding, haze, and antioxidant properties.* Polymers, 2023. **15**(13): p. 2806. 10.3390/polym15132806.
20. Labet, M. and W. Thielemans, *Synthesis of polycaprolactone: a review.* Chem. Soc. Rev., 2009. **38**(12): p. 3484-3504. 10.1039/B820162P
21. Mohamed, R.M. and K. Yusoh, *A review on the recent research of polycaprolactone (PCL).* Adv. Mat. Res., 2016. **1134**: p. 249-255. 10.4028/www.scientific.net/AMR.1134.249.
22. Bartnikowski, M., et al., *Degradation mechanisms of polycaprolactone in the context of chemistry, geometry and environment.* Prog. Polym. Sci., 2019. **96**: p. 1-20. 10.1016/j.progpolymsci.2019.05.004.
23. Guarino, V., et al., *Polycaprolactone: synthesis, properties, and applications.* EPST, 2002: p. 1-36. 10.1002/0471440264.pst658.

24. Ho, C.M.B., et al., *3D printed polycaprolactone carbon nanotube composite scaffolds for cardiac tissue engineering.* Macromol. Biosci., 2017. **17**(4): p. 1600250. 10.1002/mabi.201600250.
25. Wang, W., et al., *Morphological, mechanical and biological assessment of PCL/pristine graphene scaffolds for bone regeneration.* Int. J. Bioprinting, 2016. **2**(2): p. 95-104. 10.18063/IJB.2016.02.009.
26. Liu, K., et al., *Microstructures and properties of polycaprolactone/tricalcium phosphate scaffolds containing polyethylene glycol fabricated by 3D printing.* Ceram. Int., 2022. **48**(16): p. 24032-24043. 10.1016/j.ceramint.2022.05.081.
27. Muwaffak, Z., et al., *Patient-specific 3D scanned and 3D printed antimicrobial polycaprolactone wound dressings.* Int. J. Pharm., 2017. **527**(1-2): p. 161-170. 10.1016/j.ijpharm.2017.04.077.
28. Park, I.-K., et al., *Solvent-free bulk polymerization of lignin-polycaprolactone (PCL) copolymer and its thermoplastic characteristics.* Sci. Rep., 2019. **9**(1): p. 7033. s41598-019-43296-2.
29. Kadam, K.L., C.Y. Chin, and L.W. Brown, *Continuous biomass fractionation process for producing ethanol and low-molecular-weight lignin.* Environ. Prog. Sustain. Energy., 2009. **28**(1): p. 89-99. 10.1002/ep.10348.
30. Sadeghifar, H. and A. Ragauskas, *Perspective on technical lignin fractionation.* ACS sustain. Chem. Eng., 2020. **8**(22): p. 8086-8101. 10.1021/acssuschemeng.0c01348.
31. Wang, Y., et al., *A review on catalytic depolymerization of lignin towards high-value chemicals: solvent and catalyst.* Fermentation, 2023. **9**(4): p. 386. 10.3390/fermentation9040386.
32. Costa, C.A.E., et al., *Lignin valorization for added-value chemicals: Kraft lignin versus lignin fractions.* Chemengineering, 2023. **7**(3): p. 42. 10.3390/chemengineering7030042.
33. Liu, R., et al., *Fractionation of lignin with decreased heterogeneity: based on a detailed characteristics study of sequentially extracted softwood kraft lignin.* ACS Sustain. Chem. Eng., 2021. **9**(41): p. 13862-13873. 10.1021/acssuschemeng.1c04725.
34. Wang, L., et al., *Tailored thermosetting wood adhesive based on well-defined hardwood lignin fractions.* ACS Sustain. Chem. Eng., 2020. **8**(35): p. 13517-13526. 10.1021/acssuschemeng.0c05408.
35. Gao, C., et al., *One-pot depolymerization, demethylation and phenolation of lignin catalyzed by HBr under microwave irradiation for phenolic foam preparation.* Compos. B. Eng., 2021. **205**: p. 108530. https://doi.org/10.1016/j.compositesb.2020.108530.
36. Zinovyev, G., et al., *Getting closer to absolute molar masses of technical lignins.* ChemSusChem, 2018. **11**(18): p. 3259-3268. 10.1002/cssc.201801177.
37. Meng, X., et al., *Determination of hydroxyl groups in biorefinery resources via quantitative 31P NMR spectroscopy.* Nat. Protoc., 2019. **14**(9): p. 2627-2647. s41596-019-0191-1.
38. Diment, D., et al., *Study toward a More Reliable Approach to Elucidate the Lignin Structure–Property–Performance Correlation.* Biomacromolecules, 2023. **25**(1): p. 200-212. 10.1021/acs.biomac.3c00906.
39. Gigli, M. and C. Crestini, *Fractionation of industrial lignins: opportunities and challenges.* Green Chem., 2020. **22**(15): p. 4722-4746. 10.1039/D0GC01606C.
40. Liu, R., et al., *Influence of carbohydrates covalently bonded with lignin on solvent fractionation, thermal properties, and nanoparticle formation of lignin.* ACS Sustain. Chem. Eng., 2022. **10**(44): p. 14588-14599. 10.1021/acssuschemeng.2c04498.
41. Pan, C., et al., *Effects of ethanol pretreatment on dissolution and structural changes of lignin from steam-exploded wheat straw.* Bioresources, 2019. **14**(3): p. 6958-6969. 10.15376/biores.14.3.6958-6969.
42. Sette, M., R. Wechselberger, and C. Crestini, *Elucidation of lignin structure by quantitative 2D NMR.* Chem. Eur. J., 2011. **17**(34): p. 9529-9535. 10.1002/chem.201003045.

43. Pang, T., et al., *Lignin fractionation: Effective strategy to reduce molecule weight dependent heterogeneity for upgraded lignin valorization.* Ind. Crops Prod., 2021. **165**: p. 113442. 10.1016/j.indcrop.2021.113442.
44. Choi, J.-H., et al., *Thermal properties of ethanol organosolv lignin depending on its structure.* ACS omega, 2021. **6**(2): p. 1534-1546. 10.1021/acsomega.0c05234.
45. Najarro, M.C., et al., *Tuning the lignin-caprolactone copolymer for coating metal surfaces.* ACS Appl. Polym. Mater., 2020. **2**(12): p. 5767-5778. 10.1021/acsapm.0c01026.
46. Capanema, E.A., M.Y. Balakshin, and J.F. Kadla, *A comprehensive approach for quantitative lignin characterization by NMR spectroscopy.* J. Agric. Food Chem., 2004. **52**(7): p. 1850-1860. 10.1021/jf035282b.
47. Hatakeyama, T., S. Yamashita, and H. Hatakeyama, *Thermal properties of lignin-based polycaprolactones.* J. Therm. Anal. Calorim., 2021. **143**: p. 203-211.
48. Vega, J.F., et al., *Effect of molecular weight distribution on Newtonian viscosity of linear polyethylene.* Rheol. Acta, 2012. **51**: p. 81-87. 10.1007/s00397-011-0594-6.
49. Middleman, S., *Effect of molecular weight distribution on viscosity of polymeric fluids.* J. Appl. Polym. Sci., 1967. **11**(3): p. 417-424. 10.1002/app.1967.070110309.
50. Kozmiski, S.J., *Effect of Molecular Weight Distribution on Viscosity-shear Rate and Die Swell Behavior in Homologous Polystyrene Blends*. 1984: The Pennsylvania State University.
51. Wickramasinghe, S., T. Do, and P. Tran, *FDM-based 3D printing of polymer and associated composite: A review on mechanical properties, defects and treatments.* Polymers, 2020. **12**(7): p. 1529. 10.3390/polym12071529.
52. Tlegenov, Y., W.F. Lu, and G.S. Hong, *A dynamic model for current-based nozzle condition monitoring in fused deposition modelling.* Prog. Addit. Manuf., 2019. **4**: p. 211-223. 10.1007/S40964-019-00089-3.
53. Zhang, H., et al., *Fibre bridging and nozzle clogging in 3D printing of discontinuous carbon fibre-reinforced polymer composites: Coupled CFD-DEM modelling.* Int. J. Adv. Manuf. Technol., 2021. **117**(11): p. 3549-3562. 10.1007/s00170-021-07913-7.
54. Candal, M.V., et al., *Thermo-rheological effects on successful 3D printing of biodegradable polyesters.* Addit. Manuf., 2020. **36**: p. 101408. 10.1016/j.addma.2020.101408.
55. Patti, A., et al., *Predicting the printability of poly (Lactide) acid filaments in fused deposition modeling (FDM) technology: rheological measurements and experimental evidence.* ChemEngineering, 2022. **7**(1): p. 1. 10.3390/chemengineering7010001.
56. Thumsorn, S., et al., *Rheological behavior and dynamic mechanical properties for interpretation of layer adhesion in FDM 3D printing.* Polymers, 2022. **14**(13): p. 2721. 10.3390/polym14132721.
57. Arrigo, R. and A. Frache, *FDM printability of PLA based-materials: the key role of the rheological behavior.* Polymers, 2022. **14**(9): p. 1754. 10.3390/polym14091754.
58. Ilyés, K., et al., *The applicability of pharmaceutical polymeric blends for the fused deposition modelling (FDM) 3D technique: Material considerations–printability–process modulation, with consecutive effects on in vitro release, stability and degradation.* Eur. J. Pharm. Sci., 2019. **129**: p. 110-123. 10.1016/j.ejps.2018.12.019.
59. Das, A., et al., *Rheology, crystallization, and process conditions: The effect on interlayer properties in three-dimensional printing.* Phys. Fluids, 2022. **34**(12). 10.1063/5.0128660.
60. Weng, Y., et al., *Investigation of interlayer adhesion of 3D printable cementitious material from the aspect of printing process.* Cem. Concr. Res., 2021. **143**: p. 106386. 10.1016/j.cemconres.2021.106386.
61. Kim, S.-H., et al., *Non-Einstein Viscosity Phenomenon of Acrylonitrile–Butadiene–Styrene Composites Containing Lignin–Polycaprolactone Particulates Highly Dispersed by High-Shear Stress.* ACS omega, 2019. **4**(6): p. 10036-10043. 10.1021/acsomega.9b01043.

62. Domínguez-Robles, J., et al., *Poly(caprolactone)/lignin-based 3D-printed dressings loaded with a novel combination of bioactive agents for wound-healing applications*. SM &T, 2023. **35**: p. e00581. 10.1016/j.susmat.2023.e00581.
63. Suo, F., et al., *Development of lignin-based 3D-printable light responsive shape memory materials: Design of optically controlled devices*. Int. J. Biol. Macromol., 2024: p. 132943. 10.1016/j.ijbiomac.2024.132943.
64. Liu, B., et al., *Preparation, shape memory properties and application research of PLA/PCL-based shape memory polymers doped with Al2O3 and lignin*. J. Appl. Polym. Sci., 2024. **141**(16): p. e55252. 10.1002/app.55252.

Chapter 7: Ethanol-Fractionated Lignin Caprolactone Copolymer for Wood Coating Application

Banchamlak Bemerw Kassaun[1,2], Luyao Wang[2], Oskar Backman[2], Chunlin Xu[2], Pedram Fatehi*[1,2]

[1]Department of Chemical Engineering, Lakehead University, 955 Oliver Road, Thunder Bay, ON P7B 5E1, Canada,

[2]Laboratory of Natural Materials Technology, Faculty of Science and Engineering, Åbo Akademi University, Turku, Finland.

Submitted to ACS Chemistry and Engineering

The contribution of Banchamlak Bemerw Kassaun to this work was the conception of the original draft, visualization, validation, formal analysis, data curation, and conceptualization.

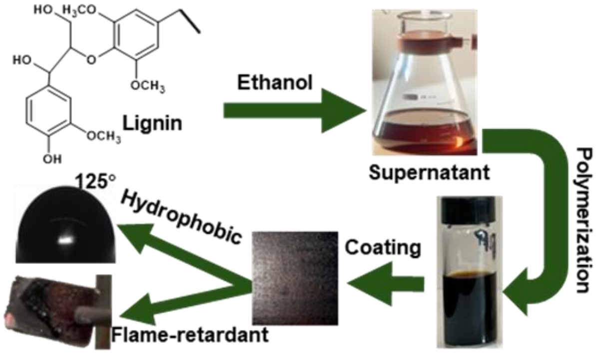

7.1. Abstract

The variation in the characteristics of lignin has significantly influenced its potential use for coating applications. In this work, we examined the polymerization of birch alkali (BL), wheat straw alkali (WL), and softwood kraft lignin (SKL) with caprolactone (CL) before and after ethanol fractionation in the solvent-free system. The average molecular weight (Mw), total hydroxyl group, and thermal stability of lignin were altered considerably after ethanol fractionation, affecting its reactivity to ring-opening polymerization with CL and, thus, the characteristics of the final polymers. The fractionated lignin improved CL ring-opening polymerization, converting more lignin OH to ester linkages and reducing the steric endurance for PCL polymerization. Polymers derived from ethanol-fractionated lignin had varied lower glass transition temperatures and lower viscosity than unfractionated ones. SKL and WL polymerization with CL was markedly more affected by ethanol fractionation because the reactivity of unfractionated lignin with CL was much lower than that of fractionated lignin, which is correlated with the intrinsic variability of lignin's molecular composition, which is influenced by the lignin source in WL and the extraction method in SKL. The wood coating performance of fractionated lignin-caprolactone polymers was much superior to their unfractionated counterparts with higher water contact angle (WCA) values and flame-retardant properties. The wheat straw fractionated lignin (WLE)-caprolactone (WLEP) polymer exhibited superior WCA (125°) and LOI (27.5 %) to other lignin-caprolactone polymers derived from other lignin sources, which was stable after sand abrasion and knifing. The superior coating performance of WLEP on wood surfaces is attributable to the heightened reactivity of WLE with CL and an increased polymerization of PCL on the lignin backbone.

Keywords: lignin, ethanol fractionation, lignin-caprolactone polymers, coating, hydrophobic, flame-retardancy.

7.2. Introduction

Polycaprolactone (PCL) is a biodegradable polyester recognized for its biocompatibility and adaptability produced via ring-opening polymerization of ε-caprolactone (CL) in the presence of a catalyst [1, 2]. Owing to PCL's non-toxicity and simplicity of processing, it is used in tissue engineering, drug delivery systems, biodegradable implants and coating [3]. Nonetheless, PCL is expensive and exhibits limited thermal stability and mechanical properties [4, 5]. Initiatives to increase the thermal and mechanical characteristics of PCL involve combining it with other polymers (i.e. chitosan, gelatin, and starch) and additives (i.e. hydroxyapatite or graphene oxide) [6].

Lignin, a readily accessible and cost-effective polymer, is garnering interest in enhancing the mechanical and thermal characteristics of PCL when used as an addition in composite formulations [7]. Lignin is an appealing choice for manufacturing caprolactone-based polymers due to the potential of aliphatic and phenolic hydroxyl groups that can initiate cyclic ester monomer ring opening and subsequent polymerization [8, 9]. Lignin-based caprolactone polymers are sustainable, ecologically benign biopolymers gaining significant influence in cutting-edge research fields in polymer science and material engineering [10-14]. In addition, the incorporation of lignin in PCL is reported to improve the UV stability and degradability of PCL materials [15]. Moreover, employing lignin as an initiator for the ring opening polymerization (ROP) of CL and the subsequent polymerization of PCL on the lignin backbone has been documented as an effective approach to enhance the thermal stability and mechanical qualities of PCL [16]. The utilization of lignin-caprolactone polymer for coating applications is garnering interest due to the distinctive combination of lignin and PCL features, wherein the PCL chain enhances the film-forming capability of lignin, while the lignin component augments the mechanical, thermal, and UV protective attributes of the coatings.

Lignin is an irregular, complex, three-dimensional macromolecule rich in guaiacyl (G), syringyl (S), and p-hydroxyphenyl (H) alcohol [17]. The chemical structure of lignin is dependent on the source and the method of lignin extraction from lignocellulosic biomass [18]. Guaiacyl-rich lignin is mainly derived from softwood plants, while syringyl lignin is predominantly present in hardwoods [19]. Grass lignin has a proportion of guaiacyl, syringyl, and p-hydroxyphenyl groups [20]. The source of lignin may also determine its accessibility and cost [21]. Agricultural wastes, such as straw, provide an abundant and cost-effective source of lignin that might be advantageous for large-scale applications [22, 23]. In this respect, the variability in the physicochemical characteristics of lignin may affect the reactivity of lignin with CL for lignin-caprolactone production. For example, Li et al. examined lignin from different botanical sources (G-type pine lignin, S/G type poplar lignin, and C-type vanilla seeds lignin) and extraction methods (kraft and ethanol organosolv pulping) [24]. The findings indicated that the reaction of lignin and caprolactone occurred irrespective of the lignin feedstock source and extraction method; however, the resultant polymer's thermal properties depended on the lignin source and type. Regardless of the lignin source, the products suffered from lignin heterogeneity observed in double melt temperature in the catechyl (C-type) lignin.

The solvent fractionation of lignin reduces lignin heterogeneity and complexity, resulting in homogenous lignin that can be easily used to produce lignin-based copolymers [25, 26]. Xie et al. performed a successive solvent fractionation of kraft lignin for lignin-caprolactone copolymerization [27]. The resultant polymer showed improved mechanical, UV barrier, and enzymatic biodegradability. However, this report did not study if the lignin source can impact the properties of the generated polymer despite the valuable insights from previous research on the impact of lignin quality.

Applying lignin-caprolactone polymer is an excellent alternative to conventional coating polymers. Najarro et al. reported that kraft lignin-caprolactone copolymer had better-film-forming affinity and adhesion toward stainless-steel substrate [28]. However, the discussion of inherent coating performances, such as surface hydrophobicity, currently needs to be addressed. Lignin possesses intrinsic hydrophobic characteristics [29], rendering lignin-caprolactone polymers attractive as protective coatings for moisture-exposed surfaces, such as wood, by inhibiting moisture absorption. Such coating would contribute to preserving the material's structural integrity and durability. Moreover, lignin is thermally stable and somehow possesses flame-retardancy upon exposure to fire. Specifically, it experiences thermal degradation,resulting in the formation of a substantial char layer that serves as a barrier, inhibiting the propagation of flames and diminishing the emission of combustible gases [30, 31]. Therefore, lignin-caprolactone polymers may benefit applications with essential fire resistance, such as wood used for construction or furnishings.

This study selected three widely available lignins (birch alkali lignin (BL), wheat straw alkali lignin (WL), and softwood kraft lignin (SKL)). It examined the impact of lignin quality variation in the synthesis and characteristics of the lignin-caprolactone polymer, before and after lignin's ethanol fractionation for wood coating uses. A comprehensive study was conducted on the resulting polymer's thermochemical and viscoelastic characteristics. Furthermore, the water contact angle values, smoke density, limiting oxygen index values, and flame assessments were employed to assess the efficacy of these induced polymers as a protective layer on a wooden surface. The durability and adhesion of the coatings were evaluated via sandpaper abrasion and knifing on the coated samples, followed by water contact angle analysis. This work exhibits how the characteristics of lignin can impact its valorization and, ultimately, its application in wood coating applications.

7.3. Experimental Section

7.3.1. Materials

Wheat straw alkali (WL), birch alkali lignin (BL), and spruce kraft lignin (SKL) were supplied by CH-Bioforce Oy (Espoo, Finland), ethanol (96%), hexane (99%), ε-caprolactone (CL), dibutyltin dilaurate (DBTDL, 95%), methanol (95%), Acetone (95%), dimethyl sulfoxide (DMSO-d6), chloroform (CDCl3), anhydrous pyridine, endo-N-hydroxy-5-norbornene-2,3-dicarboximide, chromium (III) acetylacetonate (Cr(acac)3, 2-chloro-4,4,5,5-tetramethyl-1,3,2-dioxaphospholane (Cl-TMDP), dimethyl sulfoxide-d6 (DMSO-d6), chloroform-d containing 0.03%, tetramethylsilane (TMS), polycaprolactone (PCL, 80,000 g/mol) was purchased from sigma Aldrich. Stain grade pine wood and a 2”, 50.8 mm hand brush were bought from Home Depot Canada.

7.3.2. Ethanol Fractionation of Lignin

Wheat straw alkali lignin (WL), birch alkali lignin (BL), and spruce kraft lignin (SKL) were separated into fractions using ethanol. The solvent and lignin were mixed at a ratio of 7:1 by weight. After stirring for 2 hours, the mixture was separated into insoluble and soluble components using a vacuum filter. The ethanol-soluble portion (BL_E, WL_E, and SKL_E) was extracted and subjected to rotary evaporation to separate the lignin from ethanol. Afterward, specimens were gathered and dehydrated in a 60°C oven for 48 h. **Equation S7.1** (Appendix 7A) was employed to quantify the yield of lignin fractionation.

7.3.3. Lignin-Caprolactone Polymerization

WL, BL, and SKL, together with their ethanol-soluble forms (WL_E, BL_E, and SKL_E), were subjected to ring-opening polymerization with caprolactone without a solvent. This process resulted in the formation of lignin caprolactone polymers (WLP, BLP, SKLP, WL_EP, BL_EP, and SKL_EP). Caprolactone served as a ring-opening polymerization (ROP) monomer, lignin was utilized as a micro initiator, and DBTDL acted as a catalyst. The lignin was combined with CL (1.1 CL/OH, mmol/g ratio) at a nitrogen temperature of 50°C and agitated for 30 min. DBTDL was gradually introduced into reaction flax by the weight percentage ratio of lignin (1wt.%). The mixture was then heated to a temperature of 150°C and stirred magnetically at 250 rpm. After the reaction had been completed after 7h, the resulting product was cooled to the ambient temperature, and the mixture was subjected to several washes with chilled methanol to eliminate impurities. Ring-opening polymerization (ROP) is a kind of polymerization in which the reactive center of a polymer chain is at the terminal end [32]. This reactive center can open the ring structure of cyclic monomers (CL) and form a longer polymer chain. The -COO- group is created by the cleavage of the CL ring and its combination with the OH group of lignin, forming an ester bond. This process leaves a -OH group at the end of the CL chain, which then combines with CL monomers to facilitate the growth of a PCL molecule.

7.3.4. Wood Surface Coating

The lignin-caprolactone polymers (WLP, BLP, SKLP, WL_EP, BL_EP, and SKL_EP) were solubilized in acetone (1:10 wt./wt. ratio of lignin and acetone). A stain-grade pine wood surface was coated with the polymer solution using a 20” 50.8 mm hand brush and left to dry at room temperature.

7.4.5. Characterization

7.4.5.1. Structural Characterization of Lignin and Lignin-Caprolactone Polymers

The average molecular weight of WL, BL, SKL, WL_E, BL_E, SKL_E, WLP, BLP, SKLP, WL_EP, BL_EP, and SKL_EP was determined using size exclusion chromatography (SEC) with a multiangle light scattering detector and a differential refractive index concentration detector (MALS(IR)). Samples were prepared by drying them in a vacuum oven at a temperature of 40°C. The samples were placed in a clean HPLC vial at 10 mg/mL concentration in a mixture of DMSO and 0.05M lithium bromide (LiBr) eluent. Before conducting SEC analysis, the samples were filtered using 0.2 μm Nylon filters. The separation was conducted using a Jordi Gel glucose mixed-bed guard column with a diameter of 50 mm and length of 10 mm and a Jordi Gel GBR mixed-bed column with a diameter of 250 mm and length of 10 mm. The molecular weight analysis was conducted with the following parameters: a flow rate of 0.5 mL min-1, a column temperature of 60°C, an injection volume of 100 μL, and a dn/dc value of 0.15 mL g-1. Astra software, version 7.3.3, was used to assess the data [33].

The quantification of hydroxyl groups in WL, BL, SKL, WL_E, BL_E, SKL_E, WLP, BLP, SKLP, WL_EP, BL_EP, and SKL_EP by ^{31}P NMR [34]. The samples were prepared by dissolving 20 mg of vacuum oven-dried samples (at a temperature of 40°C) in a solvent mixture of 0.55 mL of anhydrous pyridine and deuterated chloroform ($CDCl_3$) (in a ratio of 1.6:1, volume/volume). This solvent mixture also contained a relaxation reagent of chromium(III) acetylacetone (Cr(acsac)3, at a concentration of 1.3 μmol) and an internal standard of endo-N-hydroxy-5-norbornene-2-3-dicarboximide (at a concentration of 12 μmol). The internal standard and lignin ratio was established as 0.6 mmol g-1. Before the ^{31}P-NMR experiment, the hydroxyl groups were phosphorylated using 0.1 mL of 2-chloro-4,4,5,5-tetramethyl-1,3,2-dioxaphospholane for 30 minutes. The Cr(acac)3 concentration was maintained at 0.002 M to ensure the full relaxation of the phosphorus nuclei prior to the application of the radiofrequency pulse. The spectrum was acquired using a pulse delay of 10 s, an acquisition duration of 2.0 s, and 64 scans. **Equation S7.2** was employed to determine the grafting % of CL onto the hydroxyl group of lignin, utilizing the hydroxyl group as a reference.

^{1}H-NMR and HSQC NMR studies were conducted on the WL, BL, SKL, WL_E, BL_E, SKL_E, WLP, BLP, SKLP, WL_EP, BL_EP, and SKL_EP samples. The ^{1}H-NMR apparatus was configured with 16 scans, a 3.28 s acquisition time, 1 s relaxation time, and a 90° pulse, all performed at ambient temperature. WL, BL, SKL, WL_E, BL_E, and SKL_E, samples were created by dissolving the samples, which had been dried in a vacuum oven at 40°C, in a solution of 80 mg/mL DMSO. On the other hand, WLP, BLP, SKLP, WL_EP, BL_EP, and SKL_EP samples were prepared by dissolving 80 mg of the samples in 0.75 mL of $CDCl_3$, corresponding to 0.03% of TMS by volume. The HSQC NMR spectra were obtained using the HSQCEDETGPSISP2.3 pulse sequence, with a relaxation delay of 2.0s and an acquisition time of 0.15s. A total of 256 increments were recorded, with 80 scans per increment. The findings were evaluated using the Top Spin 4.02 program. The linkages between the lignin's and degree of polymerization (n) in the PCL chain segments were quantified using the aromatic groups as internal standard and ^{1}H-NMR spectra of the lignin's and lignin-caprolactone polymers, respectively, according to **Equation S7.2-7.7**.

7.4.5.2. Thermal Analysis of Lignin and Lignin-Caprolactone Polymers

The thermal stability of WL, BL, SKL, WL_E, BL_E, SKL_E, WLP, BLP, SKLP, WL_EP, BL_EP, and SKL_EP samples was evaluated using a Q500 thermogravimetric analyzer manufactured by TA Instrument in the United States. Approximately 10 milligrams of samples dried in a vacuum oven at 40°C were measured and placed into an alumina disposable crucible (T 2101127, China). The samples were then heated from 30°C to 800°C at 10°C per min in a nitrogen environment with a 15 mL/min flow rate. The samples' glass transition temperature (Tg) and melt temperature (Tm) were determined using a Discovery DSC 250 calorimeter. The measurements were conducted in a heating-cooling-heating cycle, with constant nitrogen flow at a 15 mL/min rate. The samples, which had been dried in a vacuum oven at 40°C, were measured and placed into a Tzero pan (T 140829, Switzerland) covered with a Tzero lid (T 140826, Switzerland). The samples were then moved to the calorimeter, where they were placed beside a reference, an empty sealed Tzero pan. The samples were analyzed using TRIOS v5.5.5.1.5 software to determine their Tg and Tm.

7.4.5.3. Rheological Analysis of Lignin-Caprolactone Polymers

The rheological properties of WLP, BLP, SKLP, WL$_{E}$P, BL$_{E}$P, and SKL$_{E}$P were assessed by melt rheological characterization by temperature ramp experiment using MCR 702 MultiDrive rheometer (Anton Paar GmbH) equipped with a PP25 parallel plate (diameter: 25 mm and gap: 0.5 mm). The samples were heated at 1°C per minute, starting at 130°C. The experiment continued until a temperature was reached when the first indication of a crossover between the storage and loss modulus was observed. The duration of data capture for each data point was 10 seconds.

7.4.5.4. Surface Wettability Analysis of Lignin-Caprolactone-Coated Wood Surfaces

The surface wettability of WLP, BLP, SKLP, WL$_{E}$P, BL$_{E}$P, and SKL$_{E}$P-coated wood surfaces was evaluated using an optical tensiometer and the sessile drop method (Theta Lite, Bolin Scientific, Finland). The experiment involved depositing a liquid droplet, with a volume of 6-10 µL, onto the flat surface of the coated surface. The contact angle of the droplet was visually assessed using a camera for a duration of 10 s. The contact angle was studied using dedicated software that focuses on a single aspect, the measurement was conducted in their respective locations, and the average value was provided.

7.4.5.5. Flame-retardancy analysis of Lignin-Caprolactone-Coated Wood Surfaces

The limiting oxygen index (LOI) of uncoated wood WLP, BLP, SKLP, WL$_{E}$P, BL$_{E}$P, and SKL$_{E}$P-coated wood were determined by NETZSCH TAURUS equipment, a limiting oxygen index (LOI) analyzer from Germany following ASTM D2863 [35]. The samples were prepared in a dimension of 140mm × 20mm × 10mm, and five replicas were used for each sample. The smoke emission characteristics of uncoated wood

WLP, BLP, SKLP, WL$_E$P, BL$_E$P, and SKL$_E$P-coated wood were assessed by ASTM D2843-99 via smoke density test device AIC-2843, Advanced Instrument Co., Ltd, from China. The specimens, measuring 42mm × 42mm × 4mm, were inserted into the apparatus and exposed to a pressure of 0.14 MPa of propane gas for 250 s following ignition [36]. The samples' smoke density rating (SDR) and the light absorption curves were examined and displayed. The SDR metric assesses the concentration of smoke, whereas the light absorption curve quantifies the degree to which smoke particles absorb light during the burning process. Both measures were derived from the light absorption data. The samples were exposed to a powerful propane gas flame to replicate actual fire situations to commence combustion.

7.4. Results and Discussion

7.4.1. Characteristics of Ethanol Fractionated Lignin

7.4.1.1 Molecular Weight and Molecular Weight Distribution of Lignin’s

The average molecular weight (Mw) and polydispersity (ĐM) of lignin (WL, BL, and SKL) and their ethanol-soluble fractions (WL$_E$, BL$_E$, and SKL$_E$) are displayed in **Table 7.1**. The Mw of BL was higher, whereas SKL exhibited a lower Mw, although its ĐM was much larger than that of the other samples. The lower Mw and higher ĐM of SKL are the result of kraft pulping’s severe conditions, such as a high temperature and sodium sulfide, which break down the lignin into smaller fragments while the alkali pulping retains more of lignin’s original polymeric structure [37]. Ethanol fractionation generally reduced the Mw and ĐM of lignin types. The decrease in Mw and ĐM is caused by the reduction in heterogeneity of lignin resulting from the selective solubility of lignin components in ethanol [37]. The ethanol fractionation significantly affected the Mw and ĐM values of SKL. This characteristic is also consistent with the yield, which shows the highest yield for SKL$_E$ **Table 7.1**. The higher solubility of kraft lignin (SKL) compared to alkali lignin (BL and WL) in ethanol resulted in a higher yield, but its Mw and ĐM were reduced significantly due to its large original ĐM. The kraft process introduces more hydrophobic groups into the lignin structure, enhancing its solubility in less-polar solvents like ethanol [38, 39]. The higher Mw

(**Table 7.1**) of BL and WL could result in their lower solubility in ethanol [40]. Furthermore, the structural characteristic differences between the lignin sources could affect their solubility, which will be discussed in the coming NMR discussions.

7.4.1.2. Structural characterization of lignin's

The ^{1}H NMR and ^{31}P NMR spectra of BL, WL, SKL, BL_E, $WL_{E,}$ and SKL_E polymers are presented in **Figure 7.1**a-b. The ^{1}H NMR spectra showed aromatic protons (6.0-7.5 ppm), methoxy proton (3.75 ppm), aliphatic proton (0.85-2.2 ppm), and DSMO solvent (2.5 ppm) in **Figure 7.1**a [41]. The ethanol-soluble fractioned lignin (SKL_E, WL_E, and BL_E) shows stronger aliphatic signals that belong to an ethanol residue (1-1.5 ppm) [42]. The ^{31}P NMR spectra revealed the aliphatic, guaiacyl, C5-substituted, and carboxylic hydroxyl groups in the lignin's **Figure 7.1**b and their quantities in **Table 7.1**.

The number of hydroxyl groups in lignin rose following ethanol fractionation, with the most significant increase seen in SKL_E (19.29%). This aligns with the previouSKLy noted changes in yield and Mw **Table 7.1.** When comparing the change in specific hydroxyl groups, a carboxylic group in BL_E has a substantial change of 8.47%. In contrast, the p-hydroxyphenyl group in WL_E has a change of 14.29%, and the guaiacyl hydroxyl groups in SKL_E lignin have a change of 32.89% **Table 7.1**. This demonstrates that variation in the source and type of lignin affects the functional groups of lignin differently during ethanol fractionation.

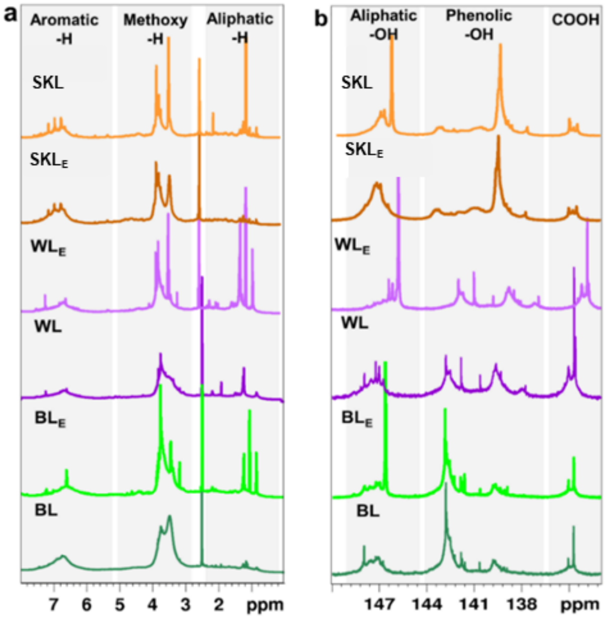

Figure 7.1. ^{1}H NMR (a) and ^{31}P NMR (b) of lignin and ethanol fractionated lignin.

In addition, the interunit linkages and substructures of the lignin were analyzed by HSQC NMR to understand the changes further. The spectra are presented in **Figure 7.2**(a-d), and the δ_C/δ_H ppm are presented in **Table S7.1**. Quantitative HSQC NMR was applied to evaluate the inter-unit linkages using the guaiacol (G_2) and syringyl ($S_{2,6}$) signals as an internal standard described according to **Equation (S7.2-S7.5)**, and values are listed in **Table** 7.1 [43]. The oxygenated aliphatic region (δ_C/δ_H 40-120/2.5-6.0) showed signals assigned and presented in **Figure 7.1**(a-b).

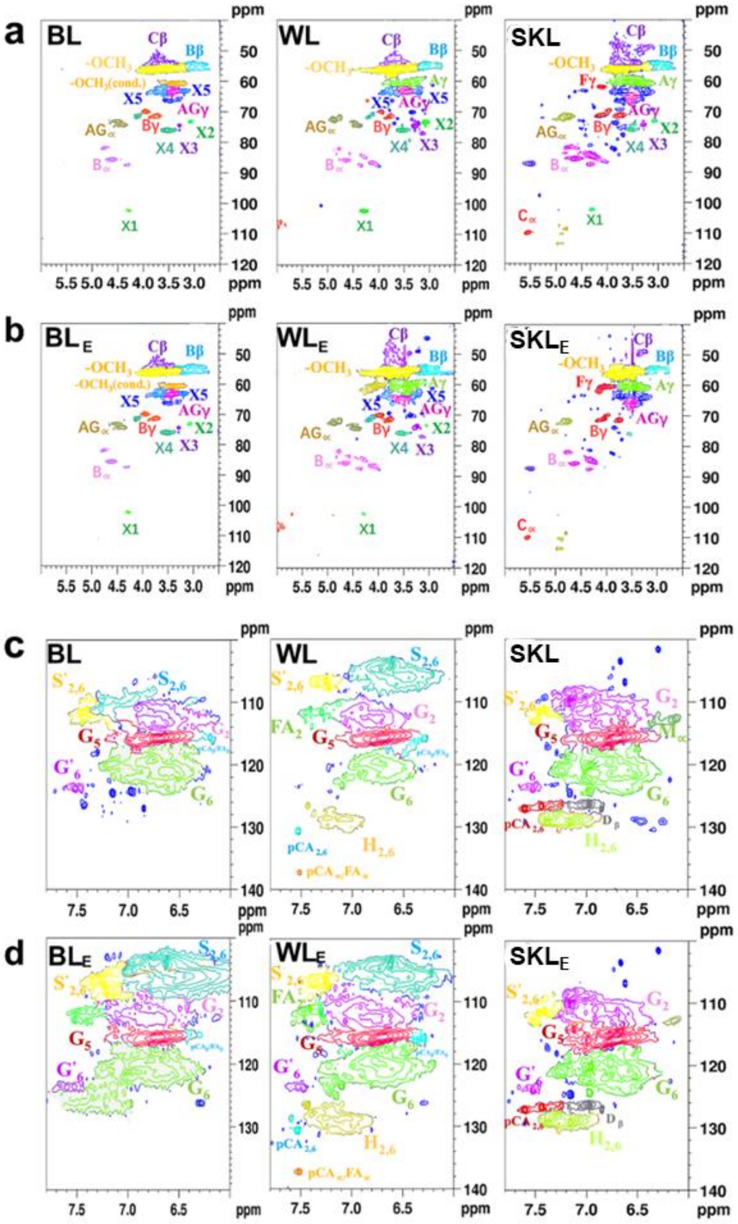

Figure 7.2. HSQC spectra significant oxygenated aliphatic linkages (a-b) and aromatic linkages (c-d) of lignin and ethanol soluble counterparts.

The dominant interunit linkage in all lignin is the diacylglycerol-β-aryl ether link (β-O-4) followed by pinoresinol (β−β′) and minor amounts of phenylcoumaran (β-5′). Relative to the original lignin, the ethanol-fractionated lignin shows a significant reduction in the β-O-4 linkages than β−β and β-5′ **Table 7.1**. This reduction could result from consuming β-O-4 linkages due to the ethanol fractionation [44]. Furthermore, the aromatic linkages (δ_C/δ_H 100-140/6.0-8) were analyzed, and the results are presented in **Figure 7.1**(c-d). The results indicate a much higher intensity of the S units in BL_E and WL_E than the original lignin. The rise in the S units aligns with the findings of P-NMR, which indicate an increase in the phenolic hydroxyl group.

7.4.1.3. Thermal properties of lignin's

The thermal properties of lignin samples were assessed before and after ethanol-fractionated lignin using TGA and DSC (**Figure 7.3(**a-c)). Generally, the ethanol-fractionated lignin has a lower T_o (onset temperature) and $T_{50\%}$ (the temperature at which 50% of the weight was lost) and a higher DTG_{max} (maximum degradation temperature) than the original lignin in **Figure 7.3**a-b. Compared to the unfractionated counterparts, the lower average molecular weight of the ethanol-fractionated lignin could be the reason for the lower T_o and $T_{50\%}$. The increased phenolic hydroxyl group (**Table 7.1**) of BL_E and WL_E could be a contribution of the higher DTG_{max} since a higher number of phenolic hydroxyl groups could result in a higher intermolecular hydrogen bonding interactions between lignin molecules contributing a higher temperature requirement for maximum degradation [45]. On the other hand, the significantly lower average molecular weight of SKL_E than SKL could be the reason for the slight decrease in DTGmax (**Table 7.1**).

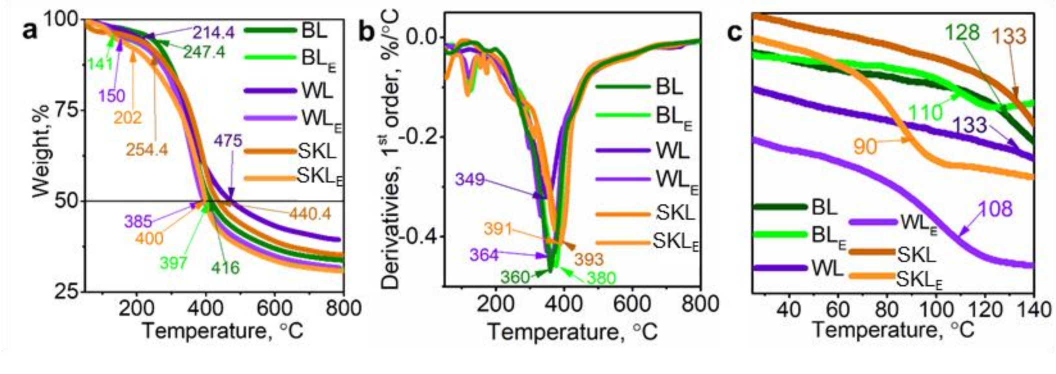

Figure 7.3. TGA (a), DTG (b), and DSC (c) of lignin's before and after ethanol fractionation.

The glass transition (T_g) of lignin was analyzed using DSC, and results are presented in **Figure 7.3c**. In general, the T_g of the ethanol-fractionated lignin was lower than their unfractionated counterparts; the reduced T_g in the ethanol-fractionated parts is attributed to the reduced Mw, narrower ĐM (**Table 7.1**), and alteration in the hydroxyl group, which will increase the chain mobility of lignin and thus reduce its T_g.

Table 7.1. Average molecular weight (Mw), polydispersity (Dm), hydroxyl groups, degree of polymerization, Tm, and percentage grafting of lignin and lignin caprolactone polymers.

Sample	**Mw, g mol^{-1}**	**Dm**	**Hydroxyl group, mmol/g**					**Linkages, %**			**DP**	**Yield ,% /Grafting, %**	**T_m**
			Aliphatic	**C5 substituted**	**Guaiacyl**	**p-hydroxyphenyl**	**Carboxylic acid**	**β-O-4**	**β-5**	**β-β**			-
BL	22870	3	1.4	2.1	0.5	-	0.6	14	7.8	13	-	-	-
BL_E	38827	1	1.4	2.2	0.5	-	0.6	3.6	4.4	2	-	54	-
WL	70280	1.5	1.5	1.6	1	0.3	1	5.6	3.8	7	-	-	-
WL_E	37590	1.2	1.5	1.7	1	0.3	1	5.2	5.1	7.5	-	50	-
SKL	16930	8.4	2.2	1.6	1.5	0.2	0.4	13	8.6	11.5	-	-	-
SKL_E	3210	1.8	2.6	1.7	2.0	0.2	0.5	6.7	4.6	6.1	-	57	-
BLP	72880	-	0.3	0.5	0.2	-	0.2	-	-	-	5.2	16	47
$\text{BL}_\text{E}\text{P}$	40230	-	0.3	0.4	0.2	-	0.2	-	-	-	4.9	26	49
WLP	-	-	-	-	-	-	-				1.3	-	-
$\text{WL}_\text{E}\text{P}$	2195	-	0.3	0.3	0.3	0.06	0.2	-	-	-	8.3	33	33
SKLP	-	-	-	-	-	-	-	-	-	-	1.9	-	-
$\text{SKL}_\text{E}\text{P}$	658	-	0.5	0.3	0.4	0.03	0.1	-	-	-	4.0	39	29

7.4.2. Characteristics of Lignin-Caprolactone Polymers

7.4.2.1. Structural Characteristics of Lignin-Caprolactone Polymers

The original lignin and ethanol-fractionated lignin were polymerized with caprolactone (CL) in the presence of catalysis. Lignin-(OH) was a macroinitiator with $Sn(Oct)_2$ catalyst and CL as a monomer. The amount of the hydroxyl group on the lignin-caprolactone polymers after polymerization is assessed by ^{31}P NMR (**Figure S7.1**a), and the quantification of hydroxyl groups is presented in **Table 7.1**. As SKLP and WLP were not soluble in ^{31}P NMR solvent, their NMR analysis could not be conducted. The insolubility of SKLP and WLP in ^{31}P NMR solvents could result from greater lignin crosslinking and a more rigid appearance at room temperature (**Figure S7.2**). The ^{31}P NMR quantification of the other samples shows a reduction in the hydroxyl groups compared to lignin. The total grafting percentage was calculated according to **Equation S7.6** and presented in **Table 7.1**, showing that SKL$_E$P has the highest grafting ratio. This could result from the ethanol fractionation of SKL, which shows a higher hydroxyl group in SKL$_E$ and presents more reactive sights for CL than the other lignin (**Table 7.1**). In addition, the percentage replacement of each functional group was calculated, and the results are presented in **Figure S7.1**b.

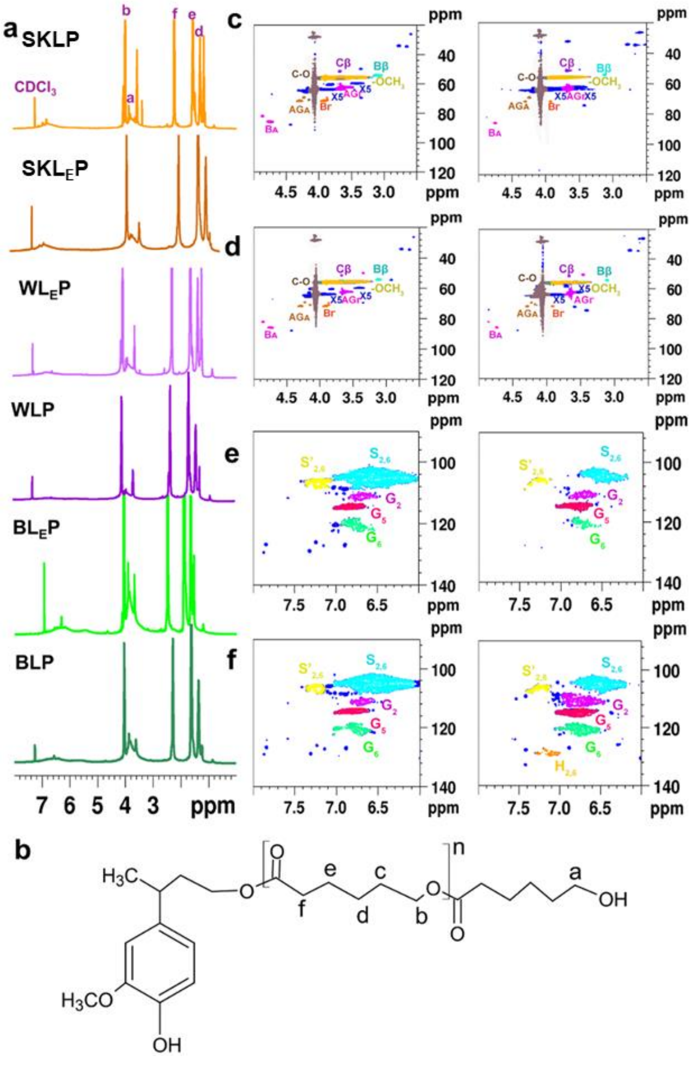

Figure 7.4. ^{1}H NMR (a), model structure of lignin monomer after caprolactone polymerization (b), oxygenated aliphatic regions of BLP and WLP (c), aliphatic regions of BL$_E$P and WL$_E$P (d), aromatic regions of BL and WL (e), aromatic linkages of BL$_E$P and WL$_E$P (f).

The involvement of p-hydroxyphenyl hydroxyl groups in SKL_EP and WL_EP was greater, but the replacement of aliphatic hydroxyl groups was more pronounced in BL_EP. The increased substitution of p-hydroxyphenyl hydroxyl groups over aliphatic hydroxyl groups in SKL_EP and WL_EP is attributed to the superior reactivity of phenolic hydroxyl groups, which is influenced by resonance stabilization, electron density, limited steric factors, and the acidity of phenolic hydroxyls, leading to enhanced nucleophilic properties [46]. Conversely, hardwood lignin (BL_E) lacks p-hydroxyphenyl (phenolic) hydroxyls, resulting in a higher conversion of aliphatic hydroxyl groups [47].

The ^{1}H-NMR spectra of all the polymers are depicted in **Figure 7.4**a, and the model lignin-caprolactone polymer is depicted in **Figure 7.4**b. The ^{1}H NMR spectra of all the lignin-caprolactone polymers show a peak of $CDCl_3$ (7.24), aromatic region (7-6) ppm indicating the presence of intact lignin aromatic structure, $-CH_2O-$ (a) at 3.9-4.1, and -COH (b) at 3.6-3.7 ppm representing the repeating and end-group of a PCL chain, respectively. In addition, methoxy (3.3-3.9), aliphatic-H of $-CH_2-$ at 1.32 (d), $-CH_2-$ (e and c) at 1.57, $-COCH_2-$ (f) at 2.24 ppm, which are a result of PCL chains as can be further supported by **Figure S7.3**.The presence of the PCL peaks in the lignin ^{1}H NMR spectrum indicates the polymerization's success on the lignin types. The degree of polymerization (DP) was calculated according to **Equation S7.7**, and the results are presented in **Table 7.1**. The DP of WL_EP is the greatest, while WLP's is the lowest. The alteration in DP is a clear indicator of the impact of ethanol fractionation, which decreases the average molecular weight of WL_E (**Table 7.1**), hence enhancing the development of the PCL chain on the lignin backbone due to less steric hindrance [48]. In ^{1}H-NMR and ^{31}P-NMR spectra (**Figure S7.2**), the decrease in the total hydroxyl groups of lignin (**Table 7.1**) confirms the polymerization of CL into PCL and its attachment to the lignin backbone. The oxygenated aliphatic linkage and aromatic regions of the C-H correlation signals were assessed by HSQC NMR of all the lignin-caprolactone polymers, as shown in **Figure 7.4**c.

The lignin-caprolactone polymers share similar linkages with lignin in the oxygenated aliphatic region δ_C/δ_H 50-100/2.5-5 ppm (**Figure** 7.**2**). While the aliphatic region δ_C/δ_H 10-80/0.5-2.5 appears to have dominant aliphatic signals compared to fractionated lignin (**Figure 7.2**a-b). The aromatic linkages of $S_{2,6}$, $S'_{2,6}$, G_2,

G_5, and G_6 are identified and depicted in **Figure 7.4**e-f. The presence of aromatic linkage signals in all the lignin caprolactone polymers results from strong aromatic linkages in the lignin (**Figure** 7.**2**c-d). This shows that the lignin caprolactone polymers have maintained lignin's aromatic structure.

7.4.2.2. Molecular Weight of Lignin-Caprolactone Polymers

The lignin-caprolactone polymers generated via unfractionated lignin (BLP) show a higher Mw than samples generated via the fractionated lignin (BL_EP) (**Table 7.1)**. The lower Mw of the lignin-caprolactone polymer synthesized by ethanol soluble fraction of lignin (BL_EP) indicates the reduced complexity and more uniform structure because of ethanol fractionation. The Mw of the fractionated lignin-caprolactone polymers exhibited a substantial increase compared to the fractionated lignin, as indicated in **Table 7.1**. This finding further proves that an aliphatic polyester chain is chemically attached to the lignin structure (**Figure 7.4**b).

7.4.2.3. Thermal Properties of Lignin-Caprolactone Polymers

The TGA analysis for lignin-caprolactone polymers shows a higher T_o, $T_{50\%}$, and DTG_{max} than fractionated lignin and unfractionated counterparts (**Table 7.1**). The thermal properties show improvement by an elevated T_o for the lignin caprolactone polymers in **Figure 7.5**a-b compared to the lignin (**Figure 7.3**a-b). This is due to the higher average molecular weight of the polymers after lignin-caprolactone polymerization, which resulted in the grafting of PCL chains to the lignin backbone, improving its thermal stability. The T_o, $T_{50\%}$, and DTG_{max} of lignin-caprolactone polymers produced by fractionation (WL_EP and SKL_EP) were lower than those of their unfractionated counterparts (WLP and SKLP), except for BLP and BL_EP, which exhibited no significant difference. The notable alteration in the cases of WL_EP and SKL_EP aligns with the reduced average molecular weight of the lignin-caprolactone polymers produced by the fractionated components; however, the lesser impact on BL_EP is attributable to the much larger average molecular weight of the polymer.

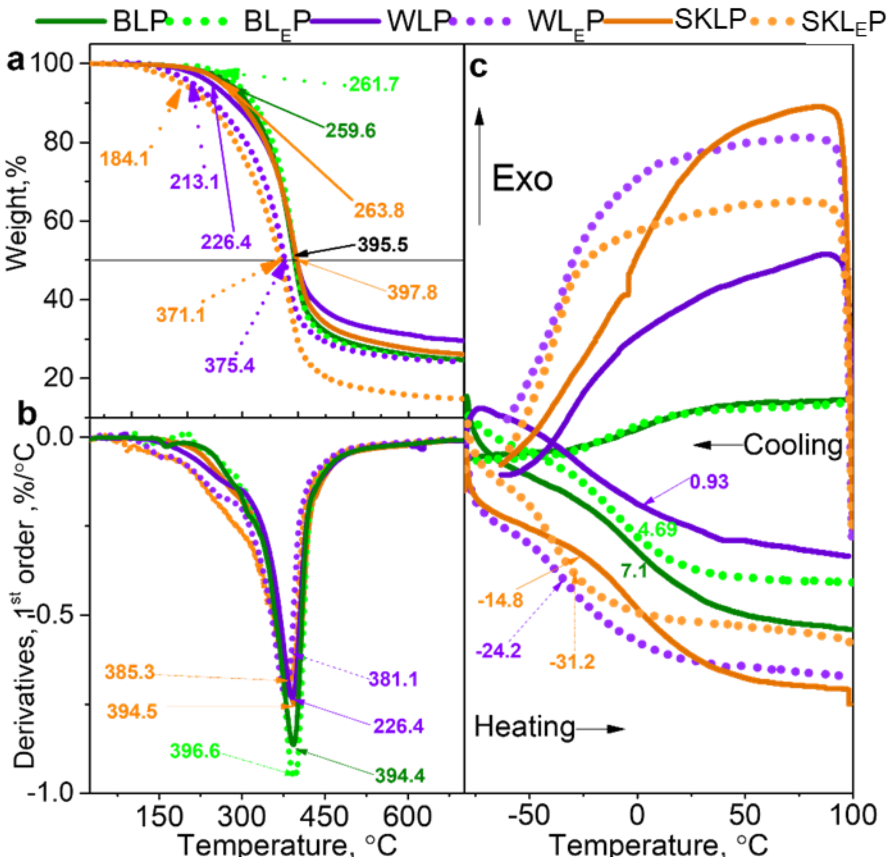

Figure 7.5. TGA (a), DTG (b), and DSC based on the 2nd heating and cooling cycle (b) of lignin-caprolactone polymer.

Between the fractionated lignin caprolactone polymers, SKL$_E$P shows a lower T_o, $T_{50\%}$, and DTG$_{max}$, which is consistent with the lower average molecular weight of SKL$_E$P and SKL$_E$ compared to the other samples (**Table 7.1**).

DSC analysis was conducted to further understand the thermal properties change because of the polymerization (**Figure** 7.**5**c). It is crucial to note that the melt temperature (T_m) was observed for the lignin-caprolactone polymers at the first heating cycle and recorded in **Table 7.1**, which was not observed for the fractionated and unfractionated lignin (**Figure 7.3**). The presence of T_m in lignin-caprolactone indicates that the grafting of PCL chains on the lignin backbone successfully changed lignin to a thermoplastic polymer. Conversely, the absence of these melting peaks in subsequent heating cycles and their absence from WLP and SKLP is linked to the shorter chain length of the PCL chains on the lignin backbone. This could result from the lower concentration of CL/OH (1.1 mmol), leading to a short PCL chain length (DP from **Table 7.1**) in the lignin molecular structure. The random structure of lignin limits the molecular mobility of a shorter chain of PCL in lignin [16]. The lower T_m is for SKL_EP, consistent with its Mw and DP values (**Table 7.1**). The T_g is obtained from the 2nd heating cycle and indicated in **Figure** 7.**5**c, along with the cooling cycles showing the crystallization of the samples. The lignin-caprolactone polymers show lower T_g than unpolymerized and unfractionated lignin (**Figure 7.5**c). The decrease in the polymers' T_g may be ascribed to increased free volume inside the polymers. This increase in free volume allows for molecular mobility facilitated by the grafting of PCL onto the lignin backbone [16]. The unfractionated lignin-caprolactone polymers have a lower T_g compared to the fractionated lignin-caprolactone polymers. This aligns with the lowered T_g following ethanol fractionation of all lignins, attributed to diminished Mw and decreased complexity, which enhance the mobility of the lignins (**Figure 7.3**c). The ethanol-fractionated lignin-caprolactone polymers have the highest T_g for BL_EP, and SKL_EP exhibits the lowest T_g. This aligns with the Flory-Fox theory, which posits that polymers with larger Mw exhibit elevated T_g, whereas those with lower molecular weights have reduced T_g [49].

7.4.2.4. Rheological Properties of Lignin-Caprolactone Polymers

Rheological properties are crucial for polymer characterization, providing information on a melt polymer's molecular entanglement and relaxation, affecting the overall performance. Precisely, rheological properties, such as viscosity, determine the coating polymer drying time, leveling, adhesion, texture, and mechanical properties [50]. The temperature ramp-down experiment in **Figure 7.6**a-c shows a complex viscosity, storage modulus (G'), loss modulus (G''), and tan delta of BLP, BL_EP, WL_EP, and SKL_EP. The experiment for WLP and SKLP was not documented due to the absence of polymer melting at any temperature. The lignin-caprolactone polymers' complex viscosity, G' and G'', dropped as the temperature ascended (**Figure 7.6**a-b). As temperature rises, the complex viscosity and modulus decline suggest that heat triggers molecular chain motion, decreasing internal resistance to flow [51, 52]. Consequently, the polymer becomes flexible as the temperature increases [53]. Among all the samples analyzed, BLP shows a higher complex viscosity and modulus throughout the temperature range, while SKL$_E$P shows the lowest. This directly indicates the higher Mw of BLP and lower average molecular weight of SKL$_E$P (**Table 7.1**).

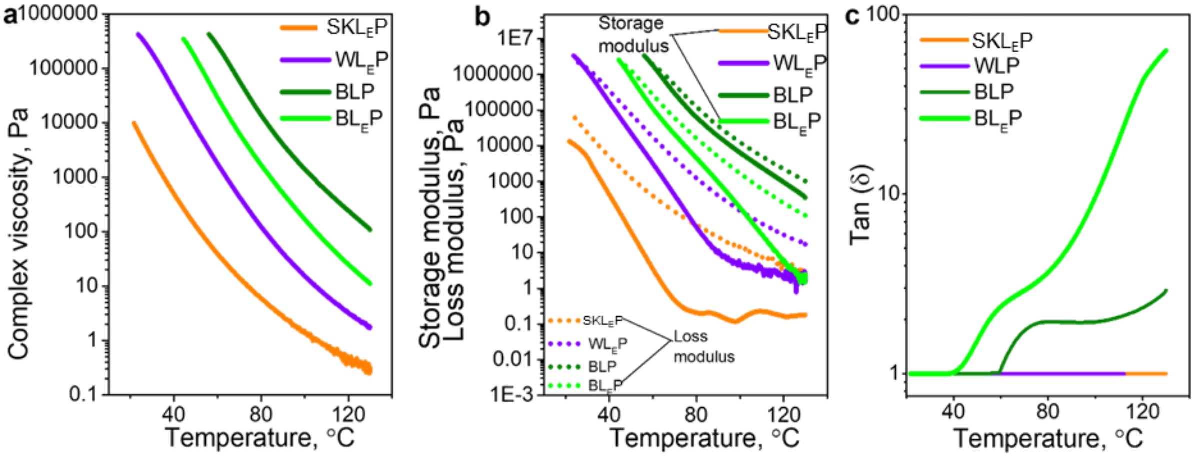

Figure 7.6. Complex viscosity (a), storage (solid lines), and loss modulus (short dots) (b), and tan delta (c) of lignin-caprolactone polymers.

Furthermore, the point at which G' and G'' intersect (i.e., cross-over point) appears at a lower temperature for ethanol-fractionated lignin-caprolactone polymers, while BLP cross-over appears at a higher temperature (55 °C) (**Figure 7.6**b). This offers a glimpse into the phase transition of polymers as they change from a liquid-like state to a more solid-like throughout the cooling process [54]. This transition is connected to the drying or solidification of the polymer. The tan delta profile of the lignin-caprolactone polymers is indicated in **Figure 7.6**c. BLP shows a higher tan delta than the fractionated lignin-caprolactone polymer. The lower tan delta values of the fractionated lignin-caprolactone polymers are an indication of the effect of the lower Mw of lignin-caprolactone polymers (**Table 7.1**) because of lignin fractionation before polymerization, which in turn affects the rheological properties of the polymers. Among the fractionated lignin-caprolactone polymers, SKL$_E$P shows the lowest tan delta. This result is consistent with the Mw, DP, and grafting percentage analysis discussed in previous sections (**Table 7.1**) [55]. The tan delta value that remained at one across a range of temperatures indicates that WL$_E$P and SKL$_E$P have a more balanced viscoelastic behavior, indicating that the molecular structure of these two polymers is consistently elastic and viscous, regardless of temperature [56]. This indicates that SKL_EP and WL_EP polymers will have lower resistance to flow during coating applications.

7.4.2. Performance of Lignin-caprolactone as a coating on wood surface

The pine-grade wood was coated with each polymer after dissolving the polymers in acetone. The hydrophobic/hydrophilic characteristics and combustibility of the coated wood were analyzed, and the results are presented in **Figures 7.7** and 7.**8**. All the coated woods exhibited a higher water contact angle (WCA) value **Figure 7.7**a-b than uncoated wood (34°) **Figure S7.4**. However, the WCA values of the lignin-caprolactone polymers produced using unfractionated lignin exhibit a lower WCA value than the polymers synthesized using fractionated lignin (**Figure 7.7a-b)**. Furthermore, the polymer films on the wood surface produced from the unfractionated lignin have a coarser appearance than those made from the fractionated lignin (**Figure 7.7**a-b). This coarser appearance is prominent in WLP and SKLP-coated surfaces, possibly due to the limited solubility of those polymers in acetone for coating formulation **Figure S7.5**. The increased hydrophobicity of lignin-caprolactone polymers synthesized after lignin fractionation can be directly related to the lower number of free hydroxyl groups in the polymers and due to longer PCL chains, as indicated by a higher DP (**Table 7.1**). Among the polymers produced from fractionated lignin-caprolactone, WL_EP has the largest WCA. The higher WCA of WL_EP can be directly correlated to the higher DP of PCL replacing the hydrophilic (free hydroxyl) groups of fractionated lignin, resulting in a higher contact angle value of the induced polymer (**Table 7.1**).

Replacing lignin hydrophilic hydroxyl groups with hydrophobic PCL segment reduces the surface energy and makes it less attractive to water molecules [27]. The WCA study indicates that the fractionation affecting lignin's reactivity towards CL and the chain development of PCL on the lignin backbone might positively impact the coating performance of lignin-caprolactone polymers. The adhesion of the fractionated lignin-caprolactone polymers to the wood surface is evaluated via sandpaper abrasion and knifing as shown in **Figure S7.6** and followed by WCA analysis; results are presented in **Figure 7.7**c-d. The WCA preserved its initial WCA after 120 cm of sandpaper abrasion on the covered wood surfaces with all polymers. A minor decrease is noted after 150 cm, although not much greater; likewise, the knifing did not alter the WCA of the coated surfaces. This test demonstrates that the mechanical characteristics of the polymer are robust and exhibit strong adherence to the wood surface [57, 58].

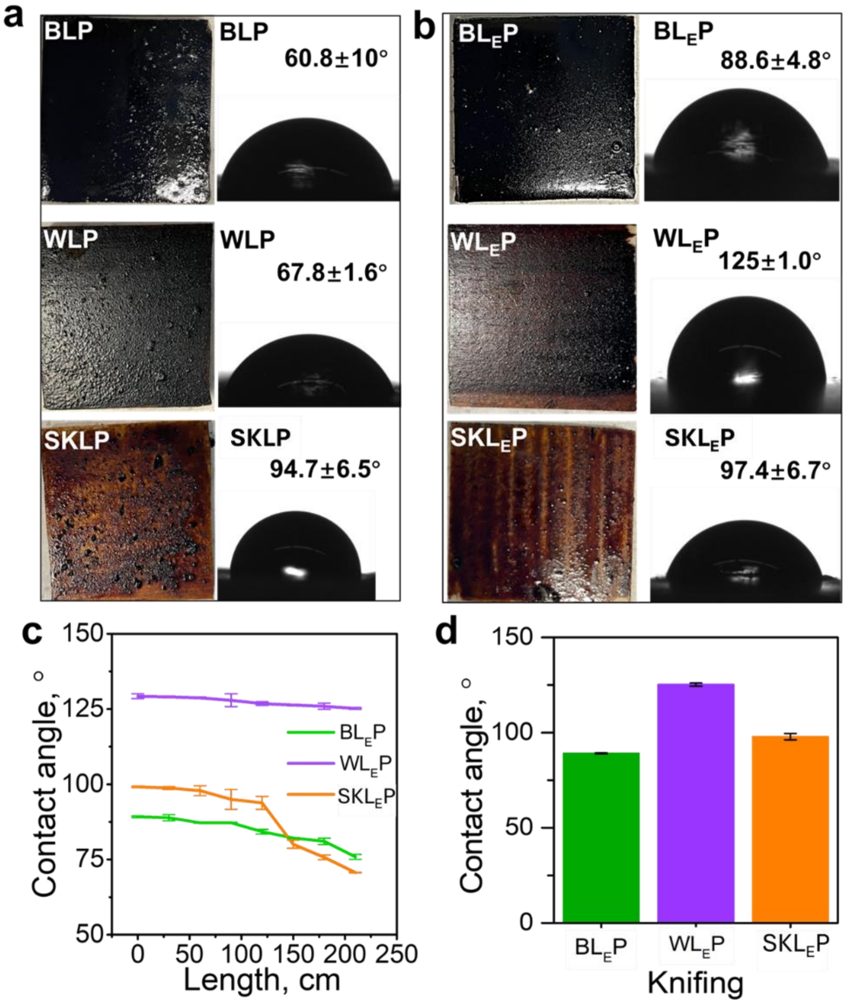

Figure 7.7. The appearance of wood coated with lignin-caprolactone polymers and water contact angle (WCA) values. Lignin-caprolactone polymers (a), unfractionated lignin-caprolactone polymers (b), sand-abraded contact angles at different lengths (c), and contact angles after knifing (d).

The flame-retardant characteristics of the coated woods were characterized via light absorption percentage, smoke density rating, LOI, and flame test results, which are presented in **Figure 7.8**a-f. The coated samples show a lower light absorption percentage, lower smoke density rating, and higher LOI than the uncoated wood sample. This indicates that the lignin-caprolactone coating decreased the flammability of wood by offering a protective layer. The lignin-caprolactone polymer's enhanced flame retardancy is attributable to its intrinsic flame-retardant properties, which stem from its superior thermal stability, char production, radical scavenging capacity, and physical barrier features [59]. The fractionated lignin-caprolactone polymers show 1) a higher light absorption percentage in the first 100 s of the analysis and 2) an overall smaller smoke density than their unfractionated counterparts. Conversely, the LOI values of all fractionated lignin-caprolactone polymers were somewhat elevated compared to the unfractionated lignin-caprolactone polymers, with the greatest value (27.5%) observed for BL_EP and WL_EP, and the lowest for WLP and SKLP (26% and 26.5%, respectively).

This aligns with the TGA and DTG findings (**Figure 7.5).** This slight discrepancy in the flame-retardant characteristics of the polymers could result from the limited solubility of WLP and SKLP in acetone, limiting the coverage of the wood with the polymers (**Figure S7.6**). In addition, the lower LOI of SKL_EP can be understood from the thermal stability of the polymers, as discussed in section 3.2.3, where SKL_EP had the lowest T_o, which can explain the lower LOI. However, DTG_{max} was not significantly different from the other polymers, indicating lower overall smoke density [60-63]. The slower combustion of SKLP and SKL_EP than BLP and BL_EP, as indicated by smoke density and light absorption values, can be explained by the higher $T_{50\%}$ (**Figure 7.5**) [64-66]. The link between a polymer's thermal stability and smoke density creation can be associated; as the thermal degradation temperature rises, the chemical bonds within the material deteriorate more swiftly, resulting in the emission of volatile chemicals. These substances facilitate the generation of smoke. Elevated temperatures often lead to more thorough burning, hence decreasing smoke density. Nevertheless, insufficient temperature for full combustion may result in increased smoke density due to unburned particulates [67, 68].

The flame test was conducted to further understand the flammability of the fractionated lignin-caprolactone-coated wood surfaces in a real-life fire, and the results are depicted in **Figure 7.8**c-f. Uncoated wood, when exposed to propane gas, experienced continuous ignition with a flame that lasted for 60 seconds, consuming more than half of the sample. All fractionated lignin-caprolactone polymer-coated wood samples exhibited a self-quenching property during the initial two ignitions, indicating a higher flame retardancy.

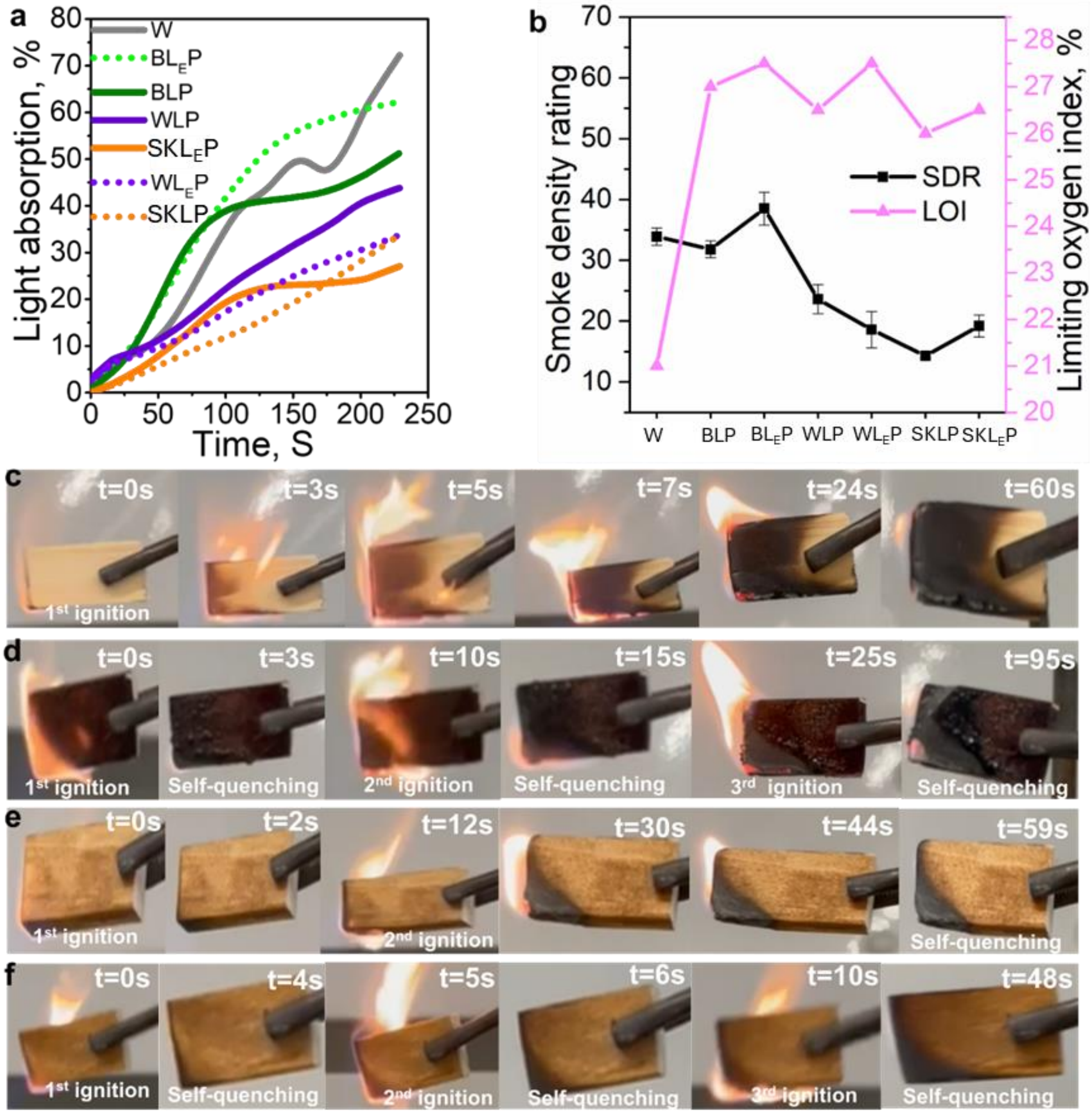

Figure 7.8. Light absorption values (a), smoke density and LOI (b) of fractionated and unfractionated lignin-caprolactone polymers, flame test on uncoated wood (c), BL_EP (d), SKL_EP (e), and WL_EP coated wood (f).

The enhanced flame retardancy and increased hydrophobicity of the lignin-caprolactone polymers synthesized from ethanol-fractionated lignin indicate that this lignin variant may be an effective precursor for the polymerization of lignin-caprolactone, yielding superior hydrophobic and flame-retardant polymers suitable for coating applications. The disparity in the characteristics of lignin-caprolactone polymers generated under analogous circumstances from various lignin sources after ethanol fractionation with diverse attributes highlights the importance of lignin selection for synthesizing lignin-caprolactone polymers.

7.5. Overall Performance

Lignin is increasingly utilized in formulation for wood coatings due to its unique hydrophobic and flame-retardant properties, as shown in **Table 7.2**. The utilization of lignin in coatings mainly entails composite formulations, whereby lignin is integrated as a component to provide specific properties; nonetheless, limited information exists regarding the efficacy of lignin as a polymer, particularly as a thermoplastic polymer for wood coatings. Applying lignin as a polyol in polyurethane formulations predominates the study on approaches utilizing lignin as a polymer covering for wood surfaces. However, employing lignin at elevated concentrations affects PU-coated polymers' mechanical characteristics and hydrophobicity, as seen in **Table 7.2.** This study is distinguished by utilizing a greater lignin concentration of as high as 73.4% for polymerizing lignin-caprolactone for wood coating, exhibiting effective hydrophobic properties with WCA of 125° and flame-retardant performance with LOI of 27.5%. Moreover, this study also demonstrated how the lignin type and source can influence the coating efficacy of lignin-based polymer.

Table 7.2. Comparison of existing literature on lignin-based wood coatings.

Lignin type	Modifications	Formulation	Max lignin con., %	LOI, %	WCA, °	Ref.
Softwood kraft lignin	Hydroxtethylation, esterification	Modified lignin, water	NA	NA	137	[69]
Softwood kraft lignin	1H, 1H, 2H, 2H-perfluorodecyl-triethoxysilane grafting	Epoxy resin, modified lignin, acetone composite	34.8	NA	164.7	[70]
Organosolv lignin	Colloidal lignin micro-nanospheres	Colloidal lignin micro-nanospheres, waterborne PU	60	NA	73	[71]
Organosolv lignin	NA	Water-borne acrylic, CNC, Lignin	5	NA	52.45	[72]
Kraft lignin	Phosphorylation, Vinylation	Lignin as a polyol in PU synthesis	25	NA	10	[73]
Kraft lignin	Lignin nanoparticles	Epoxy, Lignin nanoparticles	20	NA	120	[74]
Kraft lignin	NA	Lignin, urea, ammonium dihydrogen phosphate, composite	10	39.5	NA	[75]
Alkali lignin	Carboxymethylation	Lignin phytic acid, urea, glyoxal, PU	10	41.5	NA	[76]
Brich alkali lignin	Ethanol fractionation, ROP caprolactone polymerization	Lignin-caprolactone polymer, acetone	73.4	27.5	88.6	This work
Wheat straw alkali lignin			66.7	27.5	125	
Softwood kraft lignin			60.5	26.5	97.4	

"PU"-polyurethane, "CNC" cellulose nanocrystal, "NA" not reported.

7.6. Conclusion

This study examined the effects of ethanol fractionation on birch alkaline (BL), wheat straw alkali (WL), and softwood kraft (SKL) lignins, their reactivity to lignin-caprolactone polymerization, and their performance as a coating in wood surfaces. Ethanol fractionation greatly impacted lignin's average molecular weight (Mw), polydispersity (ĐM), total hydroxyl group, thermal stability, and reactivity to caprolactone (CL) ring-opening polymerization. Decreased β-O-4 links and Mw could be linked to lower TGA onset temperature and glass transition temperatures (T_g) for all polymers compared to the unfractionated counterpart. The ethanol fractionation effect on SKL was more significant than on WL and BL due to SKL's higher hydrophobic groups and lower molecular weight, resulting in higher solubility, reduced Mw, and increased hydroxyl group. The reactivity of lignin with CL and the degree of PCL polymerization on lignin backbone was significantly dependent on the source, type and ethanol fractionation of lignin. Similarly, the thermal and rheological properties of lignin-caprolactone polymers were significantly affected by the fractionation, and the source lignin and type of lignin were caused by the difference in Mw. In addition, the ethanol fractionation before the copolymerization improved the film-forming ability, hydrophobicity, and flame-retardant performance of the coated wood. The WL ethanol fractionated-caprolactone polymeric coating on the wood surface showed the highest hydrophobicity with a water contact angle of 125° and a limiting oxygen index of 27.5 %. This study, for the first time, showed that lignin from diverse sources, after ethanol fraction with caprolactone polymerization, showed a higher hydrophobicity and flame-retardancy when applied as a coating material.

7.7. References

1. De Hoe, G.X.R., *Sustainable Cross-linked Polymers*. 2019.
2. Merckle, D.C., *Ring Opening Copolymerization Synthesis of 3D Printable Polyesters for Tissue Regenerative Devices*. 2024.
3. Mohamed, R.M. and K. Yusoh, *A review on the recent research of polycaprolactone (PCL)*. Adv. Mat. Res., 2016. **1134**: p. 249-255. 10.4028/www.scientific.net/AMR.1134.249.
4. Malikmammadov, E., et al., *PCL and PCL-based materials in biomedical applications*. J. Biomater., 2018. **29**(7-9): p. 863-893. 10.1080/09205063.2017.1394711.
5. Dash, T.K. and V.B. Konkimalla, *Polymeric modification and its implication in drug delivery: poly-ε-caprolactone (PCL) as a model polymer*. Mol. Pharm., 2012. **9**(9): p. 2365-2379. 10.1021/mp3001952.
6. Homaeigohar, S. and A.R. Boccaccini, *Nature-derived and synthetic additives to poly (ε-caprolactone) nanofibrous systems for biomedicine; an updated overview*. Front. Chem., 2022. **9**: p. 809676. 10.3389/fchem.2021.809676/full.
7. Pucciariello, R., et al., *Lignin/poly (ε-caprolactone) blends with tuneable mechanical properties prepared by high energy ball-milling*. J. Polym. Environ., 2010. **18**: p. 326-334. 10.1007/s10924-010-0212-1.
8. Santos, C.C.O., et al., *Lignin valorization through polymer grafting by ring-opening polymerization and its application in health, packaging, and coating*. J. Environ. Chem. Eng., 2023. **11**(3): p. 109691. https://doi.org/10.1016/j.jece.2023.109691.

9. Labet, M. and W. Thielemans, *Synthesis of polycaprolactone: a review.* Chem. Soc. Rev., 2009. **38**(12): p. 3484-3504. 10.1039/B820162P
10. Lee, J.J.C., et al., *Lignin-g-polycaprolactone as a form-stable phase change material for thermal energy storage application.* J. Energy Storage, 2022. **56**: p. 106118. https://doi.org/10.1016/j.est.2022.106118.
11. Laurichesse, S. and L. Avérous, *Synthesis, thermal properties, rheological and mechanical behaviors of lignins-grafted-poly(ε-caprolactone).* Polymer, 2013. **54**(15): p. 3882-3890. https://doi.org/10.1016/j.polymer.2013.05.054.
12. Park, I.-K., et al., *Solvent-free bulk polymerization of lignin-polycaprolactone (PCL) copolymer and its thermoplastic characteristics.* Sci. Rep., 2019. **9**(1): p. 7033. s41598-019-43296-2.
13. Bass, G.F. and T.H. Epps, *Recent developments towards performance-enhancing lignin-based polymers.* Polym. Chem., 2021. **12**(29): p. 4130-4158.
14. Parit, M. and Z. Jiang, *Towards lignin derived thermoplastic polymers.* Int. J. Biol. Macromol., 2020. **165**: p. 3180-3197.
15. Yang, W., et al., *Biodegradable poly (lactic acid)-poly (ε-caprolactone)-nanolignin composite films with excellent flexibility and UV barrier performance.* Compos. Commun., 2020. **22**: p. 100497.
16. Hatakeyama, T., S. Yamashita, and H. Hatakeyama, *Thermal properties of lignin-based polycaprolactones.* J. Therm. Anal. Calorim., 2021. **143**: p. 203-211.
17. Ralph, J., C. Lapierre, and W. Boerjan, *Lignin structure and its engineering.* Curr. Opin. Biotechnol., 2019. **56**: p. 240-249.
18. Kazzaz, A.E. and P. Fatehi, *Technical lignin and its potential modification routes: A mini-review.* Ind. Crops Prod., 2020. **154**: p. 112732.
19. Santos, R.B., et al., *Lignin structural variation in hardwood species.* J. Agric. Food Chem., 2012. **60**(19): p. 4923-4930.
20. Bose, S.K., et al., *Lignin content versus syringyl to guaiacyl ratio amongst poplars.* Bioresour. Technol., 2009. **100**(4): p. 1628-1633.
21. Nadányi, R., et al., *Lignin modifications, applications, and possible market prices.* Energies, 2022. **15**(18): p. 6520.
22. Rousu, P., P. Rousu, and J. Anttila, *Sustainable pulp production from agricultural waste.* Resour. Conserv. Recycl., 2002. **35**(1-2): p. 85-103.
23. Fernández-Rodríguez, J., et al., *Lignin valorization from side-streams produced during agricultural waste pulping and total chlorine free bleaching.* J. Clean Prod., 2017. **142**: p. 2609-2617.
24. Li, M., et al., *Synthesis and Characterization of Lignin-grafted-poly(ε-caprolactone) from Different Biomass Sources.* New Biotechnol., 2021. **60**: p. 189-199. https://doi.org/10.1016/j.nbt.2020.10.005.
25. Liu, R., et al., *Fractionation of lignin with decreased heterogeneity: based on a detailed characteristics study of sequentially extracted softwood kraft lignin.* ACS Sustain. Chem. Eng., 2021. **9**(41): p. 13862-13873. 10.1021/acssuschemeng.1c04725.
26. Gigli, M. and C. Crestini, *Fractionation of industrial lignins: opportunities and challenges.* Green Chem., 2020. **22**(15): p. 4722-4746. 10.1039/D0GC01606C.
27. Xie, D., et al., *Effect of the lignin structure on the physicochemical properties of lignin-grafted-poly (ε-caprolactone) and its application for water/oil separation.* ACS Sustain. Chem. Eng., 2022. **10**(50): p. 16882-16895.
28. Najarro, M.C., et al., *Tuning the lignin-caprolactone copolymer for coating metal surfaces.* ACS Appl. Polym. Mater., 2020. **2**(12): p. 5767-5778. 10.1021/acsapm.0c01026.
29. Alwadani, N., N. Ghavidel, and P. Fatehi, *Surface and interface characteristics of hydrophobic lignin derivatives in solvents and films.* Colloids Surf., 2021. **609**: p. 125656. https://doi.org/10.1016/j.colsurfa.2020.125656.

30. Mandlekar, N., et al., *An overview on the use of lignin and its derivatives in fire retardant polymer systems*. Lignin-trends and applications. Vol. 9. 2018: IntechOpen, London, UK. 207-231.
31. Solihat, N.N., et al., *Recent developments in flame-retardant lignin-based biocomposite: manufacturing, and characterization.* J. Polym. Environ., 2022: p. 1-21.
32. Guofu, Q., et al., *Grafting modification of lignin via ring-opening polymerization.* Prog. Chem., 2020. **32**(10): p. 1547.
33. Zinovyev, G., et al., *Getting closer to absolute molar masses of technical lignins.* ChemSusChem, 2018. **11**(18): p. 3259-3268. 10.1002/cssc.201801177.
34. Meng, X., et al., *Determination of hydroxyl groups in biorefinery resources via quantitative 31P NMR spectroscopy.* Nat. Protoc., 2019. **14**(9): p. 2627-2647. s41596-019-0191-1.
35. Tomak, E.D. and A.D. Cavdar, *Limited oxygen index levels of impregnated Scots pine wood.* Thermochim. Acta., 2013. **573**: p. 181-185. 10.1016/j.tca.2013.09.022.
36. An, S.J., et al., *Long-term lithium-ion battery performance improvement via ultraviolet light treatment of the graphite anode.* J. Electrochem. Soc., 2016. **163**(14): p. A2866. 10.1149/2.0171614jes.
37. Ponnuchamy, V., et al., *Fractionation of lignin using organic solvents: A combined experimental and theoretical study.* Int. J. Biol. Macromol., 2021. **168**: p. 792-805.
38. Guo, M., et al., *Hydrothermal depolymerization of kraft lignins with green C1–C3 alcohol–water mixtures.* Energy Fuels, 2021. **35**(19): p. 15770-15777.
39. Goldmann, W.M., et al., *Solubility and fractionation of Indulin AT kraft lignin in ethanol-water media.* Sep. Purif. Technol., 2019. **209**: p. 826-832.
40. Sameni, J., S. Krigstin, and M. Sain, *Solubility of lignin and acetylated lignin in organic solvents.* BioResources, 2017. **12**(1): p. 1548-1565.
41. Pan, C., et al., *Effects of ethanol pretreatment on dissolution and structural changes of lignin from steam-exploded wheat straw.* Bioresources, 2019. **14**(3): p. 6958-6969. 10.15376/biores.14.3.6958-6969.
42. Zuriarrain, A., et al., *Quantitative determination of ethanol in cider by 1H NMR spectrometry.* Food Control, 2015. **50**: p. 758-762. https://doi.org/10.1016/j.foodcont.2014.10.024.
43. Sette, M., R. Wechselberger, and C. Crestini, *Elucidation of lignin structure by quantitative 2D NMR.* Chem. Eur. J., 2011. **17**(34): p. 9529-9535. 10.1002/chem.201003045.
44. Pang, T., et al., *Lignin fractionation: Effective strategy to reduce molecule weight dependent heterogeneity for upgraded lignin valorization.* Ind. Crops Prod., 2021. **165**: p. 113442. 10.1016/j.indcrop.2021.113442.
45. Choi, J.-H., et al., *Thermal properties of ethanol organosolv lignin depending on its structure.* ACS omega, 2021. **6**(2): p. 1534-1546. 10.1021/acsomega.0c05234.
46. Cui, C., et al., *Toward Thermoplastic Lignin Polymers; Part II: Thermal & Polymer Characteristics of Kraft Lignin & Derivatives.* BioResources, 2013. **8**(1).
47. Kumar, S., et al., *Lignin and its applications with polymers.* J. Biobased Mater. Bioenergy, 2009. **3**(1): p. 1-24.
48. Liu, P., et al., *Effect of lignin-based monomer on controlling the molecular weight and physical properties of the polyacrylonitrile/lignin copolymer.* Int. J. Biol.l Macromol., 2020. **164**: p. 2312-2322.
49. Stoddart, A., W.J. Feast, and S.P. Rannard, *Synthesis and thermal studies of aliphatic polyurethane dendrimers: a geometric approach to the Flory–Fox equation for dendrimer glass transition temperature.* Soft Matter, 2012. **8**(4): p. 1096-1108.
50. Reynolds, P.A., *The rheology of coatings*. The Chemistry and Physics of Coatings. 2004. 26.

51. Wietor, J.-L., et al., *Effects of branching and crystallization on rheology of polycaprolactone supramolecular polymers with ureidopyrimidinone end groups.* Macromolecules, 2011. **44**(5): p. 1211-1219.
52. Kotula, A.P. and K.B. Migler, *Evaluating models for polycaprolactone crystallization via simultaneous rheology and Raman spectroscopy.* J. Rheol., 2018. **62**(1): p. 343-356.
53. Dorgan, J.R., J.S. Williams, and D.N. Lewis, *Melt rheology of poly (lactic acid): Entanglement and chain architecture effects.* J. Rheol., 1999. **43**(5): p. 1141-1155.
54. Yu, R., et al., *Rheology and relaxation processes in a melting thermotropic liquid–crystalline polymer.* J. Appl. Polym. Sci., 2007. **104**(6): p. 3780-3787.
55. Tanner, R.I., *Engineering rheology*. Vol. 52. 2000: OUP Oxford.
56. Piau, J.M. and J.F. Agassant, *Rheology for polymer melt processing*. 1996: Elsevier.
57. Scrinzi, E., et al., *Evaluation of aesthetic durability of waterborne polyurethane coatings applied on wood for interior applications.* Prog. Org. Coat., 2011. **72**(1-2): p. 81-87.
58. Kanokwijitsilp, T., et al., *Development of abrasion resistance SiO2 nanocomposite coating for teak wood.* Prog. Org. Coat., 2016. **93**: p. 118-126.
59. Yang, H., et al., *Lignin-derived bio-based flame retardants toward high-performance sustainable polymeric materials.* Green Chem., 2020. **22**(7): p. 2129-2161.
60. Gracik, T.D. and G.L. Long, *Prediction of thermoplastic flammability by thermogravimetry.* Thermochim. Acta, 1992. **212**: p. 163-170.
61. Liodakis, S., I. Antonopoulos, and V. Tsapara, *Forest fire retardancy evaluation of carbonate minerals using DTG and LOI.* J. Therm. Anal. Calorim., 2009. **96**: p. 203-209.
62. Chiu, H.T., et al., *A study of the combustion and fire-retardance behaviour of unsaturated polyester/phenolic resin blends.* Polym. Degrad. Stab., 2000. **70**(3): p. 505-514.
63. Bernal, S.A., et al., *Characterization of supplementary cementitious materials by thermal analysis.* Mater. Struct., 2017. **50**: p. 1-13.
64. Chiang, C.-L. and C.-C.M. Ma, *Synthesis, characterization, thermal properties and flame retardance of novel phenolic resin/silica nanocomposites.* Polym. Degrad. Stab., 2004. **83**(2): p. 207-214.
65. Beuria, P.C., et al., *Study on kinetics of thermal decomposition of low LOI goethetic hematite iron ore.* In. J. Min. Sci. Technol., 2017. **27**(6): p. 1031-1036.
66. Burris, S.C., D. Li, and J.T. Riley, *Comparison of heating losses and macro thermogravimetric analysis procedures for estimating unburned carbon in combustion residues.* Energy Fuels, 2005. **19**(4): p. 1493-1502.
67. Liu, X., J. Hao, and S. Gaan, *Recent studies on the decomposition and strategies of smoke and toxicity suppression for polyurethane based materials.* RSC Adv., 2016. **6**(78): p. 74742-74756.
68. Mensah, R.A., et al., *Characterisation of the fire behaviour of wood: From pyrolysis to fire retardant mechanisms.* J. Therm. Anal. Calorim., 2023. **148**(4): p. 1407-1422.
69. Hua, Q., et al., *Aqueous dispersions of esterified lignin particles for hydrophobic coatings.* Front. Chem., 2019: p. 515.
70. Liu, X., et al., *Preparation and Performance of Lignin-Based Multifunctional Superhydrophobic Coating.* Molecules, 2022. **27**(4): p. 1440.
71. Song, X., et al., *Valorization of Lignin from Biorefinery: Colloidal Lignin Micro-Nanospheres as Multifunctional Bio-Based Fillers for Waterborne Wood Coating Enhancement.* ACS Sustain. Chem. Eng., 2022. **10**(35): p. 11655-11665. 10.1021/acssuschemeng.2c03590.
72. Jusic, J., et al., *Improving sustainability in wood coating: Testing lignin and cellulose nanocrystals as additives to commercial acrylic wood coatings for bio-building.* iForest, 2021. **14**(6): p. 499.

73. Puyadena, M., et al., *Phosphorus-containing lignin intermediates as reactive bio-based flame-retardants for polyurethane and acrylic coatings for wood.* Ind. Crops Prod., 2024. **220**: p. 119261. https://doi.org/10.1016/j.indcrop.2024.119261.
74. Henn, K.A., et al., *Colloidal Lignin Particles and Epoxies for Bio-Based, Durable, and Multiresistant Nanostructured Coatings.* ACS Appl. Mater. Interfaces, 2021. **13**(29): p. 34793-34806. 10.1021/acsami.1c06087.
75. Lin, C.-f., et al., *Phosphorylated and carbamylated Kraft lignin for improving fire- and biological-resistance of Scots pine wood.* Int. J. Biol. Macromol., 2024. **276**: p. 133734. https://doi.org/10.1016/j.ijbiomac.2024.133734.
76. Yu, F., et al., *Modification with lignin-based N-P flame retardant to improve the flame retardancy and smoke suppression of wood.* Chem. Eng. J., 2024. **493**: p. 152827. https://doi.org/10.1016/j.cej.2024.152827.
77. Crestini, C., et al., *On the structure of softwood kraft lignin.* Green Chem., 2017. **19**(17): p. 4104-4121. 10.1039/C7GC01812F.
78. Tran, F., et al., *Selective modification of the β–β linkage in DDQ-treated Kraft lignin analysed by 2D NMR spectroscopy.* Green Chem., 2015. **17**(1): p. 244-249. 10.1039/C4GC01012D.
79. Wilcox, K.G., et al., *Persistence length of α-helical poly-l-lysine.* Soft Matter, 2022. **18**(35): p. 6550-6560. 10.1039/D2SM00921H.
80. Faravelli, T., et al., *Detailed kinetic modeling of the thermal degradation of lignins.* Biomass Bioenergy, 2010. **34**(3): p. 290-301. 10.1016/j.biombioe.2009.10.018.
81. Hao, P., et al., *Sliding behavior of water droplet on superhydrophobic surface.* Europhys. Lett., 2010. **90**(6): p. 66003. 10.1209/0295-5075/90/66003.
82. Guo, Y., W. Gao, and P. Fatehi, *Hydroxypropyl sulfonated kraft lignin as a coagulant for cationic dye.* Industrial Crops and Products, 2018. **124**: p. 273-283.
83. An, L., et al., *One-step silanization and amination of lignin and its adsorption of Congo red and Cu (II) ions in aqueous solution.* International Journal of Biological Macromolecules, 2020. **159**: p. 222-230.
84. Fodil Cherif, M., et al., *Comparison of the physicochemical properties and thermal stability of organosolv and kraft lignins from hardwood and softwood biomass for their potential valorization.* Waste and Biomass Valorization, 2020. **11**: p. 6541-6553.
85. Zhang, X., et al., *An approach to evaluate polyacrylamide-type polymers' long-term stability under high temperature and high salinity environment.* Journal of Petroleum Science and Engineering, 2019. **180**: p. 518-525.
86. Lokman, I.M., U. Rashid, and Y.H. Taufiq-Yap, *Meso-and macroporous sulfonated starch solid acid catalyst for esterification of palm fatty acid distillate.* Arabian Journal of Chemistry, 2016. **9**(2): p. 179-189.
87. Lan, Z., et al., *Transparent, high glass-transition temperature, shape memory hybrid polyimides based on polyhedral oligomeric silsesquioxane.* Polymers, 2019. **11**(6): p. 1058.
88. Tian, J., Y. Yang, and J. Song, *Grafting polycaprolactone onto alkaline lignin for improved compatibility and processability.* Int. J. Biol. Macromol., 2019. **141**: p. 919-926. 10.1016/j.ijbiomac.2019.09.055.
89. Sette, M., H. Lange, and C. Crestini, *Quantitative HSQC analyses of lignin: a practical comparison.* Comput. Struct. Biotechnol. J., 2013. **6**(7): p. e201303016. 10.5936/csbj.201303016.
90. Burton, M. and K.C. Kurien, *Effects of solute concentration in radiolysis of water.* J. Phys. Chem. A., 1959. **63**(6): p. 899-904. 10.1021/j150576a031.
91. Krueger, J.S. and M.S. Lewis-Beck, *Goodness-of-fit: R-squared, SEE and 'best practice'.* Pol. Anal., 2007. **15**(1): p. 2-4.
92. Khuri, A.I. and J.A. Cornell, *Response surfaces: designs and analyses*. 2018: CRC press.

93. Arbaoui, A. and C. Redshaw, *Metal catalysts for ε-caprolactone polymerisation*. Polym. Chem., 2010. **1**(6): p. 801-826. 10.1039/B9PY00334G

94. Zhang, X.-Q., et al., *Dual-component system dimethyl sulfoxide/licl as a solvent and catalyst for homogeneous ring-opening grafted polymerization of ε-caprolactone onto xylan*. J. Agric. Food Chem., 2014. **62**(3): p. 682-690. 10.1021/jf4036047.

95. Zhuravlev, E., et al., *Kinetics of nucleation and crystallization in poly (ε-caprolactone)(PCL)*. Polymer, 2011. **52**(9): p. 1983-1997. 10.1016/j.polymer.2011.03.013.

96. Liu, H., et al., *Lignin, a biomass crosslinker, in a shape memory polycaprolactone network*. J. Polym. Sci. A. Polym. Chem., 2019. **57**(20): p. 2121-2130. 10.1002/pola.29483.

97. Wen, J.-L., et al., *Recent advances in characterization of lignin polymer by solution-state nuclear magnetic resonance (NMR) methodology*. Materials, 2013. **6**(1): p. 359-391.

Chapter 8: Conclusion and Future Perspectives

8.1. Highlights of this Thesis

The functionalization of lignin via silsesquioxane copolymerization in an aqueous system provides lignin with higher hydrophobicity and more excellent thermal stability. A water-based coating formulation with aluminum phosphate binder for wood coating showed higher water contact angle and flame-retardant characteristics. This highly hydrophobic characteristic of lignin is attributed to replacing lignin hydrophilic groups with hydrophobic Si-O-C linkages. The flame-retardant characteristics of the formulation were mainly extrapolated from the inherently charring characteristics of lignin coupled with the heat shield composed of a silicon-oxygen network structure that would protect the organic structure. This thesis also successfully incorporated more than 50 wt.% of lignin in a water-based polyurethane formulation for an improved hydrophobic, thermal, flame-retardant and recyclable polyurethane film. This incorporation of lignin-silsesquioxane copolymer in water-based polyurethane was achieved with the use of sulfoethylated lignin as a dispersant. The formulation characteristics were also exhibited when wood, paper and metal surfaces were coated with the formulation. In a similar fashion the incorporation of lignin-silsesquioxane copolymer in hydrophobic natural rubber latex improved the thermal, mechanical and hydrophobic characteristics of the resulting composite films. The mechanical and hydrophobic properties of the lignin-natural rubber films were stable even when exposed to a higher thermal environments, abrasion and moisture. In addition, due to the higher hydrophobicity of the films and the slightly oleophilic characteristics of the films application is recommended to the separation of oil and water mixture.

The application of lignin for filament deposition-three-dimensional (3D) printing were successfully achieved by carefully tailored by controlling the molecular weight and molecular weight distribution of lignin via ethanol fractionation and subsequent grafting and ring opening polymerization with caprolactone to a polycaprolactone polymerization on lignin backbone by controlling the viscosity, degree of polymerization and melt temperature. The mechanical properties, hydrophobic, and printability of lignin-caprolactone polymer improved due to the lower molecular weight and reduced complexity, resulting in improved steric accessibility for the caprolactone polymerization. This ethanol fractionation before functionalization makes it possible for the lignin-caprolactone polymer to be used for filament extrusion and 3D printing, with the original lignin representing more than 40 % of the overall polymer. In a similar fashion, the characteristics of lignin from different sources (hardwood, softwood, and grass lignin) from two extraction methods (alkali and kraft treatments) for caprolactone polymerization after ethanol fractionation was correlated to the overall performance of the resultant polymer as a coating on wood surfaces. The ethanol fractionation before the copolymerization also improved the film-forming ability, hydrophobicity, and flame-retardant performance of the lignin-caprolactone-based coating, creating a new frontier for the application of lignin-caprolactone polymer for a hydrophobic and flame-retardant coating.

As a conclusive remark, we have established facial but high-performance synthesis approaches to integrate lignin, a waste stream biopolymer, in coating composite films and 3D printing. This can provide new possibilities for achieving a profitable value chain for the biorefinery process.

8.2. Future Perspectives

In terms of lignin functionalization in a solvent free system for hydrophobic lignin, it is an efficient method to integrate lignin in hydrophobic polymers, such as polyurethane and natural rubber latex, is quite promising. Future research could focus more on integrating the methods employed in this thesis in industrial coating environments. In addition, the exploration of the generated lignin polymers for polyurethane could be further explored with the concept of nano lignin to further increase the concentration of lignin and improvement of mechanical properties would be an interesting thing to investigate for the future. The application of superhydrophobic lignin-natural films for oil-water separation efficiency should be investigated, and the application of the films for various oil spills would be necessary for potential applications.

Lignin fractionation is proved to be an effective strategy to decrease the complexity of lignin and improve the 3D printability of lignin. The potential use of the 3D printable polymers for applications in tissue engineering and scaffold could benefit from the biocompatibility of and antioxidant properties of lignin.

Appendix 3A. Supporting information: Solvent-Free Lignin-Silsesquioxane Wood Coating Formulation with Superhydrophobic and Flame-Retardant Functionalities

*Banchamlak Bemerw Kassaun[1]and Pedram Fatehi[1,2]**

[1]Biorefining Research Institute, Lakehead University, 955 Oliver Road, Thunder Bay, Ontario, P7B 5E1 Canada.

[2]Laboratory of Natural Materials Technology, Åbo Akademi University, Henrikinkatu 2, Turku FI-20500, Finland

Corresponding author: pfatehi@lakeheadu.ca

NMR analysis. H-NMR and HSQC analysis samples were prepared using 60-70 mg of oven-dried copolymers or WAPMSS were dissolved in 1 mL of D_2O and 2 µL of 40% NaOD, while 60 -70 mg of SKL was mixed in 1 mL of DMSO–d_6 for 12 h at room temperature.[77, 78] ^{1}H NMR test parameters were 16 scans, 3.28 sec acquisition time with 1 s relaxation, and 90° pulse at room temperature. HSQC NMR analysis was conducted using 13 ppm spectra width in the F2 (^{1}H) dimension with 2048 data point (155 ms acquisition time), 165 ppm spectra width in the F1 (^{13}C) dimension with 256 data point (6.2 ms acquisition time), a 1.5 s pulse delay, and sixteen scans at room temperature, which was assessed by Bruker pulse program "hsqcetgpsisp2.3 software. As described previously, the phenolic, aliphatic, and carboxylic hydroxyl groups of SKL and copolymers were quantified by ^{31}P-NMR analysis [34]. In short, 50-60 mg of oven-dried (at 60°C) samples were dissolved in 1 mL mixture of chloroform-d ($CDCl_3$) and pyridine (1:1.6 vol/vol) followed by the addition of 52 µL (5 g/L) relaxing agent (chromium (III) acetylacetonate). The mixture was stirred at 120 rpm for 12 h. Then, 200 µL of phosphorylating reagent (2-chloro-4,4,5,5-tetramethyl-1,3,2-dioxaphospholane (TMDP) was introduced to the sample solutions, and the mixture was agitated at 120 rpm for 1 h. After that, 50 µL internal standard (cyclohexanol, (20 g/L)) was added to the mix, and the system was agitated for 30 min. Then, the solutions were transferred to NMR tubes and analyzed by the NMR instrument with 1024 scans per sample with a 90° pulse width and 5-sec relaxation delay.

Light scattering analysis. Five concentrations (0.2, 0.6, 1.2, 1.6, and 2.1 mg/mL) of each copolymer were prepared in a 15 % NaOH solution (i.e., they are not soluble in water or any solvent), which were stirred for 24 hours and at room temperature. After filtration using 0.45 μm nylon filters, the samples were analyzed by the instrument via Brookhaven Zimm plot software [79]. A BI-DNDC differential refractometer (Brookhaven Instruments Corporation, NY, USA) at 620 nm was used to measure the refractive index increment (dn/dc) of the solutions containing the samples. First, 1 mg/mL of the polymer solutions was prepared in 15 % NaOH, which was stirred for 24 hours at room temperature. Analyses were conducted in triplicate immediately after filtration using 0.45 μm nylon membrane syringe filters, and the average values were reported. The shape factor was determined by dividing the value of R_g from the SLS analysis by the value of R_h from the DLS analysis [79].

Powder wettability. The Washburn method measures the capillary rise of the liquid into particles. In a series of experiments, 100 mg of SKL or WSL copolymer was placed into a cylindrical glass tube with an open base bottom, which was then covered with filter paper and taped three times to ensure proper packing. As the powder holder was immersed into the liquid, the amount of liquid absorbed by the powder bed was measured as a function of time.

$$W^2 = {}^{C\rho\gamma l cos\theta\ t}/_{2\eta} \qquad \textbf{(S3.1)}$$

Where W is the weight of absorbed water (g), C is a geometric constant (0.04), ρ is the liquid density (0.998 g/mL), γ is surface tension (72.8 mN/m), L is the length of the powder glass probe (5.5 mm), η is the viscosity of the liquid (0.01 g/cm.s), and t is measurements time (300 s).

Thermal analysis. The instrument was loaded with 10-10.36 mg of dried samples in a Tzero® aluminum pan. The analysis was conducted in a nitrogen environment with a flow rate of 10 mL/min and a heating rate of 10°C/min from 25°C to 800°C [80]. In this analysis, 7 to 10 mg of oven-dried (60°C) samples were placed in a Tzero® aluminum pan and fed to the DSC instrument. The thermal history of samples was erased by heating them from 20°C to 250°C and then cooling to 20°C at a rate of 5.0°C/min. The T_g of SKL and copolymers was obtained by performing a second heating cycle from 20 to 250°C.

Contact angle analysis. In this test, a droplet of liquid with a diameter of 6-10 µm was placed on the wood surface coated with different formulations, and the contact angle of the droplet and the coated surface was measured visually by a camera for 50 s.

The tilting method was used to measure the sliding angle of water on the wood surface. In this test, first, a water droplet (between 6 and 10 µL) was placed on the coated wood at a flat configuration (180°) on the tilting stage, and the wood sample stage was incrementally tilted until the droplet started to slide [81]. Both analyses were performed on wood surfaces coated with all the formulations (1/0.25, 1/0.5,1/0.75, 1/1, 1/1.25, 1/1.5, 1/75, and 1/2 wt. ratio of WSL10/AP), and control samples (uncoated wood, AP coated and AP-SKL coated wood).

Water droplet adhesion. First, a water droplet (10 µL) was delicately positioned on an adhesion probe ring, and the probe was lowered until the water droplet adhered to the coated surface. After 2 min, the probe was elevated with a velocity of 5 µm/s, and adhesion force results were collected. This analysis was conducted on coated wood surfaces with AP, SKL-AP, and WSL10-AP at 1/1 wt. ratio formulations. The procedure was performed three times in three different areas of the coated samples.

Scanning electron microscopy (SEM). The samples were gold-coated before the SEM observation. The conditions for this experiment were 5.0 kV accelerating voltage in a vacuum (10^{-4}–10^{-3} Pa) with 100× to 10,000× magnifications.

Table S3.1. Taguchi L9 4×3 parameters (Lignin: oligomer molar ratio, Temperature, Time, and pH) and three levels for each factor.

Samples	Lignin: oligomer mmol/mmol ratio	Temperature, °C	Time, h	pH
WSL1	1: 0.4	80	72	12
WSL 2	1: 0.4	40	24	10
WSL 3	1: 2.3	60	24	12

WSL 4	1: 2.3	40	72	11
WSL5	1: 1.1	60	72	10
WSL 6	1: 2.3	80	48	10
WSL7	1: 1.1	40	48	12
WSL8	1: 1.1	80	24	11
WSL 9	1: 0.4	60	48	11
WSL10	1: 1.2	60	48	11

$$\% \, Yield = \frac{dry\ mass\ of\ WSL}{dry\ mass\ of\ SKL+WAPMSS} \times 100 \text{---} \tag{S3.1}$$

$$\% \, grafting = \left(\frac{\frac{Si}{29} * Mw}{100 - \frac{Si}{29} * Mw} \right) * 100 \text{---} \tag{S3.2}$$

Si is the silicon content of copolymers, and M_W is the molecular weight of WAPMSS (i.e., 211 g/mol).

Table S3.2. % Organic element and Si from XPS.

Copolymers	**CHNS**				**XPS**			
	N [%]	**C [%]**	**H [%]**	**S [%]**	**O [%]**	**Si [%]**	**Grafting [%]**	**Yield [%]**
SKL	0	62.66	5.05	29.54	19.45	0	N/A	N/A
WSL1	3.58	49.77	5.49	1.09	21.29	6.71	59.74	72.28
WSL2	1.72	53.91	6.38	1.23	24.44	6.2	55.19	60.84
WSL3	2.95	44.92	6.18	1.28	21.32	11.65	103.72	68.58
WSL4	3.23	44.08	6.27	1.22	24.09	14.16	126.06	70.79
WSL5	3.06	46.32	5.92	0.934	23.15	13.31	118.50	71.23
WSL6	2.86	44.86	6.12	1.19	24.08	14.19	126.33	76.08
WSL7	3.94	43.67	5.98	0.83	22.10	12.19	108.52	76.08
WSL8	2.84	51.87	6.42	1.13	22.43	11.60	103.27	72.46
WSL9	2.62	50.01	6.59	1.28	22.22	9.30	82.79	73.00
WSL10	3.10	53.6	5.60	0.65	23.41	13.64	140.00	78.00

Note: % grafting was calculated using Eq 1 and % yield based on weight.

Table S3.3. ^{1}H-^{13}C HSQC cross peak signals labels, **δ_C /δ_H** ppm, and groups.

Label	δ_C /δ_H (ppm)	groups
OCH3	55.5/3.70	C-H in -OCH3 (methoxy)
B_{β}	53.29/3.44	C_{β}-H_{β} phenylcoumaranan β-5
C_{β}	53.6/3.0	C_{β}-H_{β} resinol β-β
A_{Υ}	60/3.4	C_{Υ}-H_{Υ} in β-O-4'
C_{Υ}	62.8/3.7	C_{γ}-H_{γ} in phenyl coumarane
P_{Υ}	61.5/4.1	C_{γ}-H_{γ} in p-hydroxycinnamyl alcohol end groups
B_{Υ}	70.8/3.7,4.1	Cγ-Hγ in resinol units
A_{α}	71.4/4.7	C_{α}-H_{α} in β-O-4′ linkage
A_{β}	83.6/4.27	C_{β}–H_{β} in β-O-4 linked to G unit
B_{α}	84.6/4.6	C_{α}-H_{α}in resinol units
C_{α}	87/5.5	Cα-Hα in phenylcoumaran substructures
G_2	110.6/6.7	C_2-H_2 in guaiacyl units
G_2'	108.8/7.04	C_2-H_2 in oxidized (C_{α}=O) guaiacyl units
G_5	115.9/6.7	C_5-H_5 in guaiacyl units
G_6	119.1/6.7	C_6-H_6 in guaiacyl units
G6'	122.9/7.5	C_6-H_6 in oxidized (C_{α}=O) guaiacyl units
D_{β}	126.3/6.8	C_{β}-H_{β} in cinnamaldehyde end groups
$H_{2,6}$	127.1/7.1	C2,6-H2,6 in p-hydroxybenzoate unit

Table S3.4. Atomic percentage concentration of primary bonds from C1s spectra and Si 2p deconvoluted for SKL, WAPMSS, and WSL copolymers from XPS analysis.

Bonds	SKL	WSL2	WSL6	WSL5	WSL10	WAPMSS
C-C	65.4	45.4	45.2	39.3	31.2	64.97
C-O	26.4	41.1	38	46.5	58.7	-
C=O	8.2	6.2	2.8	5	0.01	-
C-Si	NA	8.3	14	8	10	29.02

C-N	NA	NA	NA	NA	NA	6.1
Si-C	NA	15	18.5	22.2	37	38.84
Si-O-Si	NA	2.2	10.6	13.1	1.8	44.16
Si-O-C	NA	50	70.5	64.5	60	NA

Table S3.5. Mw, R_g, R_h, and shape factor of SKL and WSL copolymers.

Copolymers	**MW (g/mol)**	**R_g (nm)**	**R_h (nm)**	**~R_g/R_h**
SKL	(7.59 ± 0.89) 10^4	17.1 ± 28.1	10 ± 0.002	1.7
WSL 1	(1.43 ± 0.26) 10^5	23.9 ± 4.3	20 ± 0.01	1.1
WSL 2	(1.14 ± 0.14) 10^5	30.3 ± 17.1	20 ± 0.002	1.5
WSL 3	(1.53 ± 0.23)10^5	38.1 ± 16.2	30 ± 0.003	1.2
WSL 4	(1.83 ± 0.55) 10^5	21.9 ± 14.1	6.3 ± 0.029	1.4
WSL 5	(1.40 ± 0.18) 10^5	17.1 ± 8.1	9.6 ± 0.004	1.7
WSL 6	(1.80 ± 0.12) 10^5	36.2 ± 7.41	30.4± 0.004	1.1
WSL 7	(1.14 ± 0.14) 10^5	30.3 ± 17.1	30.3 ± 17.1	1.5
WSL 8	(1.85 ± 0.25) 10^5	44.01 ± 13	40.3 ± 0.001	1.0
WSL 9	(1.33 ± 0.09) 10^5	37.0 ± 7.9	24.8 ± 0.001	1.4
WSL 10	(2.14 ± 0.23) 10^5	58.0 ± 8.4	78 ± 0.04	0.74

Table S3.6. Atomic percentage concentration of major bonds at different temperatures (from TGA) for sample WSL10 from XPS analysis.

Temperature, °C	**room**	**10-220**	**10-360**	**10-420**	**10-520**	**10-620**	**10-800**
Atomic con.	%	%	%	%	%	%	%
C	68.0	68.0	63.5	49.8	42.0	36.0	24.8
O	15.0	21.0	25.0	29.0	32.0	38.0	44.5
Si	11.5	5.0	10.0	20.0	25.0	25.0	30.7
N	5.5	6.0	1.5	1.2	1.0	1.0	0.0
C-C	40.0	40.6	32.5	36.5	27.0	25.6	16.7
O-C=O	0.0	0.0	0.0	6.6	0.0	11.0	0.0
C-O-C	13.0	23.8	32.1	15.0	11.0	20.0	5.9
C=O	0.0	9.5	9.1	13.7	28.0	0.0	12.9
C-Si	37.0	26.2	25.9	28.0	34.0	43.0	64.5
Si-C	37.0	64.0	69.0	68.0	17.0	51.0	5.0
Si-O-Si	1.8	5.0	4.0	30.0	36.0	34.0	40.0
Si-O-C	60.0	31.0	26.0	1.4	46.0	14.0	55.0

Tubiscan Stability Index analysis

The generated transmittance signals of the transmitted light and the backscattered signal of the backscattered light (BS) are a function of the copolymer's height. As discussed previously, the Turbiscan Stability Index (TSI) of samples was determined.

Table S3.7. Settling rate for components of coating formulation (WSL10-AP) at different WSL/AP ratios.

Formulation	**WSL 10: AP wt. ratio**	**Rate of settling, mm/hr**		
		00:30	**1:00**	**2:00**
F1	1:0.25	50	0.6	0.5
F2	1:0.5	22.5	2.8	0.4
F3	1:0.75	21.4	62.9	0.4
F4	1:1	23.8	1.86	0.5
F5	1:1.25	10	22	32
F6	1:1.5	15	11.7	10.8
F7	1:1.75	15	7.7	7.6
F8	1:2	12	10	9.7

Note: 20 g WSL in 1 L water

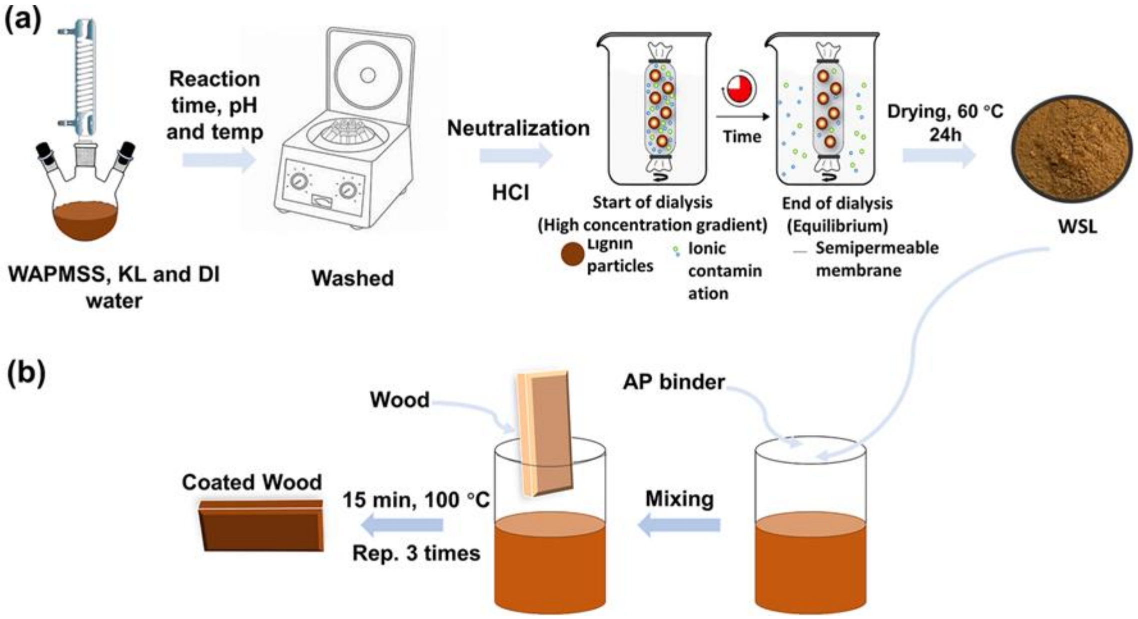

Figure S3.1. The preparation schematics illustrate the SKL and WAPMSS copolymerization(a), coating formulation, and wood coating (b).

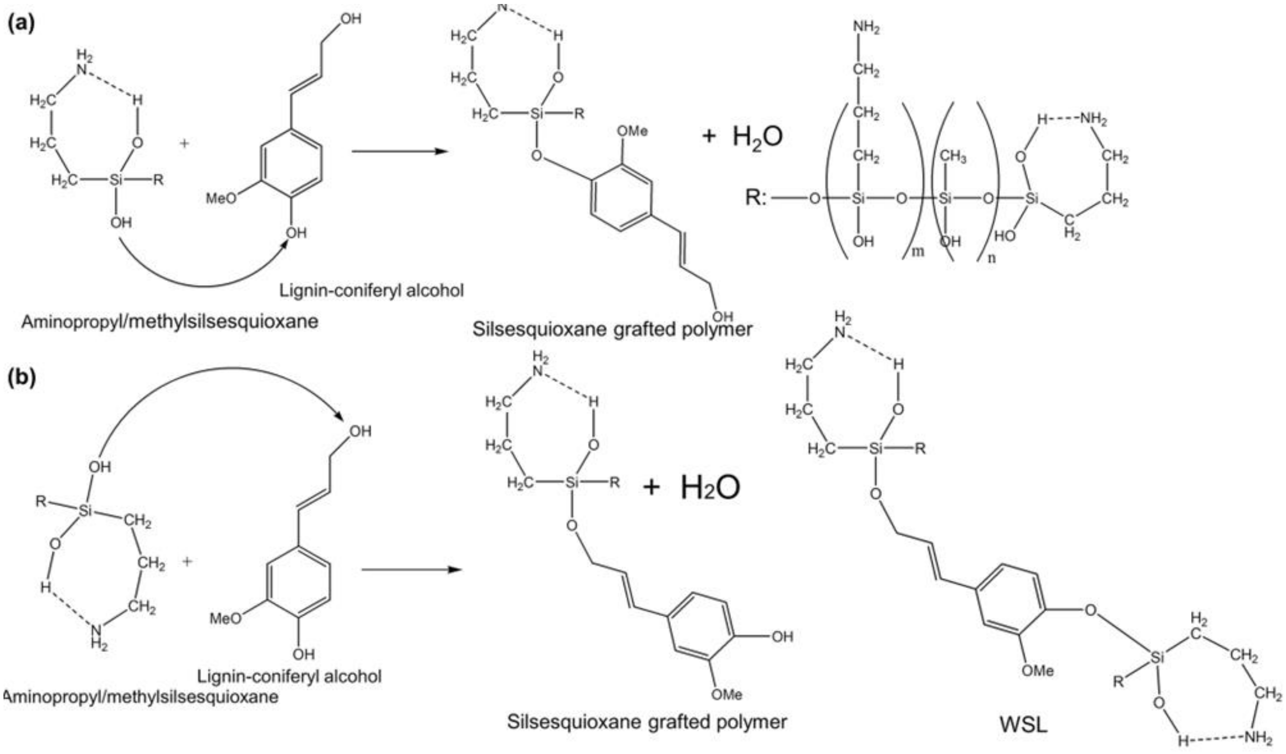

Figure S3.2. Reaction mechanism for grafting of kraft lignin and aminopropyl/methylsilsesquioxane polycondensation in phenolic OH(a) and Aliphatic OH (b).

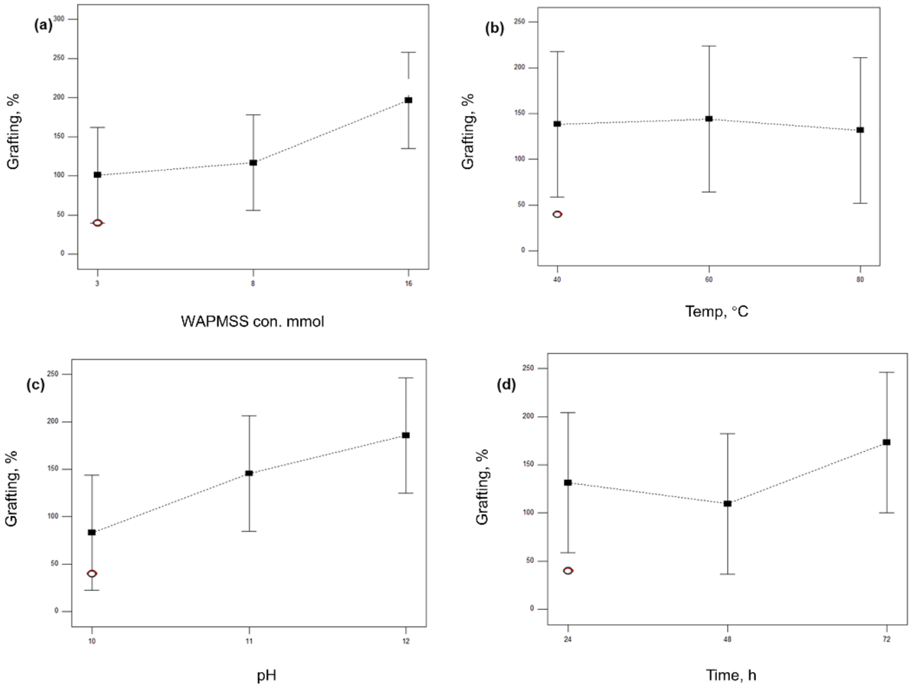

Figure S3. 3. Effect of WAPMSS concentration, temperature, pH, and time in the grafting ratio of the copolymerized sample. The grafting ration is calculated following equaiton S1 from the original document.

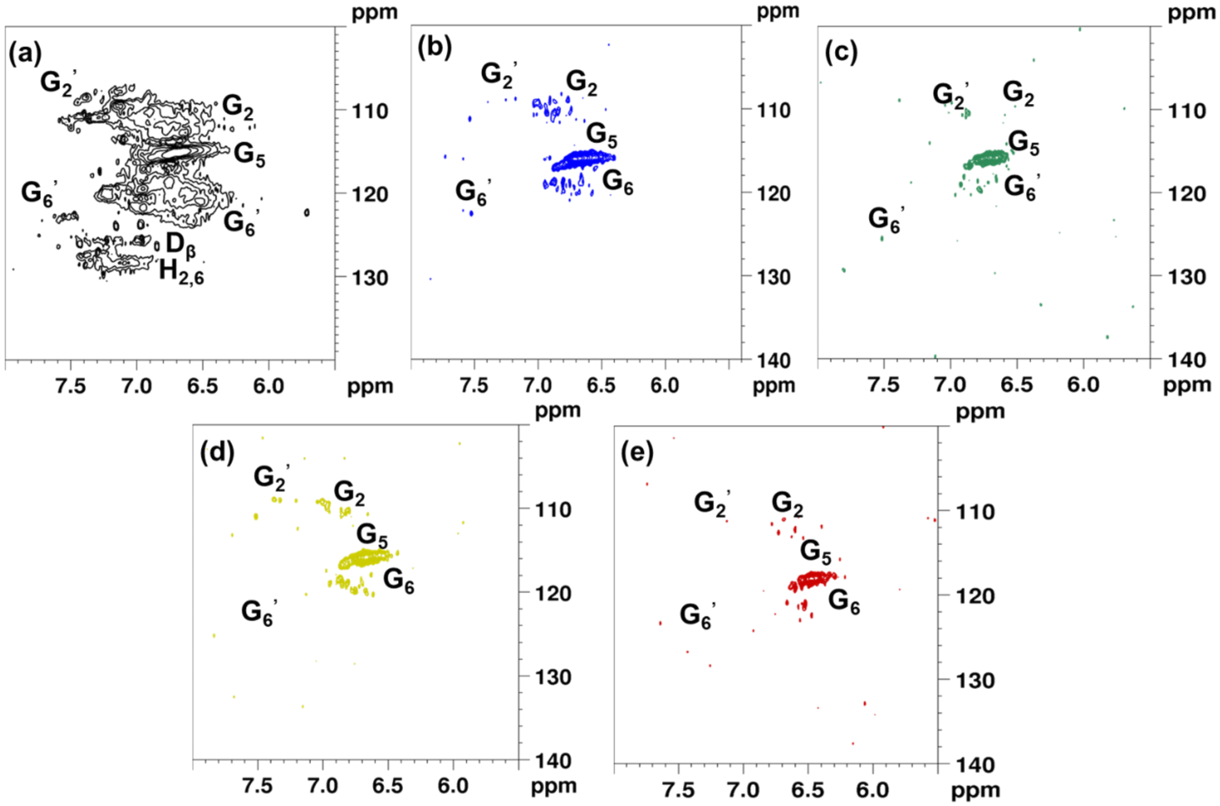

Figure S3.4. aromatic region HSQC peak assignment for SKL (a), WSL2 (b), WSL5 (c), WSL6(d), and WSL10 (e).

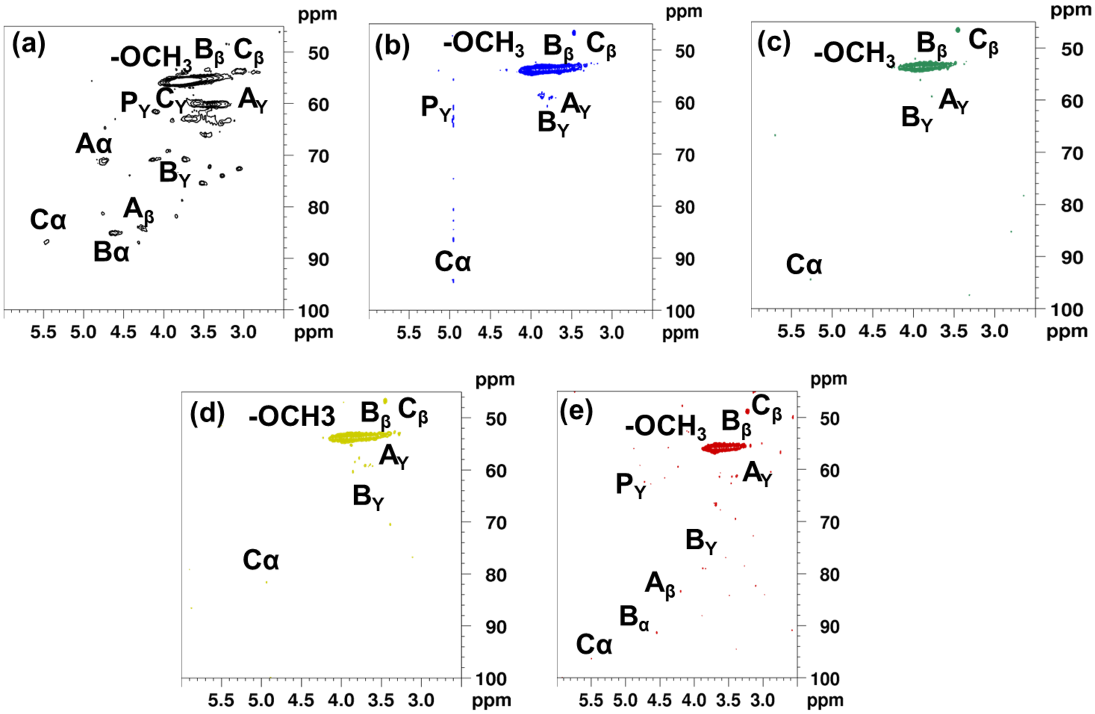

Figure S3.5. Methoxy region HSQC peak assignment for SKL (a), WSL2 (b), WSL5 (c), WSL6(d), and WSL10 (e).

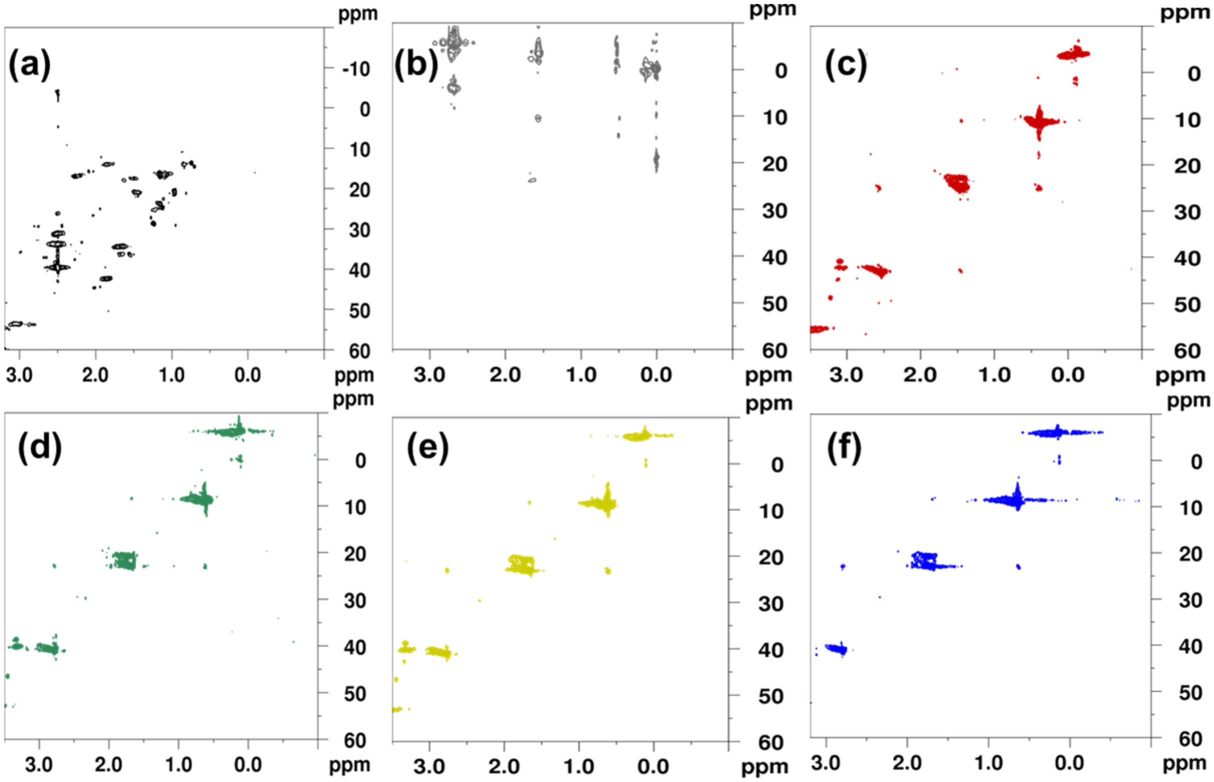

Figure S3.6. Aliphatic C-C linkages HSQC peak assignment for SKL (a), WSL2 (b), WSL5 (c), WSL6(d), and WSL 10 (e).

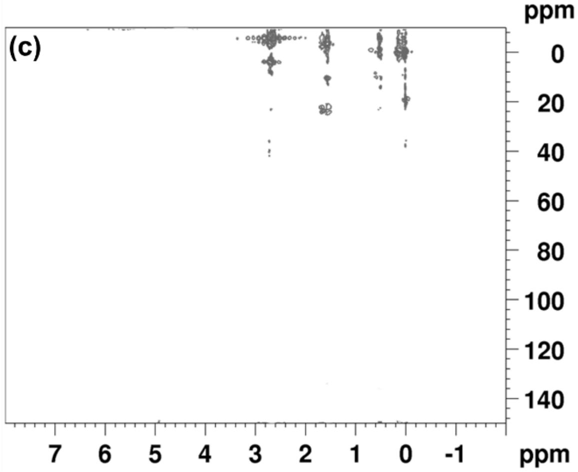

Figure S3.7. HSQC of WAPMSS

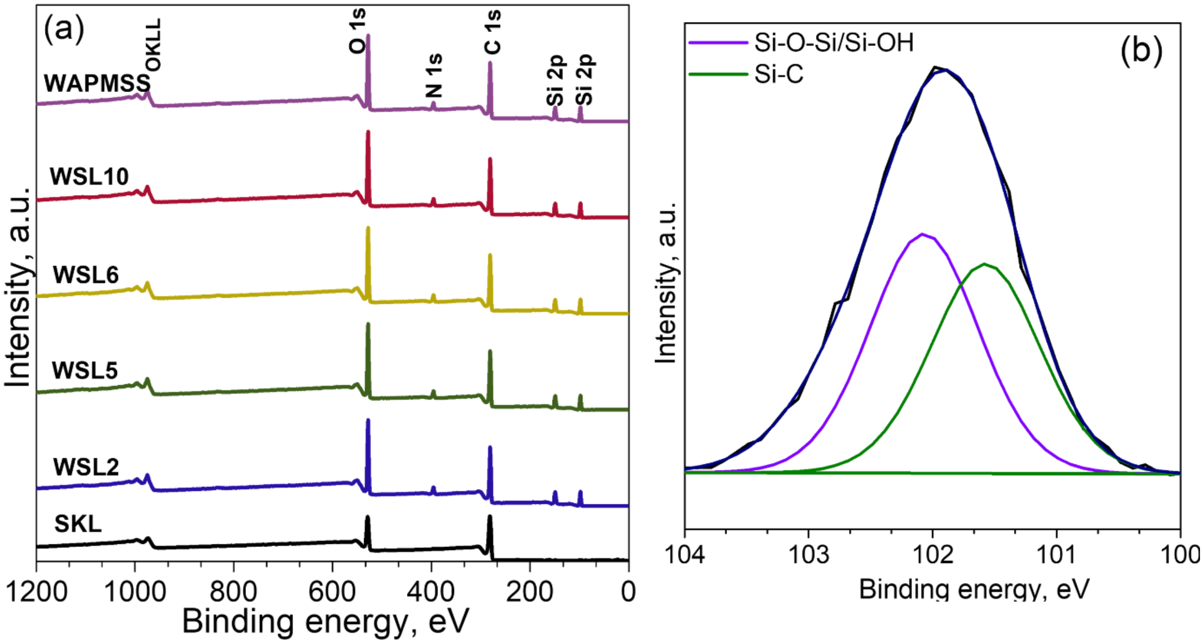

Figure S3.8. XPS wide spectra for SKL, WAPMSS and WSL copolymers (a) and Si 2p for WAPMSS (b)

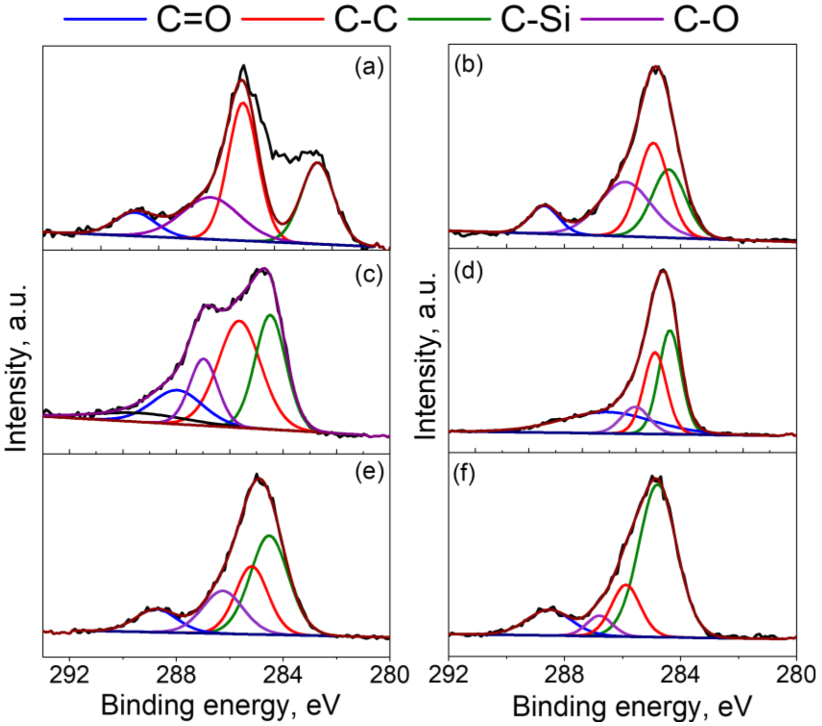

Figure S3.9. C1s spectra fitting for WSL10 at different temperatures 10-220°C (a) 10-360 (b) 10-420 (c) 10-520 (d) 10-620 (e) 10-800 (f).

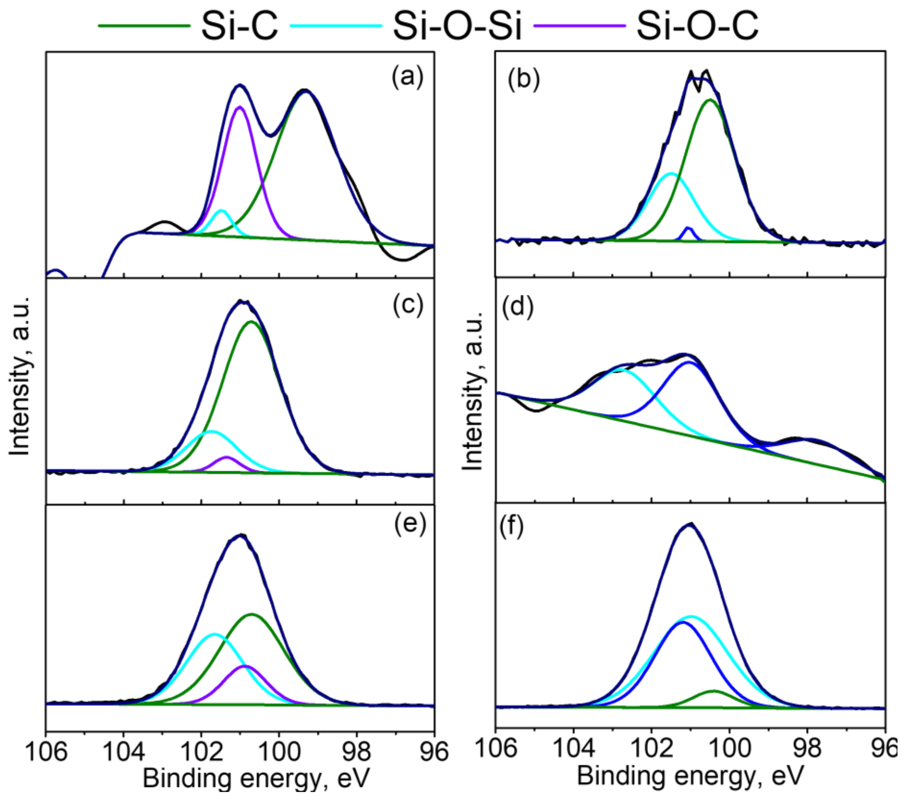

Figure S3.10. Si 1p spectra fitting for WSL at different temperatures 10-220°C (a) 10-360 (b) 10-420 (c) 10-520 (d) 10-620 (e) 10-800 (f).

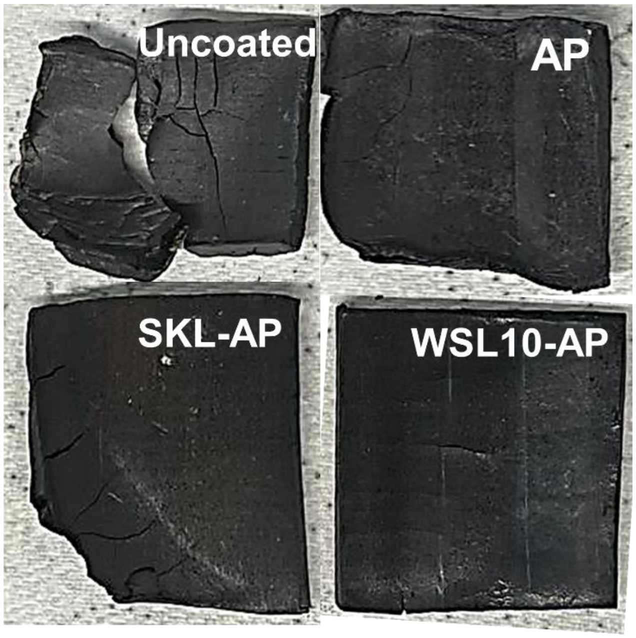

Figure S3.11. Apperance of the coating after smoke density test.

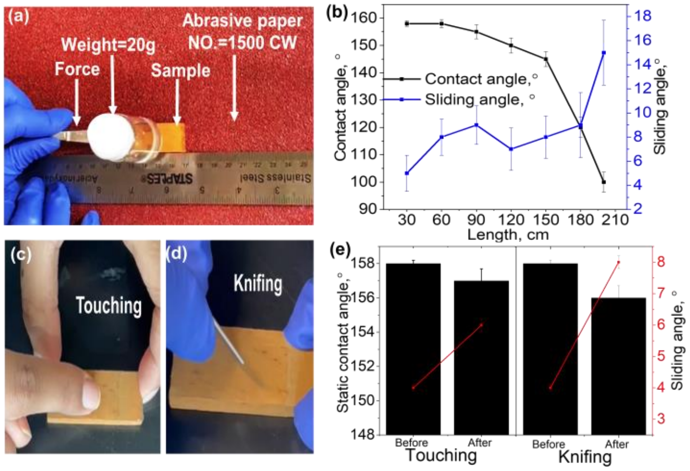

Figure S3.12. Interfacial bonding assesment of the coating by friction with abrastion paper (a), water contact angle after abrastion (b), the finger touching test (c), knifing of coating (d) and water contact angle and sliding angle after touching and knifing (e).

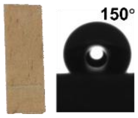

Figure S3.13. Apperance and water cotact angle value of coating after six month of storage.

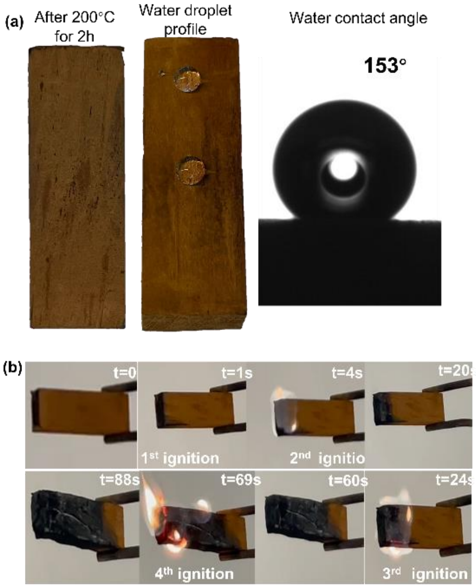

Figure S3.14. Appearance of WSL10-AP 1/1 wt. ratio coated wood after exposure to temperature at 200°C for 2h, water contact angle values (a), and flame test (b).

Appendix 4A. Supporting information: Superhydrophobic Lignin Incorporated Natural Rubber Film for Oil Water Separation

*Banchamlak Bemerw Kassaun, Pedram Fatehi**

Biorefining Research Institute, Lakehead University, 955 Oliver Road, Thunder Bay, Ontario, P7B 5E1 Canada.

First Author, email: bkassaun@lakeheadu.ca, address: 955 Oliver Road, Thunder Bay, ON, Canada, P7B5E1

Corresponding author, email: pfatehi@lakeheadu.ca, address: 955 Oliver Road, Thunder Bay, ON, Canada, P7B5E1

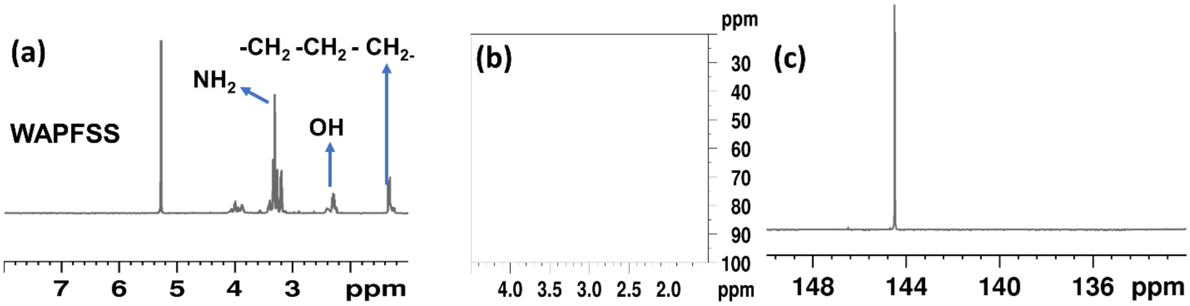

Figure S4.1. ^{1}H NMR (a), HSQC (b), and ^{31}P NMR of WAPFSS

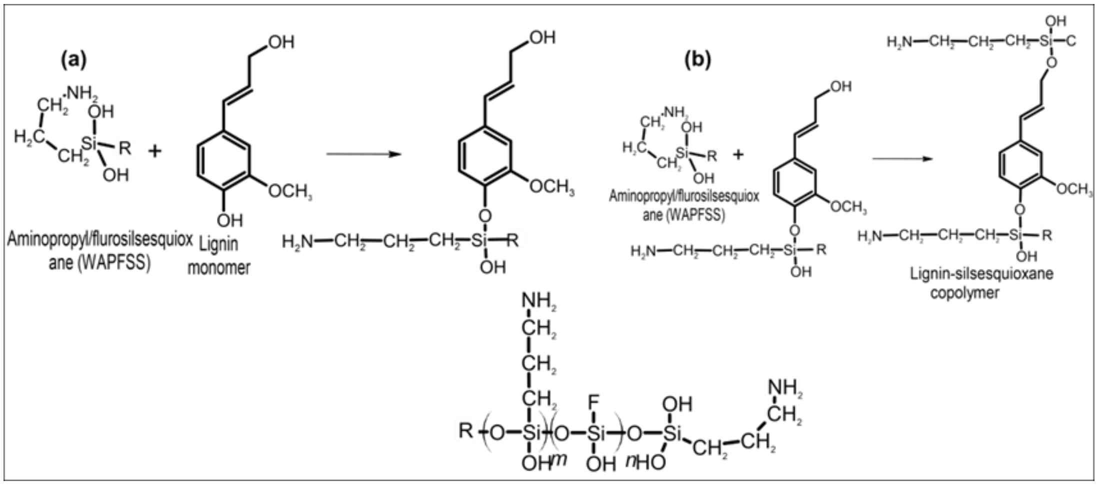

Figure S4.2. Conversion of lignin hydroxyl groups in two Si-O-C via the grafting, phenolic hydroxyl (a), aliphatic hydroxyl (b)

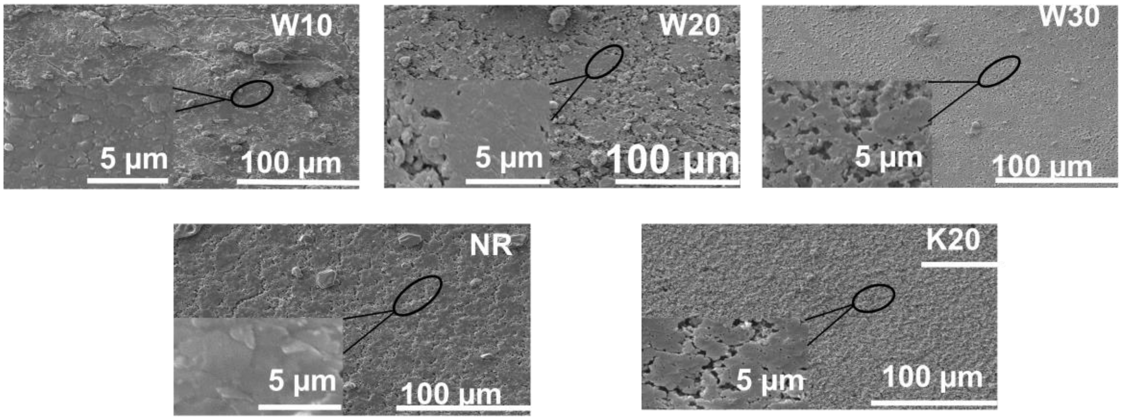

Figure S4.3. SEM images at 100× and 10000× resolutions of NR and NR-lignin films

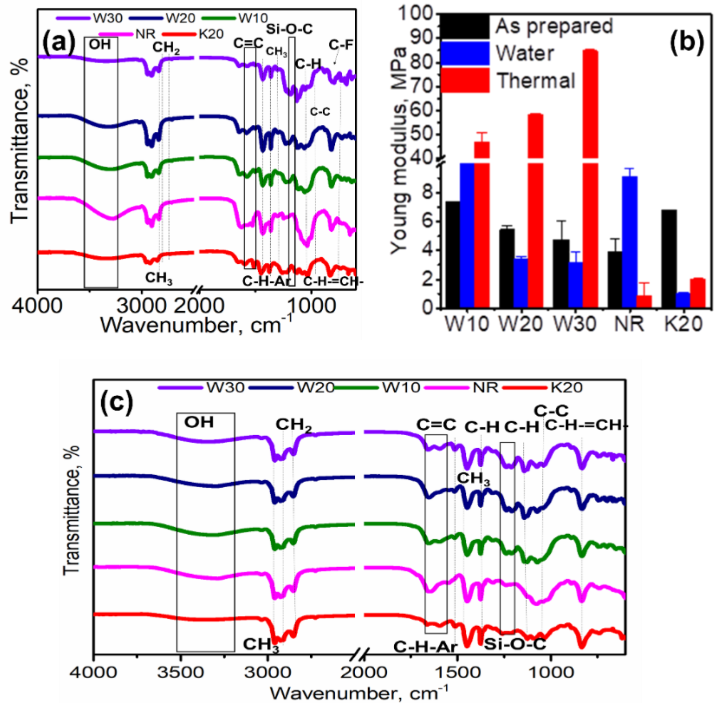

Figure S4. 4. FTIR as prepared (a), young modulus of NR and NR composite films before any treatment after water treatment and thermal treatment (b) and FTIR after thermal treatment (c)

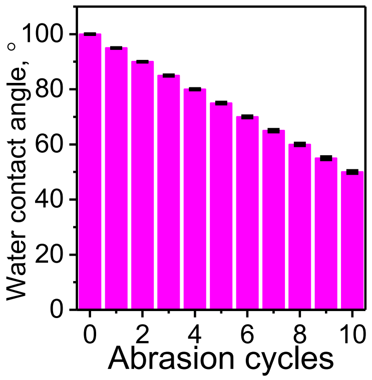

Figure S4. 5. Water contact angle after abrasion for pure NR films.

Table S4.1. ^{31}P-NMR quantification of aliphatic, phenolic, carboxylic hydroxyl of SKL and WSF.

Samples	Aliphatic OH, mmol/g	Phenolic OH, mmol/g	Carboxylic OH, mmol/g
SKL	2.15	3.92	0.76
WSF	0.93	2.18	0.36

Appendix 5A. Supporting information: Lignin as Superhydrophobic agent and Dispersant for Superhydrophobic and Flame-Retardant Polyurethane Composite Coating

Banchamlak Bemerw Kassaun,[1] Yu Liu,[2] Fangong Kong,[2] Pedram Fatehi[1]*

Submitted to Chemical Engineering Journal

[1]Green Processes Research Center and Chemical Engineering Department, Lakehead University, 955 Oliver Road, Thunder Bay, ON P7B5E1, Canada

[2]State Key Laboratory of Biobased Material and Green Papermaking, Qilu University of Technology, Shandong Academy of Sciences, Jinan 250353, China

Corresponding author: email: pfatehi@lakeheadu.ca

Number of tables: 2 (S1-S2)

Number of figures: 13 (S1-S13)

Reaction yield. The reaction yield was calculated by measuring the reaction product before and after the silanization and sulfoethylation lignin modifications.

$$\%\, Yield = \frac{dry\ mass\ of\ A}{dry\ mass\ of\ SKL+B} \times 100 \qquad \textbf{(S5.1)}$$

"A" stands for either WL or SL. "B" refers to WAPMSS (3-(triethoxysilyl)propyl methacrylate) for the process of silanization or sodium 2-bromoethanesulfonate for sulfoethylation. According to the equation the results for WL were 80% and for SL the reaction yield was 75%.

Nuclear magnetic resonance (NMR). For H-NMR and HSQC, 60-70 mg of oven-dried WL sample were dissolved in 1 mL of D_2O and 2 μL of 40% NaOD, while 60-70 mg of SKL and SL was mixed in 1 mL of DMSO–d_6 at room temperature for 12 hours. ^{1}H NMR test parameters were 16 scans, 3.28 sec acquisition, 1 s relaxation, 90° pulse at room temperature. Bruker pulse prog "hsqcetgpsisp2.3 software was utilized for the HSQC analysis using 13 ppm spectra width in the F2 (^{1}H) dimension with 2048 data points (155 ms acquisition time), 165 ppm in the F1 (^{13}C) dimension with 256 data points (6.2 ms acquisition time), a 1.5 s pulse delay, and sixteen scans at room temperature. As previously established, P-NMR quantified the phenolic, aliphatic, and carboxylic hydroxyl groups of SKL, WL, and SLs. To proceed, 50-60 mg of oven-dried samples was dissolved in 1 mL of chloroform-d ($CDCl_3$) and pyridine (1:1.6 vol/vol) at 60°C. Then, 52 μL (5 gL^{-1}) of relaxing agent (chromium (III) acetylacetonate) was added to the mixture, and the mixture was stirred at 120 rpm for 12 h. After adding 200 μL of phosphorylating reagent (TMDP) to the sample solutions, the mixture was agitated at 120 rpm for 1 h. Afterward, 50 μL of internal standard (cyclohexanol, 20 gL^{-1}) was added to the system, and the system was stirred for another 30 min. After that, the solutions were placed in NMR tubes and analysed under the set-up conditions of 1024 scans per sample, 90° pulse width, and 5 sec relaxation delay.

Table S5.1. Quantify the proportions of aliphatic, aromatic, and carboxylate hydroxyl groups in the samples.

Samples	**Aromatic hydroxyl, mmol/g**	**Aliphatic hydroxyl, mmol/g**	**Carboxylic hydroxyl, mmol/g**

SKL	3.92	2.15	0.76
WL	0	0	0
SL	2.45	2.45	0.67

Molecular weight analysis. The molecular weight (MW) of SKL, WL, SL and KLT was measured by static light scattering (SLS) technique 26. This method utilized laser light scattering equipment attached to a goniometer (BI-200SM, Brookhaven Instruments Corporation, NY, USA) to analyze the MW of polymers in solutions at 35 mW and 637 nm at ambient temperature. The MW were calculated by measuring scattered light intensity at 20° to 155° scattering angles. Five concentrations of each copolymer (0.2, 0.6, 1.2, 1.6, and 2.1 mg/mL) were mixed in 15% NaOH for 24 hours at room temperature. The equipment analyzed samples using Brookhaven Zimm plot software after filtering with 0.45 µm nylon filters. A BI-DNDC differential refractometer (Brookhaven Instruments Corporation, NY, USA) measured the refractive index increment (dn/dc) of the polymers in solutions at 620 nm.

Fourier Transform Infrared Spectroscopy (FTIR)

Fourier Transform Infrared Spectroscopy (FTIR) was used to analyze the samples' structure. In this set of experiments, 60-80 mg of dried, crushed lignin derivatives were deposited on the Total Reflectance (ATR) crystal of Bruker Tensor 37 (Bruker, Germany) with a PIKE MIRacle Diamond Attenuated FTIR instrument. Then, 32 scans were conducted for each sample with a resolution of 4 cm^{-1} at a wavenumber range of 500 and 4000 cm^{-1}.

Solubility and charge density

The charge quantity of lignin samples was measured using a Particle Charge Detector (Mutek, PCD 04, Germany) with a poly(diallyldimethylammonium chloride) (Poly DADMAC) (0.005 M) as a standard cationic solution.

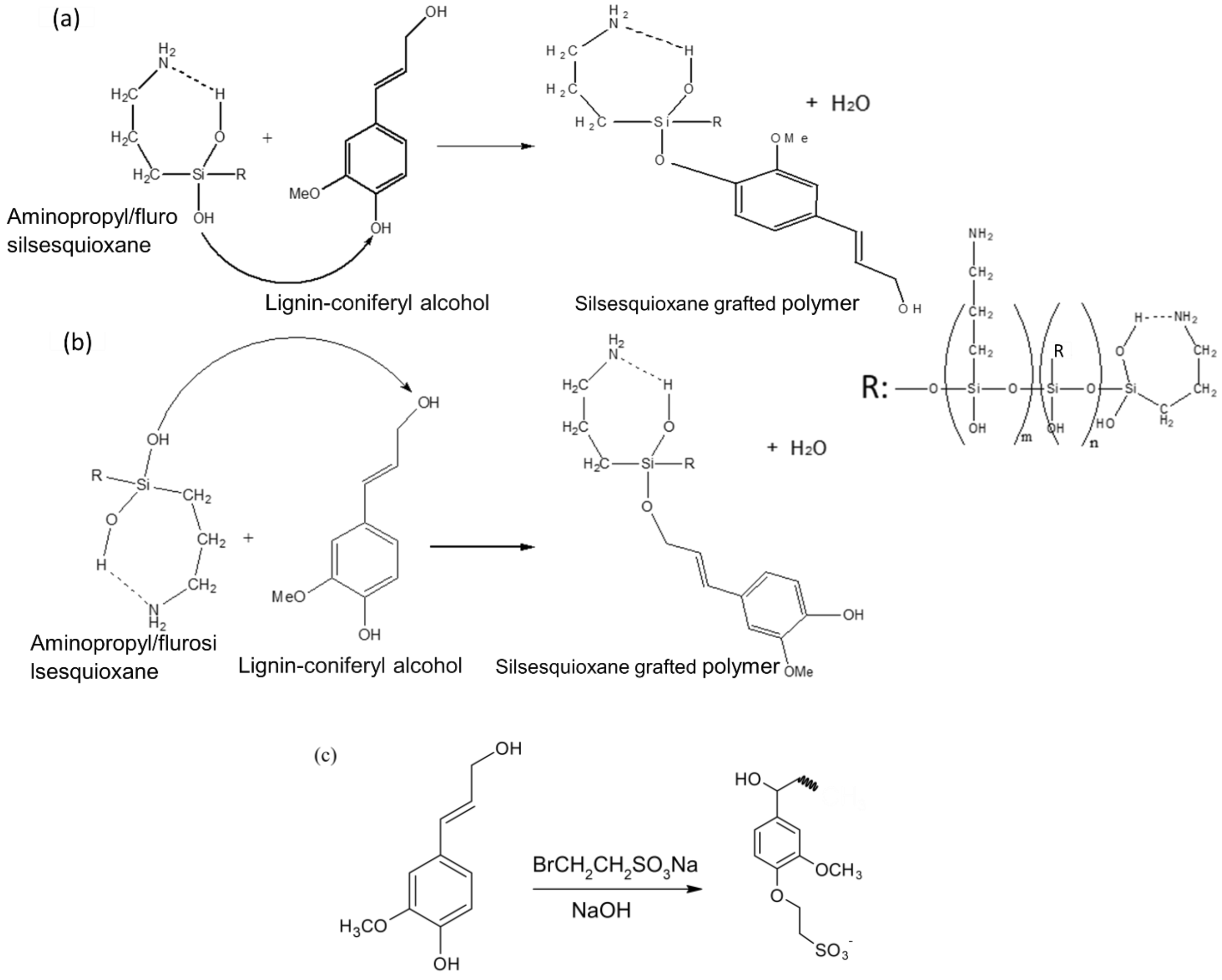

Figure S5.1**.** Reaction pathway of SKL and WAPMSS (a and b) and sulfoethylation reaction pathway (c)

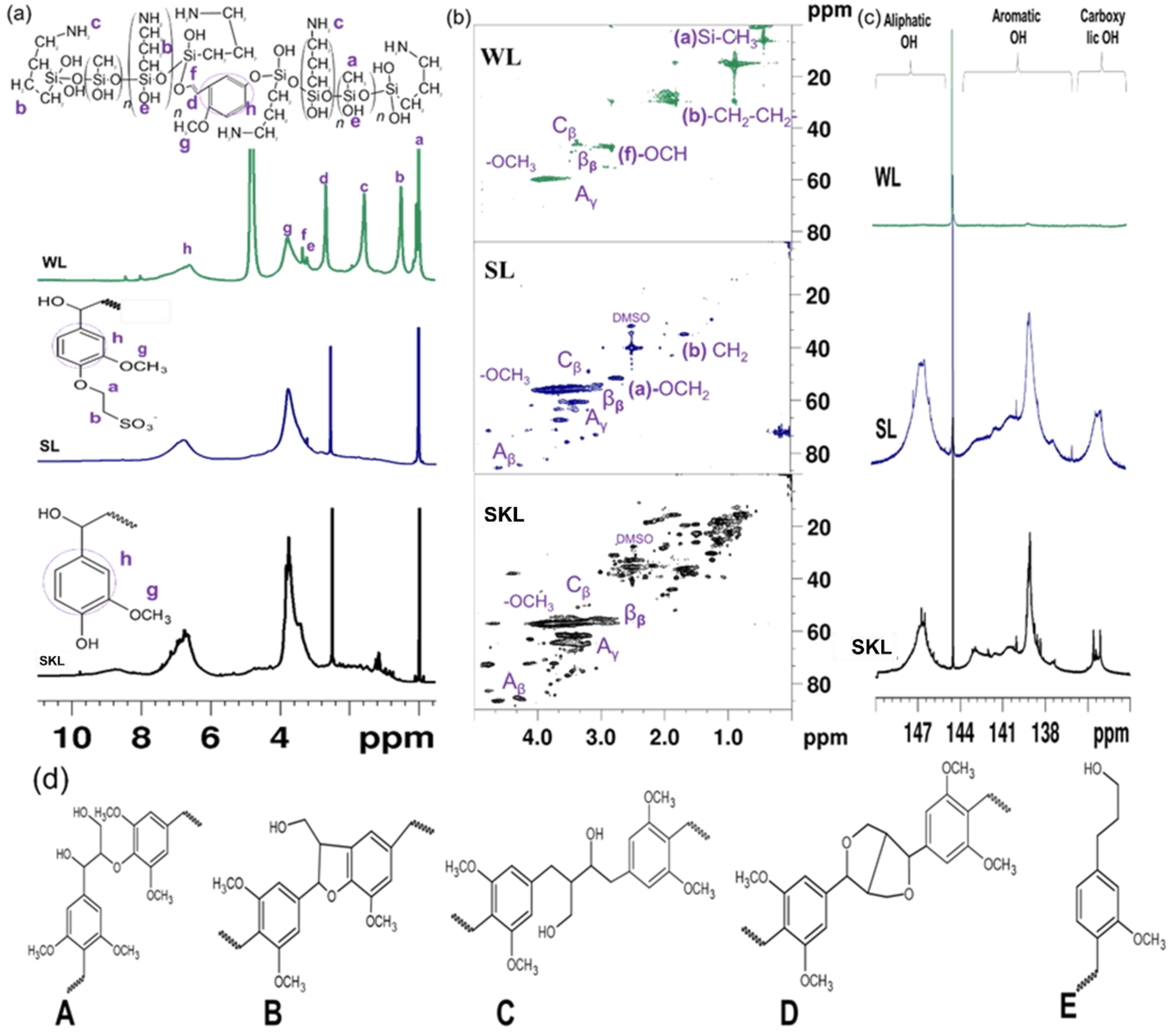

Figure S5.2. ^{1}H-NMR (a), HSQC (b), ^{31}P-NMR (concentration of hydroxyl groups is mmol/g) (c) of Structure of SKL, SL and WL and major linkages (c) (A) β-aryl ether (β-O-4) linkages: (B) phenyl-coumaran structure (β-5′/α-O-4′); (C) secoisolariciresinol substructure; (D) resinol substructure (β-β); (E) guaiacyl propanol unit.

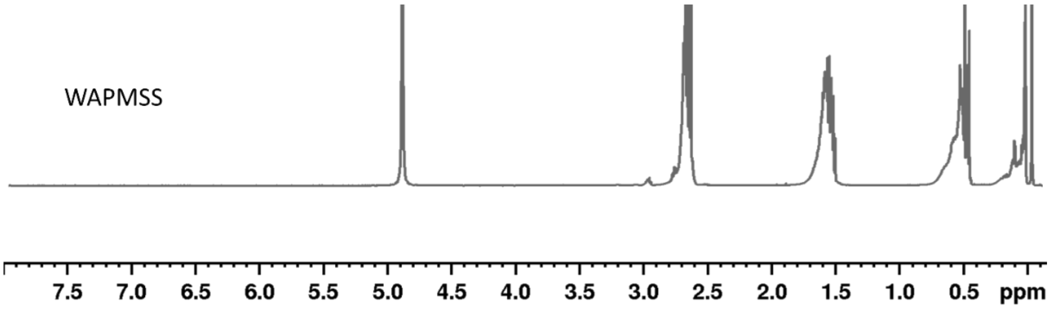

Figure S5.3. H-NMR for Aminopropyl/methyl silsesquioxane (WAPMSS) oligomer in D$_2$O and NaOD

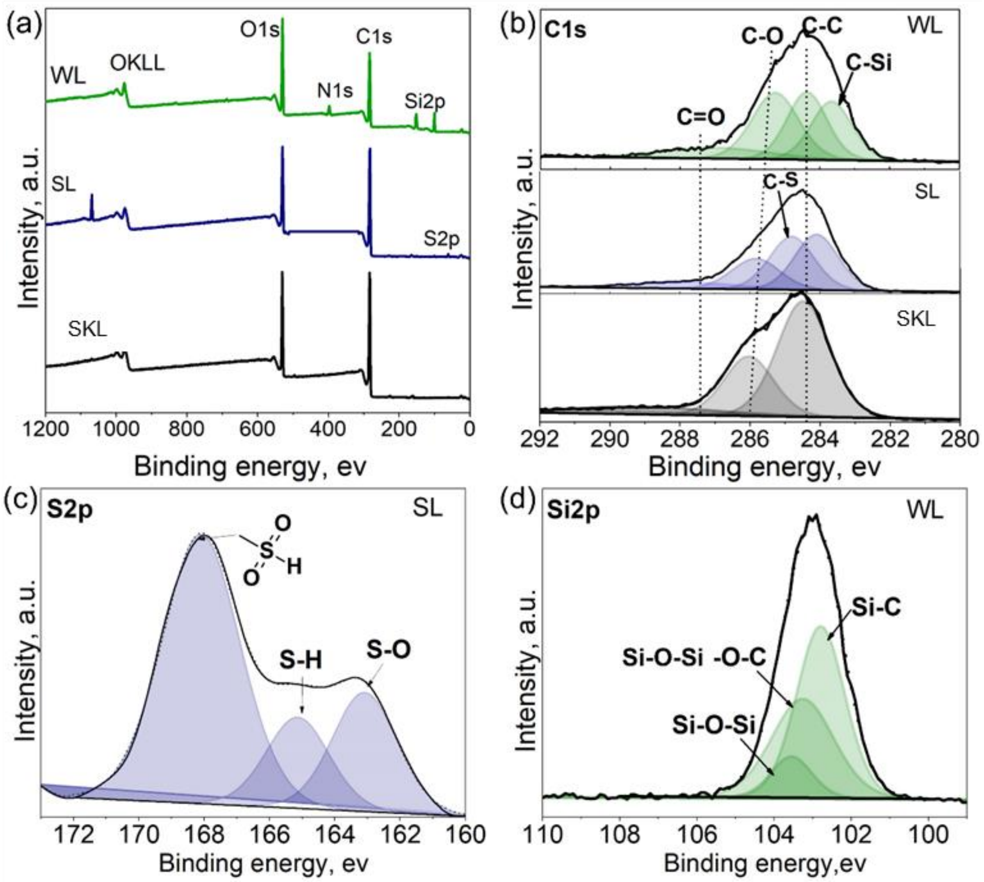

Figure S5.4. XPS wide spectra (a), C1s peaks deconvolution for SKL, SL, and WL (b), S2p peaks deconvolution for SL (c), and Si 2p peaks deconvolution for WL (d).

Fourier-transform infrared spectroscopy (FTIR)

The FTIR spectra of SKL, SL, and WL are shown in Figure S1. The transmittances at 1600, 1510, and 1425 cm^{-1} are distinctive peaks of aromatic ring vibrations for SKL. These distinctive peaks are present in both SL and WL, aligned with ^{1}H NMR and HSQC analyses. The transmittance peak at 3340 cm^{-1} is attributed to the aliphatic and phenolic OH stretching of SKL. A reduction in the intensity of the phenolic hydroxyl group peak is noticed for SKL and WL. This information can be used to support P-NMR results, as it confirms that phenolic OH groups of lignin were occupied by sulfoethyl groups for SL. According to P-NMR, silanol groups occupied all of the hydroxyl groups in WL. The signal at 1080 cm^{-1} in the SL FTIR spectra refers to the symmetric stretching vibration of the SO_3H group. Hence, the observed decrease in the peak corresponding to the phenolic hydroxyl group and the emergence of the SO_3H stretching vibrational group confirm the sulfoethylation of SL, as indicated by both FTIR and XPS analyses. The WL spectra indicated transmittance at 3750 cm^{-1} corresponding to free silanol (Si-OH) groups in organosilicon compounds. The transmittance at 3005 cm^{-1} corresponds to sp^2, which is the contribution of C-H associated with silicon. In addition, the high transmittance at 835 and 785 cm^{-1} is one of the characteristics of $Si\text{-}CH_3$. The siloxanes (Si-O-Si) had more intense infrared bands between 1008 and 1000 cm^{-1}. The presence of the mentioned transmittance signals on WL, aligned with the H-NMR, HSQC, and XPS analyses, confirmed the successful silanization of lignin.

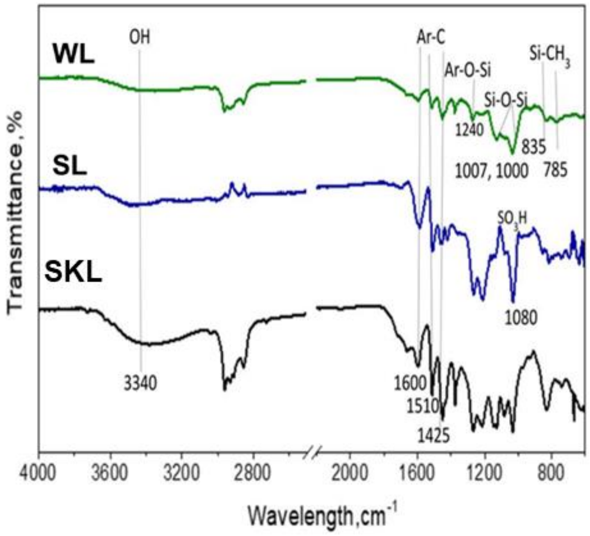

Figure S5.5. FTIR spectra for SKL, SL, and WL

Solubility, charge density, molecular weight (M_W), and thermal properties

The solubility and charge density of SKL and SL are listed in Table 1. The aim of this study was to examine the impact of sulfoethylation and silanization on the characteristics of the resultant polymers. However, because of the complete insolubility of the WL in aqueous solutions, it was not possible to quantify its charge density. In contrast, the process of sulfoethylation resulted in the formation water soluble SL. The solubility was enhanced by 6 gL^{-1} and the charge density was increased by 1.3 $mmolg^{-1}$ when sulfoethylation was applied on SKL. The enhanced solubility and charge density of sulfonated lignin (SL) can be ascribed to the presence of the sulfonate group covalently bonded to the phenolic group of lignin [82]. Also, the MW of SL and WL was higher, than that of SKL. The increase in the MW is attributed to the grafting of sulfoethyl group in the case of SL and grafting of WAPMSS molecules to the SKL structure for WL. The significantly higher Mw of WL is attributed to amine group from WAPMSS could induce further side reaction on the lignin backbone [83], such as the condensation crosslinking reaction, which was confirmed by NMR, FTIR, and XPS analyses.

In addition, the thermal treatment response of the polymers was analyzed using TGA and DSC, and results are presented in Table 1. The onset temperature (T_o), the temperature at which 50% weight loss ($T_{50\%}$), and the maximum decomposition temperature (DTG_{max}) were utilized to characterize the thermal sensitivity of the samples. SKL displayed a rapid weight loss at approximately 291°C with a 50% weight loss at approximately 510°C. Due to the intricacy of lignin biomacromolecules, its complete breakdown occurred between 510 and 520°C [84]. The decomposition of SL sample started at a lower temperature of 200 °C and50% of weight loss was observed 100°C lower than SKL. Also, the complete decomposition of the sample occurred at 415°C. This decrease in the thermal stability of the copolymer can be attributed to the destabilization of the polymer chain in the presence of the sulfonic acid group [85]. The desulfonation process for sulfonated materials includes a thermal desulfonation step that takes place at temperatures ranging from 200 to 400°C. This step mostly involves the release of SO_2 [86].

WL displayed a more distinctive decomposition behavior than SKL. The decomposition of WL started at higher temperatures, i.e., approximately 336°C, and 50% weight loss exhibited at a temperature higher than 600°C. The enhancement in the decomposition temperature of the WL was observed due to the condensation or crosslinking reaction of WAPMSS within SKL macromolecules, as evidenced by NMR, XPS, and FTIR analyses. Furthermore, the integration of Si into the WL macromolecular structure can be the reason for the rise in the maximum degradation temperature from 520°C to 669°C and to the increase in char residue from 2 % to 40 % for SKL and WL correspondingly [83].

The glass transition, T_g, of, SKL, SL and WL is listed in Table 1. $T_g$is strongly reliant on the molecular structure and crosslinking density of a polymer [87]. The T_g of SL polymer was not significantly higher than SKL. The T_g decrease was also observed for KLT (lignin treated the same way as SL without the reagent) which could be due to the removal of specific lost segments from the lignin macromolecular structure or the presence of active deprotonated sites in lignin structure during the pretreatment with NaOH and isopropanol. This potentially creates additional space within the molecular structure, allowing for increased molecular movement and ultimately leading to a decrease in the T_g.

Table S5.2. Solubility, charge density, molecular weight, onset temperature (T_o), temperature at 50% weight loss ($T_{50\%}$) glass transition temperature (T_g).

Samples	**Solubility, gL^{-1}**	**Charge density, mmol/g**	**Mw*10^5, g/mol**	**To °C**	**T_{50} %, °C**	**DTG_{max}, °C**	**T_g, °C**
SL	10	2.1 ± 0.05	(1.87±0.64)	200	410	415	153
SKL	4	0.8±0.02	(1.75±0.15)	291	510	520	158
WL	ND	ND	(2.14 ± 0.23)	336	600	669	185
KT	9	1.5±0.04	(1.51±0.24)	311	398	372	123

ND not determined.

± standard deviation

However, the T_g of WL was significantly higher than SKL due to the silanization of SKL. In this case, the crosslinking of WAPMSS and SKL through copolymerization led to the formation of a crosslinked structure, which effectively decreased the available space for chain movement. This reduction in chain mobility resulted in an elevated T_g. Consequently, the enhancement in the T_g can be attributed to the rise in molecular weight (as shown in Table 1) and the presence of a rigid silsesquioxane structure in the material, as well as possible crosslinking network because of chain reaction induced by the amine group from the oligomer [83].

Coating formulation visual appearance

Figure S5.6. Visual appearance of Coating formulations.

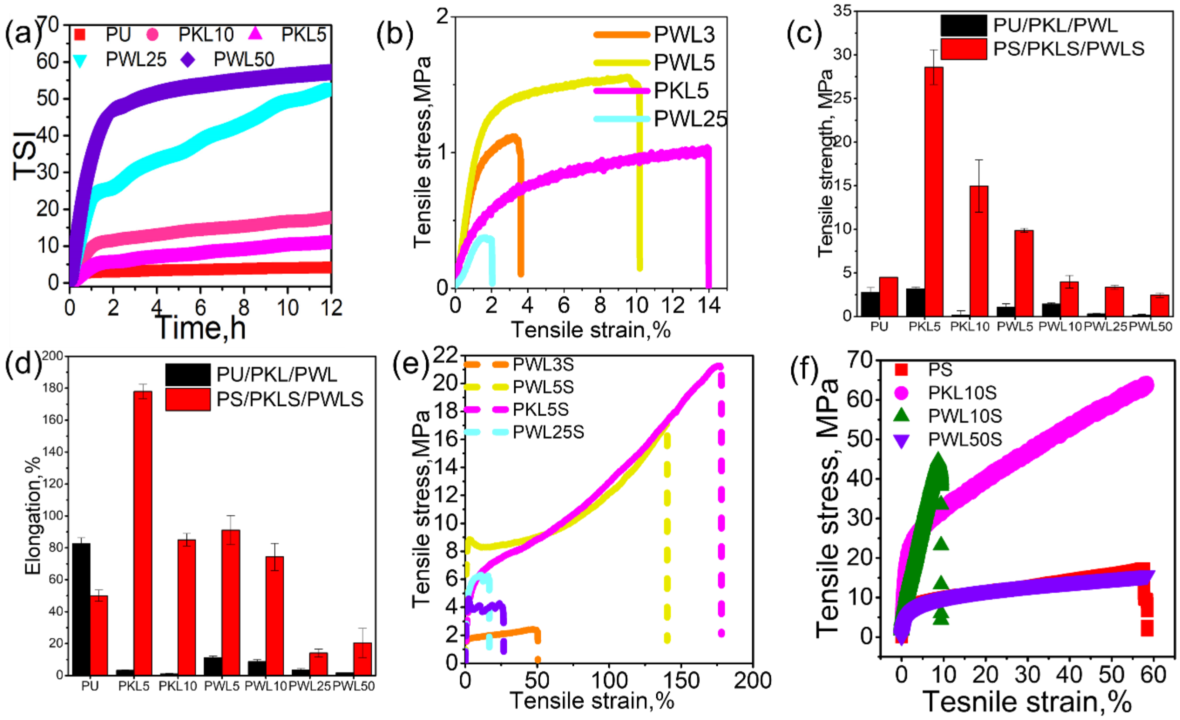

Figure S5.7. TSI (a), stress-strain of films (b), tensile strength (c), elongation at break (d), stress-strain after introduction of SL(S) of films (e), and stress-strain after recycling (f).

Figure S5.8. The appearance of PKL15 film without SL and with SL.

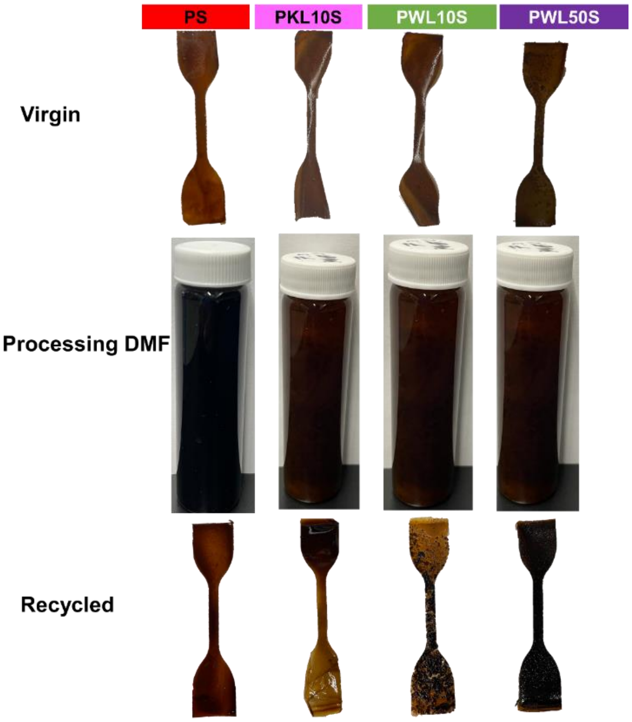

Figure S5.9. Recyclable behavior of PU films via solution casting DMF as a solvent.

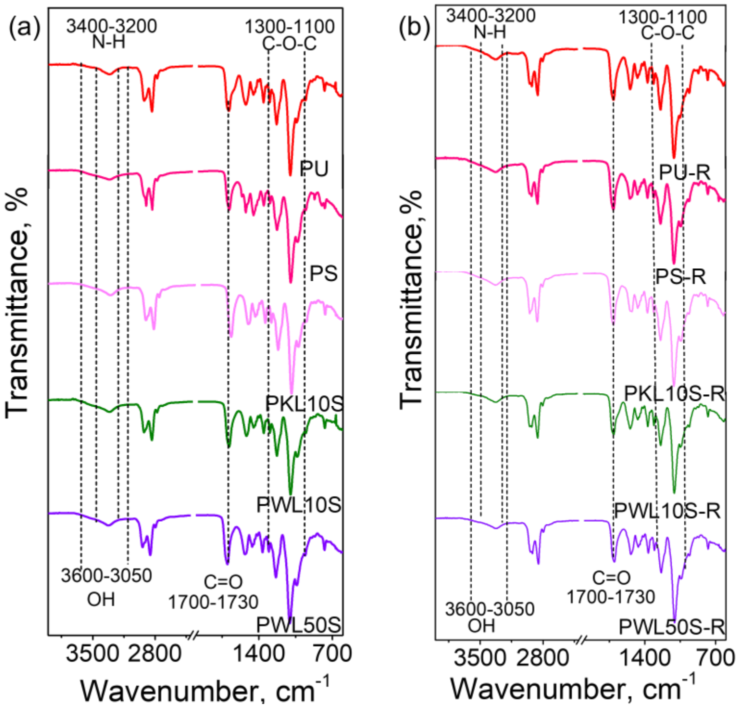

Figure S5.10. FTIR spectra of PU films as prepared (a) and after recycling (b)

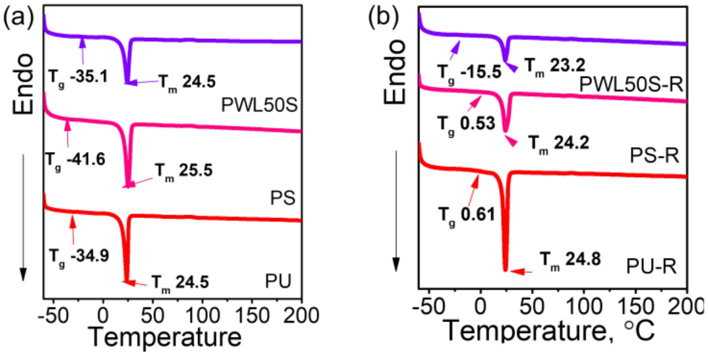

Figure S5.11. DSC graph showing melt temperature (T_m) and glass transition (T_g) temperatures for as prepared (a) and reprocessed PU films (b).

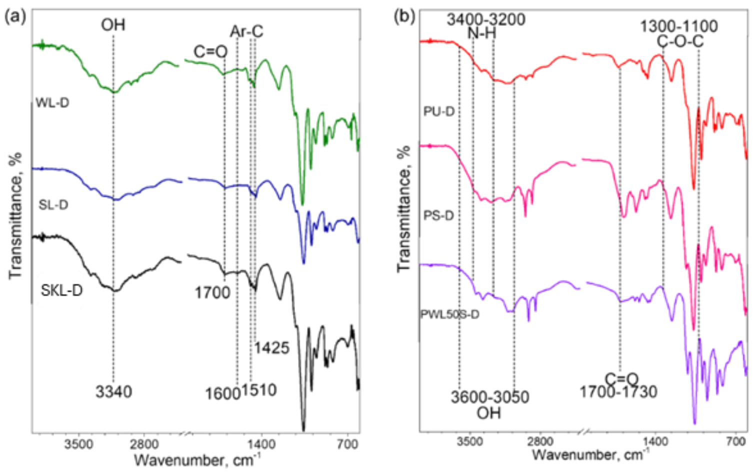

Figure S5.12. FTIR spectra of SKL, SL, and WL polymers after degradation (a), PU, PS, and PWL50S after degradation (b)

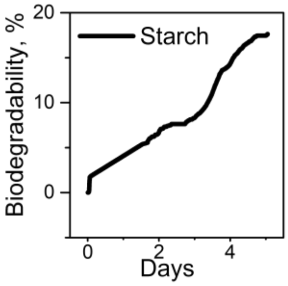

Figure S5.13. Biodegradability of starch.

Appendix 6A. Supporting information : 3D printable lignin-caprolactone copolymer

Banchamlak Bemerw Kassaun[1,2], Luyao Wang[2], Oskar Backman[2], Chunlin Xu[2], Pedram Fatehi[1,2]*

[1]Department of Chemical Engineering, Lakehead University, 955 Oliver Road, Thunder Bay, ON P7B 5E1, Canada, [2]Laboratory of Natural Materials Technology, Faculty of Science and Engineering, Åbo Akademi University, Turku, Finland.

$$\mathrm{Yield}(\%) = \frac{\mathrm{Wt}}{\mathrm{Wo}} \times 100 \qquad \textbf{(S6.1)}$$

Wt is the final weight, and Wo is the initial lignin (g) weight.

$$xi = \frac{Xi - X_c}{\Delta x_i}, i = 1,2,3 \dots\dots\dots\dots\dots z\text{-} \qquad \textbf{(S6.2)}$$

xi, dimension less value of an independent variable: Xi is the real value of an independent variable, X_c is the actual value of an independent variable at the center point, and ΔXi is the step change of the real value of the variable “i”.

$$N = 2p(p - 1) + C_p \qquad \textbf{(S6.3)}$$

N is the number of experiments, p is the number of factors, and Cp is the number of center points,

$$Y = f(x_{1,} x_{2,} x_{3,} \ldots\ldots\ldots\ldots\ldots\ldots x_{c,} + \mathrm{e} \qquad \textbf{(S6.4)}$$

Where f is the actual response function of an unknown format, and e is the error that illustrates the differentiation. The behavior of the response surface was examined for the response function of Y sing the second-order polynomial equation.

$$Y = \beta_o + \sum_{a=1}^{c}(\beta_a x_a) + \sum_{a=1}^{c}(\beta_{aa} x_a{}^2) + \sum a \sum_{b\leq 2}^{c} \beta_{ab}\, x_a\, x_b + e_a \qquad \textbf{(S6.5)}$$

Y is the response; x_a and x_b are variables (a and b range from 1 to c) β_0 is the model intercept coefficients; β_a, β_{aa}, and β_{ab} are interaction coefficients of linear, quadric, and second-order terms, respectively; c is the number of independent parameters (c=3 in this study); e_a is the error.

$$\alpha = \frac{\mathrm{BL_{OH}} - \mathrm{BLPCL_{OH}}}{\mathrm{BL_{OH}}} \times 100 \qquad \textbf{(S6.6)}$$

BL-OH -concentration of lignin hydroxyl groups, BLPCL-OH- concentration of BL-PCL hydroxyl groups, and α- the percentage of [CL] grafting [88].

$$n = (\frac{Ib}{Ia} + 1) \qquad \textbf{(S6.7)}$$

Ib and Ia correspond to the PCL chain's repeating and terminal ^{1}H NMR methylene intensities [12]. Besides the semi-quantitative strategy, another quantitative strategy is based on HSQC spectra, which selected “aromatic units” as IS. Particularly, the method uses a cluster of signals representative of all C9 units, i.e., IS. The choice of the 0.5IS2,6 + IG2 signals as IS is for hardwood lignin [89]. The results expressed how much linkage (<1.0) per aromatic ring.

$$\mathrm{IC9\ units} = 0.5\mathrm{IS}_{2,6} + \mathrm{IG}_2 \text{ (hardwood lignin)} \qquad \textbf{(S6.8)}$$

Where IS2,6 is the integration of S2,6, including S and S', IG2 is the integral value of G_2. IC_9 represents the integral value of the aromatic ring. According to the internal standard (IC9), the amount of IX% could be obtained by the following formula,

$$\mathrm{IX\%} = \mathrm{IX/IC9} \times 100\% \qquad \textbf{(S6.9)}$$

Where IX is the integral value of the α-position of A (β-O-4), B (β-β), C (β-5), and D (β-1), the integration should be in the same contour level.

Table S6.1. Minimum and maximum levels of three factors in terms of coded and uncoded symbols.

Factor	Name	Units	Type	Levels

				-1	0	+1	Std. Dev.
A	CL/OH	Mmol g^{-1}	Numeric	0.86	1.73	2.60	0.6152
B	Reaction time	Minutes	Numeric	120	420	720	212.13
C	Catalyst Conc	Wt. %	Numeric	0.50	0.75	1.00	0.1768

Table S6.2. Optimization parameters conditions limit and response parameters desirable goals.

Name	Goal	Lower Limit	Upper Limit	Lower Weight	Upper Weight	Importance
CL/OH	in range	0.86	2.6	1	1	3
Reaction time	in range	120	720	1	1	3
Catalyst Con.	minimize	0.5	1	1	1	3
Viscosity	maximize	194.2	10287	1	1	3
Melt Temperature	maximize	45	110	1	1	3
DP	maximize	3.52	10.13	1	1	3

Table S6.3. The birch alkali lignin interunit linkages ppm and groups from HSQC analysis.

Label	**Birch alkaline lignin δ_C /δ_H (ppm)**	**Groups**
-OCH$_3$	(54.6-57.2)/(4.1-3.2)	C-H in -OCH3 (methoxy)
-OCH$_3$(cond.)	(59.7)/(3.18-3.90)	Methoxy from 2/6 condensed units
B$_\beta$	(53.8-54.5)/(3.1-2.9)	B in resinol **β-β** units
C$_\beta$	53.0/3.47	B in phenylcoumaranan **β-5** units

A_{Υ}	60/3.4	ϒ in **β-O-4**
B_{Υ}	62.8/3.7	C_{γ}-H_{γ} in phenylcoumarane **β-5'**
X2	72.6/3.04	2 in β-D-xylopyranoside
X3	73.8/3.24	3 in β-D-xylopyranoside
X4	75.3/3.57	4 in β-D-xylopyranoside
X1	101.7/4.29	1 in β-D-xylopyranoside
B_{α}	85.0/4.68	α in resinol **β-β** units
AG_{α}	70.9/4.75	α in **β-O-4 linked to G** units
AG_{γ}	63.4/3.47	C_{γ}-H_{γ} in aryl glycerol unit
C_{α}	84.9/4.62	C_{α}-C_{α} in resinol **β-β'** units
$S_{2,6}$ (etherified)	103.3/6.72	2 and 6 in syringyl unit
$S_{2,6}$ (free phenolic)	105.7/6.49	2 and 6 in non-etherfied syringyl unit
$S'_{\mathbf{2,6}}$	106.1/7.22	2 and 6 in C_{α} oxidized syringyl unit
G_2	110.6/6.7	2 in guaiacyl units
G_2'	108.8/7.04	2 in non-etherified guaiacyl units
FA_2	115.1/6.94	2 in ferulic acid (ester)
$pCA_{2,6}$	130.4/7.51	2,6 in p-coumaric acid (ester)
pCA_{β}/FA_{β}	116.3/6.45	β in p-coumaric acid (ester) (pCAβ) and ferulic acid (ester) (FAβ)
G_5	115.9/6.7	5 in guaiacyl units
G_6	119.1/6.7	6 in guaiacyl units
G6'	122.9/7.5	6 in oxidized (C_{α}=O) guaiacyl units
$pCA_{\propto}/FA_{\propto}$	144.9/7.51	∝ in p-coumaric acid (ester) ($pCA_{\propto}$) and ferulic acid (ester) ($FA_{\propto}$)
$M_{\propto}$	111.95/6.13	∝ in aryl enol ether
D_{β}	126.3/6.8	β in cinnamaldehyde end groups
$H_{2,6}$	127.1/7.1	C2,6-H2,6 in p-hydroxybenzoate unit

Table S6.4. Coded and actual levels of reaction parameters (caprolactone to lignin hydroxyl concentration, reaction time, and catalyst concentration) and response variable (viscosity and melt temperature).

Run	Coded variables			Real variables			Response		
	A	B	C	A: CL/OH	B: reaction time	C: catalyst con.	Viscosity	Melt temp.	DP
				[mmol g^{-1}]	[minutes]	[wt.%]	[P]	[°C]	
BL$_E$P1	-1	0	-1	0.86	420	0.5	194.2	108	3.52
BL$_E$P2	+1	0	-1	2.6	420	0.5	546.83	48	7.02
BL$_E$P3	0	-1	-1	1.73	120	0.5	250.27	47	5.54
BL$_E$P4	+1	+1	-1	2.6	720	0.75	1519.5	52	7.82
BL$_E$P5	0	0	0	1.73	420	0.75	1505.6	50	5.91
BL$_E$P6	-1	0	1	0.86	420	1	3210.6	53	4.6
BL$_E$P7	0	0	0	1.73	420	0.75	3337.6	50	7.82
BL$_E$P8	+1	-1	0	2.6	120	0.75	734.55	48	7.6
BL$_E$P9	0	+1	+1	1.73	720	1	10287	50	6
BL$_E$P10	-1	-1	0	0.86	120	0.75	546.45	100	3.86
BL$_E$P11	-1	+1	0	0.86	720	0.75	2720.9	110	5.6
BL$_E$P12	0	0	0	1.73	420	0.75	330.61	50	4.74
BL$_E$P13	0	+1	-1	1.73	720	0.5	1231.1	100	6.83
BL$_E$P14	0	0	0	1.73	420	0.75	1323.3	50	5.61
BL$_E$P15	+1	0	+1	2.6	420	1	1200.4	54	10.13
BL$_E$P16	0	-1	+1	1.73	120	1	5323.8	45	5.93
BL$_E$P17	0	0	0	1.73	420	0.75	4748.2	55	7.69

Table S6.5. Analysis of variance (ANOVA) for viscosity linear model.

Source	Sum of Squares	df	Mean Square	F-value	p-value	
Model	5.040e^{+07}	3	1.680e^{+07}	3.88	0.0350	significant
A-CL/OH	8.917e^{+05}	1	8.917e^{+05}	0.2060	0.6574	
B-Reaction time	9.909e^{+06}	1	9.909e^{+06}	2.29	0.1542	
C-Catalyst Conc	3.960e^{+07}	1	3.960e^{+07}	9.15	0.0098	
Residual	5.627e^{+07}	13	4.328e^{+06}			
Lack of Fit	4.375e^{+07}	9	4.861e^{+06}	1.55	0.3552	not significant
Pure Error	1.252e^{+07}	4	3.130e^{+06}			
Cor Total	1.067e^{+08}	16				

R^2=0.847, adjusted R^2= 0.8954

Table S6.6. Analysis of variance (ANOVA) for melt temperature quadratic model.

Source	**Sum of Squares**	**df**	**Mean Square**	**F-value**	**p-value**	
Model	10421.03	9	1157.89	11.31	0.0021	significant
A: CL/OH	6384.50	1	6384.50	62.37	< 0.0001	
B: Reaction time	648.00	1	648.00	6.33	0.0400	
C: Catalyst Conc	242.00	1	242.00	2.36	0.1680	
AB	9.00	1	9.00	0.0879	0.7754	
AC	4.00	1	4.00	0.0391	0.8489	
BC	576.00	1	576.00	5.63	0.0494	
A^2	2227.37	1	2227.37	21.76	0.0023	
B^2	51.58	1	51.58	0.5039	0.5007	
C^2	151.58	1	151.58	1.48	0.2631	
Residual	716.50	7	102.36			
Lack of Fit	696.50	3	232.17	36.43	0.9914	not significant
Pure Error	20.00	4	5.00			
Cor Total	11137.53	16				

R^2=0.936, adjusted R^2=0.94

Table S6. 7. Analysis of variance (ANOVA) for degree of polymerization linear model.

Source	Sum of Squares	df	Mean Square	F-value	p-value	
Model	31.22	3	10.41	10.12	0.0010	significant
A-CL/OH	28.09	1	28.09	27.31	0.0002	
B-Reaction time	1.38	1	1.38	1.34	0.2679	
C-Catalyst Conc	1.76	1	1.76	1.71	0.2138	
Residual	13.37	13	1.03			
Lack of Fit	6.08	9	0.6757	0.3708	0.9004	not significant
Pure Error	7.29	4	1.82			
Cor Total	44.59	16				

R^2=0.7002, adjusted R^2=0.631,

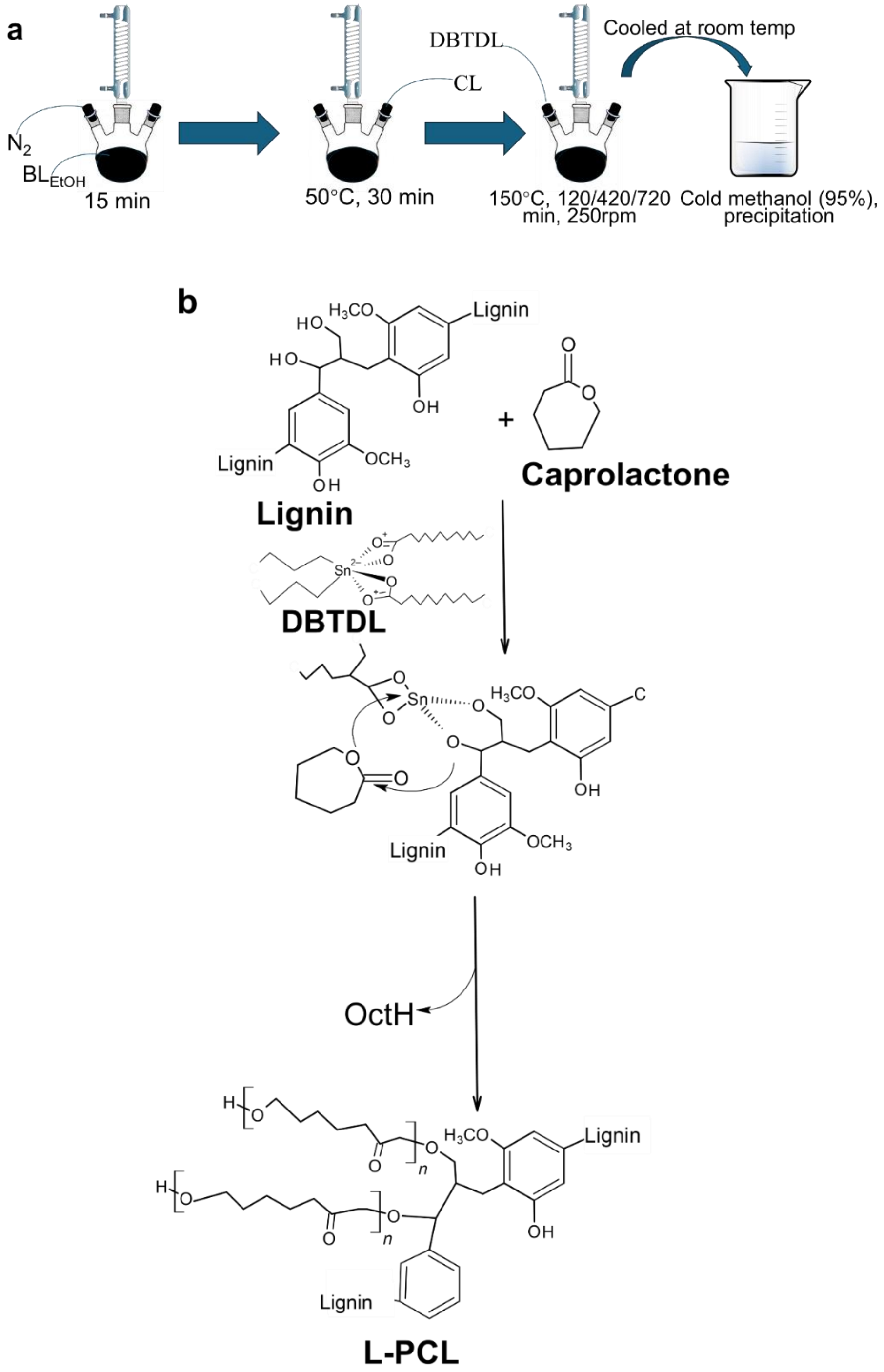

Figure S6.1. Preparation of BL-PCL (a) and Schematic representation of lignin-polycaprolactone (BL-PCL) synthesis using DBDTL as a catalyst, lignin as a micro initiator, and caprolactone (CL) monomer (b).

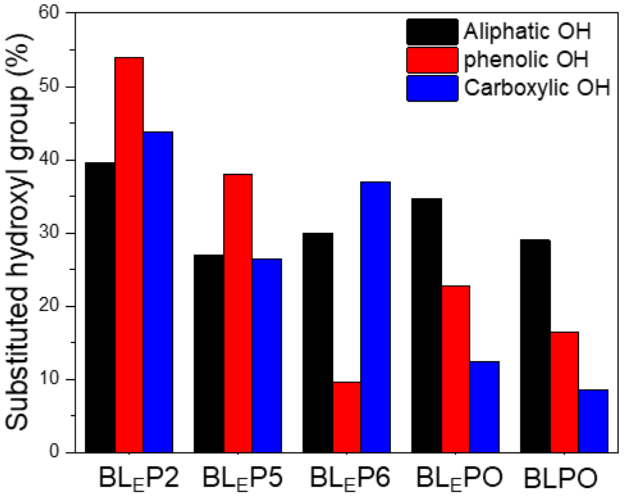

Figure S6.2. Substitution of hydroxyl groups of BL-PCL polymers after grafting caprolactone into lignin.

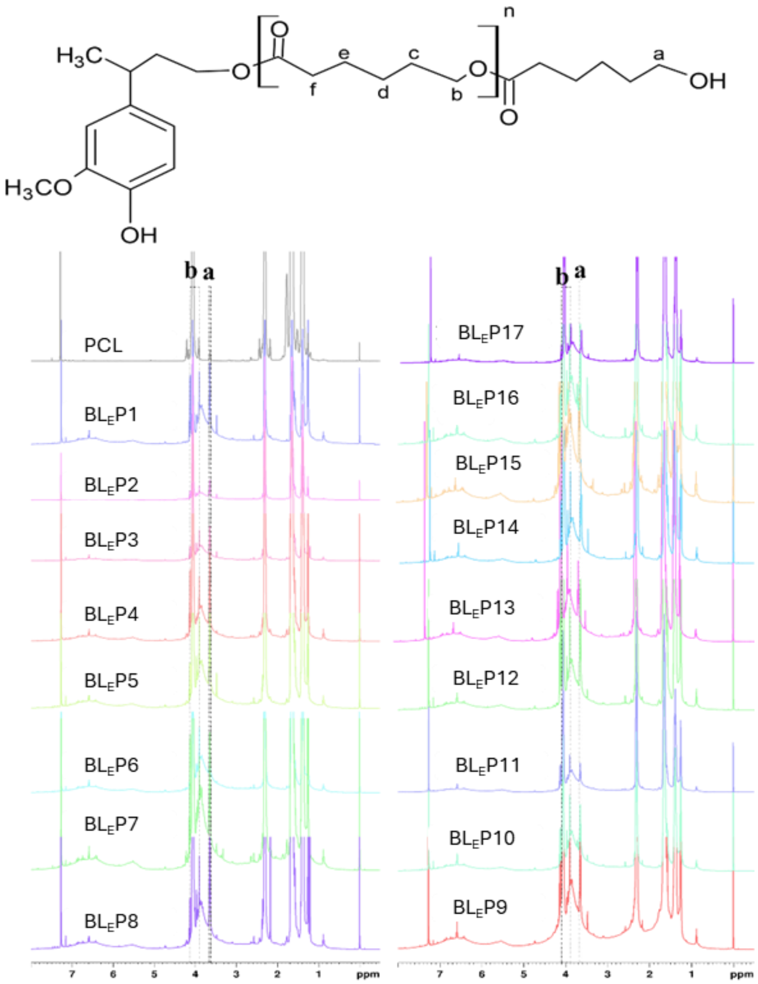

Figure S6.3. ^{1}H NMR spectra for all the polymers generated using the BBD-RSM design and reference commercial PCL sample.

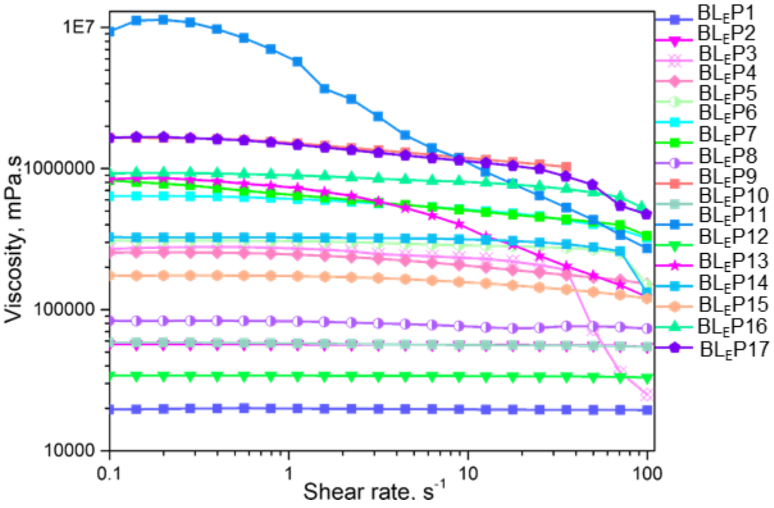

Figure S6.4. Viscosity at the melt temperature for all the polymers was generated using the BBD-RSM design.

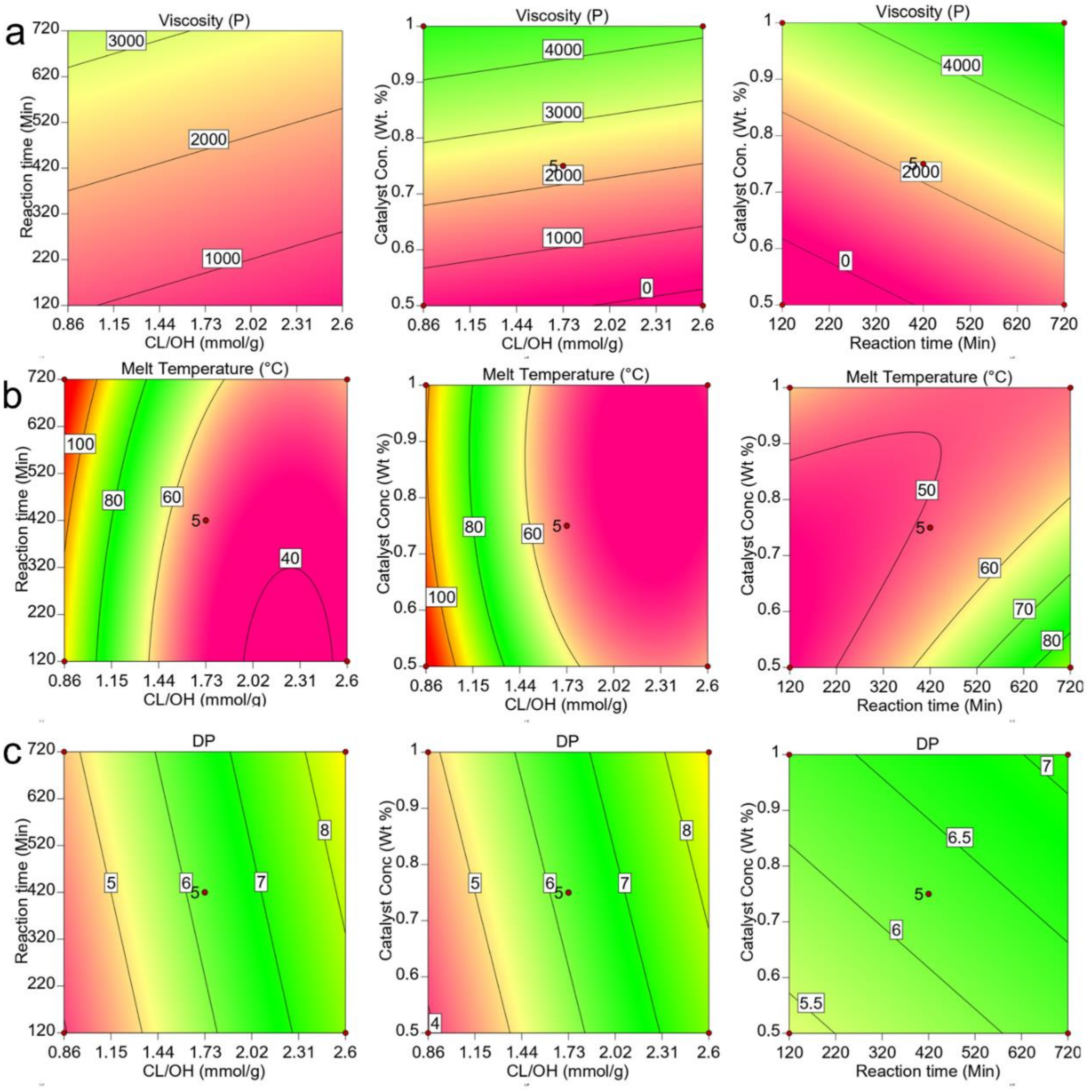

Figure S6.5. Contour graphs of two-factor interactions of CL/OH, reaction time, and catalyst concentration on viscosity (a), melt temperature (b), and degree of polymerization (c).

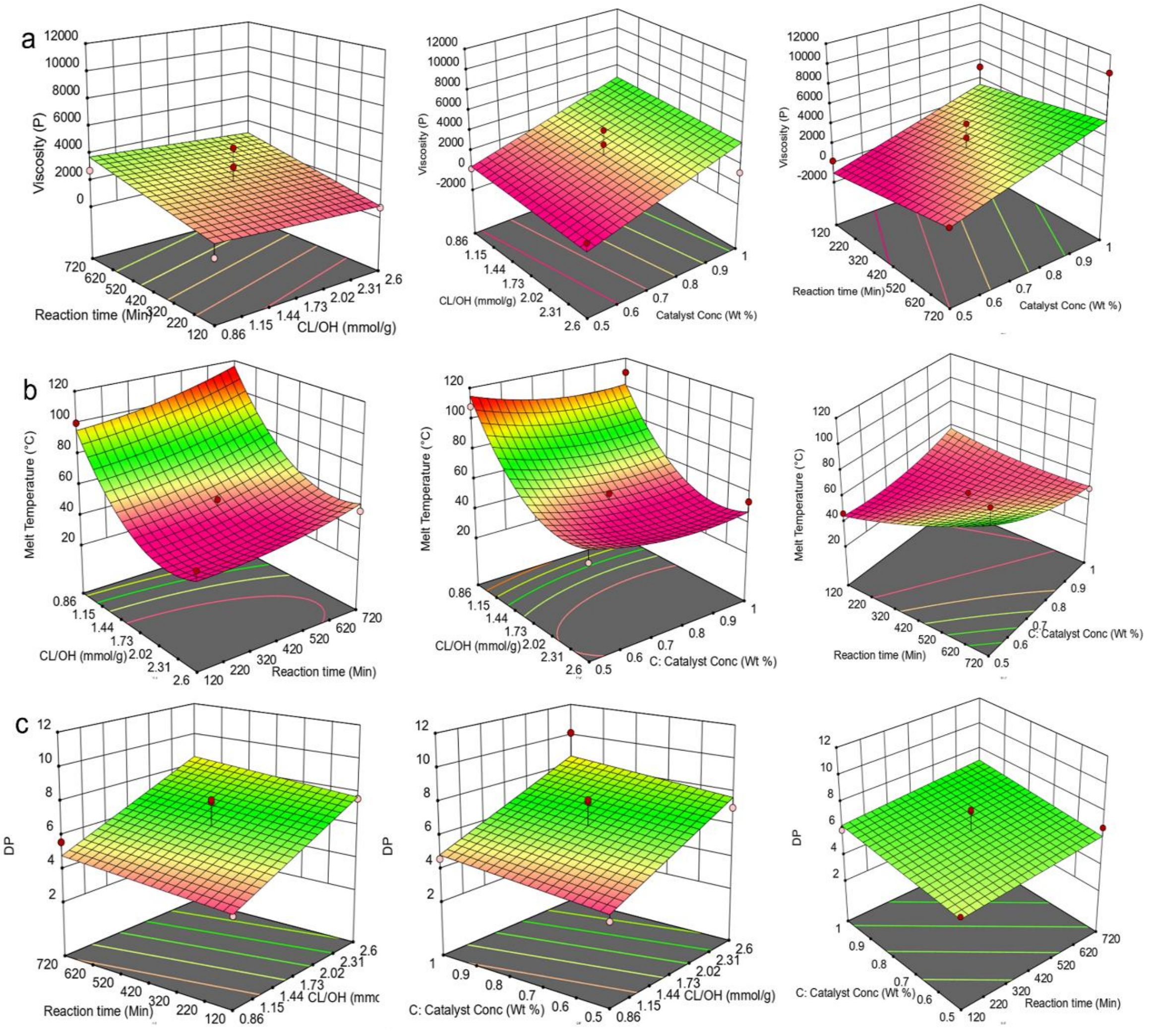

Figure S6.6. The three-dimensional (3D) plots of CL/OH, reaction time, and catalyst concentration on viscosity (a), melt temperature (b), and degree of polymerization (c).

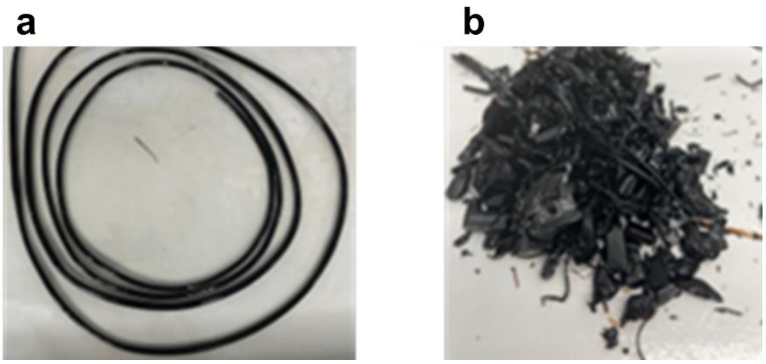

Figure S6.7. The appearance of BLPO filament (a), the appearance of BLPO when melted to make a film (b).

The BBD-RSM modeling for the lignin-caprolactone polymers

The BBD-RSM in design expert software optimized the reaction conditions and created a lignin caprolactone polymer with the required melt temperature and flow properties. Based on the model analysis, the data for the response viscosity is fitted in a linear model, as presented in **Table S6.3**. The relationship between viscosity and the experimental parameters (CL/OH, reaction time, and catalyst concentration) is shown in **Equation S6.10.** The coefficient of determination (R^2) is the ratio of the explained variation to the total variation and measures the degree of fit [90]. A good model fit that can predict the response variable using a predictor variable shows an R^2 closer to 1 [91]. This means that the response model evaluated in this study can explain the effect of experimental parameters on viscosity with an R^2 of 0.847, an adjusted R^2 of 0.895, and a confidence interval of 95%. In addition, the model's significance is evidenced by an F-value (3.88) and a low probability value (P=0.03). A P-value lower than 0.05 indicates that the model is statistically significant, whereas a value higher than 0.1 indicates that the model is not significant. In this case, the linear effect of catalyst concentration is a considerable model term. The Lack of fit F-value of 1.55 implies the lack of fit is insignificant relative to the pure error. The relationships between the viscosity and CL/OH, melt temperature, and DP are shown in **Figure S6.6**a and **Figure S6.5**a. Each plot shows the effects of two variables within their studied ranges, with the other variable fixed to zero level. The shape of the contour plot shows the nature and extent of the interactions between factors. An elliptical contour plot indicates a prominent interaction, whereas a negligible effect appears as a circular contour plot [92].

As can be seen from the plots, the viscosity increased with increasing catalyst concentration. The role of a catalyst in the viscosity of a lignin caprolactone polymer has yet to be investigated. However, the literature on the polymerization of lignin caprolactone polymer indicates that a catalyst plays a role in activating the reaction between lignin and the cyclic caprolactone polymer [28]. Metal complexes with unoccupied p, d, or f orbital functions are coordination catalysts rather than anionic initiators. These catalysts facilitate the synthesis of polymers with large molecular weights via the coordination/insertion process [93]. The molecular weight of BL_EP6 is higher than BL_EP5 (**Table 6.3**). Even though the CL/OH ratio is higher for BL_EP5, the catalyst concentration of BL_EP6 is higher, which leads to higher molecular weight and viscosity (**Table 6.3**).

$$\mathrm{Viscosity(P)} = -5274.2 - 383.7\frac{\mathrm{CL}}{\mathrm{OH}}\left(\frac{\mathrm{mmol}}{\mathrm{g}}\right) + 3.709\ \mathrm{reaction.time(min)} + 8899.7\mathrm{Catalyst\ con.\ (wt.\%)}\text{-} \qquad \textbf{(S6.10)}$$

$$\mathrm{Melt\ temperature\ (°C)} = 2.14.3 - 138.6\frac{\mathrm{CL}}{\mathrm{OH}}\left(\frac{\mathrm{mmol}}{\mathrm{g}}\right) + 0.13\mathrm{reaction\ time\ (min)} - 106.8\mathrm{catalyst\ con.\ (wt.\%)} - 0.0057\frac{\mathrm{CL}}{\mathrm{OH}}\left(\frac{\mathrm{mmol}}{\mathrm{g}}\right)\mathrm{reaction\ time(min)} + 4.59\frac{\mathrm{CL}}{\mathrm{OH}}\mathrm{catalyst\ con.\ (wt.\%)} - 0.16 \times \mathrm{reaction\ time(min)} \times \mathrm{catalyst\ con.\ (wt.\%)} + 30.4\frac{\mathrm{CL}}{\mathrm{OH}}\left(\frac{\mathrm{mmol}}{\mathrm{g}}\right)^2 + 0.000039\mathrm{reaction\ time(min.)}^2 + 96\mathrm{catalyst\ con.\ (wt.\%)}^2 \qquad \textbf{(S6.11)}$$

$$\mathrm{Degree\ of\ polymerization(DP)} = 0.54 + 2.2\frac{\mathrm{CL}}{\mathrm{OH}}\mathrm{(mmol/g)} + 0.001\mathrm{reaction\ time\ (min)} + 1.88\mathrm{catalyst\ con.\ (wt.\%)}\text{-} \qquad \textbf{(S6.12)}$$

Based on the model analysis, the data for the melt temperature can be fitted in a quadratic model, as presented in **Table S6.5**. The relationship between melt temperature and the experimental parameters (CL/OH, reaction time, and catalyst concentration) is shown in **Equation S6.11**. The response model evaluated in this study can explain the effect of experimental parameters on melt temperature with an R^2= 0.936, adjusted R^2=0.946, and a confidence interval of 95%. In addition, the model F-value of 11.31 and P-values were less than 0.05, implying that the model is significant. The effect of the CL/OH ratio, reaction time, the interaction of reaction time and catalysis concentration, and the square of the CL/OH ratio are significant. The lack of fit F-value of 36.43 implies that the lack of fit is insignificant.

The relationships between the melt temperature and the three factors are shown in **Figure S6.4**b and **Figure S6.5**b. Each plot shows the effects of two variables within their studied ranges, with the other variable fixed to zero level. The plots show that the T_m decreased with increased CL/OH ratio and catalyst concentration, while the increase in reaction time seems to increase the melt temperature. The decrease in T_m with an increase in CL/OH ratio and catalyst concentration might be due to increased initiation and activation of the caprolactone monomer for ROP, resulting in increased chain growth of PCL in the lignin backbone as evidenced by the DP (**Table S6.3**) [12, 94]. The increase in T_m with an increase in reaction time could be related to increased chain entanglements and stronger intermolecular forces [12]. Nevertheless, extended reaction durations result in heightened chain branching or degradation, potentially reducing the melting temperature [95].

Based on the model analysis, the data for the DP can be fitted in a linear model, as presented in **Table S6.6**. The relationship between DP and the experimental parameters (CL/OH, reaction time, and catalyst concentration) is shown in **Equation S.6** The response model evaluated in this study can explain the effect of experimental parameters on DP with an R^2=0.7002, adjusted R^2=0.631, and a confidence interval of 90%. In addition, the model F-value of 10.12 and P-values were less than 0.05, implying that the model is significant. In this case, the concentration of CL/OH shows a statistically significant effect on the DP of lignin-PCL polymers, as shown by a P-value of 0.0002. The lack of fit F-value of 36.43 implies that the lack of fit is insignificant.

The relationship between DP and the three factors is shown in **Figure S6.6**c and **Figure S6.5**c. Each plot shows the effects of two variables within their studied ranges, with the other variable fixed to zero level. Increased CL/OH ratio, reaction time, and catalysis concentration increase the DP. An increased CL/OH ratio means increased polymerization rate and higher DP. At the same time, prolonged reaction time allows for more extensive polymerization, leading to higher molecular weight and longer polymer chains, and higher catalyst concentration would lead to faster polymerization rates and higher DP by providing more active sites for the polymer chain initiation. However, excessive caprolactone concentration, longer reaction time, and higher catalyst concentration could hurt the resultant polymer, leading to the creation of undesired by-product or incomplete polymerization, undesired side reactions such as chain branching/degradation, and crosslinking or gelation, respectively [88, 95, 96]. Therefore, optimizing the CL/OH ratio, reaction time, and catalyst concentration is crucial to achieving the desired balance between DP, viscosity, and melt temperature.

The primary objective of the experimental analyses was the nature of the BL-PCL polymer to be 3D printable. For a polymer to be 3D printable by the extrusion method, shear thinning, and melt temperature are essential characteristics. Since lignin has shear thickening and doesn't have a melt temperature, the DP of PCL plays a significant role in achieving a shear thinning and melt temperature of lignin-caprolactone polymers. Therefore, the optimization function in the design expert software was used to obtain the optimal conditions for the polymerization of lignin-caprolactone polymer reaction conditions, as discussed in the methodology (**Table S6.2**).

Appendix 7A.Supporting information: Lignin-caprolactone polymer for coating: Effect of lignin source, type, and fractionation.

$$\text{Yield}(\%) = \frac{\text{Wt}}{\text{Wo}} \times 100 \qquad \textbf{(S7.1)}$$

Wt is the final weight, and Wo is the initial lignin (g) weight.

Besides the semi-quantitative strategy, another quantitative strategy is based on HSQC spectra, which selected "aromatic units" as IS. Particularly, the method uses a cluster of signals representative of all C9 units, i.e., IS [97]. The results expressed how much linkage (<1.0) per aromatic ring.

IC9 units = $0.5IG_2$ (Softwood kraft lignin) **(S7.2)**

IC9 units = $0.5IS_{2,6} + IG_2$ (hardwood lignin (birch alkali lignin)) **(S7.3)**

IC9 units = $0.5IS_{2,6} + IG_2 + 0.5IH_{2,6}$ (grass lignin(wheat straw lignin)) **(S7.4)**

$$\alpha = \frac{\text{BL}_{\text{OH}} - \text{BLPCL}_{\text{OH}}}{\text{BL}_{\text{OH}}} \times 100 \qquad \textbf{(S7.5)}$$

Where IG_2 is the integral value of G_2, $IS_{2,6}$ is the integration of $S_{2,6}$, including S and S'. IH_2 is the integral value of $H_{2,6}$. IC9 represents the integral value of the aromatic ring. According to the internal standard (IC9), the amount of I_X% could be obtained by the following formula:

$$IX\% = IX/IC9 \times 100\% \qquad \textbf{(S7.6)}$$

Where IX is the integral value of the α-position of A (β-O-4), B (β-β), C (β-5), and D (β-1), the integration should be in the same contour level.

BLOH -concentration of lignin hydroxyl groups, BLPCLOH- concentration of BL-PCL hydroxyl groups, and α- the percentage of [CL] grafting.

$$n = \left(\frac{Ib}{Ia} + 1\right) \qquad \textbf{(S7.7)}$$

Ib and Ia correspond to the PCL chain's repeating and terminal ^{1}H NMR methylene intensities.

Table S7. 1. The softwood kraft, birch alkali, wheat straw alkali lignin interunit linkages ppm and groups from HSQC analysis.

Label	**Lignin** **δ_C/δ_H (ppm)**	**Groups**
$-OCH_3$	(54.6-57.2)/(4.1-3.2)	C-H in -OCH3 (methoxy)
$-OCH_3$(cond.)	(59.7)/(3.18-3.90)	Methoxy from 2/6 condensed units
B_β	(53.8-54.5)/(3.1-2.9)	B in resinol **β-β** units
C_β	53.0/3.47	B in phenylcoumaranan **β-5** units
A_Υ	60/3.4	ϒ in **β-O-4**
B_Υ	62.8/3.7	C_γ-H_γ in phenylcoumarane **β-5'**
X2	72.6/3.04	2 in β-D-xylopyranoside
X3	73.8/3.24	3 in β-D-xylopyranoside
X4	75.3/3.57	4 in β-D-xylopyranoside
X1	101.7/4.29	1 in β-D-xylopyranoside
B_α	85.0/4.68	α in resinol **β-β** units
AG_α	70.9/4.75	α in **β-O-4 linked to G** units
AG_γ	63.4/3.47	C_γ-H_γ in aryl glycerol unit
C_α	84.9/4.62	C_α-C_α in resinol **β-β'** units
$S_{2,6}$ (etherified)	103.3/6.72	2 and 6 in syringyl unit
$S_{2,6}$(free phenolic)	105.7/6.49	2 and 6 in non-etherfied syringyl unit
$S'_{\mathbf{2,6}}$	106.1/7.22	2 and 6 in C_α oxidized syringyl unit
G_2	110.6/6.7	2 in guaiacyl units
G_2'	108.8/7.04	2 in non-etherified guaiacyl units
FA_2	115.1/6.94	2 in ferulic acid (ester)
$pCA_{2,6}$	130.4/7.51	2,6 in p-coumaric acid (ester)
pCA_β/FA_β	116.3/6.45	β in p-coumaric acid (ester) (pCAβ) and ferulic acid (ester) (FAβ)
G_5	115.9/6.7	5 in guaiacyl units
G_6	119.1/6.7	6 in guaiacyl units
G6'	122.9/7.5	6 in oxidized (C_α=O) guaiacyl units
$pCA_{\propto/}FA_\propto$	144.9/7.51	∝ in p-coumaric acid (ester) ($pCA_\propto$) and ferulic acid (ester) ($FA_\propto$)
$M_\propto$	111.95/6.13	∝ in aryl enol ether

D_{β}	126.3/6.8	β in cinnamaldehyde end groups
$H_{2,6}$	127.1/7.1	C2,6-H2,6 in p-hydroxybenzoate unit

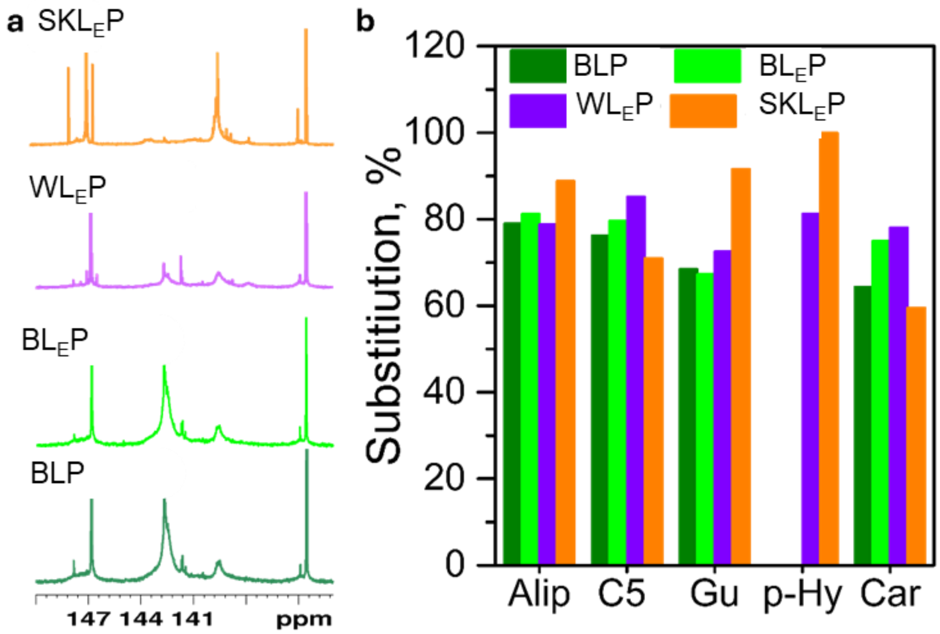

Figure S7. 1. ^{31}P NMR spectra of lignin-caprolactone polymers (a), substitution of hydroxyl groups (aliphatic, C5 substituted, guacamole, p-hydroxyphenyl, and carboxylic acid) (b).

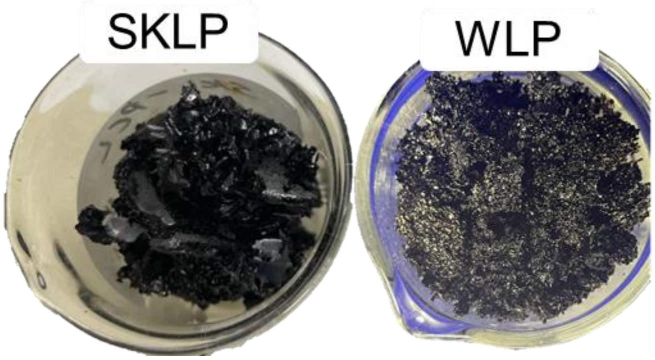

Figure S7. 2. SLP (softwood kraft lignin-caprolactone polymer) (a) and WLP (wheat straw alkali lignin-caprolactone polymer (b) appearances.

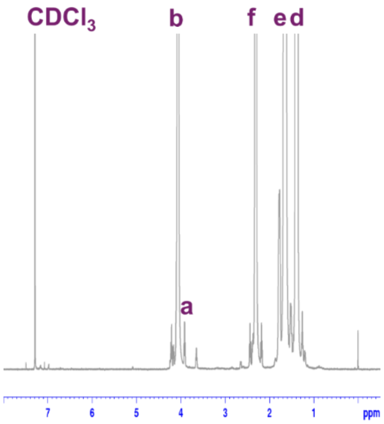

Figure S7. 3. ^{1}H NMR spectra of polycaprolactone polymers

Figure S7. 4. Wood contact angle

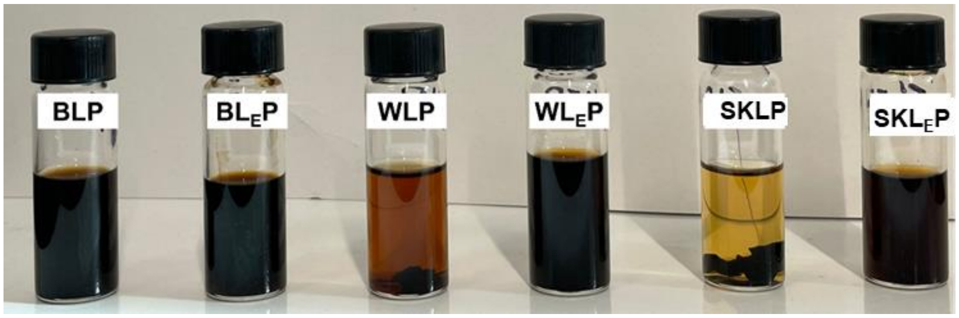

Figure S7. 5. Appearance of Lignin-caprolactone polymers in acetone

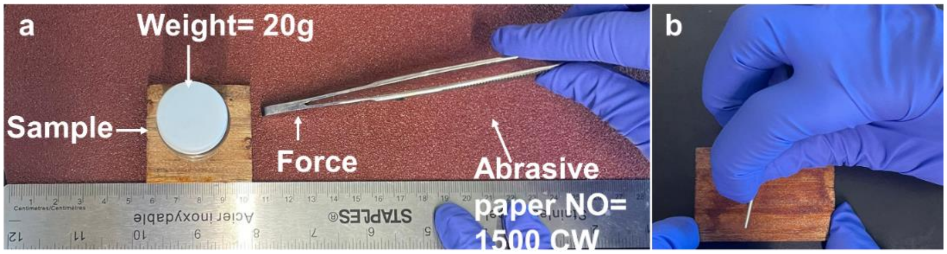

Figure S7. 6. Sand abrasion (a), and Knifing (b)